KEK Progress Report 2021-6
December 2021

KEK-MSL REPORT 2020

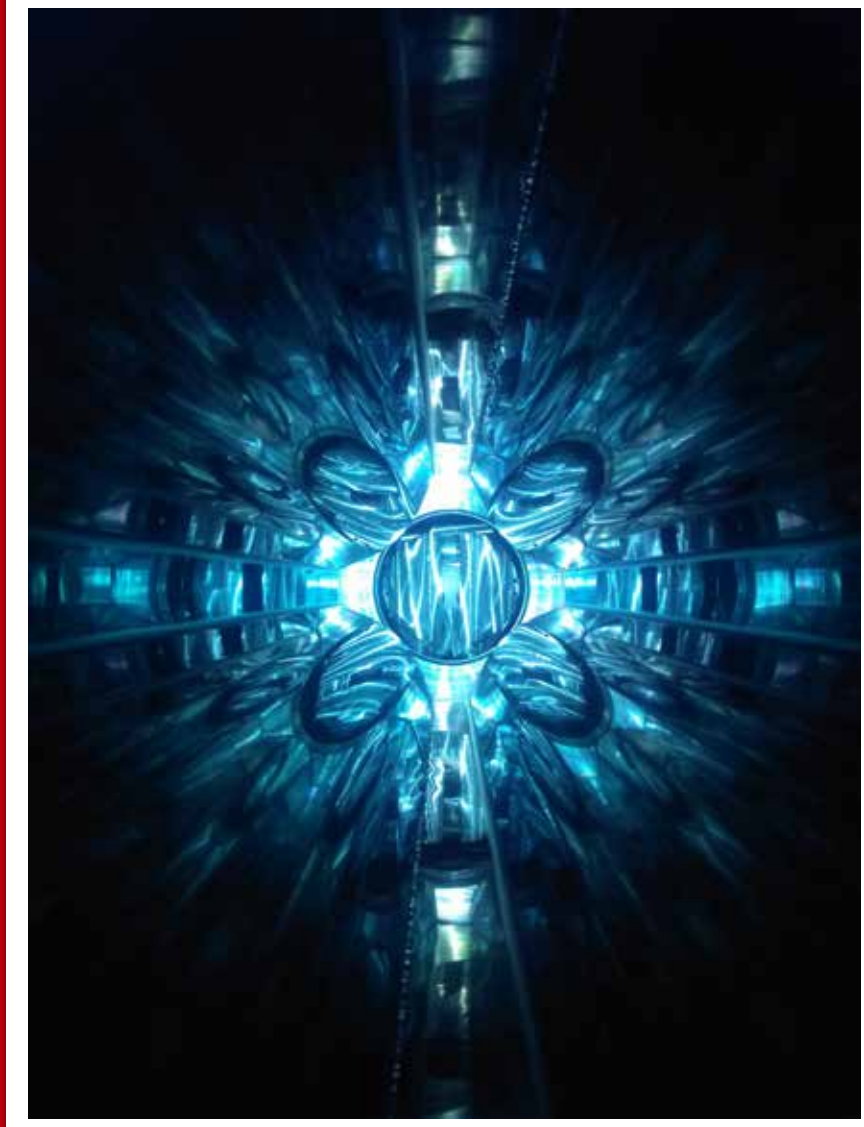

Muon Science Laboratory
Institute of Materials Structure Science
High Energy Accelerator Research Organization

KEK Progress Report 2021-6 M

KEK Reports are available from :

High Energy Accelerator Research Organization (KEK)
1-1 Oho, Tsukuba-shi,
Ibaraki-ken, 305-0801
JAPAN

Phone: +81-29-864-5137
Fax: +81-29-864-4604
E-mail: irdpub@mail.kek.jp
Internet: https://www.kek.jp/en

KEK-MSL REPORT 2020

Edited by Koichiro Shimomura

Preface

We are pleased to deliver this Annual Report on KEK-MSL activities in FY2020.
Due to the worldwide outbreak of COVID-19, the J-PARC MLF muon facility was forced to stop the beam from April 20 to 30. And in November, the beam was stopped again for an extended maintenance period of the neutron source. We would like to take this opportunity to apologize for any inconvenience this may have caused to users.

At the D-line, various interdisciplinary research, such as non-destructive elemental analysis of historical materials, have become popular. At the S-line, many materials and life science researces were performed in the S1 area. At the U-line, steady development of lasers is ongoing. In addition to these, many other developments are reported in this facility report. We are also glad to deliver fresh reports on many new results over diverse fields found in the scientific and oversea activities sections.

Above all, it is a great pleasure to announce that Professor Emeritus K. Nagamine was awarded the Orders of the Sacred Treasure this year.

Finally, I would like to acknowledge all of those who contributed to this REPORT, and express my thanks to Ms. N. Ichimura for her editorial work.

Koichiro Shimomura
Professor
Head of Muon Science Laboratory
IMSS, KEK

Table of Contents

Facility Report

Scientific Activities

REPORT OF THE INTERNATIONAL ADVISORY COMMITTEE ON THE J-PARC PROJECT

Appendix

Pictures:

Cover..... *Inside view of the floral-shaped beam duct to the S1 area.*
Facility Report..... *Inside view of the laser amplifier pumping module.*
Scientific activity.... *A snap shot of the first beam commissioning for the CYCLOPS spectrometer in the S1 area (January 2021).*

Facility Report

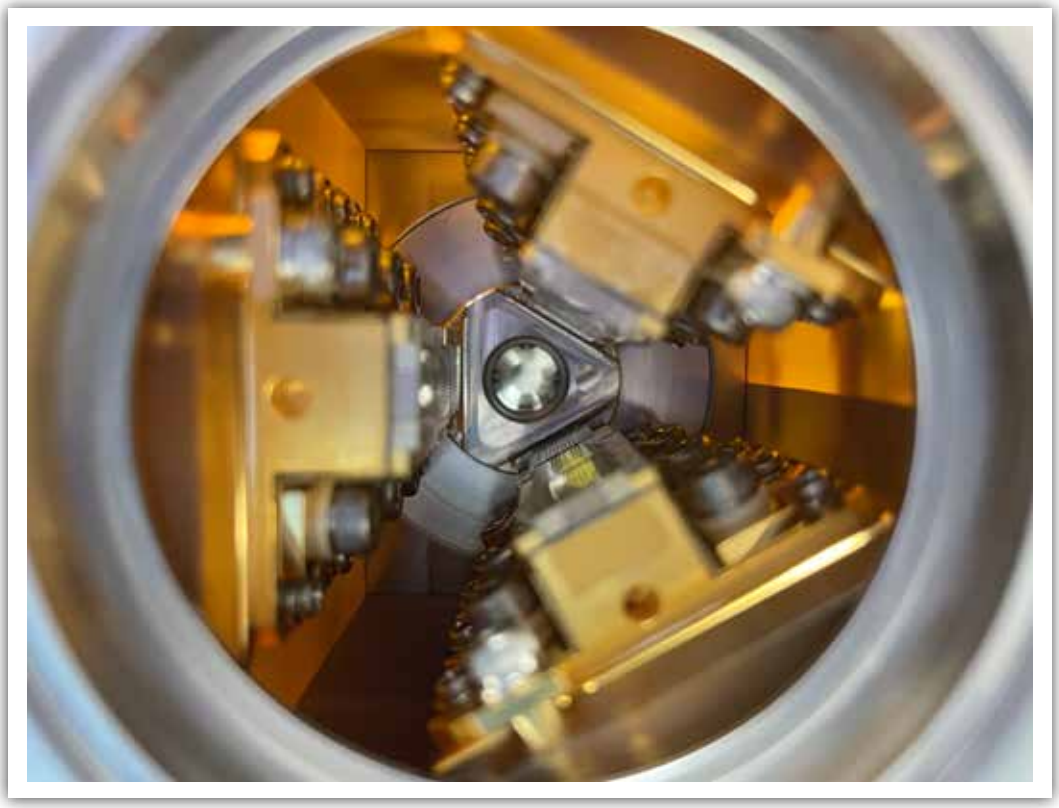

MUSE Facility Overview

R. Kadono[1,2], K. Shimomura[1,2], A. Koda[1,2], P. Strasser[1,2], T. Yamazaki[1,2], S. Kanda[1,2], S. Takeshita[1,2], Y. Ikedo[1,2], Y. Kobayashi[1,2], J. G. Nakamura[1,2], T. Yuasa[1,2], N. Kawamura[1,2], Y. Oishi[1,2], Y. Nagatani[1,2], S. Matoba[1,2], S. Nishimura[1,2], S. K. Dey[1,2], W. Higemoto[2,3], and T. U. Ito[2,3]

[1]*Muon Science Laboratory, Institute of Materials Structure Science, KEK*
[2]*Muon Science Section, Materials and Life Science Division, J-PARC Center*
[3]*Advanced Science Research Center, JAEA*

1. Development of real-time temperature monitoring system for the muon target

Real-time monitoring of the target temperature is extremely important to prevent severe accidents in the rotating target system. While thermocouples have been installed on the cool-ing jacket to measure the temperature rise due to thermal radiation from the rotating target, the slow response of thermocouples (typically in minutes) makes it difficult to detect a sudden temperature rise caused by some serious trouble such as target rotation stoppage. For the real-time temperature detection, we have been developing a monitoring system based on the infra-red (IR) camera.

Figure 1a shows the temperature distribution of the rotating target during the 1-MW operation observed by the IR camera. The high-temperature part (shown in yellow) can be ob-served flowing from the center of the target to the right (the direction of rotation). The measured temperature rise of the rotating target at the start of the beam operation is shown in Fig. 1b, where it takes about one hour using thermocouples to reach the actual temperature inferred from the IR camera.

The real-time sensitivity of the IR camera is also demonstrated by the temperature fluctuations associated with the fluctuations of the irradiated beam shown in Fig. 1b. The analysis regarding the relationship between the temperature change and thermal conductivity upon proton beam irradiation is in progress for the 1-MW operation.

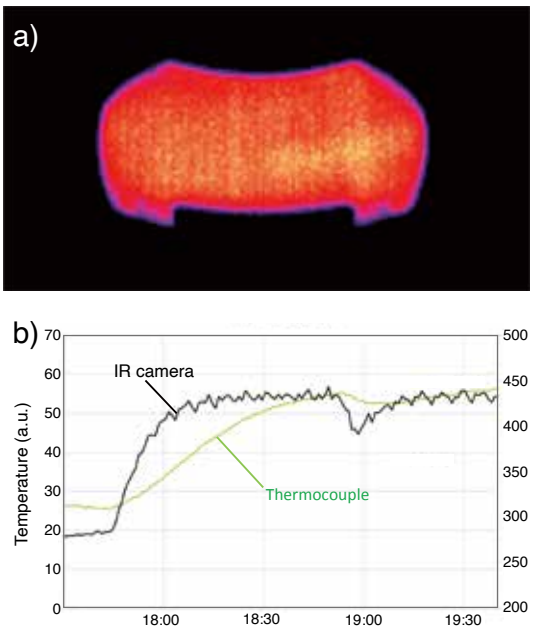

Fig. 1: a) An infrared (IR) camera image of the rotating target during 1-MW-beam operation. b) Temperature rise of the rotating target upon resumption of the beam operation. The temporary beam halt at around 18:50 is clearly identified by the target temperature monitored by the IR camera.

2. Construction of the H-Line

The H-line is a new beamline under construction since FY2012 in Experimental Hall #1 of the MLF building. Its layout drawing is shown in Fig. 2. It is a general-purpose beamline that can deliver both decay and surface muons and has branches to two experimental areas named H1 and H2. The designed surface muon flux reaches 10^8 muons/s with a proton beam power of 1 MW owing to a large acceptance (108 mSr) capture solenoid and other beamline magnets with large apertures.

In FY2020, the construction of the main (upstream) part of the H line and the first branch (to the H1 Area) progressed to secure the minimal components required to deliver muons to the H1 Area for beam commissioning. All vacuum devices were connected (see Fig. 2), electrical cabling and cooling water piping for two bending magnets (HB1 and HB2) were conducted, and a safety interlock system was implemented to be incorporated into the whole MLF system. Although the capture solenoid (HS1), transportation solenoids (HS2 and HS3), focusing quadrupole triplets, and a DC-separator are not ready, the surface muon flux is expected to be 6×10^5 muons/s without these components. In the next summer shutdown, we plan to conduct the remaining works such as electrical cabling and cooling water piping of all magnets and installation of a DC separator and beam slits to achieve the design intensity of 10^8 muons/s.

Progress was also made in preparing the second branch of the H-line (to the H2 Area). Since the muon g-2/EDM experiment proposed for the H2 Area requires a 50-meter LINAC to accelerate

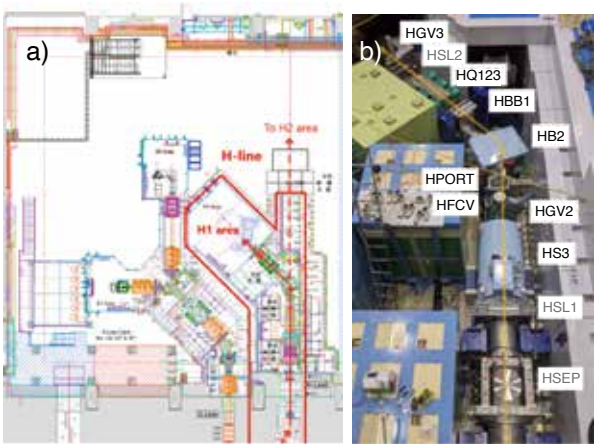

Fig. 2: a) A layout drawing of the H-line, and b) a snapshot showing vacuum devices for the beamline to the 1st branch, which were connected during the summer shutdown in FY2020.

muons to 212 MeV, the construction of an extension building is planned on the east side of the MLF where the parking lot is located. In FY2020, the detailed design of the extension building was completed, and geotechnical investigation and buried cultural property research were conducted on the construction site.

3. Laser system for Ultra-slow muons

Ultra-slow muons can be generated by resonant optical ionization of thermal muonium from hot-W foil target. Light pulses of 122.09 nm (Lyman-α) and 355 nm are required for the $1s$ to $2p$ state excitation and $2p$ to ionization, respectively. The high power pulsed coherent Lyman-α light source is one of the key elements for the efficient generation of ultra-slow muons.

In FY2020, more than 10 μJ Lyman-α pulses have been stably generated from 212.556 nm and 820 nm light pulses using the two-photon-resonant four-wave-mixing method attained by nonlinear wavelength conversions of a 100 mJ 1062.78 nm pulse delivered from Nd:YGAG (1 at.% Nd doped $Y_3Ga_2Al_3O_{15}$) ceramic laser amplifiers. Although we are targeting 1J-level 1062.78 nm pulses to achieve the required Lyman-α output power, the problem of Ga inhomogeneity in Nd:YGAG has prevented for years the realization of the large-aperture laser medium (>10 mm in diameter) for the amplifier required for this purpose.

To overcome this problem, we have been developing Nd:YSAG ceramic (Ga substituted with Sc), and a newly fabricated middle-size (ϕ9 mm, 112 mm long) Nd:YSAG ceramic was delivered for testing the amplification gain and wavefront distortion. While the amplification gain was satisfactory, distortion of the transmitted wavefront was exposed, which resulted in the reduction of the wavelength conversion efficiency in the subsequent

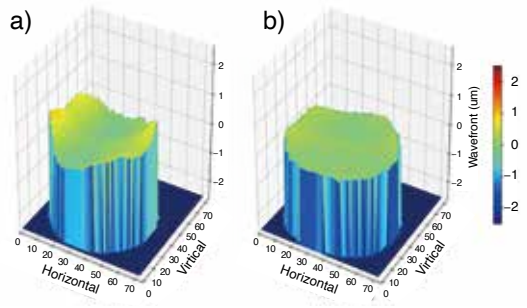

Fig. 3: The wavefront distortion in Nd:YSAG ceramic for final amplifier before (a) and after (b) after the compensation by a deformable mirror system.

stages due to the collapsed beam shape. In order to compensate for the distortion occurring inside the Nd:YSAG ceramic, we introduced an active 40-segment deformable mirror combined with the Shack-Hartmann wavefront sensor that was placed before and after the amplifier, respectively. The measured wavefront distortion is shown in Fig. 3, where the distortion is removed after the compensation. The method obtained by these studies will be applied to a practical laser system to implement the enhancement of Lyman-α optical intensity.

4. Construction of the S2 Area

The S2 Area is under construction for the precise measurement of the muonium 1s-2s transition energy by the resonant laser ionization (S1-type proposal by Okayama U. group, supported by Kakenhi). To allow for the laser experiment and ensure safety, the entire area is shaded by walls and removable roofs. The muon beam interlock system is almost the same as that for the S1 Area. A laser hut has been installed next to the S2 Area for immediate access. The hut is made of a marine container, so that it can be easily moved by crane. The construction of the S2 Area has been nearly completed in the summer shutdown of FY2020. The rest of the work will be completed after the approval from the Nuclear Regulatory Commission to deliver the first beam in the early FY2021.

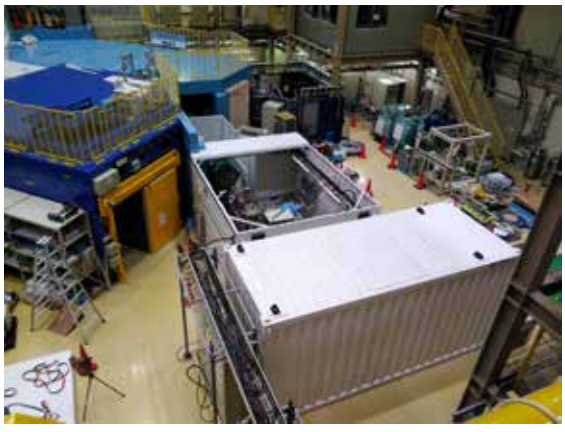

Fig. 4: A snapshot of the S2 Area (with roofs temporally removed) and laser hut viewed from the downstream of the S-line.

Present Status of Muon-beam Source

N. Kawamura[1,2], S. Matoba[1,2], Y. Kobayashi[1,2], and A. Koda[1,2]

[1]*Muon Science Section, Materials and Life Science Division, J-PARC Center*
[2]*Muon Science Laboratory, Institute of Materials Structure Science, KEK*

The muon production target and the frontend part of each muon beamline are located in the M2 tunnel as well as the primary beamline, as shown in Fig. 1. This area is crucial for the stable and safe operation of the whole MLF facility containing not only MUSE but also JSNS.

1. Muon production target

In FY2019, the rotating target was replaced with the new one due to trouble in the 1st rotating target. The 2nd target has been operated without any essential troubles. So far, the new target is working healthy under 500/600 kW proton-beam operation.

In addition to the conventional monitors like thermometers on the cooling jacket and the torque meter, an infra-red thermometer that monitors the target temperature more directly is under development. The details are reported separately [1]. The new monitor will be added to the target safety system to compose a layered system.

To secure a spare target early, fabrication of the 3rd target starts in the next fiscal year under the multi-year plan.

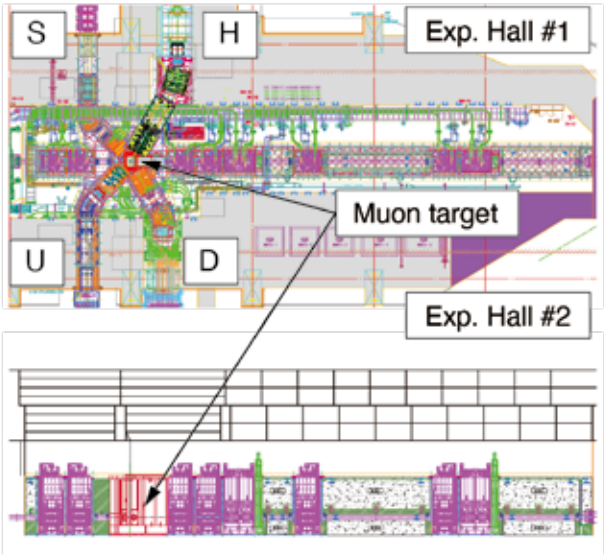

Fig. 1: The horizontal (upper) and the vertical sectional view (lower) of the M2 tunnel. The proton beam is transported from the left side to the right side of the neutron target through the tunnel.

2. Buffer tank system

Due to spallation reactions, lots of radioisotopes are generated in the target. The main residual activities in the target are tritium and ^{7}Be after a short cooling period. The tritium is generated by 0.5 TBq/year under 1 MW operation according to a simulation. The radiation dose from the residual activities in the target is orders of magnitude lower than that in the surrounding metallic parts in the target assembly. In addition to this, tritium emits only low-energy β rays. Thus, the contribution of the tritium is not serious to the external exposure if it stays in the target. However, tritium can diffuse in the hot graphite and evaporate from the target surface. In general, tritium forms a volatile chemical state, easily spreads out and sticks on the surface of devices, and eventually increases the risk of internal exposure.

The buffer tank system [2] accumulated the operation data of the released tritium from the target. Since the 2nd target installation in the summer of 2019, the data of the fresh target was obtained. Figure 2 shows the tritium release rate determined by the tritium contained in the vacuum exhaust gas. The emission rate is presumed to be proportional to the square root of the diffusion coefficient, $\sqrt{D}$, leading to the estimation that D is about 60 times greater at 1 MW (700 deg C) than that at 600 kW (500 deg C). This seems consistent with the reported value of ~ 40 in similar isotropic graphite (IG-110 by TOYO TANSO Inc.) [3], although the absolute value of D seems different.

This kind of data accumulation is important for safety and continuous operation. Toward a comprehensive understanding of tritium behavior, we are promoting collaboration with the experts in Hydrogen Isotope Research Center (HRC), Toyama University. The elementary process is studied using the equipment in HRC. The results are fed back to the MUSE operation, not only to the regular operation but also to the reconstruction of the scenario of storing the spent targets. The original scenario was considered at the early stage of the facility construction. Since then, the situation has been changed; (1) early realization of the rotating target of which lifetime is expected to be around 10 years, (2) more serious contamination in the hot cell where the spent target will be cut into three pieces to reduce the volume, (3) possible more serious effect of tritium in the target, and so forth. We will start to consider the new scenario taking all these issues

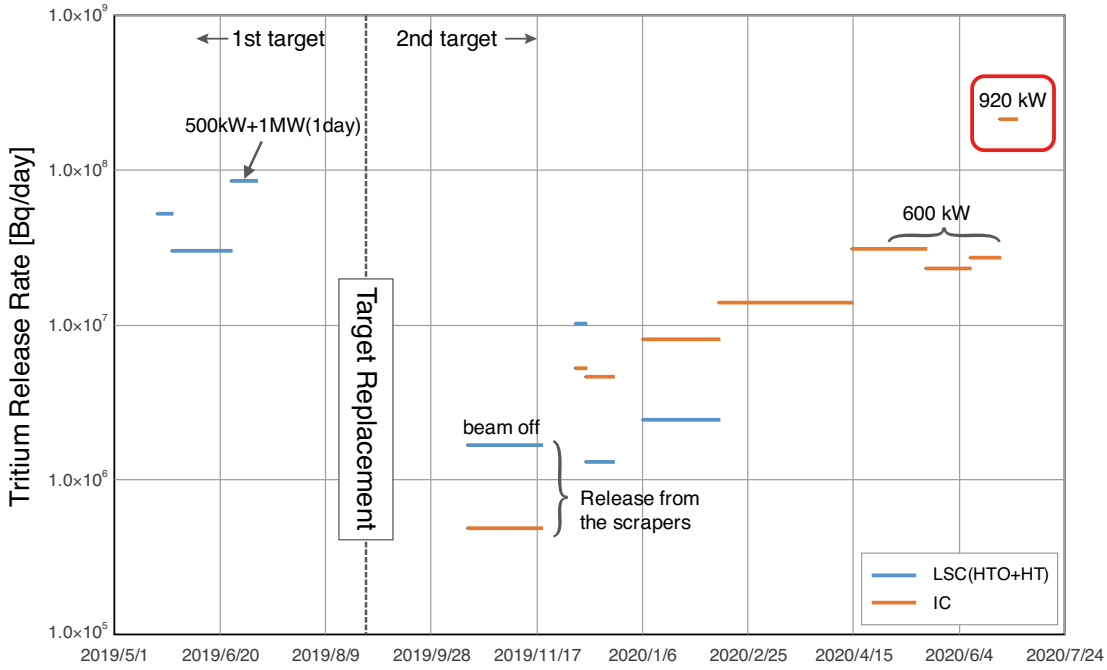

Fig. 2: The released tritium from the target. The vacuum exhaust from the beamline around the muon target and its downstream is stored in the buffer tank during the beam operation and is exhausted on the maintenance day after the radiation survey with the liquid scintillator (blue lines) and the ionization chamber (orange lines). The tritium release rate was determined by the stored tritium in the buffer tank devided by the accumulation period which corresponds to each line length. The amount of tritium was measured either by a liquid scintillator after pre-treatment of leachate in water (blue lines) or by an ionization chamber (orange lines).

3. The H-line construction

The H-line devices in the M2 tunnel were mainly installed in 2012 [4] and 2014 [5]. In this fiscal year, we performed the cabling and piping works connecting to the magnets and the vacuum components. Almost all the work of the H-line in the M2 tunnel was completed in this fiscal year. Figure 3 shows a snapshot taken at the beginning of October, just before closing the radiation shield on the H-line. Towards the first beam in the H-line, the radiation application was submitted to the regulatory agency on 5/Oct/2020, and the permission was noticed on 15/Jun/2021. Details of the present status in the H-line are separately reported [6].

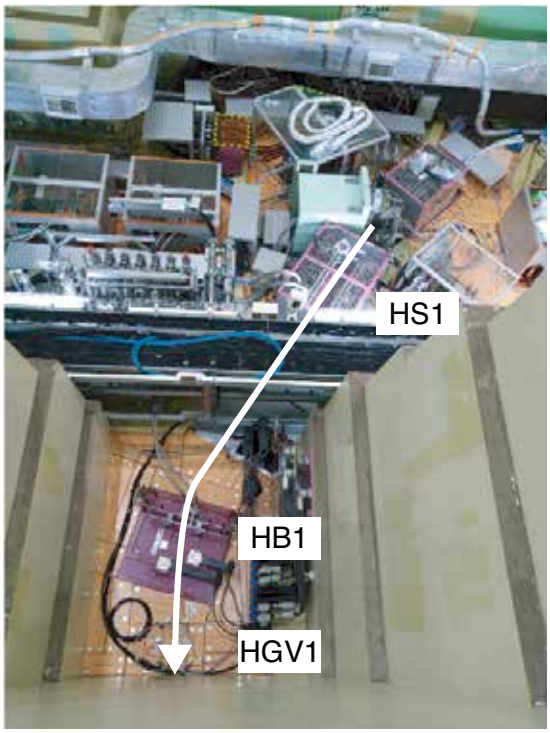

Fig. 3: Top view of the H-line taken on 5/Oct/'20.

References

[1] S. Matoba *et al.*, *ibid.*

[2] N. Kawamura *et al.*, JPS Conf. Proc. **33** (2021) 011146(1-6), https://doi.org/10.7566/JPSCP.33.011146.

[3] H. Atsumi *et al.*, J. Vac. Soc. Jpn. **49** (2006) 49–55.

[4] N. Kawamura *et al.*, KEK Prog. Rep. **2013-3** (2013) 7–8.

[5] N. Kawamura *et al.*, KEK Prog. Rep. **2015-4** (2015) 10–11.

[6] T. Yamazaki *et al.*, *ibid.*

Development of Monitoring System for the Muon Rotating Target Using an Infrared Camera

S. Matoba[1,2] and N. Kawamura[1,2]

[1]*Muon Science Laboratory, Institute of Materials Structure Science, KEK*
[2]*Muon Science Section, Materials and Life Science Division, J-PARC Center*

It is important to measure the temperature of the muon-production rotating target (hereinafter referred to as "rotating target") in order to detect problems of rotating target quickly.

Thermocouples have been installed on the cooling jacket to measure the temperature rise due to thermal radiation from the rotating target. Since the time constant of the thermocouples is on the order of minutes, it is not possible to stop the accelerator quickly in case of a significant temperature rise. In order to construct a rapid temperature detection system for rotating targets, we have installed an infrared camera (ULVVIPS-04171SL made by Vision-Sensing Co., Ltd.).

Figure 1 shows the temperature distribution of the rotating target during the 1-MW operation observed by the infrared camera. The high-temperature part (shown in yellow) can be observed flowing from the center of the target to the right, the direction of rotation.

Figure 2 shows the measured temperature rise of the rotating target at the start of beam operation. The temperature rise is saturated in about one hour using thermocouples attached to the cooling jacket, while the temperature is constant in 30 minutes using the infrared camera.

The infrared camera is also sensitive to the temperature change when the beam is temporarily stopped. As described above, rapid detection of temperature fluctuation by beam irradiation was achieved.

The beam power dependence of the temperature at the center of the rotating target is shown in figure 3, which is considered to be the beam spot temperature of the rotating target. As the beam power increases, the temperature of the rotating target also increases. We are analyzing the change of temperature and thermal conductivity by proton beam irradiation.

The infrared camera has been irradiated with cobalt-60 gamma rays and has been confirmed to be able to withstand up to 5 Gy of exposure. A glass dosimeter installed near the camera has been used to measure the radiation dose, which is estimated to be about 3 Gy at the end of March 2021. However, due to frequent errors in the electronic circuitry, which are presumably caused by the single event upset by neutrons, the camera operation time is low at about 30% of the available operation time. We are planning to develop a new infrared camera with measures such as shielding of the circuitry to increase the camera uptime.

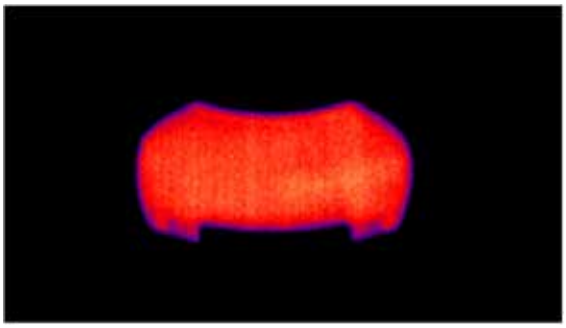

Fig. 1: Infrared camera image of the rotating target during 1-MW beam operation.

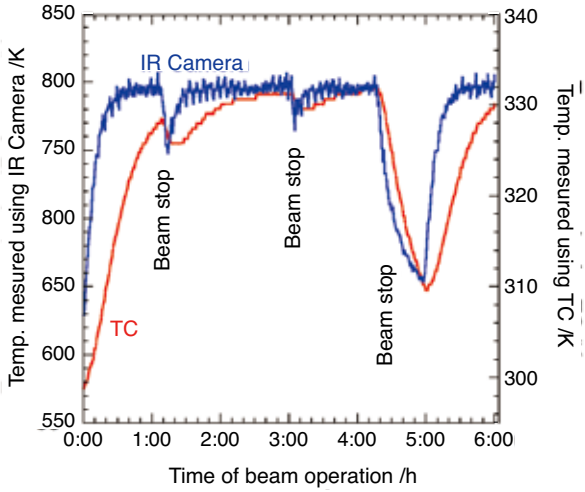

Fig. 2: Temperature rise of the rotating target at the start of beam operation. The temperatures dropped when the proton beam was temporarily stopped.

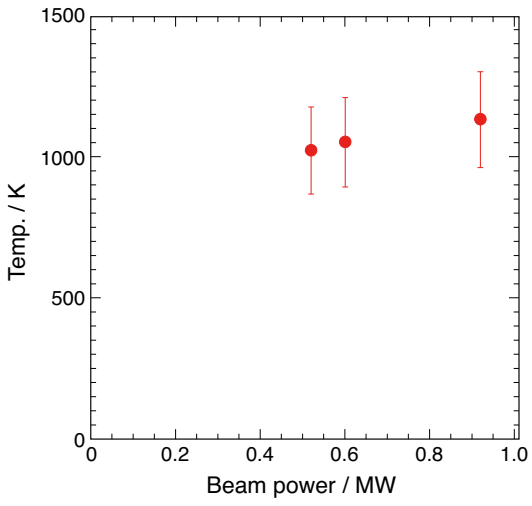

Fig. 3: Beam power dependence of temperature at the center of the rotating target.

Current Status of μSR Experiment at D1

W. Higemoto[1,2,3] and A. Koda[2,4]

[1]*Advanced Science Research Center, JAEA*
[2]*Muon Science Section, Materials and Life Science Division, J-PARC Center*
[3]*Department of Physics, Tokyo Institute of Technology*
[4]*Muon Science Laboratory, Institute of Materials Structure Science, KEK*

At the D-line, muons are delivered to the D1 and/or the D2. At the D1-area, the μSR spectrometer is installed as a main and fixed instrument. Since high momentum muon, surface muon, and negatively charged muon are available at the D1, all type of μSR measurements, except for the ultra-slow μSR, can be carried out. In particular, unique sample environments, such as very low-temperature by using the dilution refrigerator, high pressure *etc* were possible to carry out only at the D1. Figure 1 shows the μSR spectrometer with the dilution refrigerator and the fly-past chamber. Here, we report recent zero magnetic field condition of the D1.

Fig. 1: μSR spectrometer with the dilution refrigerator and the fly-past chamber at the D1.

Zero-Field condition at D1

Normally, a very weak magnetic field exist at the experimental Hall. Main origin of the magnetic field is the terrestrial magnetism with a magnitude of 0.2-0.3G. In addition, the normal and superconducting magnets are used to obtain muon beams and extra magnetic fields also exist at the sample position. For a μSR experiment, a zero magnetic field condition at the sample position is one of the important experimental circumstance to obtain precise state of a sample. In particular, large response to an external magnetic field is made for a superconductor (Meissner effect or formation of flux line lattice) and reduction of a residual field is crucial to understand essential property of materials.

At D1, magnetic fields at the sample position is estimated by using four triple-axis flux-gate magnetic probes which are located near center of the D1 spectrometer. To obtain a zero magnetic field condition, feedback currents are applied to three pairs of the correction coils. This feedback system was installed to the Iroha system and a zero field can be obtained dynamically when we are measuring μSR data.

However recently, we found sometimes the zero-field feedback system is not well working and finite residual magnetic field exist at the sample position. This problem is found at 2020A and the zero field condition was not able to be confirmed for some zero field μSR data, unfortunately. Currently, to check a magnetic field condition, we put another 3-axis magnetic probe at close to sample position. We also check the magnetic field distribution under the zero magnetic field condition. Figure 2 shows the position dependence of the residual magnetic fields. When the zero field feedback system is correctly working, the residual magnetic field at center of the D1 spectrometer is less than 0.02G for all the directions. This is enough small magnitude for usual sensitivity of our measurements. For μSR, a magnetic field condition is very important and we need further development to confirm a status of the experimental circumstance.

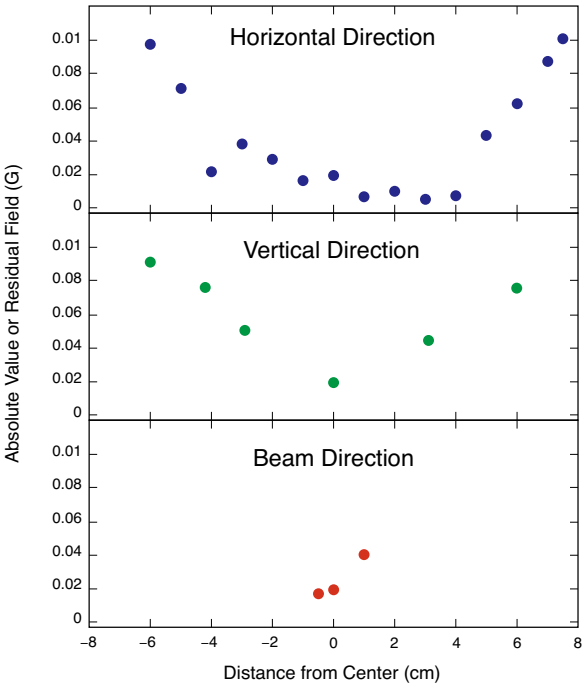

Fig. 2: Position dependence of the residual magnetic field for each directions. For this measurements, no sample is mounted to the D1 spectrometer.

Muon Beamlines and Control System
(Manufacturing of Spare Coils, and Installation of PPS Equipment for H1 Area)

T. Yuasa[1,2], Y. Kobayashi[1,2], H. Fujimori[1,2], N. Kawamura[1,2], Y. Ikedo[1,2], T. Yamazaki[1,2], A. Koda[1,2], K. Sakai[3], A. Watanabe[4], S. Sakata[4], M. Meguro[4], and K. Kawabata[4]

[1]*Muon Science Laboratory, Institute of Materials Structure Science, KEK*
[2]*Muon Science Section, Materials and Life Science Division, J-PARC Center*
[3]*Japan Atomic Energy Agency, JAEA*
[4]*NAT Co., Ltd.*

1. Introduction

We report on the manufacturing of spare coils for a bending magnet in D-line and the installation of the personnel protection system (PPS) for the H1 experimental area.

The bending magnet DB2 is installed in the decay muon beamline (D-line) at the Materials and Life Science Facility (MLF) of J-PARC. The existing DB2 is a dipole magnet and over 40 years have passed since its production; therefore, we plan to exchange the degraded coils with new ones. The production and performance inspection of the new coils were carried out. The hollow conductor, which was produced last year, was used for the new coils as coil material [1]. The installation of the PPS equipment for the H1 area in the first experimental hall of MLF started in FY2020. The first experimental area constructed on the H-line is called H1 area. The PPS for the H1 area was installed, and status signals from the power supplies of the magnets, which bring muon beams to the H1 area, were connected to the PPS, and the existing PLC was update in the first experimental hall.

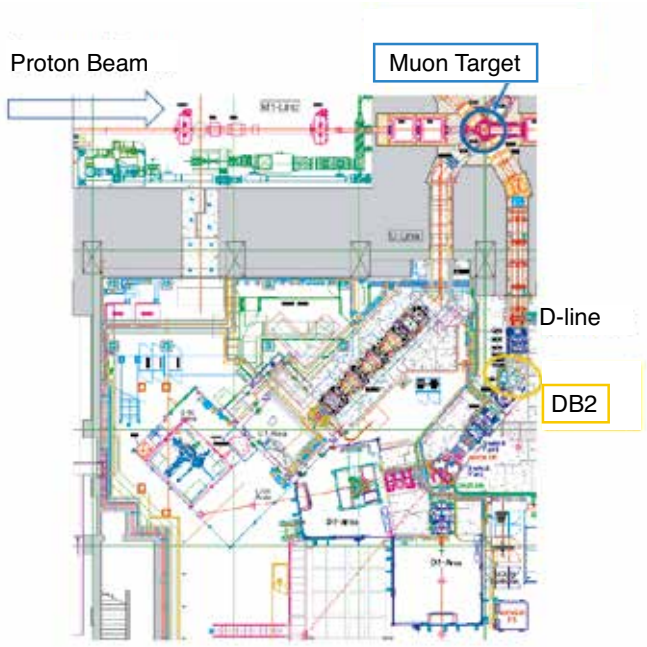

Fig. 1: Decay muon beamline (D-line).

2. Manufacturing of spare coilsn

As shown in Fig. 1, DB2 bends muon beams by 40° and transports them to the downstream experimental areas. We calculated the field of DB2 with a 3-dimensional field analysis program OPERA-3d. The analysis model and actual DB2 are shown in Fig. 2.

In FY2020, we manufactured two spare coils with the same size as the existing coils so that they can be installed in the existing yoke and poles. The production drawing and the manufactured coils are shown in Fig. 3 and 4, respectively.

Fig. 2: Analysis model (left) and existing DB2 (right).

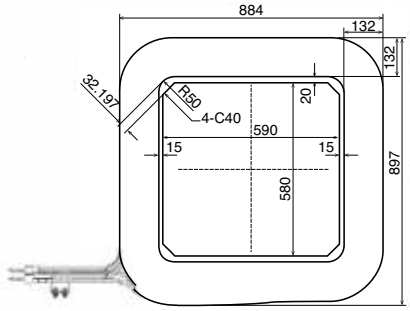

Fig. 3: Drawing of new coil.

Fig. 4: Manufactured coil.

Table 1: Result of the inspection test.

	measurement	calculation
Coil Resistance [mΩ] (at 20°C)	52.25	58.2
Inductance [mH] (at 120 kHz)	14.44	14.86
Inductance [mH] (at 1 MHz)	13.06	
Water pressure drop [MPa]	0.32	0.33
Water flow [ℓ/min] (at 0.5 MPa)	17.5	17.4
output current [A]	500	500
output voltage [V]	25.97	29
Temperature rise in cooling water Δt[°C]	7.9	12.0

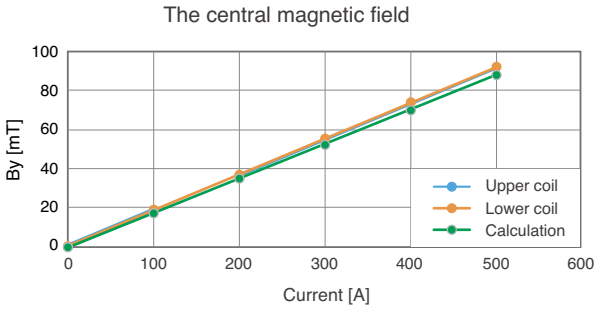

Fig. 5: Comparison between measurement and calculation of the central magnetic field.

Table 1 shows the performance test results, and Fig. 5 shows a comparison between the measured and calculated central magnetic field values of the coil. The reason why the calculated and measured values do not match exactly is expected to be due to the presence of magnetic materials (reinforcing steel bars) under the floor at the measurement location.

3. Installation of PPS equipment for H1 area

3.1 PPS devices for H1 area

Similar to other muon experimental areas [2], the PPS for the H1 area comprises an emergency beam stop button (Panic Button), a search button, a muon blocker, a safety magnet and an entrance door to the experimental area, as shown in Fig.6. The safety magnet for the H1 area is HB2 and the muon blocker is HBB1, as shown in Fig. 7.

Fig. 6: PPS devices at H1 area: entrance door (left), panic button (top right) and search button (bottom right).

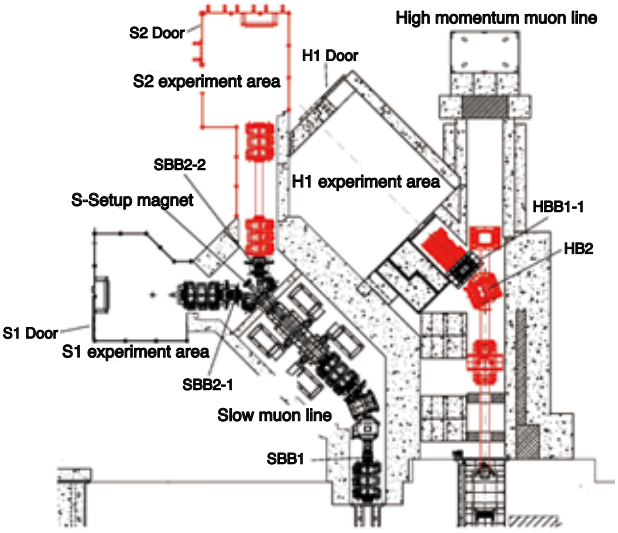

Fig. 7: H1 area in the first experimental hall of MLF.

3.2 Wiring of the PPS devices to H1 PPS

The PPS devices to display statuses and operate the PPS were wired to two control systems. One is the PPS panel located on the east side of the first experimental hall that is used to send the status signals from the PPS devices to the MLF control room, and the other is the PLC rack located on the west side of the hall. The PLC rack is equipped with three PLCs; magnet power supplies control panel, vacuum equipment control panel, and muon blocker drive panel, respectively. Regarding the magnet power supplies, it is necessary to be able to read all status signals of all the magnet power supplies. This fiscal year, the status signal of the safety magnet HB2 was added to the PPS, and the wiring for the magnet excitation permission signals was connected. The wiring system for each device is shown in Fig. 8.

3.3 Software modification

With the construction of the H1 area, it was also necessary to modify the software to properly display the new H1 area in the existing control panels. Figure 9 shows one of the screen of the control panel related to the H1 area.

4. Summary

We completed the manufacturing of the spare coils for DB2, and measured the magnetic field in FY2020. As a result, it was confirmed that the calculated and measured magnetic field values were almost identical. We plan to replace the existing coils with the newly manufactured coils in the summer of 2021. This project is currently in progress. The installation of the PPS equipment for the H1 area was completed, and we updated the PPS wiring accordingly in the first experimental hall in FY2020. We are now ready to start experiments.

References

[1] H. Fujimori *et al.*, "Muon Beamlines and Target Control System", KEK-MSL REPORT 2019, KEK Prog. Rep. **2020-4** (2020) 13–15.

[2] K. Sakai *et al.*, "Progress of General Control System for Materials and Life Science Experimental Facility at J-PARC", JAEA-Technology **2018-011** (2019) [in Japanese].

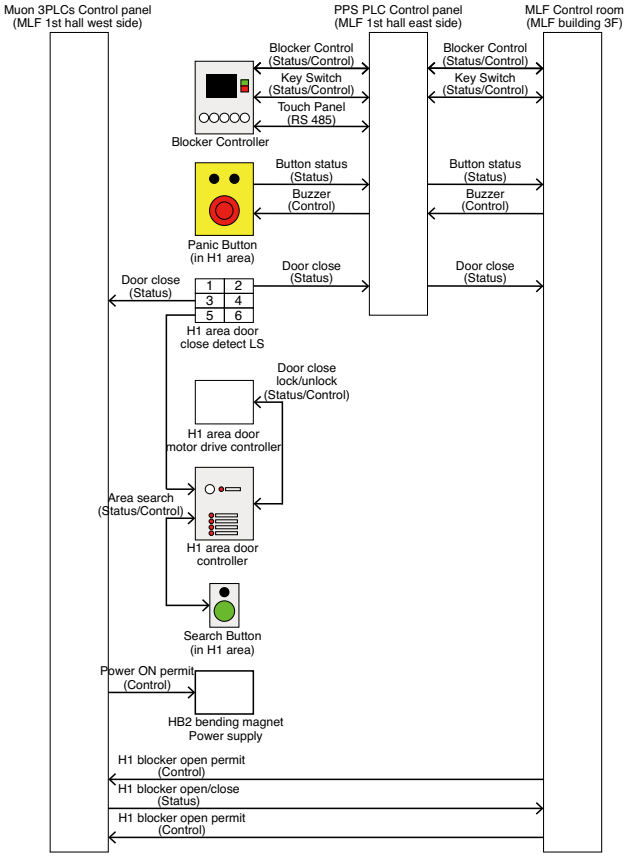

Fig. 8: PPS wiring system diagram.

Fig. 9: Screen of the magnet power supplies control panel for S-line & H-line.

Commissioning of the μSR Spectrometer at U1A in FY2020

S. Kanda[1,2], T. Adachi[1,2], Y. Ikedo[1,2], Y. Oishi[1,2], H. Li[1,2], T. Yuasa[1,2], and H. Fujimori[1,2]

[1]*Muon Science Laboratory, Institute of Materials Structure Science, KEK*
[2]*Muon Science Section, Materials and Life Science Division, J-PARC Center*

1. Introduction

At J-PARC MLF, MUSE provides the world-highest flux of pulsed muon beams. U-Line, one of the four beamlines in the facility, features an intense surface muon beam from Super-Omega [1] and Ultra Slow Muon (USM) by laser ionization of thermal muonium. The beamline has two branches: U1A for μSR studies using USM and U1B for transmission muon microscope.

The surface muon beam irradiates a resistively heated tungsten film to obtain thermal muonium atoms in a vacuum. Two laser beams resonantly ionize the muonium atoms with wavelengths of 355 nm and 122 nm. The ionized muonium has a thermal velocity corresponding to the target temperature of 2000 K, which results in a seven-digit cooling from 4 MeV to 0.2 eV. An electrostatic extractor and immersion lens focuses the ionized muonium and accelerates to 30 keV. The extracted muons are transported to the experimental areas through a magnetic bend for mass separation, electric bends for energy selection, and electric quadrupoles for focusing. Micro channel plate (MCP) detectors are placed at focal points along the transport optics to measure the flux and profile of USM. In the U1A area, a muon spin spectrometer is placed on a high-voltage stage to control injection energy from zero to 30 keV.

2. The U1A μSR spectrometer

The muon spin spectrometer at U1A consists of a longitudinal field coil and a positron detector segmented into 16 modules, 512 channels. The coils can generate a magnetic field of up to 0.4 T along the beam axis. The USM spins are rotated 90 degrees at the magnetic bend during transport, so the longitudinal field at the spectrometer is orthogonal to the average muon spin vector. The detector consists of plastic scintillator blocks, silicon photomultipliers (SiPM), and dedicated front-end electronics.

A sample is placed inside the main chamber surrounded by the coils, and a helium flow cryostat controls the temperature. A load lock chamber next to the main chamber allows sample exchange while maintaining a high vacuum.

3. Project status and tasks

Following the successful USM generation in 2016 [2] and the demonstration of USM-μSR at U1A in 2018 [3], preparations for the start of user experiments are steadily underway. In 2019, implantation depth control by the high-voltage stage was successfully demonstrated [4]. To proceed from the demonstration to the practical stage, several issues need to be addressed. The key issues are improving beam flux and quality, optimizing the spectrometer's performance, and preparing the sample environment.

For the USM flux, pulse energy improvement and spectral linewidth optimization are under study. We are also working on a step-by-step study to quantify the generation rate of muonium and the extraction efficiency of the USM with sufficient precision. The typical USM flux is about 2×10^2 Hz after the first electric bend with the Lyman-α light's pulse energy of 5 μJ.

Concerning the beam quality, the beam profile, energy, and time-of-flight spread are the performance to be considered. A simulation study has been done to optimize the parameters of the transport optics, and a computational solution has been found [5]. Experimental validation is also being understood qualitatively, and further systematic comparison of measurements and calculations will be performed.

For the spectrometer, the signal-processing electronics have been upgraded to improve performance. The operating parameters of the electronics and the SiPMs needed to be optimized, so these were determined in laboratory tests and commissioning with the beam. Positrons from the upstream of the beamline were observed at the spectrometer and reduced the μSR asymmetry. As a countermeasure for the positron background, additional lead shields were installed in front of the spectrometer. These details are described in the next section.

About the sample environment, the electric noise from the power supply of the longitudinal field coils has been disturbed the deceleration potential of the high-voltage stage. The frequency of the noise was 50 Hz, and the amplitude was 28 V peak-to-peak. This noise level limits the implantation-depth resolution of the USM, so a countermeasure is required.

4. Progress in this fiscal year

In FY2020, the muon beam was delivered from Run84 to Run86 operation cycles. There was a period in April and May when the beam was stopped due to the spread of COVID-19. After the resumption of the accelerator operation, we continued to prepare the commissioning to start user programs while making efforts to prevent the spread of infection. In this section, we report on the three main results obtained during this fiscal year.

4.1. Tests of upgraded front-end electronics for the positron detector

The spectrometers of MUSE use the dedicated front-end electronics for the positron detector. A series of ASICs called VOLUME perform analog signal processing. This year, the U1A spectrometer has been upgraded from VOLUME2012 (V2012) to a new version named VOLUME2014 (V2014).

V2014 has a pole-zero-cancelation circuit in the amplifier, which provides an undershoot-free output with appropriate parameters. As a part of the commissioning, the biases given to the amplifier were determined by observing the output waveform. In addition, the comparator threshold was determined from the relationship between the threshold and the SiPM's dark count rate. The operating voltages of SiPMs were optimized from the pulse height distribution depending on the bias voltage.

The detection efficiency of the detector for decay positrons was almost 100%, the timing resolution was 2.5 ns in the standard deviation, and no significant pileup was observed.

4.2. Suppression of decay positron background by adding the lead shield

The muonium production target is made thick enough to stop half of the beam to maximize the muonium emission rate. Muons not stopping at the target are the origin of background events at the spectrometer. Since these background muons are spread by Coulomb multiple scattering, shielding the upstream side of the spectrometer is an effective countermeasure.

A lead shield with a thickness of 5 cm was installed to cover the detectors. The shield reduced the background rate, as shown in Fig.1. The integrated rate of background events was suppressed to about 1/5.

4.3. Improvement in the injection energy resolution by modifying the power supply wiring

Electrical noise at the high-voltage stage causes uncertainty in the USM implantation depth. We modified the power supply wiring to the longitudinal field coils. The noise level was reduced to 4 V peak-to-peak, i.e., improved by a factor of seven. This level of uncertainty is small compared to the energy spread due to the position dependence of the accelerating electric field for the USM extraction.

5. Summary and outlook

The commissioning in FY2020 completed the preparation of the U1A spectrometer for use in materials science using USM. To start user programs, the beam intensity needs to be improved, which will require optimization of the extraction and transport optics. We will attempt to increase the number of USMs and to evaluate the number precisely in parallel.

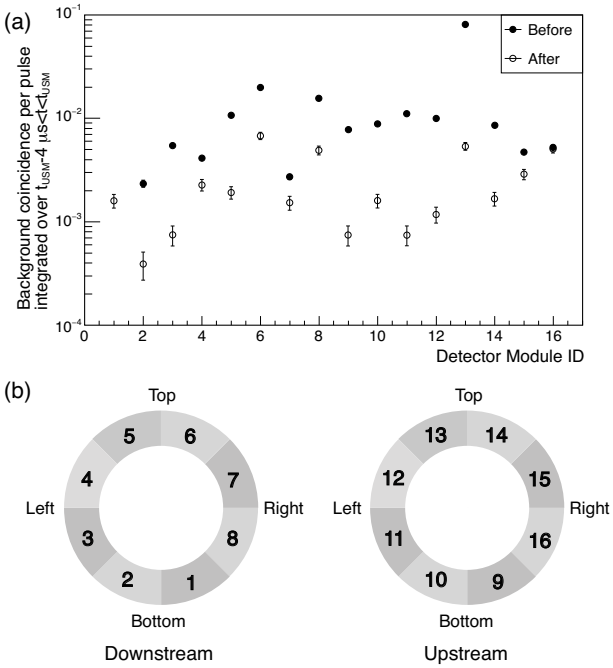

Fig. 1: Background positrons at the spectrometer: (a) comparison of the background rate before and after the installation of shielding; (b) geometrical arrangement of the detector module. Directions are from the beam perspective.

References

[1] The total beam flux is $6.4 \times 10^7 \mu^+$/s at 212 kW. Y. Miyake *et al.*, JPS Conf. Proc. **21** (2018) 011054(1-6).

[2] T. Adachi, A. D. Pant, and Y. Ikedo, KEK Prog. Rep. **2017-4** (2017) 12.

[3] T. Adachi, A. D. Pant, and Y. Ikedo, KEK Prog. Rep. **2018-2** (2018) 13.

[4] T. Adachi and Y. Ikedo, KEK Prog. Rep. **2019-3** (2019) 17.

[5] A. D. Pant *et al.*, Nucl. Instrum. Methods Phys. Res. A **929** (2019) 129–133.

The Progress of Laser System for Ultra Slow Muon Generation

Y. Oishi[1,2]

[1]*Muon Science Laboratory, Institute of Materials Structure Science, KEK*
[2]*Muon Science Section, Materials and Life Science Division, J-PARC Center*

The Lyman-α laser system for the ultra-slow muon generation is stably operating. In order to increase output laser pulse energy, several kind of laser gain medium for additional laser amplifier is developing.

Laser System for Ultra Slow Muon Generation

Ultra-slow muons can be generated by resonant optical ionization of thermal muonium from hot-W foil target. The light pulses of 122.09 nm and 355 nm is required for 1s to 2p state excitation and 2p to ionization, respectively. The high energy pulsed coherent Lyman-α light (122.09 nm) source is one of a very important elements for the efficient generation of ultra-slow muons. The design of the Lyman-α light source system is described in Ref. 1 and schematic of the light source is shown in Fig. 1. More than 10 μJ Lyman-α pulse is stably generated in a krypton/argon mixture filled gas-cell by methods of two-photon-resonant four-wave-mixing which method is required 212.556 nm and 820 nm pulses. These pulses are generated by nonlinear wavelength conversions of a 100 mJ 1062.78 nm pulse which is obtained by Nd:YGAG (1 at.% Nd doped $Y_3Ga_2Al_3O_{15}$) ceramic laser amplifiers. We were going to obtain 1 J level 1062.78 nm pulse in the initial design of amplifiers system, but there is a problem in a large-aperture laser medium (>10 mm diameter) for final amplifiers. The fabrication of ceramic as a gain medium is very difficult due to the nature of Gallium in the Nd:YGAG. In order to overcome the difficulties, we have developed Nd:YSAG (1 at.% Nd doped $Y_3Sc_2Al_3O_{15}$) ceramic and optimized the composition ratio between Scandium and Aluminum which reported in last year MSL progress report. Newly fabricated middle size (ø9 mm, 112 mm long) Nd:YSAG(1 at.% Nd doped $Y_3Sc_{1.5}Al_{3.5}O_{15}$) ceramic was delivered and inspected in the property of amplification gain at 1062.78 nm light and wavefront distortion. The amplification gain was satisfactory, but the transmitted wavefront distortion was exist, and the collapsed beam shape by the wavefront distortion made the reduction of the wavelength conversion efficiency in the subsequent stages. The measured wavefront distortion is shown in Fig. 2.

Wavefront compensation

In order to compensate for the transmitted wavefront distortion inside the Nd:YSAG ceramic, we introduced an active deformable mirror. The deformable mirror was introduced with Shack-Hartmann wavefront sensor that placed before and after amplifier, respectively as shown in Fig. 3.

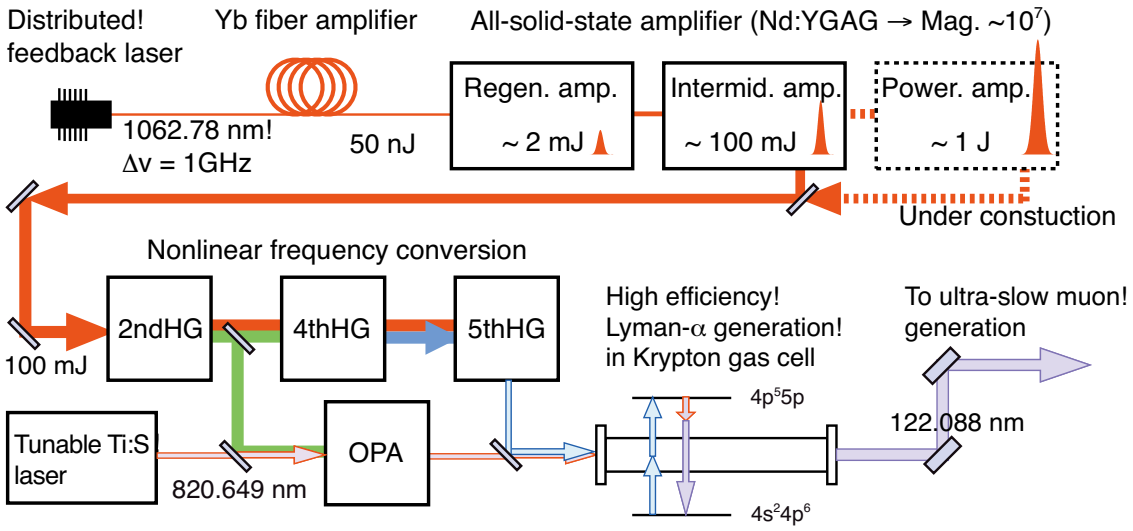

Fig. 1: Schematic of the Lyman-α laser system for the Ultra-slow muon generation.

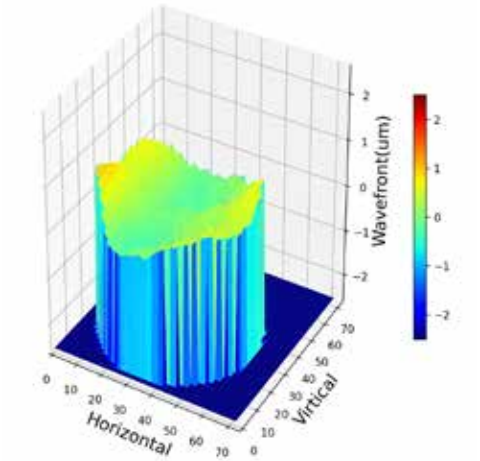

Fig. 2: The measured wavefront distortion in newly fabricated Nd:YSAG ceramic for final amplifier.

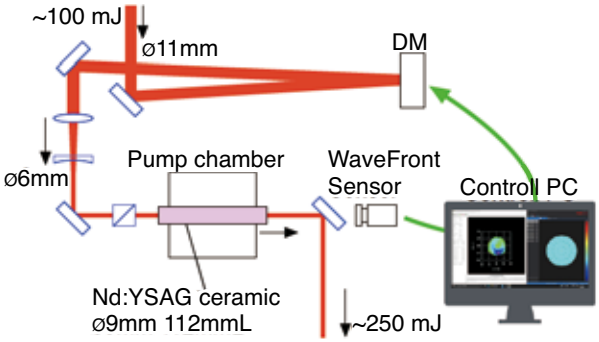

Fig. 3: The experimental setup of final amplifier and wavefront compensation system by a deformable mirror with wavefront sensor.

While deformable mirror can compensate for wavefront distortion, it can also focus the high-power laser beam to an arbitrary position in the laser system if it malfunctions, which can easily lead to the destruction of not only exchangeable optical components but also expensive nonlinear crystals. Therefore, a preliminary wavefront compensation using a nearly practical optical configuration and a He-Ne laser was used to evaluate the performance. Initially, the wavefront of the optical system was measured without the laser ceramic and with a flat mirror in place of the deformable mirror. Next, the flat mirror was replaced by a deformable mirror and the wavefront was measured. Finally, the wavefront of the entire optical system was measured after inserting the laser ceramic into the optical path. the distorted wavefront was compensated to a plane wave by adaptively applying and controlling the voltage of each piezoelectric element of the 40-segment deformable mirror. The measured wavefront of every step is shown in Fig. 4(a)-(d).

It was shown that the wavefront distortion caused by the laser ceramic can be compensated to a plane wave using a deformable mirror. The method obtained by these studies will be applied to a practical laser system to implement the enhancement of Lyman-α optical intensity.

References

[1] N. Saito *et al.*, Opt. Express **24** (2016) 7566–7574.

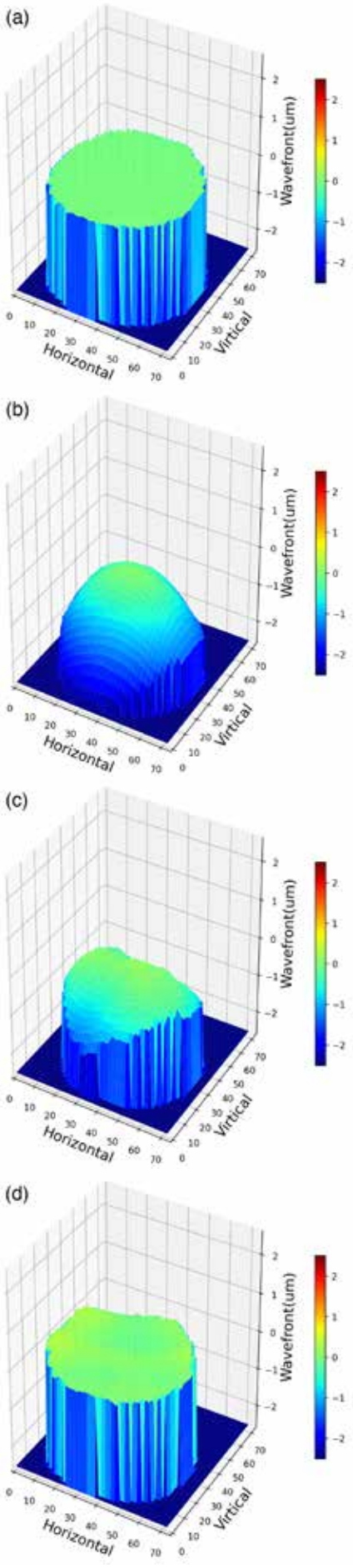

Fig. 4: (a) The measured initial optical system wavefront with flat mirror, (b) The measured wavefront with deformable mirror, (c) The measured wavefront with deformable mirror and laser ceramic, (d) The measured wavefront after compensation.

Development of Sample Environment at the S1 Area

J. G. Nakamura[1,2], A. Koda[1,2], M. Hiraishi[1], S. Doiuchi[1], S. Nishimura[1,2], H. Okabe[1], A. Hashimoto[1], H. Li[1], and R. Kadono[1,2]

[1]*Muon Science Laboratory, Institute of Materials Structure Science, KEK*
[2]*Muon Science Section, Materials and Life Science Division, J-PARC Center*

μSR experiments often use helium (He) as cryogen, and the He is collected in the recovery line after use. However, helium gas is a precious resource, and it is known that there is a global supply problem, so it is important to prepare a cryogen-free cryostat for the future sustainability of cryogenic experiments. In order to settle this issue, we have commissioned a new cryogen-free cryostat based on commercially available model: the DRY ICE 1.5 K Beamline LEMON system (Dry Lemon), supplied by ICEoxford Ltd. [1]. It is a Gifford-McMahon (GM) cooled cryogen-free variable temperature cryostat. Figure 1 shows a snapshot of this cryostat.

The cryostat can be operated at a lowest temperature of ∼1.5 K and a highest temperature of 500 K, whereas the lowest temperature achieved by existing cryogen-using top-load cryostats is 2 K [2]. The cryostat consists of sample chamber with a variable temperature insert (VTI), a He circulation line, and a GM cryocooler operated by a dedicated compressor (Fig. 2).

Before reporting the specific work, we will describe the regular cooling procedure. GM refrigerator is operated in an outer vacuum chamber (OVC), and the circulation of He is started to cool VTI. In one day, GM stage 2 (GM2) temperature reaches approximately 4.2 K, which is slightly above the temperature at which He becomes liquid. After that, by adjusting the needle valve until the pressure gauge on the circulation line shows approximately 8 mbar, liquid He can be stored in a reservoir and VTI can be cooled at the same time. He gas for heat exchange with the VTI is manually introduced into the sample chamber to cool the sample. The temperature of VTI is controlled by using PID heater parameters, which is not perfectly optimized yet. For high temperature operation (above room temperature), the sample chamber is kept in vacuum, and the sample rod for high temperature is also equipped with a heater near the sample.

Other features of this cryostat are the relatively large beam window size and the top-loading system. The former is for relatively low background of μSR spectra, and the latter is for sample mounting without increasing the temperature up to room temperature. There are three beam windows in front of the sample. These window sizes are, from the out-

Fig. 1: Snapshot of the new cryogen-free variable temperature cryostat placed at the test bench.

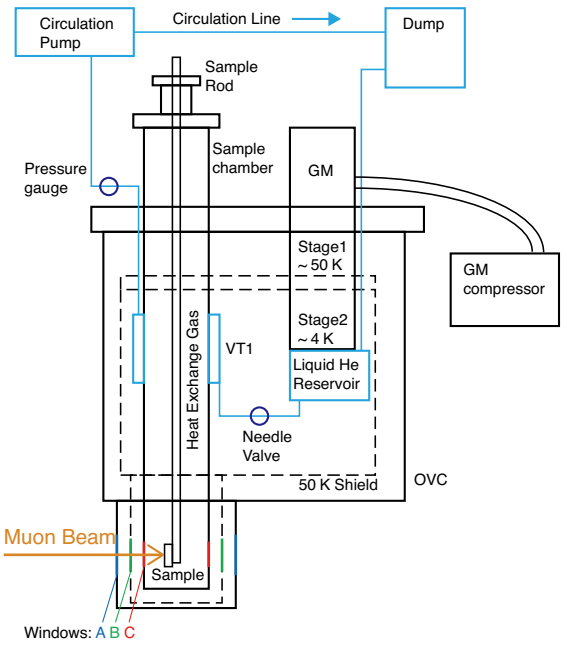

Fig. 2: Schematic diagram of the cryostat with a blue line showing He circulating line, where GM, VTI and OVC respectively denote the Gifford-McMahon refrigerator, the variable temperature insert and the outer vacuum chamber.

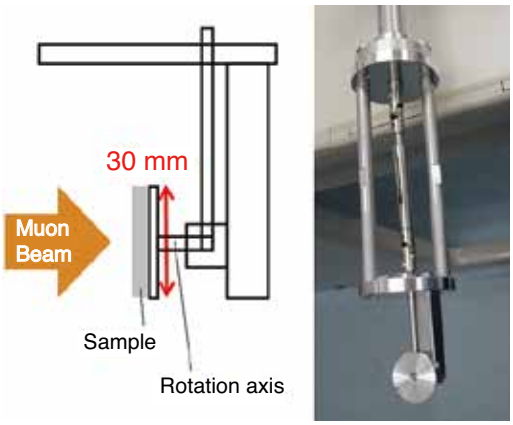

Fig. 3: Schematic diagram (left) and snapshot (right) of rotating sample rod for the top-loading cryostat

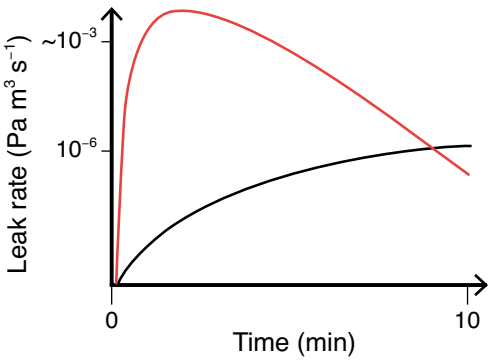

Fig. 4: Schematic of leak rate trends. The black line represents the case of gradual He gas penetration through a leakless window. The red line represents the case where there is a leak through the window.

side, ϕ 55 mm: the OVC window (A), ϕ 50 mm: the 50 K shield window (B), and ϕ 40 mm: the sample chamber window (C). As previously reported in the case of the ^{3}He cryostat [3], all windows are ϕ 35 mm in size, and the cryostat is not designed for the top-loading sample rods but using a dedicated sample holder, which are in contrast to the case of Dry Lemon.

With this top-loading cryostat, various sample rods can be used. Currently, in addition to one fixed sample rod for low temperature and one for high temperature, a rod for sample rotation was prepared for low temperature. Figure 3 shows a schematic diagram and a snapshot of the rotating rod, on which the sample can be mounted on a ϕ 30 mm aluminum disk, which can be rotated by a stepping motor in the radial direction.

We are currently commissioning this cryostat for user experiments and are dealing with the following problems. One of the typical problems in this cryostat is the vacuum leakage. One is a leak from the window, and the other is a leak from the He circulation line.

The most common leak at room temperature, the leak from the window, is as follows. In the cryostat, there are two pairs of vacuum windows: A and C shown in Fig. 2. The windows are aluminized polyimide films. The following procedure is used to leak-check before operation. First, all closed systems, i.e., He circulation line, sample chamber, and OVC, are evacuated. Then, while connecting the helium leak detector to OVC, He gas is introduced into the sample chamber using a gas bag. This is used to check for leaks from the sample chamber to OVC. Figure 4 shows schematic diagram of the trend of the leak detector. The red line is the case where there is a leak through the window C, and within 1-2 minutes, there is a sharp increase in the rate of e.g., 10^{-3} Pa m^3 s^{-1} for a typical pinhole. The black line shows the trend when there is no leak, and the rate increases slowly to approximately 10^{-6} Pa m^3 s^{-1}. This is because He gas can gradually penetrate the window at room temperature. The leak rate increases both with and without leaks, but the quantitative difference makes it possible to distinguish the presence of a leak. When a 5 L gas bag is introduced, the pressure in the sample chamber increases to approximately 70 mbar at room temperature, but if there is a leak, the pressure decreases noticeably within a few minutes: e.g., to 30 mbar in 10 min for a typical pinhole.

Before circulating He, the leak detector connection is changed to the He circulation line and He gas is sprayed on the line from the outside to check for leaks. The leak-checking can be performed, because the background rate of the line is approximately 10^{-6} Pa m^3 s^{-1}, after the circulation line has been sufficiently evacuated. After connecting the leak detector to OVC again, the He circulation is started and we can check for leaks from the circulation line to OVC at room temperature. Then, He gas is sprayed on OVC from the outside to check for leaks. When leak-checking the window A, the trend of the leak rate is similar to that shown in Fig.4. In this outer window A, it is easier to identify the leak position compared to the inner window C, because the He sprayed position can be controlled. If there are leaks in these windows, it is necessary to repair them with epoxy glue: in the window A, the glue can be applied from the outside, but in the window C, it is necessary to disassemble the cryostat (Fig. 5).

The next problem is a leak at low temperature, called a cold leak. If the leak is observed near the nitrogen liquefied temperature ($\sim$ 77 K), it is most likely due to thermal contraction. For example, if the leak is found after the VTI temperature has reached at low temperatures, it is likely to be a cold leak from the indium seal on a sample chamber flange.

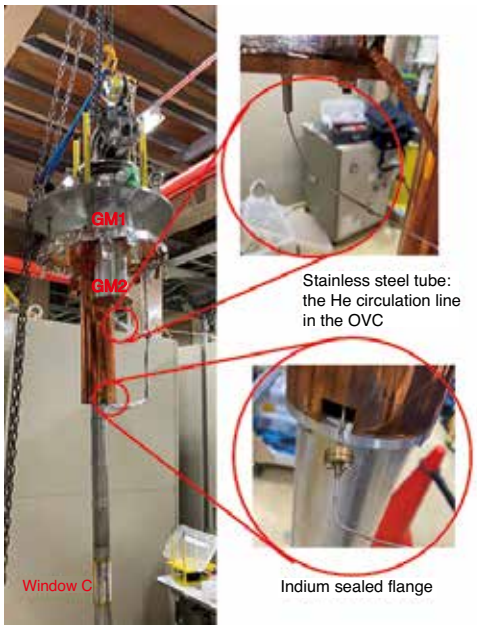

Fig. 5: Snapshot of disassembling the cryostat. Sample chamber tail is shown by removing 50 K shield.

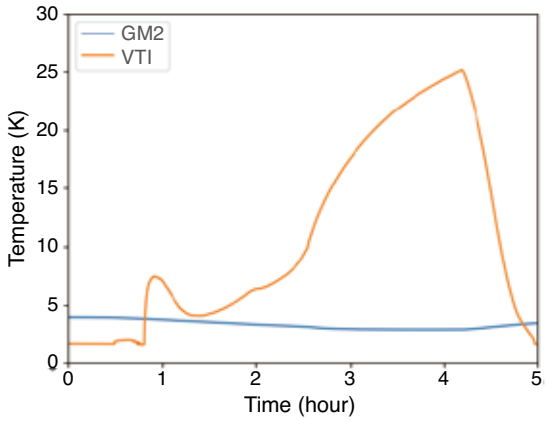

Fig. 6: Temperature trend of VTI and GM 2nd stage (GM2) with the cold leak from a circulation line.

As the cooling progresses and the VTI temperature decreases near the lowest temperature, another cold leak may be observed. Liquid He under saturated vapor pressure transitions to a superfluid state below 2.2 K. As a result, He has no viscosity and passes through a pinhole that viscous fluids cannot pass through: a phenomenon known as a super leak. Fig. 6 shows an example of the temperature trend when the super leak was observed.

The initial temperature increase up to 7 K, as seen in Fig. 6, was due to He gas leaked into OVC by the super leak, which acted as the heat exchange gas to increase the temperature of VTI. The heat shot also increased the temperature at the leak point above the superfluid transition temperature, and the leak was immediately stopped. The temperature increase of VTI stimulated release of He gas adsorbed on the vessel wall, which leads to a further temperature increase (the second peak). Since evacuating was continued during this period, it is seen that the temperature increase of VTI was slowing down from around 20 K. Besides this, decreasing of the flow rate through the needle valve due to the temperature increase of VTI also reduced the heat load at GM2, suggested by the fact that the temperature of GM2 was slightly decreasing, as shown in Fig. 6. As a result, liquid He that started to accumulate in the He reservoir gradually cooled the needle valve, and when the liquid He began to flow through the needle valve (at the VTI temperature of 25 K), rapid cooling was seen again.

In the case of the cold leak as described above, the cryostat is need to be disassembled and the following procedure is used for maintenance. One indium sealed flange is used for the circulation line (lower right part of Fig. 5), and it should be replaced first during maintenance. At that time, for increasing the circulation line pressure to atmospheric pressure, He gas is introduced into the line to prevent air from contaminating the line and blocking it during cooling. In addition, stainless steel tubes with an outer diameter of 2-3 mm are used for the part of the circulation line in OVC (upper right part of Fig. 5). If there is an oxidized solder part (shown in Fig. 5), it is necessary to replace it using solder and flux for stainless steel. The old solder should be removed with sandpaper before soldering, and it is important to remove any remaining flux as it may cause oxidation.

Because the impedance (conductance) of the He circulation line is important in any case, it is necessary to confirm that the impedance has not changed before and after the maintenance as follows. First, a gas bag filled with He is connected to the circulation line on GM refrigerator side (right side of Fig. 2), the needle valve is closed, and then the circulation line on the sample chamber side is evacuated with a vacuum pump. After the vacuum pump has been stopped, the needle valve is fully opened and the pressure rise in the circulation line is observed to roughly check the impedance. For example, a pressure rise of 300 mbar/10 sec can be checked before and after the maintenance.

References

[1] `https://www.iceoxford.com/`

[2] `https://mlfinfo.jp/en/s1/se.html`

[3] J. G. Nakamura *et. al.,* KEK Prog. Rep. **2019-3** (2019) 24–25.

H-line Construction – Recent Progress

T. Yamazaki[1,2] and N. Kawamura[1,2]

[1]*Muon Science Laboratory, Institute of Materials Structure Science, KEK*
[2]*Muon Science Section, Materials and Life Science Division, J-PARC Center*

H-line is a new beamline under construction in the east #1 experimental hall of the MLF. Its layout drawing is shown in Fig. 1. It is a general-purpose beamline [1] that can generate both decay and surface muons and has two branches named H1- and H2-area. Its design intensity of surface muons reaches 10^8 muons/s with a proton beam power of 1 MW thanks to a large acceptance (108 mSr) capture solenoid and other beamline magnets with large apertures.

At the H-line, precision measurements such as the hyperfine splitting measurement of muonium (MuSEUM experiment) [2] and the muon g-2/EDM experiment [3] are planned. Its intense beam is also suited to search for a rare process such as cLFV (charged Lepton Flavor Violation), which is forbidden in the Standard Model of particle physics (DeeMe experiment [4]). In addition, a transmission muon microscope (TμM) project, which enables us to observe thick samples non-destructively, is planned at the H2 area.

The construction of the H-line started in FY2012 and progressed intermittently. Its frontend devices such as the capture solenoid were installed in FY2012 and FY2014. Its radiation shields and beam blockers were installed in FY2016. From FY2017 to FY2019, a new electric substation for the H-line was constructed.

In FY2020, the core part and the first branch (H1 area) of the H-line were constructed. The construction was the minimum required to deliver muons to the H1 area and enable us to start beam commissioning. All vacuum apparatuses were connected (see Fig.2), electrical cabling and cooling water piping for two bending magnets (HB1 and HB2) were conducted, and a safety interlock system was implemented and combined with the whole MLF system. Though the capture solenoid (HS1), transporta-

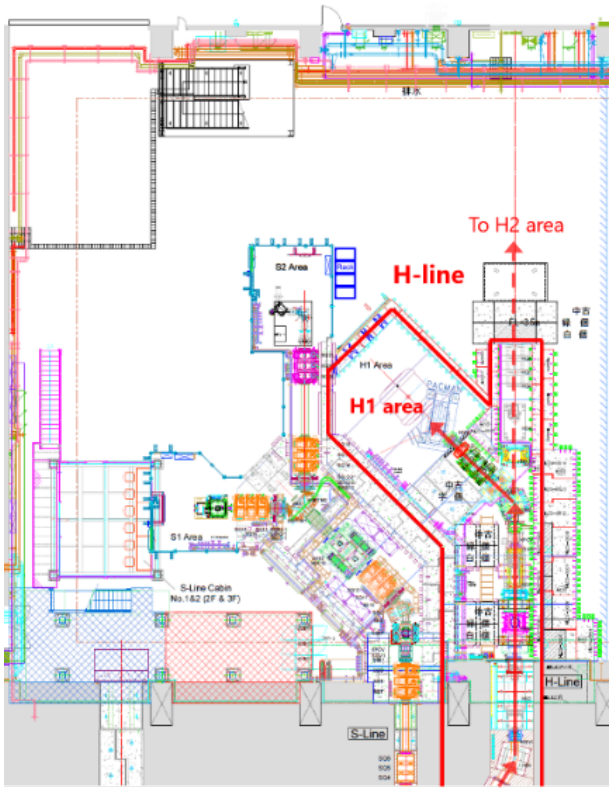

Fig. 1: A layout drawing of the H-line.

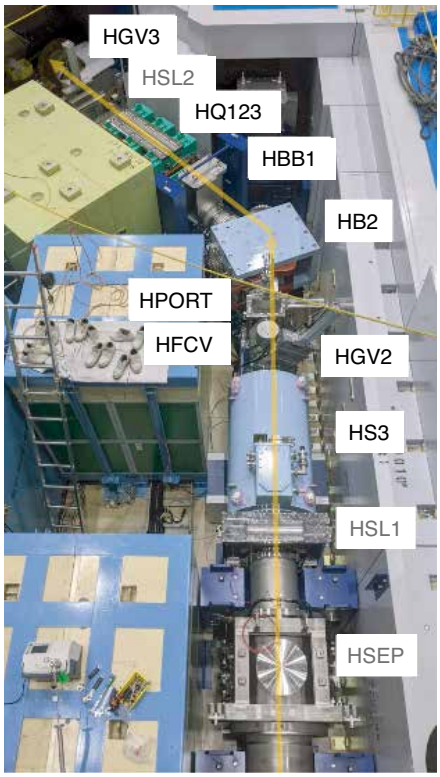

Fig. 2: All vacuum apparatuses for the 1st branch of the H-line were connected during the summer shutdown

tion solenoids (HS2 and HS3), focusing quadrupole triplets, and a DC-separator are not available yet, the rate of surface muons is expected to be 6×10^5 muons/s. In the next summer shutdown, we plan to conduct remaining works such as electrical cabling and cooling water piping of all magnets and installation of a DC separator and beam slits, and then the design intensity of 10^8 muons/s will be achieved.

The preparation for the second branch of the H-line (H2 area) also progressed. An extension building must be built for the H2 area on the east side of the MLF, where a parking lot is located because the muon g-2/EDM experiment planned at the H2 area needs to accelerate muons up to 212 MeV using a linac of about 50 m. In FY2020, the design of the extension building was detailed, and geotechnical investigation (Fig. 3) and buried cultural property research of the construction site was conducted.

Fig. 3: Geotechnical investigation of the construction site of the extension building for the H2 area.

References

[1] N. Kawamura, *et al.*, Prog. Theor. Exp. Phys. **2018** (2018) 113G01(1-12).

[2] K. Shimomura, AIP conf. proc. **1382** (2011) 245–247.

[3] T. Mibe *et al.*, Chin. Phys. C **34** (2010) 745–748.

[4] H. Natori, *et al.*, Nucl. Phys. B (Proc. Suppl.) **248-250** (2014) 52–57.

S2 Area Construction – Recent Progress

T. Adachi[1,2], N. Kawamura[1,2], A. Koda[1,2], T. Masuda[3], K. Shimomura[1,2], P. Strasser[1,2], S. Uetake[3], and T. Yamazaki[1,2]

[1]*Muon Science Laboratory, Institute of Materials Structure Science, KEK*
[2]*Muon Science Section, Materials and Life Science Division, J-PARC Center*
[3]*Division of Quantum Universe, Research Institute for Interdisciplinary Science, Okayama University*

1. Introduction

To realize the precise measurement of the Mu 1s-2s transition frequency [1] (KAKENHI 19H05606), the construction of the S2 area has been started. The S2 area is an experimental area of the surface muon beamline (S-line) in the experimental hall No.1 of the Materials and Life science experimental Facility (MLF) building. The S-line is designed to have four experimental areas; one area (S1 area) is already constructed and in operation [2, 3].

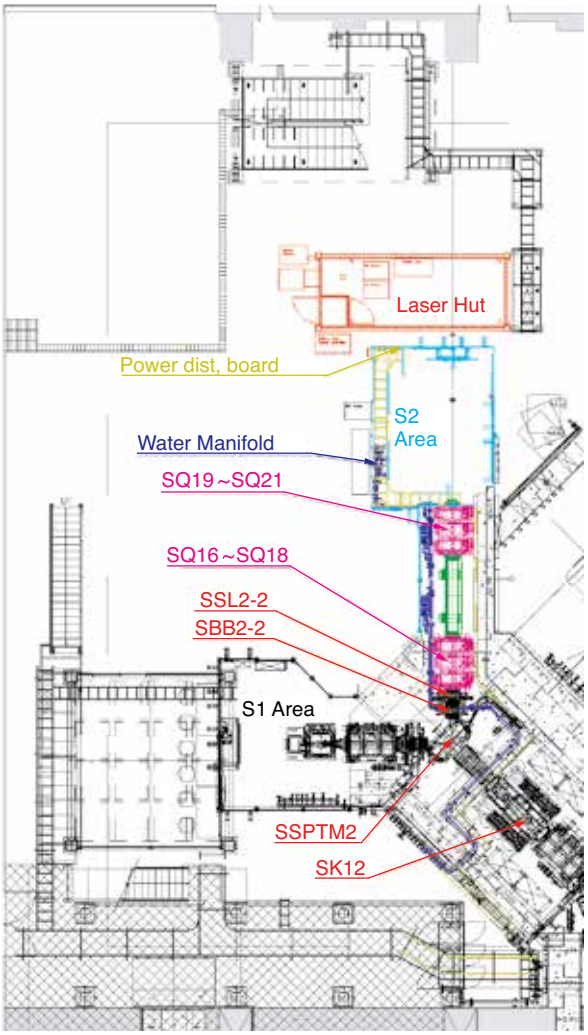

Fig. 1: A top view of the S2 area. Beamline components toward the S2 area are a kicker (SK12), a septum magnet (SSPTM2), a beam blocker (SBB2-2), a set of slits (SSL2-2), and two triplets (SQ16-18 and SQ19-21)

2. Overview of S2 area

The S2 area is located at the opposite side of the S-line from the S1 area. A top view of the S2 area is shown in Fig. 1. The kicker (SK12) can split a double-pulsed muon beam to two single-pulsed muon beams for both areas. A septum magnet (SSPTM2) leads muons to the S2 branch and two triplets (SQ16-18 and SQ19-21) guide them to the S2 area.

The Mu 1s-2s experiment uses lasers at the S2 area. So, the area is completely surrounded by walls and roofs as shown in Fig. 2. The roofs are removable for installing experimental setups. LED lights (5000 lm, 6 units) and ventilation fans (900 m^3/h, 2 units) are on the walls. A manifold of cooling water (50 l/min, 2 ports) and a power distribution board (100 V, 15 A, 4 ports) exist in the area. The beam interlock system is almost same as the S1 area. The door of the S2 area is hand-operated.

To provide lasers, a laser hut is located next to the S2 area. The laser hut is a custom-made 20-ft container, so that it can be easily craned and moved as necessary. The laser hut has no floor and the laser table or other instruments in the laser hut will be directly placed on the floor of the experimental hall. Figure 3 shows the laser hut hoisted with a crane. The laser hut has LED lights (2500 lm, 4 units), precision air-conditioner (Cooling power 7000 W), and double doors for light shielding.

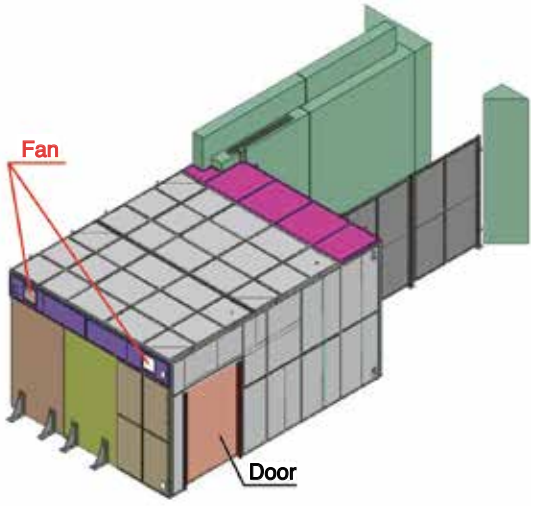

Fig. 2: An aspect of the S2 area

Fig. 3: The laser hut hoisted with a crane. Large instruments like a laser table can be installed by moving the hut to the other place.

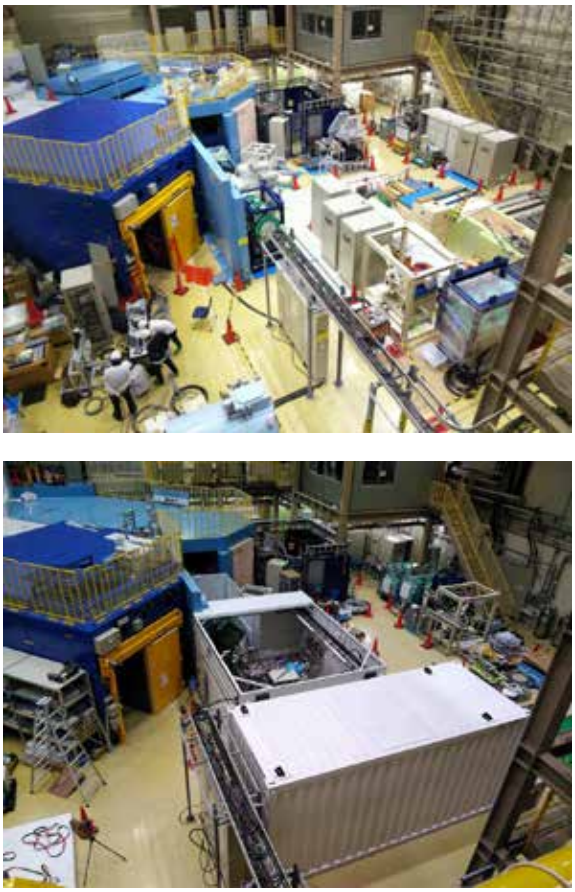

Fig. 4: The experimental hall No.1 before (Upper) and after (Lower) the construction. The roofs of the S2 area are temporary removed.

3. Construction

The construction of the S2 area has been almost finished in the summer shutdown of 2020. Figure 4 shows the experimental hall No.1 before and after the construction. Remaining construction works will be done after the allowance of the Nuclear Regulation Authority. The first beam of the S2 area is expected in the early fiscal year 2021.

References

[1] Ce Zhang *et al.*, JPS Conf. Proc. **33** (2021) 011125(1-6).

[2] A. Koda *et al.*, KEK Prog. Rep. **2014-1** (2014) 12–13.

[3] P. Strasser *et al.*, KEK Prog. Rep. **2017-4** (2017) 17–18.

Scientific Activities

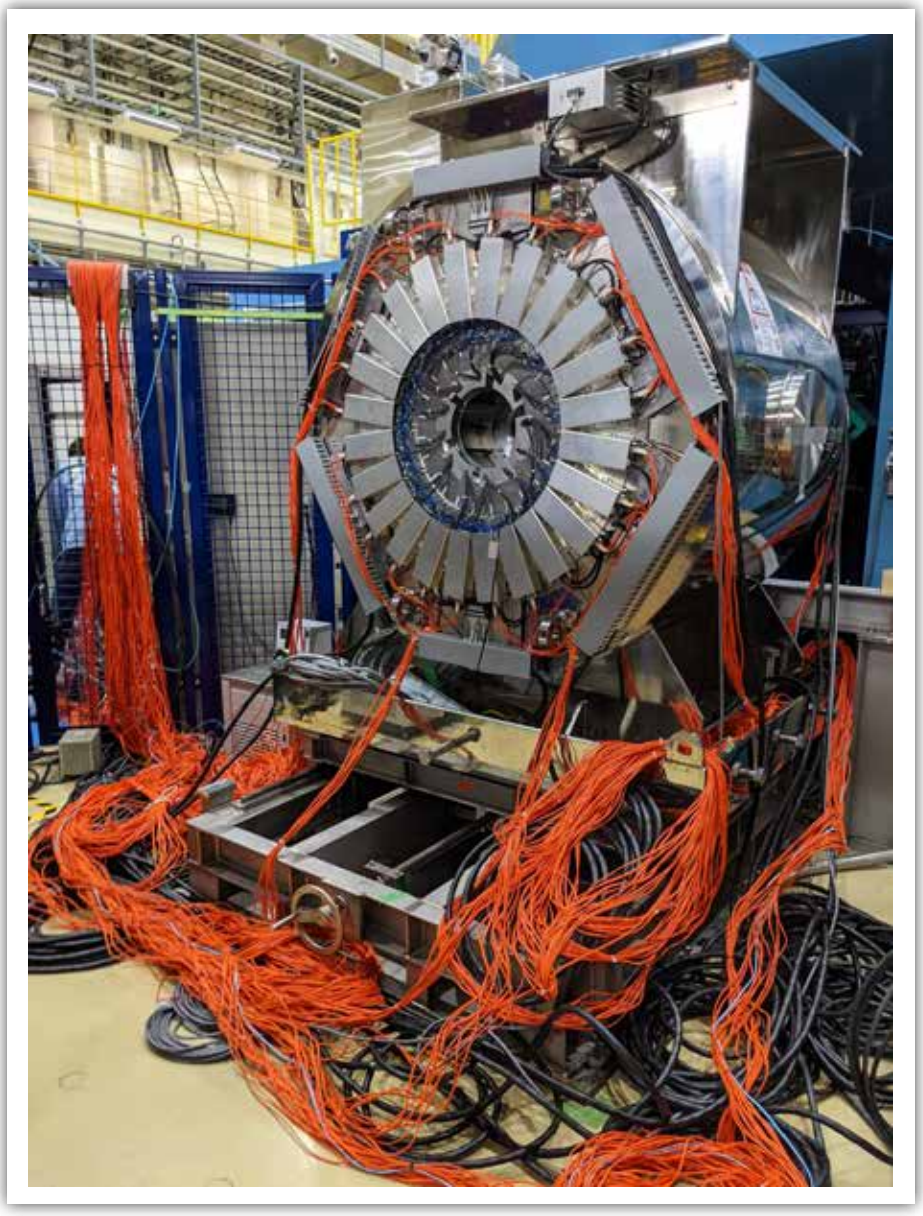

Ultra Slow Muon Beam Commisioning at U1B Area [J-PARC: 2015MS01]

Y. Nagatani[1,2], T. Yamazaki[1,2], J. Ohnishi[3], A. Goto[1], T. Yuasa[1,2], S. K. Dey[1,2], T. Adachi[1,2], and Y. Ikedo[1,2]

[1]*Muon Science Laboratory, Institute of Materials Structure Science, KEK*
[2]*Muon Science Section, Materials and Life Science Division, J-PARC Center*
[3]*Accelerator R&D Team, RIKEN Nishina Center for Accelerator-Based Science*

At the U1B area, a 5MeV transmission muon microscopy is being constructed. It will visualize thick objects ($> 10\mu$m) in nanometer resolution. Quantum coherence of the ultra-slow muon beam, and deep-penetration power of the muon beam accelerated over 5MeV give it the capabilities. At this fiscal year, we have constructed an 5MeV AVF-type muon-cyclotron (see Fig. 1) using flat-top RF acceleration.

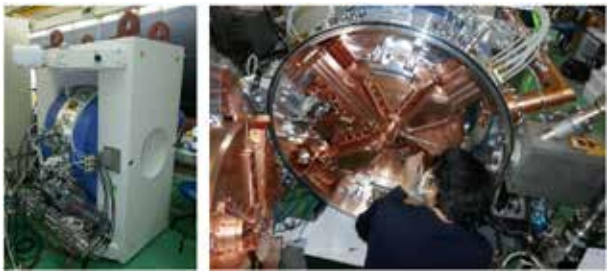

Fig. 1: Muon-cyclotron (left) and its inside (right).

1. 3D magnetic field measurement and shimming of the cyclotron magnet

The cyclotron should have quite small energy dispersion ($\Delta E/E \sim 10^{-5}$) to reduce chromatic aberration of the microscopy. The magnet of the cyclotron should give us the precisely designed magnetic field, and the discrepancy should be reduced to the order of 10^{-5}. We have developed a 3D measurement system of the magnetic field, which uses a search coil (see Fig. 2). We iteratively tuned the magnet by iron-shims of 184-pieces with 0.1 mm precision after the field measurements. Finally, the expected energy dispersion simulated based on the final field-measurement becomes $\Delta E/E \sim 6\times10^{-5}$.

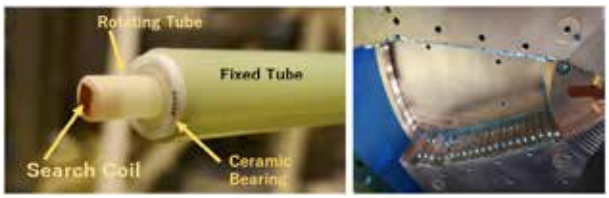

Fig. 2: Search Coil (left) and iron-shims (right).

Table 1: Expected capability of the cyclotron based on the magnetic field measurement after final shimming.

Transmission	98.6%	
Δ ***E/E***	$\mathbf{6.1\times10^{-5}}$	
	H	V
Emittance (π mm-mrad)	0.27	0.10
beta	115	34
alpha	-167	-55

2. RF Cavities of the cyclotron

Two main RF-cavities of 108MHz (main Dee) and a flat-top RF-cavities (flat top Dee) of 324MHz for muon-cyclotron are designed and constructed.

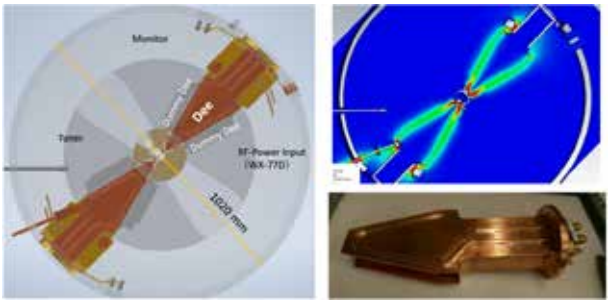

Fig. 3: Design of main Dees (left), RF fields by simulation (right-up) and the constructed body of main Dee (right-down).

3. RF Power Amplifier

The cyclotron requires CW 108MHz RF of 12-20kW to accelerate the muon beam to 5MeV energy. It also requires CW 324MHz RF less than 1kW for flat-top acceleration. The controlling system of the RFs is described in Fig. 4. The main RF is generated by combining 16 RF-amplifiers of 1.5kW (Fig. 5 right-up) by using 16-way RF-combiner (Fig. 5 center).

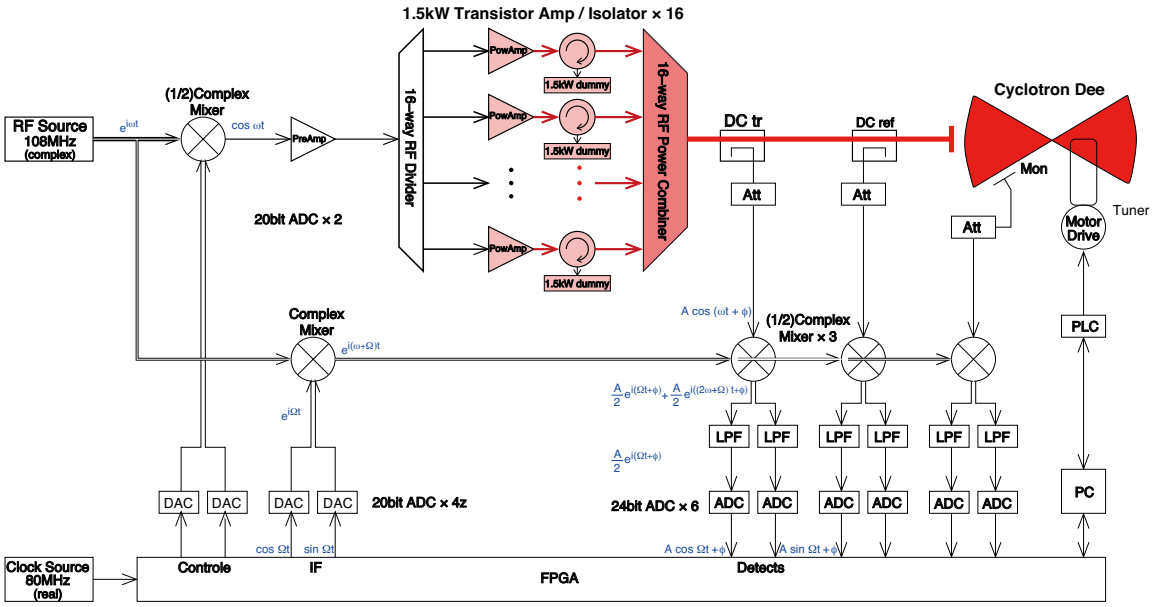

Fig. 4: Block Diagram of the RF System.

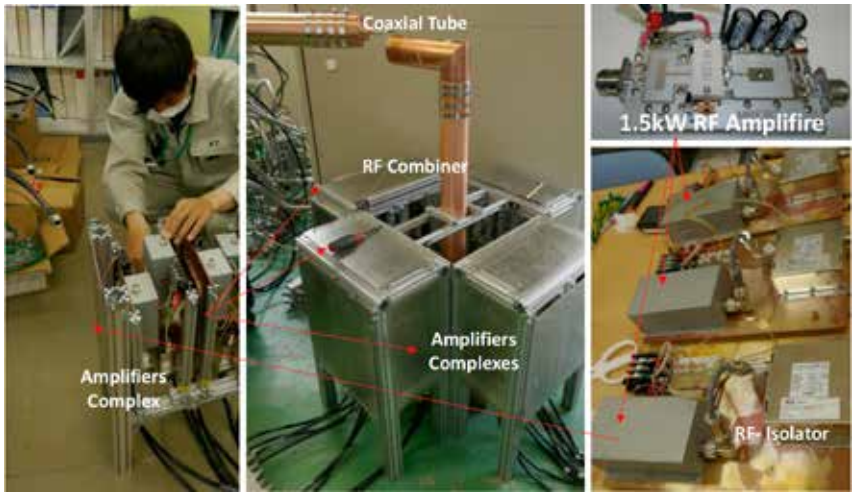

Fig. 5: 108MHz, 20kW RF Amplifier System.

New Development of Negative Muon Eexperiments Using the Latest Detector Technology for Space X-ray and γ-ray Observations. From Atomic/Molecular Physics to Non-destructive Analysis. [J-PARC: 2019MS01]

T. Takahashi, T. Azuma[1], K. Ninomiya[2], D. A. Bennett[3], P. Caradonna, I. Chiu[2], W. B. Doriese[3], M. S. Durkin[3], J. W. Fowler[3], J. D. Gard[3], T. Hashimoto[4], R. Hayakawa[5], G. C. Hilton[3], Y. Ichinohe[6], P. Indelicato[7], T. Isobe[8], T. U. Ito[4], M. Kajino[2], S. Kanda[9], M. Katsuragawa, N. Kawamura[9], Y. Kino[10], M. K. Kubo[11], T. Minami, K. Mine, Y. Miyake[9], K. Mizumoto[12], K. M. Morgan[3] S. Nagasawa, Y. Nagatani[9], T. Nakamura[13], H. Natori[9], H. Noda[14], S. Okada[15], G. C. O'Neil[3], T. Okumura[1], K. Okutsu[10],T. Osawa[4], N. Paul[3], C. D. Reintsema[3], D. R. Schmidt[7], K. Shimomura[9], P. Strasser[9], H. Suda[5], D. S. Swetz[3], M. Tampo[9], A. Taniguchi[16], S. Takeda, S. Takeshita[9], H. Tatsuno[5], K. Terada[14], Y. Tsuzuki, Y. Ueno[1], I. Umegaki[17] J. N. Ullom[3], T. Wada[13], S. Watanabe[18], G. Yabu, S. Yamada[6], and G. Yoshida[19]

Kavli IPMU, The University of Tokyo, [1]AMO Physics Laboratory, RIKEN, [2]Department of Chemistry, Osaka University, [3]NIST, US, [4]Japan Atomic Energy Agency, [5]Department of Physics, Tokyo Metropolitan University, [6]Department of Physics, Rikkyo University, [7]Laboratoire Kastler Brossel, Sorbonne Université, CNRS, France, [8]Nishina Center for Accelerator-Based Science, RIKEN, [9]Muon Science Laboratory, Institute of Materials Structure Science, KEK, [10]Department of Chemistry, Tohoku University, [11]International Christian University, [12]Tokyo University of the Arts, [13]Department of Earth Science, Tohoku University, [14]Department of Earth and Space Science, Osaka University, [15]Chubu University, [16]Institute for Integrated Radiation and Nuclear Science, Kyoto University, [17]Toyota Central Research and Development Laboratories, Inc., [18]Department of Space Astronomy and Astrophysics, ISAS, JAXA, [19]Radiation Science Center, KEK

1. Introduction

The S1 program 2019MS01 has been carried out under the Grant-in-Aid for scientific Research on Innovative Area, entitled "Toward new frontiers: Encounter and synergy of state-of-the-art astronomical detectors and exotic quantum beams". In this research area, we try to link the state-of-the-art detector technology for space X-ray and γ-ray observations to the research of "exotic" quantum beams such as negative muon, in which Japan is playing a leading role. In this project, we apply two types of detectors that have been established in space astronomy. One is a CdTe-based imaging detector, which has a high detection efficiency for hard X-rays at several 10 to 100 keV, and the other is a multi-pixel superconducting transition-edge-sensor (TES) calorimeter. We also use a set of high-resolution Ge detectors for X-ray and γ-ray spectroscopy.

By using the negative muon beam established at J-PARC, we aim to explore various applications such as (1) Precise spectroscopic measurements in atomic and molecular physics to test quantum electrodynamics (QED), and to study ultrafast dynamics triggered by a negative muon. (2) Non-destructive elemental analysis of extraterrestrial samples and archeological artifacts. Under the S1 proposal, we carried out four experiments at the

2. Precise spectroscopic measurements to study QED effects and ultrafast dynamics

In a muonic atom, the orbit of a negative muon lies very close to the positive nucleus, in a region of extremely strong electric fields. Using high precision measurements of muonic X-rays, the muonic atom becomes an ideal probe to verify QED predictions. We used the very slow and intense negative muon beam at the D2 beam line combined with multi-pixel high-resolution transition-edge-sensor (TES) calorimeters with a very high energy resolution (better than 6.0 eV FWHM resolution). We measured around 6.3 keV deexcitation X-rays associated with the $5g$-$4f$ and the $5f$-$4d$ (QED contribution of 2.3 and 5.2 eV, respectively) transitions of muonic neon atoms (μNe) isolated in the low-pressure Ne gas target. We concluded that there were no remaining bound electrons nor electron refilling from the neighboring atoms, making this an ideal case to compare with the QED theory. After detailed analysis, including on-line energy calibration and pulse pileup correction, we determined the $5g_{9/2}$-$4f_{7/2}$ transition energy to be 6297.27 eV (statistical error: 0.04 eV, systematic error: 0.07 eV), which agrees well with the most-advanced BSQED theoretical prediction

In addition, to study the deexcittaion dynamics of the muonic atom, we observed *electronic* K X rays emitted from muonic iron atoms(μFe) produced in a metal foil using the TES [1]. The excellent energy resolution allowed us to observe the asymmetric broad (covering the ∼100 eV range) profile of the electronic characteristic $K\alpha$ and $K\beta$ X rays together with the hyper satellite $K^h\alpha$ X rays around 6 keV. This signature reflects the time-dependent screening of the nuclear charge by the negative muon and the L-shell electrons, accompanied by electron side feeding from the surrounding. Assisted by a simulation, these data reveal the electronic K- and L-shell hole production and their temporal evolution on the 10-20 fs scale during the muon cascade process.

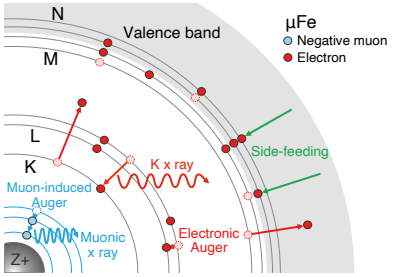

Fig. 1: Schematic drawing of the muon cascade process with the electron configuration evolution in the muonic iron atom (μFe) in Fe metal. Side feeding and electron refilling *via* radiative decay or electronic Auger decay fill the electron holes. Reproduced from Ref. [1]

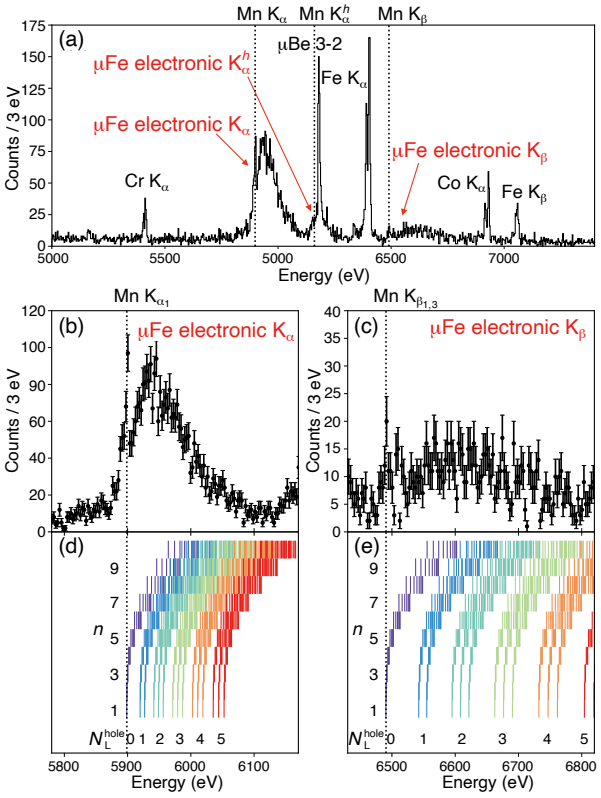

Fig. 2: (a) X-ray spectrum measured by the TES detector. Broad electronic $K\alpha$ and $K\beta$ X rays from μFe are observed. A broad tail-like structure beneath the peak of muonic X rays from μBe is identified as the hyper satellite $K^h\alpha$ X rays. Expanded spectra for (b) electronic $K\alpha$ X rays and (c) electronic $K\beta$ X rays from μFe. (d) Calculated $K\alpha$ and (e) $K\beta$ X-ray energies under different muon states (n) and electron configurations with L holes ($N_L^{\rm hole}$). See details in the main text. Regarding the muonic ℓ level, only the case of $\ell = n - 1$ is shown for clarity. Reproduced from Ref. [1]

3. Application to Non-destructive Elemental Analysis

Non-destructive elemental analysis using negative muons is a new and attractive method for studying the composition of material samples without causing damage to the samples. When a negative muon is injected in a material, it is captured by an atom and forms a muonic atom. Muon-induced characteristic X-rays have much higher energy than the fluorescence X-rays induced by electron transitions (e.g., the muonic μC-Kα is 75 keV versus the fluorescence C-Kα is 0.3 keV). Therefore, it is an ideal method for studying the amount and the distribution of light elements (such as Li and C) that are contained inside a sample. In this project, we are applying this method to quantify C, N, and O concentrations in asteroid samples collected by the Hayabusa2 mission and recovered back on Earth in Dec. 2020. Since the asteroid samples are small, we had to improve the sensitivity of detecting faint muonic X-ray lines by reducing background, mostly due to Bremsstrahlung radiation from electrons decayed from muons and muonic X-rays from the surrounding material. A new experiment setup has been designed and tested under actual beam conditions, and we have succeeded in achieving the low background level required for the analysis. It is important to note that our non-destructive method of quantifying the fraction of carbon in the powdered meteorite was found to be in good agreement with a destructive method of analysis we performed previously. Careful analysis of the data is now underway, and the results will be presented in the near future. In addition to the present setup, which uses Ge detectors, we have started to implement 3D imaging by utilizing newly developed CdTe imagers and succeeded in taking images by using coded mask aperture.

References

[1] T. Okumura *et al.*, Phys. Rev. Lett. **127** (2021) 053001(1-7).

Microscopic Mechanism of Hydrogen-sensitive Properties in Inorganic Materials: Implications from Muon study on β-MnO_2 [J-PARC: 2019MS02]

H. Okabe[1,2], M. Hiraishi[1,2], K. M. Kojima[3], A. Koda[1,2,4], R. Kadono[1,2,4], T. Ohsawa[5], N. Ohashi[5], S. Matsuishi[6], H. Hiramatsu[7], T. Kamiya[7], and H. Hosono[6,7]

[1]*Muon Science Laboratory, Institute of Materials Structure Science, KEK*
[2]*Center for Integrative Quantum Beam Science (CIQuS), Institute of Materials Structure Science, KEK*
[3]*Center for Molecular and Materials Science (CMMS), TRIUMF*
[4]*Department of Materials Structure Science, The Graduate University for Advanced Studies (Sokendai)*
[5]*National Institute for Materials Science (NIMS)*
[6]*Materials Research Center for Element Strategy, Tokyo Institute of Technology*
[7]*Materials and Structures Laboratory, Tokyo Institute of Technology*

1. Introduction

Hydrogen (H) is ubiquitous impurity stealthily intruding on various materials, often playing crucial roles in controlling their bulk properties. In particular, the revelation of H passivation in bulk silicon in 1980's focused a spotlight on the local electronic structure involving H in the field of semiconductor physics. Since then, accumulating evidence for causal relationship between H impurities and unintentional electric activities in numerous compound semiconductors and dielectrics led to intensive studies for understanding the microscopic mechanism of H-related phenomena in these materials.

The present S2-type project (2019MS02) is the continuation of the preceding S1-type research project for Element Strategy Initiative to Form Core Research Centers for Electronic Materials (2013MS01), where the research focuses on the behavior of implanted muon (Mu) as pseudo-H in oxides with rutile structure AO_2 (A denoting tetravalent cations, Ti, Sn, Mn, V, and so on) that will serve as a testing ground for our anion-molecular-orbital model developed from the local electronic structure of Mu/H in rutile TiO_2 [1, 2].

In FY2020, we reported the local electronic state of Mu in rutile-structured manganese dioxide (β-MnO_2), which has long been known as a battery material and catalyst, and obtained evidence that H contributes to electrical conduction in these materials [3]. The report also includes our first attempt to measure trace amounts of H in this compound, in collaboration with the Functional Materials Research Group of the National Institute for Materials Science (NIMS) which is a sub-center of the Element Strategy project. This is a part of the ongoing project to install a highly-hydrogen-sensitive thermal desorption spectroscopy (HHS-TDS) at the Tokai campus, serving as the complementary technique to elucidate the correspondence between the presence/absence of H in host materials and their physical properties by combining findings from Mu and bulk properties.

We also conducted μSR study on β-Ga_2O_3, a wide-gap semiconductor that is expected to be applied to power devices. The role of H impurities in β-Ga_2O_3 has been attracting much interest as one of the decisive factors for its electric activities. A preliminary result will be found in the succeeding report appearing in this volume [4].

2. Stable positions and local electronic states of Mu as pseudo-H in β-MnO_2

Manganese dioxide (MnO_2) is known as a catalyst for various chemical reactions such as deoxidants, and has recently attracted attention as a highly efficient heterogeneous catalyst for the oxidation of various types of substrates, including biomass-derived compounds [5]. Most of the applications of MnO_2 are in batteries, and MnO_2 synthesized by electrolytic method (γ-MnO_2) is used worldwide as a cathode material for lithium batteries and zinc primary batteries [6]. Artificially synthesized MnO_2 generally contains H in its crystal structure. This is believed to affect a variety of physical, chemical, and electrochemical properties.

There are two types of H (protons) in γ-MnO_2, as proposed by Ruetschi and Giovanoli [7, 8, 9]. The first type is the H associated with cation vacancies, called Ruetschi protons, which compensate for the charge on behalf of the Mn^{4+} cation. The second type is the H associated with the Mn^{3+} cation and is called the Coleman proton. It resides in the tunnel of the structure and is more mobile than the Ruetschi proton. The presence of these two types of protons has been experimentally confirmed by neutron diffraction and NMR studies [10, 11, 12, 13, 14]. However, since these protons are distinguished mainly by the difference in the length of the O-H bond, their specific positions and electronic states are unknown. In addition, it is difficult to understand the behavior of dilute H because its own signal is weak and the background H signal is falsely detected in various diffraction analyses.

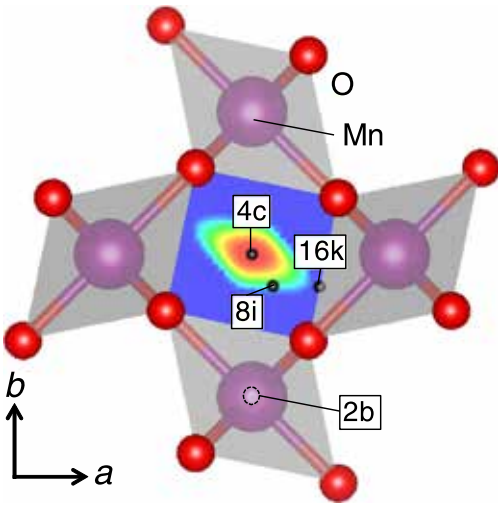

Fig. 1: Mu sites in β-MnO_2. 85% of these are at the 4*c* site, which is also the minimum of the Hartree potential by *ab initio* DFT calculations, and behave as Mu^+ states (i.e., as electron donors), whereas 15% are found to be at the Mn vacancy site and accompany a weakly bound electron (i.e., Mu^0).

MnO_2 is known to exhibit a variety of crystal polymorphs, resulting in the formation of various tunneling and layered structures, but β-MnO_2 (pyrolusite) is the simplest and most thermodynamically stable phase. The crystal structure of β-MnO_2 consists of MnO_6 octahedra shared by ridges and edges that form 1×1 tunnels (oxygen channels, see Fig. 1), which is also part of the basic structure of γ-MnO_2. The structure of β-MnO_2 is the same as that of rutile (TiO_2), which is also being actively studied as a photocatalyst and high-dielectric material, and is known to exhibit unintended *n*-type conductivity, which is thought to be due to oxygen depletion and low interstitial impurities such as H [15, 16]. If the oxygen vacancy concentration is negligibly small, H could be the main source of carriers. However, it is often difficult to separate all these different contributions in bulk property measurements.

The μSR experiment is unique in that the Mu itself behaves as pseudo-H in the material, making it possible to simulate the state of H in the dilute limit. More conveniently, β-MnO_2 is a classical antiferromagnet with a well-defined screw-type (helical) magnetic order below the Néel temperature (T_N) of 92 K [17, 18], and the position and electronic state of Mu in β-MnO_2 below T_N can be determined using the known magnetic structure as a guide.

A powder sample of β-MnO_2 (3N, Soekawa Co., Ltd.) was used in the present study. The H inclusion in the sample was observed by thermal desorption spectroscopy (TDS) placed in the National Institute for Material Science (NIMS), yielding H content of 2.918×10^{19} cm^{-3}. The temperature dependence of the magnetic susceptibility (χ) shows a kink at T_N. χ also shows a Curie-Weiss behavior with the Curie constant $C = 2.51$ emu·K/mol and the Weiss temperature $\Theta_W = -788$ K, which are in good agreement with the earlier report [16].

Conventional μSR experiments were performed using the ARTEMIS spectrometer installed in the S1 area at MUSE, J-PARC. Additional μSR experiments were conducted to resolve the detailed local field distribution using two instruments, i.e., the LAMPF spectrometer on the M20 beamline, and the NuTime spectrometer on the M15 beamline at TRIUMF, Canada, for the magnetic and paramagnetic phases of β-MnO_2, respectively. The DFT calculations were performed using the projector augmented wave approach implemented in the Vienna Ab initio Simulation Package (VASP) with the Perdew-Burke-Ernzerhof (PBE) exchange correlation potential [3].

From the muon Knight shift measurements in the paramagnetic phase ($T > T_N$), it was found that Mu is localized near the center of the oxygen-bounded tunnel called the 4*c* site in the rutile structure and/or in the 2*b* site corresponding to Mn vacancies (see Fig. 1). More detailed information on the Mu site occupancy was obtained from ZF-μSR data in the magnetically ordered phase ($T < T_N$). As shown in Fig. 2, the internal field distribution inferred from the FFT spectra is well represented by that expected at the 4*c* site under the helical magnetic order. From the relative amplitude of the μSR signal for this component (see Fig. 2c), it was found that about 85% of the implanted Mu adopts the diamagnetic state (Mu^+) at the 4*c* site over the observed T range (2-300 K) [3]. This Mu state corresponds to the Coleman proton and is consistent with the Hartree (electrostatic) potential minima from first-principles density functional theory (DFT) calculations. The inferred site is slightly different from the OH bond position (8*i* site) which is the total energy minimum when isolated H is inserted in the same DFT calculation. The difference can be understood as an isotope effect associated with the light mass of Mu. In any case, the diamagnetic state surrounded by anions is presumed to be Mu^+. This means that the electrons released from Mu upon its ionization ($Mu^0 \rightarrow Mu^+ + e^-$) are not localized in the *d*-orbitals of neighboring Mn^{4+} ions or in the vicinity of Mu itself, and that the corresponding H impurity levels are in the conduction band, i.e., they act as donors. This result is the first demonstration that the Coleman proton is an electron donor.

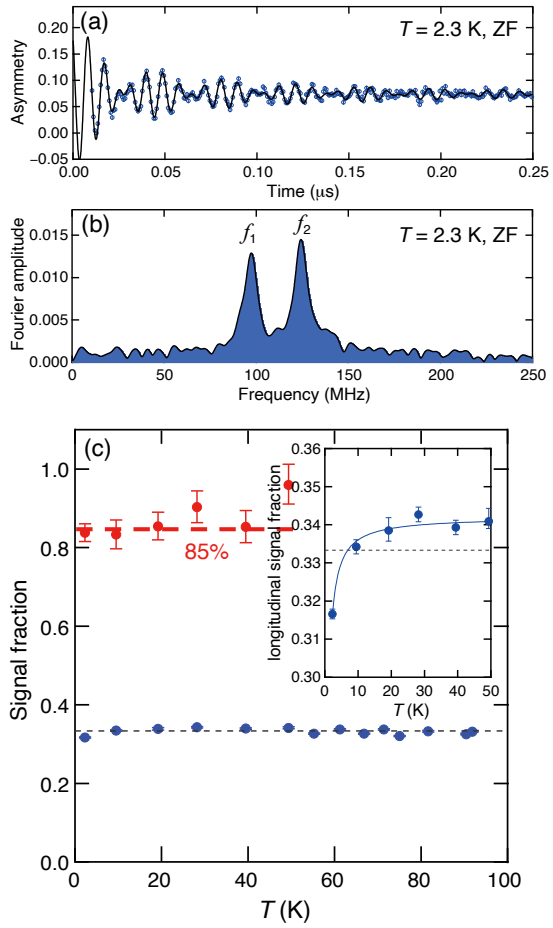

Fig. 2: (a) μSR time spectrum at 2.5 K under a zero external field. The solid line represents the result of least-squares fitting. (b) Fast Fourier transform of the time spectrum. f_1 (f_2) indicates a peak frequency. (c) Temperature dependence of the observed signal fraction (red circle) and the longitudinal signal fraction f_L (blue circle). The inset shows the enlargement below 50 K with the fitting curve using the thermal activation model. The broken line through f_L represents 1/3 of the total fraction.

On the other hand, while the remaining 15% are Mu^+ at high temperatures, they accompany weakly-bound electrons (i.e., Mu^0) at low temperatures (2.3 K). As seen in the inset of Fig. 2, the 1/3 tail exhibits a remarkable reduction below ~10 K, suggesting that a part of the diamagnetic state forms a paramagnetic Mu^0 whose residual polarization for the spin-triplet state is reduced to 1/2. Considering that the possibility of Mu occupying an O vacancy is negligible, as inferred from the TF-μSR linewidth in the paramagnetic phase ($T > T_N$), it is reasonable to attribute the origin of the missing fraction to that occupying Mn vacancies, which corresponds to naturally included Ruetschi protons. Moreover, the weakly bound electrons do not enter the d-orbitals of the Mn^{4+} ions, indicating that the electronic state can be understood by the effective mass model. This suggests that Ruetschi protons also behave as electron donors at high temperatures. Thus, considering the actual inclusion of H revealed by the TDS measurements in the present sample, these muon results provide strong evidence that the origin of n-type carriers is H impurities.

3. Acknowledgment

This work was supported by the MEXT Elements Strategy Initiative to Form Core Research Center for Electron Materials. We thank H. Sato for kindly providing β-MnO_2 specimen, and S. Takeshita and I. Yamauchi for their help during μSR experiment. Thanks are also to J. Nakamura for design and installation works for HHS-TDS, and to H. Lee for helping DFT calculations.

References

[1] K. Shimomura *et al.*, Phys. Rev. B **92** (2015) 075203(1-6).

[2] R. C. Vilão *et al.*, Phys. Rev. B **92** (2015) 081202(R)(1-5).

[3] H. Okabe *et al.*, Phys. Rev. B **103** (2021) 155121(1-9).

[4] M. Hiraishi *et al.*, KEK-MSL Prog. Rep. 2020.

[5] E. Hayashi *et al.*, J. Am. Chem. Soc. **141** (2019) 890–900.

[6] D. Glover *et al.*, *Handbook of Manganese Dioxides-Battery Grade*, Int. Battery Mater. Assoc., Cleveland (1989).

[7] P. Ruetschi, J. Electrochem. Soc. **131** (1984) 2737–2744.

[8] P. Ruetschi and R. Giovanoli, J. Electrochem. Soc. **135** (1988) 2663–2669.

[9] J. J. Coleman *et al.*, Trans. Electrochem. Soc. **90** (1946) 545–583.

[10] F. Fillaux *et al.*, J. Electrochem. Soc. **140** (1993) 585–591.

[11] M. Nagao *et al.*, J. Electrochem. Soc. **152** (2005) E230–E237.

[12] C. Pitteloud *et al.*, J. Solid State Chem. **181** (2008) 467–472.

[13] W.-I. Jung *et al.*, J. Mater. Chem. **19** (2009) 800–806.

[14] Y. Paik *et al.*, J. Am. Chem. Soc. **123** (2001) 9367–9377.

[15] Y. Noda *et al.*, Phys. Chem. Chem. Phys. **18** (2016) 13294–13303.

[16] H. Sato *et al.*, Phys. Rev. B **61** (2000) 3563–3569.

[17] H. Sato *et al.*, J. Phys. Soc. Jpn. **70** (2001) 37–40.

[18] M. Regulski *et al.*, J. Phys. Soc. Jpn. **73** (2004) 3444–3447.

Microscopic Mechanism of Hydrogen-sensitive Properties in Inorganic Materials [J-PARC: 2019MS02]

M. Hiraishi[1], H. Okabe[1], J. G. Nakamura[1], A. Koda[1,2], R. Kadono[1,2], K. Ide[3], T. Kamiya[3,4], and H. Hosono[4]

[1]*Muon Science Laboratory, Institute of Materials Structure Science, KEK*
[2]*Department of Materials Structure Science, SOKENDAI*
[3]*Materials and Structures Laboratory, Tokyo Institute of Technology*
[4]*Materials Research Center for Element Strategy, Tokyo Institute of Technology*

Hydrogen (H) plays key roles in functional materials such as electrides and semiconductors, and the local electronic structure involving H has been the subject of intensive studies for understanding the microscopic mechanism of H-related phenomena that has significant impact on the application of these materials. Muon can be regarded as a light isotope of hydrogen in the sense that the local structure of a muon-electron system is virtually equivalent with that of hydrogen. Thus, μSR provides microscopic information on the local environment of muon as a pseudo-H (Mu, which we call "Muogen") for assessing the corresponding state of H.

In this report, we present a μSR study of H/Mu in β-Ga_2O_3. β-Ga_2O_3 has been drawing much attention as a material for high-voltage power devices because of its large band gap (E_g ~4.9 eV). It is known that β-Ga_2O_3 exhibits n-type conductivity when doped with Si or Sn [1]. However, the electronic state of hydrogen has also attracted much attention because theoretical calculations have reported that interstitial hydrogen can also be the origin of n-type doping [2, 3].

β-Ga_2O_3 is composed of two (three) inequivalent Ga (O) sites. O_I and O_{II} are three-fold coordinated, while O_{III} is four-fold coordinated. As shown in Fig. 1, Ga_I and Ga_{II} are tetrahedrally and octahedrally coordinated, respectively.

μSR measurements were performed using ARTEMIS spectrometer installed at the S1 beamline in J-PARC MLF. (001) and (010) oriented single crystalline samples (Novel Crystal Technology, Inc.) were grown using edge-defined film-fed growth method [4]. The donor concentration is estimated to be 2×10^{17}cm^{-3}.

Figure 2(a) shows μSR time spectra in the (001) sample measured under zero field (ZF) and different longitudinal fields (LF) at 300 K. The spectra have two components, one that relaxes with Kubo-Toyabe function (denoted as Mu_1) and one that does not relax (Mu_2). The spectra are then analyzed by the following function,

$$A_0 G_z(t) = A_1 G_{\rm KT}(\Delta, t, B_{\rm ext}) + A_{\rm c}, \qquad (1)$$

where, A_0 and A_1 are the total and partial asymmetries, $G_{\rm KT}(\Delta, t, B_{\rm LF})$ is the static Gaussian Kubo-Toyabe function under a longitudinal field $B_{\rm LF}$, and Δ is the dipolar width (corresponding to the rms of the local field distribution) at the muon site. As shown by solid curves in Fig. 2(a), experimental data is perfectly reproduced with $\Delta = 0.1347(11)$ μs^{-1}.

We performed DFT calculations to narrow down the possible Mu_1 site(s) using the OpenMX code [5].

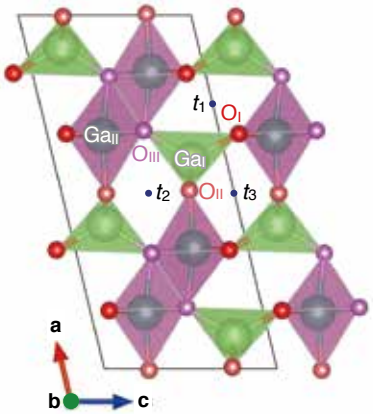

Fig. 1: Crystal structure of β-Ga_2O_3. t_i ($i = 1 - 3$) represents the tunnel positions where the b-axis dependence of $\Delta E_{\rm tot}$ was calculated (see Fig. 4).

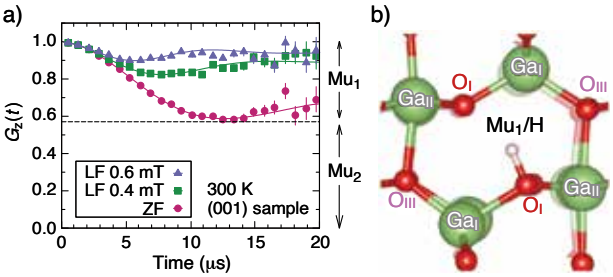

Fig. 2: (a) μSR time spectra of (001) β-Ga_2O_3 under ZF and LF measured at 300 K. The statistics of each spectrum are 100M positron events. (b) Local structure around H/Mu_1. Transparent atoms represent their original positions in perfect β-Ga_2O_3. The Origin for both relaxed and perfect lattice is O_I at the lower right.

gen) including an interstitial H was relaxed until the maximum force on atoms was less than 3×10^{-4} (Hartree/Bohr). A GGA-PBE exchange correlation functional was used under the cutoff energy of 200 Ry and K point mesh of 3×4×3. Figure 2(b) shows the relaxed local structure around H where the calculated Kubo-Toyabe relaxation rate $\Delta_{\rm sim} = 0.1371\ \mu{\rm s}^{-1}$ is fully consistent with the experimental value. H bonds to $O_{\rm I}$ with OH bond length of 0.098 nm, consistent with the Ref. [2]. We also found that $\Delta_{\rm sim} = 0.1472\ \mu{\rm s}^{-1}$ for H bonded to $O_{\rm II}$, corresponding to the local structure reported in Ref. [3], is also consistent with the experimental value. Here, it is worth stressed that these hydrogen have been reported to act as donors [2, 3]. Since the GGA-PBE method slightly overestimates the lattice constants of the unit cell in our case, we plan to re-evaluate $\Delta_{\rm sim}$ using the HSE06 hybrid functional method suited for insulators.

Figure 3(a) shows the temperature dependence of the ZF spectra of (001) sample. The initial asymmetry is independent of temperature, indicating that most of the Mu is in a diamagnetic state. This result is in contrast to the Ref. [6], which reported the existence of Mu^0 state below ∼100 K. It is also noticeable that Mu_2 (constant) term drastically changes with temperature. As inferred from the temperature dependence of fractional yield for Mu_2 $f_{Mu_2} \equiv A_c/A_0$ deduced from Eq. (1) shown in Fig. 3(b), both (001) and (010) samples have a minimum around 60 K. As no interstitial sites are free of local magnetic fields from Ga nuclei, which have 100% natural abundance, it suggests that the relaxation of the Mu_2 component is suppressed by fast diffusion of Mu itself and that its yield varies with temperature. Interestingly, it is reported in Ref. [7] that carrier concentration and mobility of FZ-grown β-Ga_2O_3 exhibit the local maximum and minimum around 50 K, respectively. While the origin of these anomalies remains unclear, we speculate that f_{Mu_2} may be related to the bulk electrical properties.

To investigate the diffusion path of Mu_2, we calculated the total energy $E_{\rm tot}$ along the b-axis in a lattice of 1×2×1 structure. Figure 4 shows the variation of the total energy $\Delta E_{\rm tot} \equiv E_{\rm tot}(\boldsymbol{r}) - E_{\rm min}$ with respect to H position $\boldsymbol{r}$, where $\boldsymbol{r}$ is position vector at the tunnel t_i ($i = 1, 2, 3$, see Fig. 1) and $E_{\rm min}$ is the global minimum of $E_{\rm tot}(\boldsymbol{r})$. While the $\Delta E_{\rm tot}$ in tunnels t_2 and t_3 exhibits a large changes of more than 0.5 eV, $\Delta E_{\rm tot}$ in t_1 is almost independent of the b-axis, with a difference of only ∼0.04 eV, suggesting that t_1 is the possible diffusion path for Mu_2. Currently, we presume that Mu_2 component corresponds to a non-equilibrium acceptor-like Mu, but bulk measurement on electrical properties and more detailed calculations are required to conclude this.

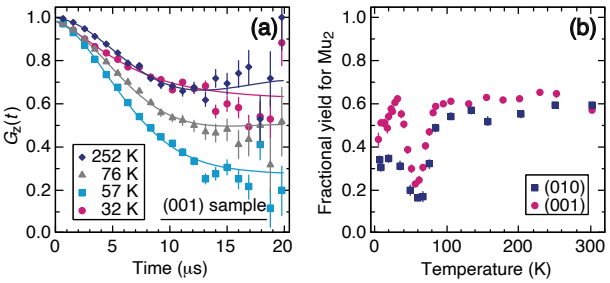

Fig. 3: (a) Temperature variations of ZF spectra in (001) sample. Fractional yield of Mu_2 f_{Mu_2} as a function of temperature.

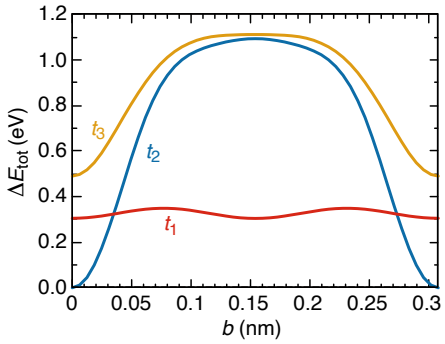

Fig. 4: $\Delta E_{\rm tot}$ profiles along the b-axis at the tunnels t_1, t_2, and t_3 (see Fig. 1).

Acknowledgment

This work was supported by the MEXT Elements Strategy Initiative to Form Core Research Center for Electron Materials (Grant No. JPMXP0112101001) and JSPS KAKENHI (Grant No. 19K15033).

References

[1] M. Orita *et al.*, Appl. Phys. Lett. **77** (2000) 4166–4168.

[2] J. B. Varley *et al.*, J. Phys. Condens. Matter **23** (2011) 334212(1-9).

[3] H. Li and J. Robertson, J. Appl. Phys. **115** (2014) 203708(1-11).

[4] A. Kuramata *et al.*, Jpn. J. Appl. Phys. **55** (2016) 1202A2(1-6).

[5] T. Ozaki, Phys. Rev. B **67** (2003) 155108(1-5).

[6] P. D. King *et al.*, Appl. Phys. Lett. **96** (2010) 062110(1-3).

[7] E. G. Víllora *et al.*, Appl. Phys. Lett. **92** (2008) 202118(1-3).

High Temperature μSR Measurement of Magnetic Field Enhancement on a Si-free Nano-crystalline Formation [J-PARC: 2019B0210]

Temperature Shift Measurements of Nano-crystalline Formation for $Fe_{81}Cu_1B_{15}Nb_3$ and $Fe_{bal.}Cu_1Nb_3Si_{15.5}B_7$ by High-temperature μSR [J-PARC: 2020B0245]

C. Ohmori, Y. Yoshizawa, A. Koda[1], Y. Miyake[1], K. Ogura[2], M. Ohta[2,3], K. Arakawa[3], and N. Hirayama[3]
Accelerator Laboratory, KEK
[1]*Muon Science Laboratory, Institute of Materials Structure Science, KEK*
[2]*Hitachi Metals, Ltd.*
[3]*Interdisciplinary Faculty of Science and Engineering, Shimane University*

1. Introduction

J-PARC delivers a 730 kW proton beam to the MLF from the 3 GeV Rapid Cycling Synchrotron (RCS) and a 510 kW beam to the T2K experiment from the Main Ring (MR). Both high-intensity beams are energized by wideband RF accelerating systems using a nanocrystalline material, FINEMET® [1]. In the MR, a magnetic annealed material, FT3L, has been used since 2014 to improve beam intensity [2]. Recently, cavity development has started for the RCS by replacing the existing cavity systems with FT3L-types. In CERN, FT3L cavities are used for the PS, PS booster, Anti-proton Decelerator and Extra Low Energy Antiptoron ring [3]. FT3L is also considered for use in new accelerator R&D in other conuntries. Improvements in cavity core materials are still important for many research fields using particle accelerators and decelerators.

2. High temperature μSR experiments for nano-crystalline research

In 2018, we studied effects of magnetic fields on nano-crystalline formation. We prepared an amorphous material, $Fe_{bal.}Cu_1Nb_3Si_{15.5}B_7$ and maintained it at the critical temperature to measure the speed of crystallization under different magnetic field strengths. The results are shown in Fig. 1. Crystallization occurred slowly under a field strength of approximately 0.01 T. We also confirmed this behavior using XRD analysis [4].

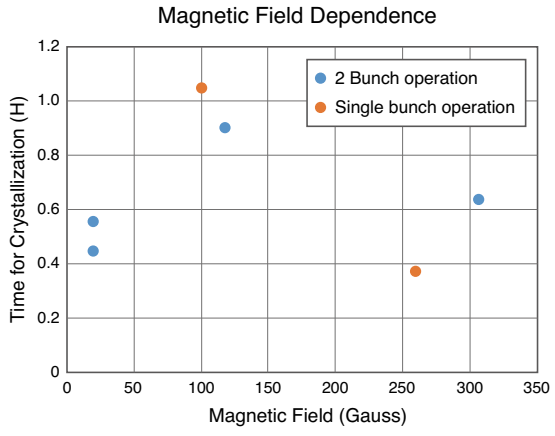

Fig. 1: Field strength dependence of nano-crystallization speed.

3. Experimental results in FY2020

In order to investigate the effects of the magnetic fields on nano-crystal formation, we measured the variation in crystallization temperature in FY2020. An amorphous sample was placed in a carbon container as before and heated at a rate of 1 °C/min. A thermo couple was used to measure the temperature of carbon container and control the heater. The temperature of the sample was monitored using the other thermo couple which was glued on it. The μSR data were collected every 3 min. The asymmetry was fitted using,

$$A_y = Aexp(-\lambda t)cos(\omega t + \theta) + A_0. \qquad (1)$$

Here, λ is the relaxation rate. A typical μSR signal is shown in Figs. 2. The upper panel shows the behavior of the para-magnetic material. Although the amorphous phase is ferro-magnetic at room temperature, it is a paramagnetic phase at 742 K because the Curie temperature is approximately 620 K. The lower figure shows that the sample became ferro-magnetic because of nano-crystal formation.

Figure 3 shows typical variations in λ at the field strength of 0.002 T, 0.01 T and 0.03 T. At both 0.01 T and 0.03 T, a large λ value of 3-4 μs^{-1} was observed because of magnetic field uniformity. To confirm the effects of the magnetic field, the field strength was rapidly changed to 0.002 T, resulting in a λ values of approximately 0.5 μs^{-1} which is as low as the values at 0.002T. Figure 4 shows normalized λ values for all field strengths: 0.002, 0.005, 0.01, and 0.03 T. The measurement at 0.002 T was repeated to confirm the reproducibility. λ exhibited two-step variations at 750 K and 770 K. Two measurements under field strength of 0.002 T showed the same behavior. The first variation was as fast as that at 0.03 T although the λ coefficient increased monotonically. The second variation under 0.002 T occurred as slow as those at 0.01 and 0.005 T. In all cases, the maximum values were between 0.5 and 0.8 μs^{-1}.

4. Discussions

The result may explain the previous result at fixed temperature [4] shown in Fig. 1. Because we set the sample temperature at 746 K as the critical temperature, the λ coefficient already has difference between 0.005-0.01 T and others as shown in Fig. 4. Temperature shift of nano-crystallization was consistent results with the previous measurements [4].

It is still unclear how difference occurred. The energy difference because of magnetic field strength is much smaller than that because of temperature. We started an approach from theoretical side as a collaboration with Shimane university to understand these behaviors.

The lower panel of Fig. 2 shows that the Lamor precession seems to continue to 8 μs. This suggests that some muons may have stopped outside the sample. So far, we have fitted the asymmetry using the eq. (1). We are working on improving fitting with another term that expresses the muons outside the sample.

5. Conclusion

In FY2020, we measured the temperature variation in the nano-crystalline formation under different magnetic field strengths. We observed different behaviors between 0.002 T, 0.005-0.001 T and 0.03 T. The new measurement may explain the previous measurement results, shown in Fig. 1 at the critical temperature.

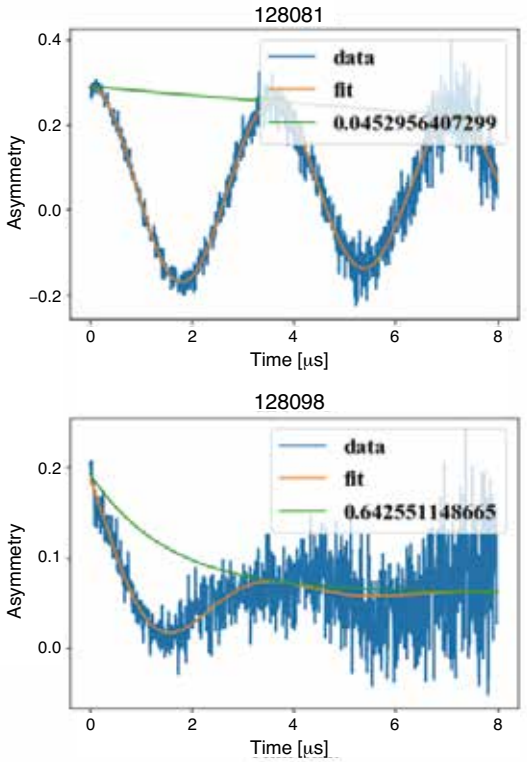

Fig. 2: μSR signals at 742 K (upper) and 787 K (lower). At 742 K, amorphous became para-magnetic because the temperature is above the Curie temperature of of the material. At 787 K, nano-crystal formation occurred and the material became ferro-magnetic. Orange and green lines show fitting results obtained using eq. (1) and the envelope given by the λ coefficient.

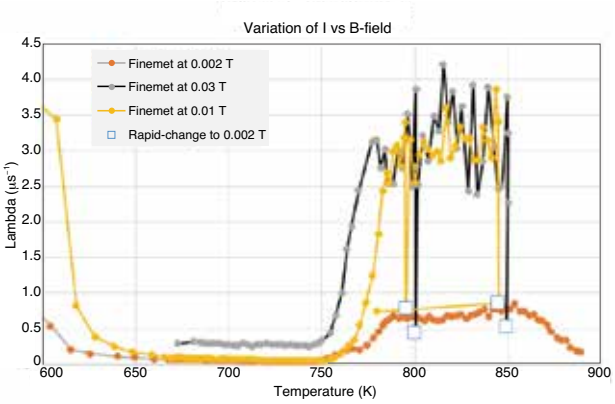

Fig. 3: Field strength dependence of nano-crystallization temperature.

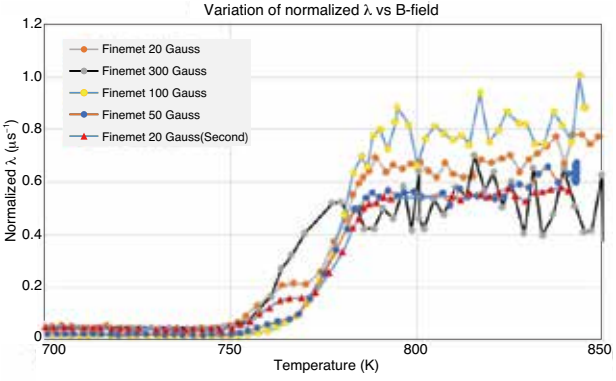

Fig. 4: Temperature variation of the normalized λ coefficient under different field strengths.

References

[1] Y. Yoshizawa *et al.*, J. Appl. Phys., **64** (1988) 6044–6046.

[2] C. Ohmori *et al.*, Phys. Rev. Accel. Beams **16** (2013) 112002(1-8).

[3] C. Ohmori *et al.*, JPS Conf. Proc. **33** (2021) 011006(1-6). Proceedings of the 3rd J-PARC Symposium (J-PARC2019)

[4] M. Ohta *et al.*, JPS Conf. Proc. **33** (2021) 011053(1-6). Proceedings of the 3rd J-PARC Symposium (J-PARC2019)

Residual Magnetic Fluctuation in Honeycomb Antiferromagnets
[J-PARC: 2019B0319]

I. Yamauchi and T. Ishibashi[1]

Department of Physics, Faculty of Science and Engineering, Saga University
[1]*Graduate School of Science and Engineering, Saga University*

1. Introduction

Forty years ago, Berezinskii [1], Kosterlitz and Thouless [2] independently found a topological phase transition, BKT transition, in the two-dimensional (2D) XY spin model accompanied by unbinding of pairs of bound vortex excitations at a finite critical temperature, $T_{\rm BKT}$. Although the original BKT transition is confined to the 2D-XY model, several theoretical studies have proposed that a 2D-Heisenberg antiferromagnet (AFM) with weak easy-plane exchange anisotropy shows the BKT transition with a three-dimensional (3D) magnetic ordering at $T_{\rm N}$ and a crossover from high-temperature isotropic 2D-Heisenberg to low-temperature 2D-XY magnet above $T_{\rm N}$ [3].

$BaNi_2V_2O_8$ is a candidate material for the 2D AFM with the BKT transition. Figure 1 shows schematic figures of the crystal structure of $BaNi_2V_2O_8$. $BaNi_2V_2O_8$ has a hexagonal structure with a space group $R\bar{3}$ and no structural phase transition has been reported down to 8 K [4]. The Ni^{2+} (spin $S = 1$) is octahedrally coordinated by six O^{2-} ions and makes honeycomb lattice by sharing the edges of the NiO_6 octahedra. The honeycomb layers are stacking along the c axis and separated by nonmagnetic Ba^{2+} and VO_4 layers. Temperature, T, dependence of magnetic susceptibility, χ, shows a broad peak at ∼150 K and shows a crossover at ∼100 K from high-T isotropic to low-T anisotropic state with 2D-XY model like behavior. Although the antiferromagnetic ordering has been confirmed by the neutron diffraction experiment below $T_{\rm N} \sim 48$ K, T dependence of specific heat shows a broad anomaly at around $T_{\rm N}$ indicating the magnetic entropy is gradually lost over wide T range. Furthermore, anomalous exponential behavior, which is theoretically suggested in the BKT transition system, has been reported in T dependence of the magnetic correlation length just above $T_{\rm N}$ by ESR and NMR measurements. [5, 6] In the magnetic ordered state, quantum fluctuation is expected from the estimated magnitude of the ordered moment $\sim 1.6\mu_{\rm B}$, which is smaller than $2\mu_{\rm B}$ expected for the $S = 1$ magnets. [4]

Previously, we conducted muon spin rotation/relaxation (μSR) experiment above 4 K on polycrystalline samples of $BaNi_2V_2O_8$, and found residual magnetic fluctuation in the antiferromagnetic state. However, it is unclear that the low energy magnetic fluctuation remains below 4 K. Thus we made further μSR investigation below 4 K.

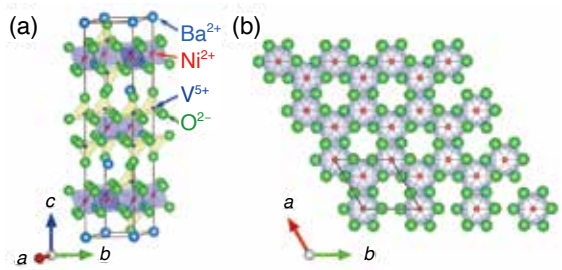

Fig. 1: (a) Crystal structure of $BaNi_2V_2O_8$ and (b) NiO_6 honeycomb layer viewed from the c axis. The light blue, red, blue, and light green balls represent Ba^{2+}, Ni^{2+}, V^{5+}, and O^{2-} ions.

2. Experiment

The polycrystalline sample was prepared by the solid state reaction method as shown in Ref. [4]. Conventional zero-field (ZF) μSR measurements were conducted on the GPS beamline of PSI, Switzerland, and longitudinal-field (LF) μSR experiments were made at the S1 and D1 beamlines of J-PARC.

3. Results and Discussion

Figure 2(a) displays ZF-μSR spectra measured in the antiferromagnetic state of $T = 9.4$, 4.0, and 1.9 K. We observed three precession signals and a relaxing "1/3" component in the ZF-μSR spectrum below $T_{\rm N}$ indicating an existence of magnetic ordering. The ZF-μSR spectra were fitted by an equation,

$$A(t) = \sum_{i=\rm a,b,c} A_i \cos(2\pi\nu_i t)\exp(-\lambda_{{\rm T},i}t) + A_{1/3}\exp(-\lambda_{\rm L}t). \quad (1)$$

The first term represents the precession signals from three different muon sites observing static internal field from the spontaneous magnetization. A_i, ν_i, and $\lambda_{{\rm T},i}$ are asymmetry, rotating frequency, and depolarization rate for each rotating signal. These three precession signals have frequencies $\nu_{\rm a} \sim$ 4 MHz, $\nu_{\rm b} \sim 5$ MHz, and $\nu_{\rm c} \sim 20$ MHz at low T.

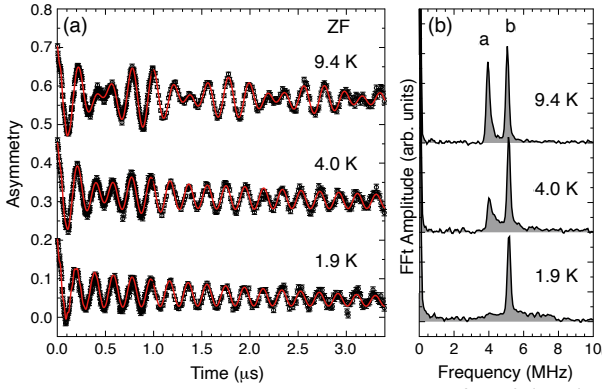

Fig. 2: (a) μSR time spectra measured at 9.4, 4.0, and 1.9 K with zero external field. The solid lines represent fitted curves by the equation. The data for different temperatures are offset vertically for clarity. (b) Fast Fourier transformation of ZF-μSR spectra shown in (a).

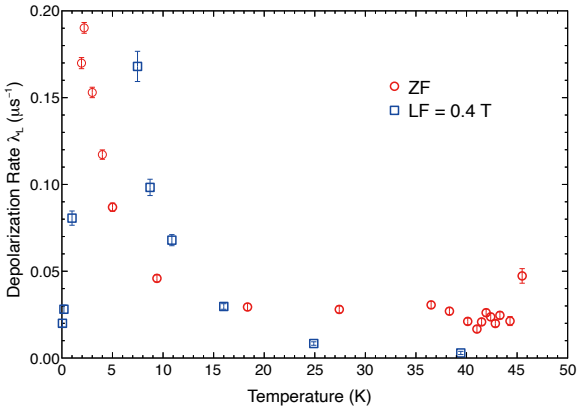

Fig. 3: Temperature dependence of depolarization rate λ_L for ZF (red circle) and LF = 0.4 T (blue square).

The second term expresses a slowly relaxing "1/3" component, which is also originating from the muon stopped in the sample since the internal field parallel to the initial polarization of the muon magnetic moment does not induce the Larmor precession. $A_{1/3}$ and λ_L are asymmetry and depolarization rate for the "1/3" component.

In Fig. 2(b), we plot fast-Fourier-transformed (FFT) μSR spectra for the time spectra shown in Fig. 2(a). We find sharp two peaks for signal "a" ($\sim$4 MHz) and "b" ($\sim$5 MHz) at 9.4 K. However, the signal "a" has broad tail in the frequency region higher than the peak frequency at 4.0 K, then, the peak structure is merged at 1.9 K. These results indicate that the distribution of magnitude of the internal field at one of the muon sites becomes very broad below 3 K by modifying the spin structure in the antiferromagnetic state.

This changing of the spin structure is corresponding to a broad peak at $\sim$ 3 K in T dependence of χ, observed in our polycrystalline sample (not shown). On the other hand, such a $\sim$ 3 K anomaly has never been found in T dependence of χ for single crystals. Therefore, we expect that the $\sim$ 3 K anomaly is generated by impurity and/or defect in the crystal. One of possible scenario is that some free spins are generated by defects in the crystal, and the spins show freezing transition at $\sim$ 3 K. However, the origin of the interaction between free spins in the magnetic ordered state of insulator is unknown at present.

Since the $\sim$ 3 K anomaly appears only in polycrystalline sample, an existence of a secondary phase is suspected as an origin of the signal "a" and its $\sim$ 3 K anomaly. However, the 4 MHz precession signal is also observed in recent μSR experiment using single crystals, which show no anomaly at $\sim$ 3 K in T dependence of χ [7]. Thus we consider that the signal "a" is coming from the main phase.

To elucidate the details of the spin dynamics, we also conducted μSR measurement under a LF of 0.4 T. T dependence of λ_L measured at ZF and LF are plotted in Fig. 3. Below 10 K, both λ_L show rapid increase with decreasing T. However, the λ_L for LF shows decreasing behavior with decreasing T below 1 K. Although the luck of the data in the T range between 1 K and 7 K, we expect that the λ_L for LF has a peak at $T = 3 \sim 5$ K. This result indicates that the characteristic frequency of the residual magnetic fluctuation slows down lower than $\sim$ 60 MHz, which is the Larmor frequency of the muon magnetic moment at 0.4 T, below $\sim$ 3 K.

References

[1] V. L. Berezinskii, Sov. Phys. JETP **34** (1972) 610–616.

[2] J. M. Kosterlitz and D. J. Thouless, J. Phys. C: Solid State Phys. **6** (1973) 1181–1203.

[3] A. Cuccoli *et al.*, Phys. Rev. B **67** (2003) 104414(1-18). ; Phys. Rev. Lett. **90** (2003) 167205(1-4).

[4] N. Rogado *et al.*, Phys. Rev. B **65** (2002) 144443(1-7).

[5] M. Heinrich *et al.*, Phys. Rev. Lett. **91** (2003) 137601(1-4).

[6] D. Waibel *et al.*, Phys. Rev. B **91** (2015) 214412(1-6).

[7] E. S. Klyushina *et al.*, Phys. Rev. B **104** (2021) 064402(1-14).

Optical Imaging of Positive Muons for the Quality Assessment of the Beams [J-PARC: 2019B0407]

S. Yamamoto, K. Ninomiya[1], N. Kawamura[2], and Y. Hirano

Graduate School of Medicine, Nagoya University
[1]*Graduate School of Science, Osaka University*
[2]*Muon Science Laboratory, Institute of Materials Structure Science, KEK*

A muon is a particle similar to an electron, with an electric charge of e^- for a negative muon and e^+ for a positive muon; however, its mass is 207 times that of an electron. A muon has a mean life-time of 2.2 μs and a negative muon decays to one electron (maximum energy of $\sim$ 50 MeV) and two types of neutrinos, while the positive muon decays to one positron (maximum energy of $\sim$ 50 MeV) and two types of neutrinos. Since these characteristics are quite different from familiar radiations such as X-rays, electrons or protons, new method for range and width determination will be possible for muon beams. Since high-intensity muon beams are now available in an experimental facility at the Japan Proton Accelerator Research Complex (J-PARC) [1-2] for variety of applications [3-5], an efficient range and width determination of the beams is desired. Also effective range and width determination will be important when muons are used for muon radiation therapy in the future [6-7]. For this purpose we tried Cherenkov-light imaging of decayed positrons in water and optical imaging of muons using plastic scintillator [8-9]. With the imaging, clear images of Cherenkov-light and plastic scintillator were obtained and these images could be used for range estimation [9].

Although the optical imaging of muons and decayed positrons are promising methods for range estimations, it was only tried for one muon beam tuning condition at D2 without collimators [9]. These imaging methods will also be useful for the imaging of muon beams with different beam sizes with collimators. For this purpose, we conducted Cherenkov-light imaging in water and optical imaging of plastic scintillator block during irradiation of 84.5-MeV/c positive muon beams with different collimator diameters using a cooled charge-coupled device (CCD) camera and evaluated the beam profiles.

Figure 1 shows a schematic drawing of optical imaging of Cherenkov-light in water phantom during irradiation of positive muons. We used fluorescein (FS) water for imaging of the decayed positrons from muon beam [10]. FS was added to water because it increased the light intensity of the decayed positrons for $\sim$ 2 times compared with water. We irradiated 84.5-MeV/c positive muon beams with different collimators that were attached in the muon beam port. One of the muon beams with different collimators was irradiated to the FS water phantom from the side. The distance between the beam port and the FS water phantom was $\sim$ 50 mm. The optical images of Cherenkov-light in water phantom were acquired using a cooled CCD camera for 300 s.

The size of the phantom was 10 cm $\times$ 10 cm $\times$ 10 cm. The phantom was made of 0.5-cm-thick black acrylic board except for the side facing the CCD camera. A phantom contained distilled water based FS water with the FS concentration of 0.02 mg/cc.

A cooled CCD camera (BITRAN, BU-50LN, Japan) was placed in a black box facing to the FS water phantom at 30 cm from the phantom surface. We used a C-mount F-1.4 lens (Computar, Japan) for the CCD camera. The side of the black box was made of thin black paper to minimize energy loss of the muon beam by the black box. The image size of the measured images by the CCD was 386 $\times$ 219 pixels.

Figure 2 shows a schematic drawing of optical imaging of plastic scintillator block during irradiation of positive muons. A plastic scintillator block was used for the light distribution measurements because the light intensity is much higher than the Cherenkov-light by the decayed positrons thus the muon beam distribution can be imaged with the op-

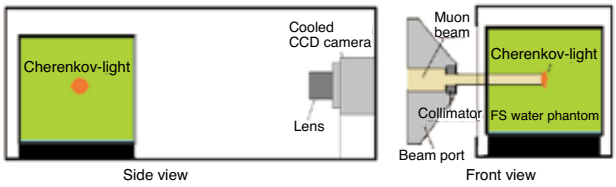

Fig. 1: Schematic drawing of Cherenkov-light imaging of water during irradiation of positive muons; side view (left) and front view (right).

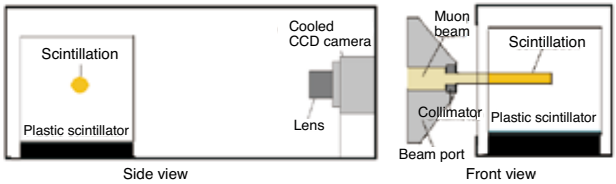

Fig. 2: Schematic drawing of plastic scintillator block during irradiation of positive muons; side view (left) and front view (right).

tical imaging [9]. The optical images of plastic scintillator block were acquired using the same cooled CCD camera for 20 s. We used a 10 cm × 10 cm × 10 cm plastic scintillator block (EJ-200, Eljen Technology, USA) for the imaging.

We processed the acquired Cherenkov-light images in FS water and images with plastic scintillator block using public domain software (ImageJ). The procedure was basically identical to those previously used for the luminescence imaging of water [11-18].

Figure 3 shows the Cherenkov-light images of water during irradiation of positive muon of 84.5-MeV/c with different collimators. Muon beams were irradiated from the left side of the images. We could observe the clear light distribution of Cherenkov-light at the center of the water phantom.

We show the depth and lateral profiles of the Cherenkov-light images in water during irradiations of muon beams with different collimator diameters in Fig. 4(A) and (B), respectively.

Figure 5 shows the measured optical images using the plastic scintillator block during irradiation of positive muon of 84.5-MeV/c with different collimators. Muon beams were irradiated from the left side of the images. We could observe the clear light distributions of scintillation in the left side to center of the plastic scintillator block. In each image, Bragg peak was observed at the end of the beam located center of the each beam. As the collimator diameter decreased, the widths of muon beams in lateral (vertical) directions were decreased.

We show the depth profiles of the optical images in plastic scintillator during irradiations of muon beams with collimators of different diameters in Fig. 6(A). We could observe the peak positions were the same between the distributions among the different collimator diameters. The lateral profiles at 20 mm depths are shown in Fig. 6(B) in which we could also observe the wider distributions for the collimators with larger diameters and widths of the beams could be determined from the profiles.

Cherenkov-light imaging of decayed positrons and optical imaging of muons with different beam diameters were possible. We conclude that optical imaging of muon beams and Cherenkov-light imaging of the decayed positrons are valuable methods for the range and width determination of the muon beams and future muon therapy.

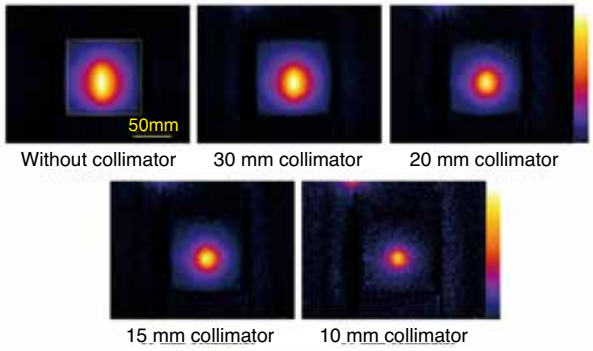

Fig. 3: Measured Cherenkov-light images of the decayed positrons from muons during irradiation of 84.5-MeV/c muon beams with different collimators.

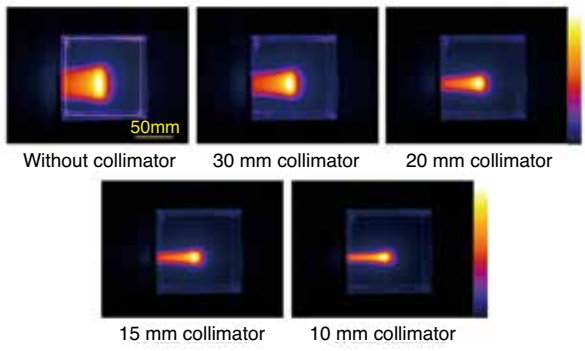

Fig. 5: Measured optical images of plastic scintillator during irradiation of 84.5-MeV/c muon beam with different collimator diameters.

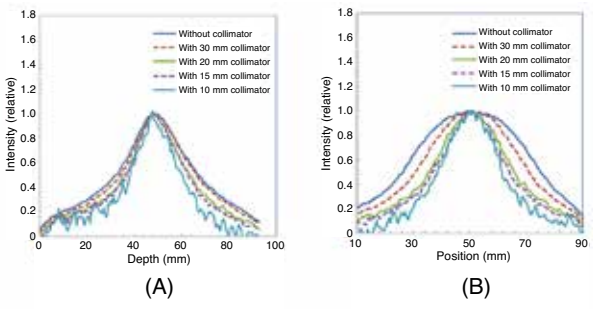

Fig. 4: Depth (A) and lateral (B) profiles for Cherenkov-light images during irradiation of 84.5-MeV/c muon beams with different collimators.

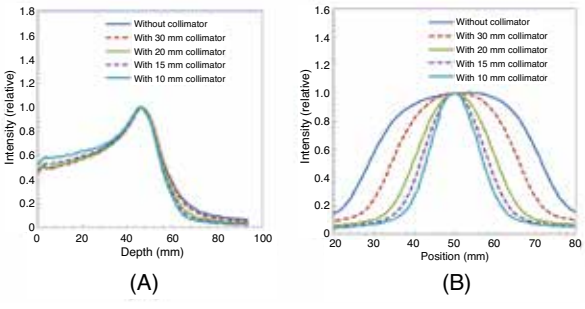

Fig. 6: Depth (A) and lateral (B) profiles estimated from optical images of plastic scintillator during irradiation 84.5-MeV/c muon beams with different collimators.

References

[1] Y. Miyake, *et al.*, Phys. Procedia **30** (2012) 46–49.

[2] R. Kadono, *et al.*, Rep. Prog. Phys. **75** (2012) 026302(1-11).

[3] K. Ninomiya, *et al.*, Bull. Chem. Soc. Jpn. **85** (2012) 228–230.

[4] K. Terada, *et al.*, Sci. Rep. **4** (2014) 5072(1-6).

[5] K. Ninomiya, *et al.*, J. Radioanal. Nucl. Chem. **319** (2019) 767–773.

[6] H. Daniel, *et al.*, Nuclear-Medizin **8** (1969) 311–319.

[7] N. V. Mokhov, *et al.*, PAC (1999) 2525–2527.

[8] Y. Hirano, *et al.*, Phys. Scr. **94** (2019) 125804(1-9).

[9] S. Yamamoto, *et al.*, Sci. Rep, **10** (2020) 20790(1-11).

[10] A. K. Glaser, *et al.*, Phys. Med. Biol. **58** (2013) 601–619.

[11] S. Yamamoto, *et al.*, Nucl. Instrum. Meth. Phys. Res., A **872** (2017) 174–180.

[12] S. Yamamoto, *et al.*, Radiation Measurements **116** (2018) 1–9.

[13] S. Yamamoto, *et al.*, Med. Phys. **42** (2015) 6498–6506.

[14] S. Yamamoto, *et al.*, Med. Phys. **43** (2016) 2455–2463.

[15] T. Yabe, *et al.*, Phys. Med. Biol. **63** (2018) 04NT02.

[16] T. Yabe, *et al.*, Phys. Med. Biol. **63** (2018) 125019(1-12).

[17] S. Yamamoto, *et al.*, Nucl. Instrum. Meth. Phys. Res., A **832** (2016) 264–270.

[18] S. Yamamoto, *et al.*, Nucl. Instrum. Meth. Phys. Res., A **883** (2018) 48–56.

Effect of Injected Carrier in $CH_3NH_3PbI_3$ on Muon Spin Relaxation
[J-PARC: 2019B0433]

S. Tanaka, T. Tanimoto[1], and M. Kitaura[1]

Faculty of Science and Engineering, Kindai University
[1]*Faculty of Science, Yamagata University*

Hybrid organic-inorganic perovskites (HOIPs) attract much attention as optoelectronic material [1]. Unique properties of HOIPs, such as a high optical absorption coefficient, a long carrier diffusion length, and a well-balanced charge transfer, are suitable for achieving the high performance of devices. One of the widely studied material in HOIPs is methylammonium lead iodide ($CH_3NH_3PbI_3$: $MAPbI_3$). The structure of $MAPbI_3$ is shown in Fig. 1 (a); the composition takes a typical ABX_3-type perovskite structure as methylammonium cation (MA^+) at the A site, lead ion (Pb^{2+}) at the B site, and iodide ion (I^-) at the X site. $MAPbI_3$ is a direct transition type semiconductor with a band gap of about 1. 55 eV. The valence band of $MAPbI_3$ consists of I 5p and Pb 6s orbitals, while the conduction band mainly consists of Pb 6p orbital [2]. The MA^+ molecule does not have any significant contribution around the band edge. On the other hand, the importance of a relationship with lattice motion, such as the formation of large phonons [3], has been pointed out for carrier transport in perovskites. We have tried to investigate the relationship between MA^+ molecules' motion and carrier transport in more detail.

In our previous experiment with program 2018B0338, we performed μSR measurements on $MAPbI_3$, $MAPbBr_3$, and $MAPbCl_3$. The results suggest that μSR observes the motion of MA^+ molecules. In addition, we attempted to observe the effect of carrier generation by light irradiation on μSR. However, no significant change was observed in the μSR time spectrum between with or without light irradiation. This may be caused by a spacial mismatch of light-induced carriers and a detection position of muon. The light absorption coefficient of HOIPs is about 10^4 to 10^5 cm^{-1}; thus, the light generation carrier is generated in the range of about 0.1 to 1 μm from the sample surface. Whereas the muon probably stops at around 300 to 400 μm from the sample surface. In the present experiment, instead of the photogeneration of the carrier, μSR measurement with the carrier injection was performed and compared to that without carrier injection.

We used a carbon nanotube (CNT) sheet (Lintec Drydeaw) as the carrier-injection electrode. The schematic experimental setup is shown in Fig. 1 (b). $MAPbI_3$ crystal was grown by the inverse temperature method [4]. The CNT-sheet electrode was attached to the top and bottom of the sample. The sample was mounted on the silver holder. Kapton film was used for the insulating sheet (Fig. 1 (c)).

μSR experiments were performed using the ARTEMIS at the S1 beamline with a conventional ^{4}He flow cryostat. For the experiments under a longitudinal field (LF), an external magnetic field was applied parallel to the direction of the initial muon

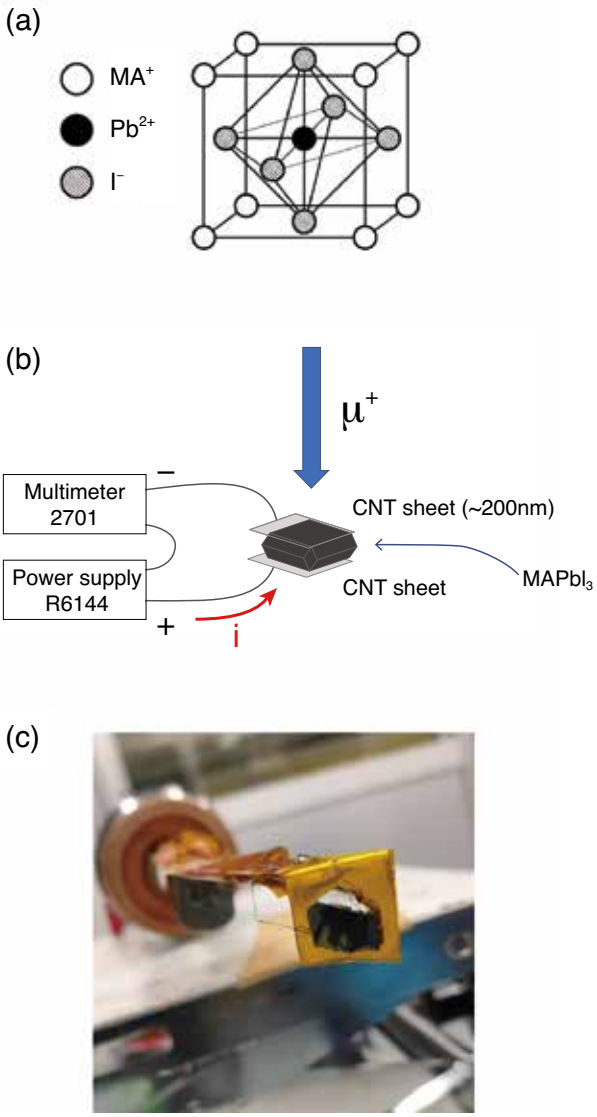

Fig. 1: (a) Schematics of the $MAPbI_3$ structure. (b) Schematics of the experimental setup. (c) Photograph of the sample.

spin polarization with 0, 20, 100, and 1000 G. For the carrier injection, the external bias voltage of ±30 and 0 V were used. The meaning of the polarity of bias is described later. Muon decay positrons were detected by counters at forward and backward positions to the initial muon spin polarization. The time-dependent asymmetry of the decay positrons was evaluated for each experimental condition.

Here we describe the experimental results. With a bias voltage of +30 V, a current of about 0.6 mA flowed. The current gradually decreased during the measurement and finally became about 0.5 mA. With a bias voltage of −30 V, almost no current flowed. As shown in Fig. 1 (b), there was no reason to show the rectified current flow for the current experimental setup. We do not have a concrete explanation for this at present.

The μSR time spectra (time-dependent asymmetry curve) of MAPbI3 with magnetic fields of 0, 20, 100, and 1000 G at 107 K are shown in Fig. 2; bias voltage of (a) 0 V (without charge injection) and (b) +30 V (with charge injection). The solid lines indicate the fitting of data points using the following relaxation function,

$$A(t) = A_0 G_{\mathrm{DKT}}(\nu, \sigma, \Gamma) + A_{\mathrm{BG}}, \qquad (1)$$

where A_0 is the initial asymmetry at $t = 0$, G_{DKT} is the dynamic Kubo-Toyabe function, and A_{BG} is the background contribution of the sample holder. Note that there are discrepancies between the fitting curves and data points after 10 μs. Thus another function could be better for the analysis. Here, as a preliminary analysis, we used the same function that we used in our previous experiment. The estimated values of the spin relaxation rate (σ) were 0.2883 ± 0.008 $\mu s^{-1}$and 0.3570 ± 0.014 μs^{-1} for 0 V and +30 V, respectively. The fluctuation frequency (Γ) of 0.987 ± 0.031 MHz and 0.690 ± 0.047 MHz for 0 V and +30 V were also estimated. Although it is difficult to evaluate the values quantitatively, it is a clear trend that the charge injection suppressed the spin relaxation. One may claim that the suppression effect might be caused not by the charge injection but by the electric field. Fig. 2 (c) is a time spectrum at the zero-field (ZF) of −30 V and 0 V. They showed almost the same time spectrum. This implies that the suppression of spin relaxation at +30 V is not the effect of the electric field but the effect of injected charges.

In summary, we performed the μSR measurements on a $MAPbI_3$ crystal. We observed the μSR time spectrum under the carrier injection condition using the CNT-sheet as the carrier-injection electrodes. It was suggested that the injected carriers in the $MAPbI_3$ suppressed the muon relaxation. The present results imply that there is a relationship between carrier transport and the MA^+ motion.

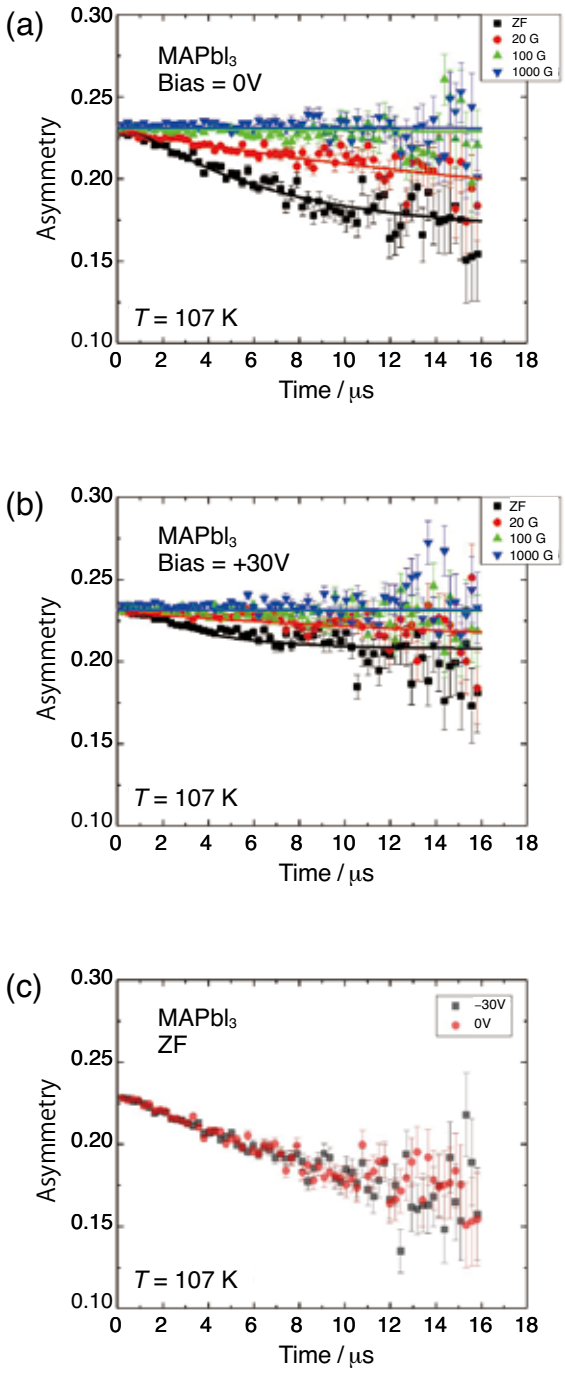

Fig. 2: μSR time spectra observed in the $MAPbI_3$ crystal. (a) without bias voltage (b) with bias voltage of +30 V (c) without bias and with bias voltage of −30 V at zero-field (ZF).

References

[1] A. K. Jena *et al.*, Chem. Rev. **119** (2019) 3036–3103.

[2] W.-J. Yin *et al.*, Appl. Phys. Lett. **104** (2014) 063903(1-4).

[3] K. Miyata *et al.*, Sci. Adv. **3** (2017) e1701217(1-9).

[4] M. I. Saidaminov *et al.*, Nat. Commun. **6** (2015) 7586(1-6).

Hydrogen Trapped Sites in Aluminum Alloys Studied by Zero-field Muon Spin Relaxation Method [J-PARC: 2020A0002]

K. Nishimura, K. Matsuda, N. Nunomura, T. Namiki, S. Lee, W. Higemoto[1], Y. Miyake[2], H. Toda[3], and K. Shimizu[4]

Faculty of Sustainable Design, University of Toyama
[1]*Advanced Science Research Center, JAEA*
[2]*Muon Science Laboratory, Institute of Materials Structure Science, KEK*
[3]*Department of Mechanical Engineering, Kyushu University*
[4]*Faculty of Science and Engineering, Iwate University*

Hydrogen embrittlement is well known phenomenon in steels. It is less well-known that some aluminum alloys also exhibit hydrogen embrittlement, such Al-Cu-Mg (called duralumin), Al-Zn-Mg (called ultra-super duralumin), etc.: those alloys have relatively high mechanical strength suitable for aeronautical applications, but their mechanical strengths certainly deteriorated in hydrogen atmosphere [1]. There are plenty of studies investigating hydrogen states in aluminum alloys; hydrogen atoms are in interstitial (octahedral, tetrahedral) sites, and with vacancies/ solid solutions/dislocations; hydrogen molecule and gases are in grain-boundaries/ micropores/ cavities. Several methods are used to investigate the behavior of hydrogen in metals, such thermal desorption spectroscopy (TDS), hydrogen microprint technique, tritium autoradiography, secondary ion mass spectroscopy, etc.[2] Hydrogen behavior, however, has been still unknown, especially their kinetic properties of atomic states in metals. Muons are likely appropriate probes to scrutinize hydrogen and vacancy behavior in aluminum alloys since in metals the chemical property of positive muon is similar to that of hydrogen. The recent density functional theory for aluminum predicts a vacancy traps a hydrogen in the tetrahedral sites and multiple hydrogen trapping is possible [3]. Therefore, we can investigate whether a muon is trapped in a tetrahedral site of a vacancy, and a hydrogen is also trapped in the nearest neighbor tetrahedral site of the same vacancy. If this is the case, their magnetic interactions bring about the faster muon spin relaxation, leading to a larger dipole width. This report presents zero-field μSR results of hydrogen-charged Al-0.2%Cu and Al-1.3%Cu alloys.

Samples were prepared of the approximately dimensions: 25×25×1 mm plate. All the samples were heat-treated at appropriate temperatures of about 770 K for one hour prior to hydrogen charging. Hydrogen was charged into the alloys by the electrical-discharging method (EDM) on the both large surfaces of the plates: these samples were noted as 1EDM. Some 1EDM alloys were again under the electrical-discharging process four days after the first EDM to increase the hydrogen content: these samples were noted as 2EDM. The samples were kept in liquid nitrogen till μSR measurement. Zero-field muon spin relaxation spectra were measured at S1 line in the temperature range from 20 to 300 K by a 20 K step, in which 30 mega muon events were accumulated at every constant temperature using double pulse mode.

Figure 1 shows zero-field μSR spectra observed for Al-1.3%Cu 2EDM (left) and non-charged (right) samples from 24 to 303 K. At 24 K, muons were most likely trapped by resolved Cu atoms [4-6]. At an elevated temperature of 165 (or 160), the spin-relaxation rates became clearly smaller than that at 24 K due to the muon de-trapping caused by thermal activation, whereas at 206 K, the relaxation rate for the 2EMD sample was larger than that at 165 K, but little change appeared for the non-charged sample at 160 and 202 K. There are two possible causes for the larger relaxation rates for the 2EDM sample at 206 K; 1) muons experienced larger magnetic fields in trapped sites provided by hydrogen atoms also trapped near-neighbor sites; 2) the number density of vacancy was larger, thus muons were trapped more frequently.

The data analysis using a Monte Carlo algorithm simulation [7] provided the temperature (T) dependences of dipole widths (Δ) and trapping rates (ν_t).

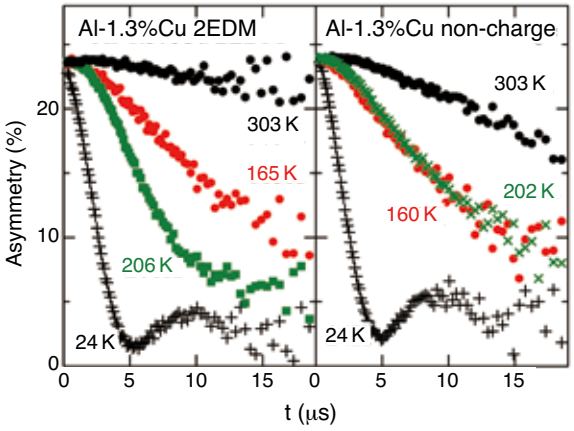

Fig. 1: Zero-field μSR spectra observed for the hydrogen charged (left) and non-charged (right) Al-1.3%Cu alloys from 24 to 303 K.

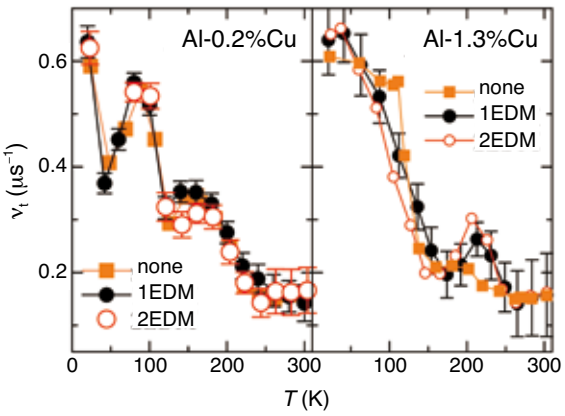

Fig. 2: Temperature dependences of deduced trapping rates for Al-0.2%Cu (left) and Al-1.3%Cu (right) samples hydrogen-charged (1EDM, black solid-circle), (2EDM, red open-circle) and non-charged (brown square).

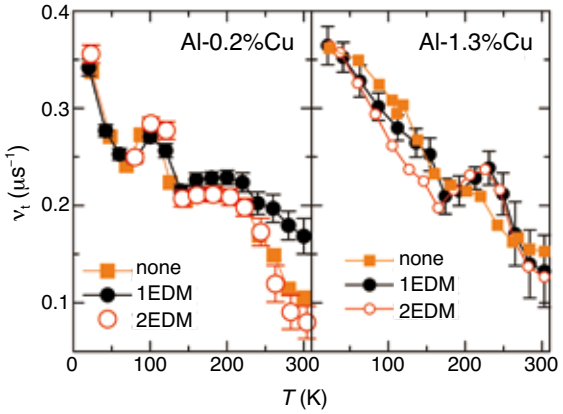

Fig. 3: Temperature dependences of dipole widths for Al-0.2%Cu (left) and Al-1.3%Cu (right), hydrogen-charged (1EDM, 2EDM) and non-charged samples.

Figure 2 compares the extracted values of trapping rates vs T for Al-0.2%Cu (left) and Al-1.3%Cu (right) non-charged, 1EDM and 2EDM samples. There is little difference on the trapping rates for the three Al-0.2%Cu samples, but there is a noticeable difference on the trapping rates between the Al-1.3%Cu non-charged and EDM samples, especially near 200 K.

Figure 3 shows the deduced temperature dependences of dipole widths for the Al-0.2%Cu (left) and Al-1.3%Cu (right). We expected a larger amount of absorbed hydrogen for Al-0.2%Cu 2EMD, but the observed Δ vs T curve resembled that of non-charged Al-0.2%Cu sample. The Δ vs T curve for Al-0.2%Cu 1EMD exhibited some deviations from those of the other Al-0.2%Cu samples above 240 K. In turn, the Δ vs T curves for Al-1.3%Cu 1EDM and 2EDM samples almost overlapped each other, deviating from that of the non-charged Al-1.3%Cu sample near 200 K.

In Fig. 1, μSR spectrum for Al-1.3%Cu 2EDM at 206 K shows a larger spin-relaxation rate than that at 165 K. From the estimated ν_t vs T and Δ vs T curves for the two samples, we could not decide whether muons interacted with hydrogen atoms or (and) there was a larger number of vacancies in 2EDM sample. Figure 4 shows the results of thermal desorption spectroscopy (TDS) for the samples two weeks after the μSR experiments. There is significant difference on the TDS profiles between the non-charged and 2EDM Al-0.2%Cu samples, however, the estimated ν_t vs T and Δ vs T curves for the two samples are quite similar. Present results indicate it is difficult to correlate the μSR results with the TDS profiles, at least for the studied samples. We suspect the observed differences in ν_t vs T and Δ vs T curves around 200 K between non-charged and EDM samples could be due to some defects.

This work is supported by KAKENHI 18H01747.

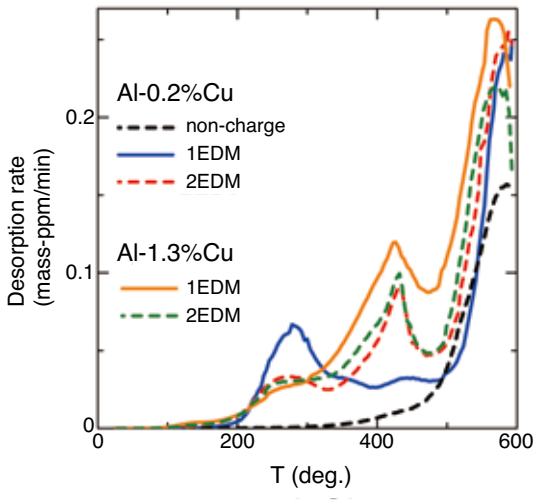

Fig. 4: Thermal desorption spectroscopy (TDS) for the non-charged (brown broken line), 1EDM (blue solid line), 2EDM (red broken line) Al-0.2%Cu, and 1EDM (yellow solid line), 2EMD (green broken line) Al-1.3%Cu samples.

References

[1] T. Tsuru *et al.*, Sci. Rep. **10** (2020) 1998(1-8).

[2] T. Izumi and G. Itoh, Mater. Trans. **52** (2011) 130–134.

[3] R. Nazarov *et al.*, Phys. Rev. B **89** (2014) 144108(1-18).

[4] K. Nishimura *et al.*, Arch. Metall. Mater. **60** (2015) 925–929.

[5] S. Wenner *et al.*, Metall. Mater. Trans. A **50** (2019) 3446–3451.

[6] K. Nishimura *et al.*, MRS2019, E3-12-O05.

[7] S. Wenner *et al.*, Phys. Rev. B **86** (2012) 104201(1-7).

Detailed μSR Studies of Thiocarbonyl-Muonium Adducts [J-PARC: 2020A0019]

S. Ito and H. Akama

School of Materials and Chemical Technology, Tokyo Institute of Technology

Carbonyl group (>C=O) is the most important functional molecular structure in organic chemistry. Also, the sulfur congener of >C=O, thiocarbonyl group (>C=S), is quite useful such as in recent organic synthesis. Compared with >C=O, thiocarbonyl group basically exhibits higher energy level of the highest occupied molecular orbital (HOMO) and lower energy level of the lowest unoccupied molecular orbital (LUMO). As one of the characteristic chemical aspects of thiocarbonyl compounds, the C=S moiety easily interacts with radical species. The regioselective radical reactions can be utilized as a key synthetic component for generation of radical intermediates leading to functional products.

As μSR studies of carbonyl compounds have been carried out in order to figure out details of radical reactions via muonium addition [1,2], μSR study of compounds bearing thiocarbonyl group has been of interest. The first μSR study was reported in 1988 [3], and the corresponding muoniated radicals were characterized according to the experimentally observed A_μ (muon hyperfine coupling constants, muon hfc). Subsequent μSR study of the muoniated thiocarbonyl compounds was utilized to determine kinetic parameters which are of biological importance [4]. Therefore, intensive structural analyses of the muoniated radicals of thiocarbonyl compounds should be continued, which would be informative to develop functional compounds.

We previously carried out a preliminary transverse-field (TF) μSR study of a sterically encumbered thioaldehyde Mes*CH=S, where Mes* = 2,4,6-tri-*tert*-butylphenyl, at TRIUMF. Muon irradiation generated the corresponding muonium adduct of A_μ = 57 MHz, indicating muonium addition to sulfur affording **1** (Fig. 1a) [5]. The observed A_μ parameter of **1** is close to a muonium adduct of thiobenzophenone (Ph_2C=S) [3]. As for **1**, the DFT-optimized structures showed considerably smaller muon hfc parameters than the experimentally characterized A_μ. The larger experimental A_μ compared with the theoretical muon hfc is relating to isotope effect of muon as the light proton surrogate. The higher zero-point energy (ZPE) of S–Mu bond would increase overlap with the neighboring p orbital of radical centre via the hyperconjugation effect. Scanning the C_{Mes*}–C–S–Mu(H) dihedral angle θ (see Fig. 1b) by altering the equilibrium θ_{opt} of 13.3° in the DFT-optimized structure of **1** [UCAM-B3LYP/6-31G(d)] was successful to estimate the experimental A_μ (Fig. 2). Elongation of the S–Mu distance would be slightly effective to simulate the experimental data A_μ.

In the 2020A0019 project, we first attempted confirmation of **1**, and carried out muon avoided lev-el-crossing resonance (μLCR) by using the ARTEMIS spectrometer equipped in the S1 line of J-PARC. A powder sample of Mes*CH=S (ca. 150 mg, 15 × 15 × 2 mm) was employed. Figure 3 displays a resonance spectrum. Although the wide scan step (50 G) was employed, it was possible to observe the resonance at ca. 2.1 kG.

μLCR gives information about spin flip and/or flop of muon, electron, and nucleus spin. Normally, μLCR experiments using anisotropic samples in-

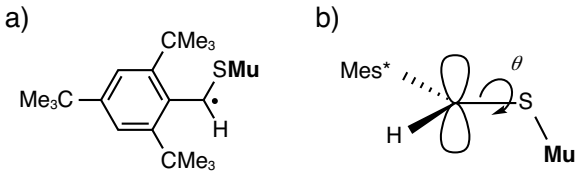

Fig. 1: a) Formula of radical **1** generated from muonium addition to thioaldehyde Mes*CH=S. b) A schematic drawing of conformation in **1** for characterization of muon isotope effect.

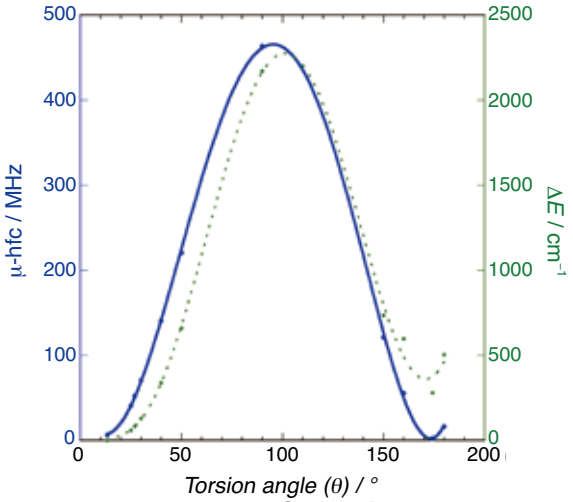

Fig. 2: A plot of the torsion angle (θ) *vs.* muon hfc (solid line, left ordinate) and ΔE_{total} (dotted line, right ordinate) for **1** at the UCAM-B3LYP/6-31G(d) level.

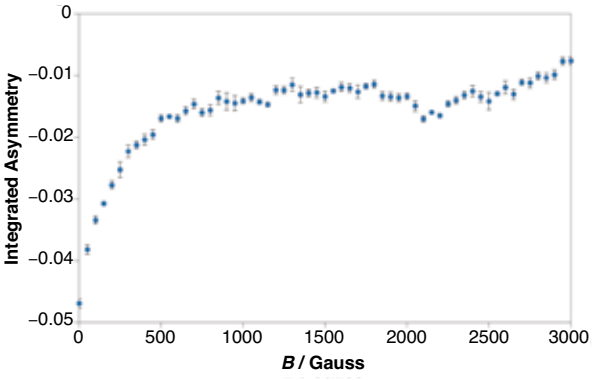

Fig. 3: A μLCR spectrum of Mes*CH=S (powder) at 298 K.

cluding crystal, solids or powder visualize the Δ_1 resonance via spin flipping of only muon. The Δ_1 resonance field [$B_{\rm res}(\Delta_1)$] correlates with the muon hyperfine coupling constant, and A_μ can be obtained according to Eq. 1. In this equation, γ_μ and $\gamma_{\rm e}$ are gyromagnetic ratios of muon and electron, respectively [6].

$$B_{\rm res}(\Delta_1) = \frac{1}{2} A_\mu \left| \frac{1}{\gamma_\mu} - \frac{1}{\gamma_{\rm e}} \right| \qquad (1)$$

Thus, it is possible to confirm that the observed μLCR peak in Fig. 2 corresponds to A_μ of 57.2 MHz, which is almost the same result as the previous TF-μSR experiment [5].

The successful characterization of **1** by μLCR measurements encouraged to attempt observation of novel muoniation processes based on radical reactions of thiocarbonyl. The previously reported regioselective muonium addition to thiobenzophenone [3] indicates advantages of thiocarbonyl to produce the π-extended organic paramagnetic species. In this work, we employed powder samples of 9*H*-xanthene-9-thione (**2**) and 9*H*-thioxanthene-9-thione (**3**) as conformationally constrained thiobenzophenone derivatives. The DFT-optimized structures of muoniated **2** and **3** showed the expected muon hfcs of 155 MHz and 96 MHz, respectively. These expected muon hfcs would be somewhat hard to observe the μLCR signal up to the field of 4 kG. Unfortunately, we observed no obvious LCR signal probably due to the larger muon hfcs than the estimated parameters by DFT calculation, indicating the light isotope effect.

The substantially larger muon hfcs of **2** and **3**, estimated by DFT calculations, indicate effects of the conformationally constrained lone pairs of the skeletal oxygen (**2**) and sulfur (**3**) contributing the π-conjugation. The incorporation of the skeletal heteroatoms in **2** and **3** would lead to avoiding contribution of the lone pair of the *exo*-sulfur atom, resulting in increasing hyperconjugation between the radical p-orbital and S–Mu bonds. According to the results and discussion mentioned above, we are designing the other π-conjugated para-magnetic radicals showing observable muon hfcs by muoniation at the C=S sulfur atom.

The authors thank Prof. Akihiro Koda and Dr. Jumpei Nakamura of KEK-IMSS for supporting at J-PARC.

References

[1] C. J. Rhodes *et al.*, Chem. Commun. **1999**, 2157–2158.

[2] C. J. Rhodes, Sci. Prog. **95** (2012) 101–174.

[3] C. J. Rhodes *et al.*, J. Chem. Soc. Chem. Commun. **1988**, 3–4.

[4] C. J. Rhodes *et al.*, Magn. Res. Chem. **38** (2000) S49–S57.

[5] S. Ito *et al.*, Phosphorus, Sulfur, Silicon, Relat. Elem. **194** (2019) 735–738.

[6] S. J. Blundell, Chem. Rev. **104** (2004), 5717–5736.

μSR Study of the Spin-1/2 One-dimensional Heisenberg Antiferromagnet $Cd_2Cu_2SO_4(PO_4)_2$ $5H_2O$ [J-PARC: 2020A0066]

M. Fujihala, A. Koda[1], H. Okabe[1], and M. Mitsuda

Department of Physics, Tokyo University of Science
[1]*Muon Science Laboratory, Institute of Materials Structure Science, KEK*

The one-dimensional quantum antiferromagnet (1D-QAFM) is an outstanding and versatile model system in quantum many-body physics. The simplest frustrated geometry in the 1D-QAFM is the J_1-J_2 model, where J_1 and J_2 stand for nearest-neighbor (NN) and next-nearest-neighbor (NNN) exchange couplings, respectively. As soon as J_2 is antiferromagnetic (AFM), i.e., $J_2 > 0$, the chain is frustrated, irrespective of the sign of J_1.

The phase diagram of J_1- J_2 model for the case of $J_1 < 0$ and $J_2 > 0$ has been calculated by Hikihara *et al.*[1]. In the case of $-1 < J_1/J_2 < -2.5$, the ground state is a vector chiral state, and the bound magnon pairs form a spin density wave (SDW) in medium fields, whereas, in high fields just below the saturation of magnetization, they transits to the quantum multipolar states which is a spin nematic state. In the case of both J_1 and J_2 couplings are AFM, the spin state is very different from the FM one. For $J_1/J_2 < 0.241$, the ground state is expected to be a Tomonaga-Luttinger spin-liquid state. For $J_1/J_2 > 0.241$, a spin gap opens, and the chain is effectively in the dimerized state. At the Majumdar-Ghosh point ($J_1/J_2 = 0.5$), an exact ground state is represented by a superposition of spin singlets. The gap opening can be assisted by a structural dimerization. However, excluding some point, the ground state and magnetic excitations are still unclear. In the spin-Peierls compound $CuGeO_3$ ($J_1/J_2 \simeq 0.35$) [2], spin-lattice coupling controls the opening of the spin gap and the formation of soliton phases in external magnetic field. Interestingly, no gapped AFM J_1-J_2 chain material without the spin-lattice coupling has been reported. While the $J_1/J_2 > 0.241$ regime has been proposed for $(N_2H_5)CuCl_3$ and $KTi(SO_4)_2 \cdot 2H_2O$ [3, 4], the presence of a spin gap in these materials remains to be probed experimentally. The lack of a suitable model material is a major obstacle to investigating the ground state and magnetic excitation of the AFM J_1-J_2 chain material.

We have recently succeeded to synthesize pure-phase of $Cd_2Cu_2SO_4(PO_4)_2$ $5H_2O$ which is a good candidate compound for the J_1-J_2 chain material.

The space group *Pnma* with lattice parameters of a =10.493(1)Å, b = 20.883(2)Å, c =6.15767(8)Å are refined by the computer program RIETAN-FP [5]. As illustrated in Fig. 1 (a) and (b), the CuO_4 plaquette planes are bridged by PO_4. Exchange pathways within the zigzag chain of this compound are shown in Fig. 1(c). The bridging angles are about 105° and 140°, thus, both J_1 and J_2 couplings are AFM. The presence of two bridging PO_4 ions for J_1 versus a single PO_4 bridge for J_2 suggests that J_2 is smaller than J_1.

Figure 2 shows the magnetic susceptibility χ, which has a broad maximum around 50 K without sharp peak, suggesting absence of long-range

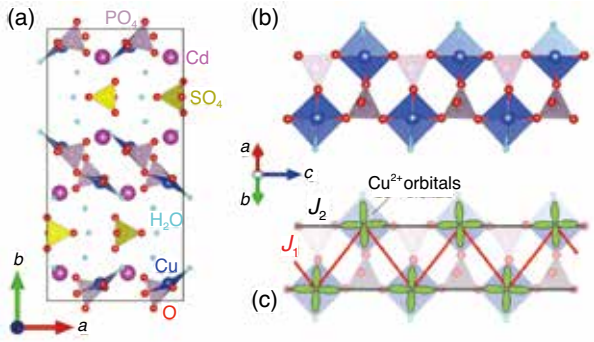

Fig. 1: (a) (b) Crystal structure of $Cd_2Cu_2SO_4(PO_4)_2$ $5H_2O$. (c) Arrangement of the Cu^{2+} orbitals in a chain. J_1 and J_2 are nearest-neighbor and next-nearest-neighbor exchange couplings.

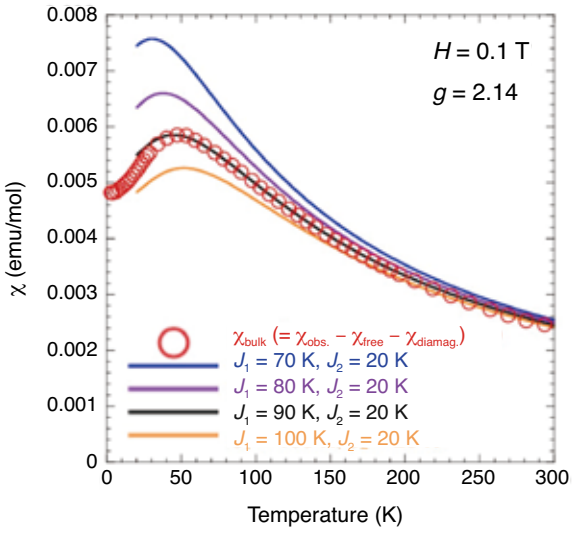

Fig. 2: Temperature dependence of the intrinsic susceptibility $\chi_{\rm bulk}$ with a theoretical curves (solid lines). The intrinsic susceptibility $\chi_{\rm bulk}$ is obtained by subtracting Pascal's diamagnetic contribution and an estimated contribution of impurity $\chi_{\rm imp}$. from the experimental data $\chi_{\rm obs}$.

ordering. The $\chi(T)$ has been calculated by full diagonalization (FD) of a $N = 18$ J_1-J_2 model using the ALPS package. The exchange interactions in this material have been estimated as $J_1 = 90$ K and $J_2 = 20$ K by comparing the magnetic susceptibility data with a theoretical curve. The exchange constant ratio J_1/J_2 is estimated to be 0.22, suggesting that the value close to that at the quantum critical point QCP ($J_1/J_2 = 0.241$).

To confirm the absence of spin ordering caused by quantum fluctuations, we performed μSR measurement.

Figure 3(a) shows the zero-field (ZF) μSR spectra at various temperatures. The spectra are best fit by a combination of two signals, one part containing a stretched exponential signal, and a second part with relaxing precession signal due to the formation of "$[H_3O]^+$-like" $H_2\mu^+O$ ions:

$$a(t) = a_1 \exp[-(\lambda t)^\beta] + a_2 G_{\rm tri}(t) \exp(-\sigma^2 t^2/2) + a_{\rm BG}$$

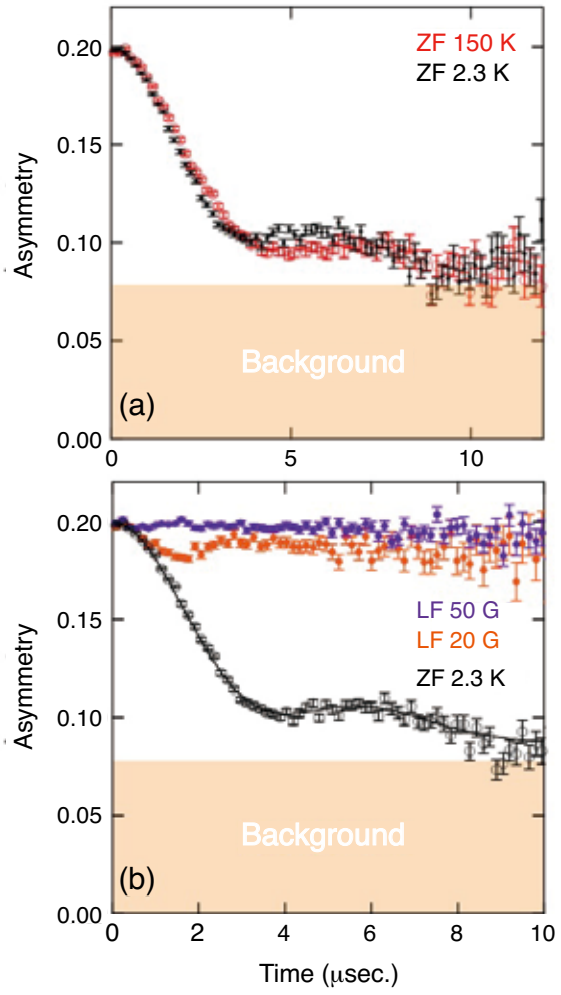

Fig. 3: (a) ZF-μSR spectra at representative temperatures. (b) μSR spectra measured at 2.3 K under several longitudinal magnetic fields. The thick lines behind the ZF data points are the fitted curves.

where a_1 and a_2 are the intrinsic asymmetries associated with the two signals, $a_{\rm BG}$ is a constant background. $G_{\rm tri}(t)$ is represented by

$$\begin{aligned} G_{\rm tri}(t) = {} & 0.28570 + 0.23429\cos(1.92058\ kt) \\ & + 0.13719\cos(1.75341\ kt) \\ & + 0.02750\cos(0.76874\ kt) \\ & + 0.18697\cos(0.60156\ kt) \\ & + 0.07655\cos(0.16718\ kt). \end{aligned}$$

Here $k = (2/d_{{\rm H}-\mu^2})^{3/2}$, in which $d_{{\rm H}-\mu}$ is the distance be-tween H and μ, i.e., the edge length of the regular triangle formed by two H and one μ [6]. The $d_{{\rm H}-\mu}$ is estimated as 1.8 Å, which is consistent with the edge length of the regular triangle of the H ions in the oxonium ion 1.6296 Å. From the fitting results, it can be estimated that $a_2 = 0.73 \times (a_1 + a_2)$ indicating that the 73% of muons stop near the H_2O. The spectra does not change considerably above and below 50 K. In addition, the spectra can be decoupled using a small applied LF field of 50 G even at 2.3 K (Fig. 3(b)).

Below 2.3 K, a Schottky-like peak in the heat capacity is observed (not shown here). There is high possibility that an quantum spin state is formed in this compound below 2 K.

These results suggest that $Cd_2Cu_2SO_4(PO_4)_2\ 5H_2O$ is a good candidate compound for the AFM J_1-J_2 chain material.

References

[1] T. Hikihara *et al.*, Phys. Rev. B **78** (2008) 144404(1-19).

[2] M. Hase *et al.*, Phys. Rev. Lett. **70** (1993) 3651–3654.

[3] D. Brown *et al.*, Inorg. Chem. **18** (1979) 2635–2641.

[4] D. Kasinathan *et al.*, Phys. Rev. B **88** (2013) 224410(1-9).

[5] F. Izumi and K. Momma, Solid State Phenom. **130** (2007) 15–20.

[6] J. Sugiyama *et al.*, Phys. Rev. B **82** (2010) 214505(1-9).

Negative Muon Spin Rotation and Relaxation on Battery Materials
[J-PARC: 2020A0078 / 2020B0322]

J. Sugiyama, K. Ohishi, I. Umegaki[1], T. Nakano[2], K. Ninomiya[3], M. K. Kubo[4], and S. Takeshita[5]

Neutron Science and Technology Center, CROSS
[1]*Toyota Central Research & Development Labs., Inc. TCRDL*
[2]*Institute of Quantum Beam Science, Graduate School of Science and Engineering, Ibaraki University*
[3]*Radioisotope Research Center, Institute for Radiation Sciences, Osaka University*
[4]*Department of Natural Sciences, College of Liberal Arts, International Christian University, ICU*
[5]*Muon Science Laboratory, Institute of Materials Structure Science, KEK*

1. Introduction

This is a new μ^-SR experiment to study Li diffusion in the future anode material, $Li_4Ti_5O_{12}$ spinel. The concept of our $\mu^{\pm}$SR study is that the diffusing species is determined with μ^-SR, while the detailed temperature dependence of the diffusion is measured with μ^+SR [1,2]. This is because we still need about 20 hours to obtain one reliable μ^-SR spectrum, despite the largest counting rate of J-PARC in the world due to the intense μ^- beam and the advanced multi-channel detector system [3].

2. Experiment

A powder sample of $Li_4Ti_5O_{12}$ was purchased from Toshima Manufacturing, Ltd. Approximately 16 g powder sample was placed in a copper container with a sample space of 36 mm diameter and 12 mm depth (see Fig. 1). The μ^-SR time spectra were measured on the decay muon beam line D1 at MUSE MLF in J-PARC. The recorded μ^-SR spectra were analyzed with musrfit.

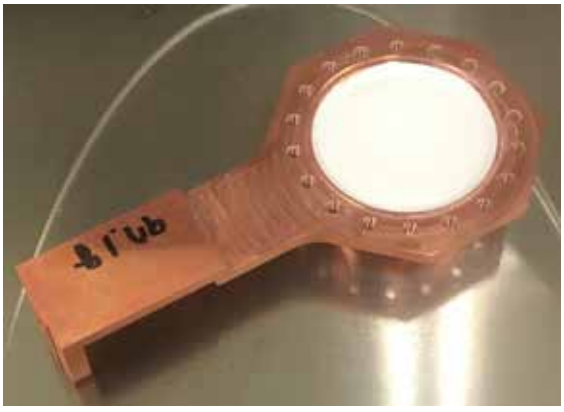

Fig. 1: A copper container filled with a white powder of $Li_4Ti_5O_{12}$.

3. Results

Figure 2 shows the temperature dependencies of the field distribution width (Δ^-) and the field fluctuation rate (ν^-) for $Li_4Ti_5O_{12}$ estimated from μ^-SR. The μ^+SR results, i.e., Δ^+ and ν^+, for the same sample were also shown in Fig. 2(b) for comparison. Since both μ^-SR and μ^+SR observe the increase in ν with temperature above 200 K, such a diffusive behavior is confirmed to be caused by Li diffusion.

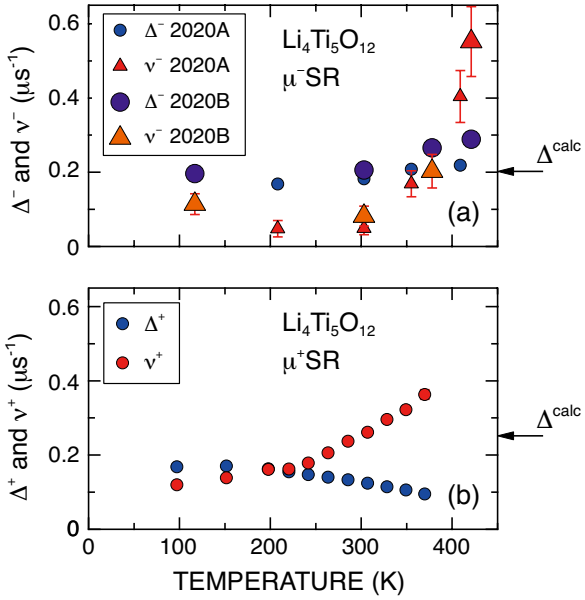

Fig. 2: The temperature dependencies of Δ and ν for $Li_4Ti_5O_{12}$: (a) the data obtained by μ^-SR and (b) those obtained by μ^+SR. Δ^{calc} represents the predicted Δ by dipole field calculations with dipelec.

References

[1] J. Sugiyama *et al.*, Phys. Rev. Research **2** (2020) 033161(1-6).

[2] J. Sugiyama *et al.*, Phys. Rev. B **102** (2020) 144431(1-7).

[3] K. M. Kojima *et al.*, J. Phys. Conf. Ser. **551** (2014) 012063(1-6).

Negative Muon Capture Process and Electronic State in Correlated Electron Systems [J-PARC: 2020A0130]

W. Higemoto[1,2], K. Ninomiya[3], T. Suzuki[1,2], Y. Miyata[2], I. Miyazaki[1,2], T. U. Ito[1], C. I-Huan[3], and M. K. Kubo[4]

[1]*Advanced Science Research Center, JAEA*
[2]*Department of Physics, Tokyo Institute of Technology*
[3]*Institute for Radiation, Osaka University*
[4]*College of Liberal Arts, International Christian University*

Phase transition based on electron correlation in a many-body system is complex phenomena. To understand the origin of the phase transition, investigation of the electronic state itself is crucial. However, it is not easy to reveal the electronic state, in particular at deep inside of the material.

We have studied electronic state in the many-body system by using negative muon characteristic x-ray ("Muonic X-ray"). It is well known that the capture ratio of a negative muon is affected by electronic state, e.g. valence number etc. By understanding relation between an electronic state and atomic capture ratio of a negative muon, we aim to establish of new technique of investigation of the electronic systems.

When a negative muon is implanted into a material, the muon is initially captured in an excited state and immediately cascades down to the muonic 1s state with characteristic muonic X-ray and/or Auger electron emissions (muon capture process). The muonic X-ray energies are very high compared to electronic X-ray energies, because of the large mass difference. We can easily identify which atom has captured a muon based on its muonic X-ray emissions, and from muonic X-ray intensity, the muon capture probability for each element in a material (capture ratio) can be determined. Today it is investigated that the initial process of muon capture depends on the electronic state[1], structure[2], molecular structure[3] *etc.* For example, there are differences in the per-atom muon capture ratio for several transition metal oxides, probably due to the difference of valence numbers. Such the effect implies that the muon capture process is strongly influenced by the electronic state of the muon-capturing atom. The intensity of muonic X-ray per muon capture was also different by chemical an environment (molecular structure) of muon capturing atom. Up to now, relation between phase transition in electronic system and muonic X-ray have not investigated at all. In particular, no study have been carried out for muon capture process in the view point of electronic state based on an electron correlation.

We investigate the relation between muon capture processes, namely muon capture ratio and electronic state in different phases in well characterized materials. V_2O_3 occurs metal-insulator transition at T_{MI} = 150 K. Above T_{MI}, V_2O_3 is paramagnetic metal and occurs phase transition to antiferromagnetic insulator with first order at T_{MI}. In this compound negative muon capture ratio had been measured only at room temperature and it was found that the value is 30% deviated from theoretical value [1]. Up to now, no low temperature measurement was reported and we intend to investigate the muon capture process, in particular muon capture ratio at above and below T_{MI}. Here, we have performed muonic X-ray measurement above and below T_{MI}.

Our experiment was carried out at the D1. We measured muonic X-ray and muon spin rotation simultaneously. Powdered specimen of V_2O_3 ($\sim$ 1g) was used. Figure 1 shows the energy dependence of counted X-ray at 300 K (metallic phase) and 50 K (insulating phase). Muonic X-rays were clearly observed down to 50 K. Tiny difference between 300 K and 50 K was seen and detail of the analysis are going on.

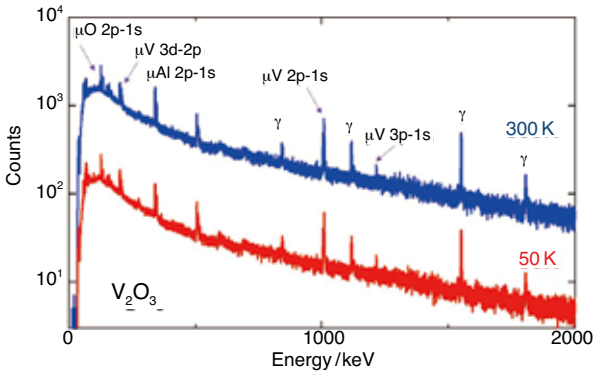

Fig. 1: Energy dependence of counted X-ray spectra in V_2O_3 at 300 K (paramagnetic metallic phase) and 50 K (antiferromagnetic insulating phase).

References

[1] S. Stanislaus *et al.*, Nucl. Phys. A **475** (1987) 630–641.
[2] H. Schneuwly *et al.*, Phys Rev A **27** (1983) 950–960.
[3] G. Yoshida *et al.*, J. Radioanal. Nucl. Chem. **303** (2015) 1277–1281. : K. Ninomiya *et al.*, J. Kor. Phys. Soc. **59** (2011) 2917–2920.

Search for the Magnetic Instability in $YbCu_4Ni$ [J-PARC: 2020A0131]

T. Taniguchi[1], K. Osato[1,2], T. Kitazawa[1,2] D. P. Sari[3,4], I. Watanabe[3], A. Koda[5] and M. Fujita[1]

[1]*Institute for Materials Research, Tohoku University*
[2]*Department of Physics, Tohoku University*
[3]*Meson Science Laboratory, RIKEN Nishina Center for Accelerator-Based Science*
[4]*College of Engineering, Shibaura Institute of Technology*
[5]*Muon Science Laboratory, Institute of Materials Structure Science, KEK*

Heavy fermion systems have rich physics regarding a quantum critical phenomena. New compounds in the vicinity of quantum critical point and excellent methods detecting the magnetism often brought a lot of knowledge of quantum critical phenomena originating from the spin degree of freedom. Recently, the quantum criticality induced electronic states, which cannot be explained by the self-consistent renormalization (SCR) theory, have attracted much attention. To study such electronic states, actual candidate materials and adequate experimental methods are required.

In this study, we focused on a novel compound $YbCu_4Ni$ which shows a power-law behavior in the the temperature dependence of the specific heat (C/T) [1]. This behavior is consistent with the quantum critical phenomena, but difficult to be explained through SCR theory. The purpose of our research is to understand the origin of the power-law behavior of C/T and the electronic states at low temperature in $YbCu_4Ni$. Magnetism usually plays the vital role of quantum criticality, and μSR is a powerful tool to obtain information on static and dynamic spin correlations. Thus, we performed muon spin relaxation (μSR) measurements using pulsed positive muon beam in Material and Life Science Experimental Facility (MLF) in J-PARC, Japan, and in RIKEN-RAL Muon Facility (RAL) in Rutherford Appleton Laboratory, UK.

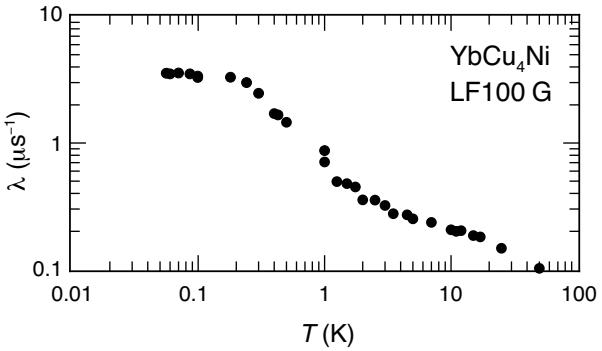

Fig. 1: Temperature dependence of the muon spin relaxation rate λ of $YbCu_4Ni$ in a longitudinal field of 100 G.

Figure 1 shows the temperature dependence of the muon spin relaxation rate λ. To derive the magnetic fluctuation of the f-electron, we applied a longitudinal magnetic field of 100 G. Rapid increases of relaxation upon cooling was observed at low temperatures below 2 K, indicating the appearance of magnetic fluctuation. The temperature dependence shows different power values for 1 K $< T$ and 0.2 K $< T <$ 1 K, indicating that the multiple spin-fluctuations coexist in this material. Below 0.2 K, λ is almost independent of the temperature. However muon spin precession was not observed down to the lowest temperature of 0.05 K. These results indicate that an instability of static magnetism is absent in $YbCu_4Ni$ near zero-field down to 0.05 K.

Here, we discuss the origin of the power-law behavior of C/T and electronic states below 0.2 K. The enhancement of λ down to 0.2 K suggests that the system locates in the vicinity of magnetic critical point. Meanwhile, the power-law behavior of C/T cannot be explained by the single component of magnetic fluctuation, suggesting the contribution of multiple spin-fluctuations on the strange behavior of C/T. Below 0.2 K, the electric resistivity is proportional to T^2 and λ is independent of the temperature. Thses result suggests that the electronic state is of coherent below 0.2 K, and recall the crossover of quantum critical behavior from the non-Fermi liquid to Fermi-liquid (FL) in $CeCoIn_5$ [2, 3] and from strange metal to spin-liquid (SL) in LiV_2O_4 [4, 5]. Further measurement, particularly neutron scattering measurement would give a clue to determine which is the electron state, FL or SL.

References

[1] J. G. Sereni *et al.*, Phys. Rev. B **98** (2018) 094420(1-8).

[2] H. Sakai *et al.*, Phys. Rev. Lett. **107** (2011) 137001(1-5).

[3] T. Taniguchi *et al.*, JPS Conf. Proc. **30** (2020) 011107(1-6).

[4] A. Koda *et al.*, Phys. Rev. B **69** (2004) 012402(1-4).

[5] H. Okabe *et al.*, Phys. Rev. B **99** (2019) 041113(R)(1-5).

μ^+SR Study of $Sm_3T_4Ge_{13}$ [J-PARC: 2020A0132]

S. Tsutsui[1,2], T. U. Ito[3], A. Koda[4], R. Higashinaka[5], T. D. Matsuda[5], and Y. Aoki[5]

[1]*Japan Synchrotron Radiation Research Institute (JASRI)*
[2]*Institute of Quantum Beam Science, Graduate School of Science and Engineering, Ibaraki University*
[3]*Advanced Science Research Center, JAEA*
[4]*Muon Science Laboratory, Institute of Materials Structure Science, KEK*
[5]*Department of Physics, Tokyo Metropolitan University*

Introduction

Much attention has been paid to quantum critical behaviors in solid state physics for recent decades. Heavy fermion behavior is one of the topics related to quantum critical behaviors. Quantum critical behaviors were discussed on the viewpoints of magnetic degrees of freedom based on Doniach's phase diagram previously [1]. For recent times, however, quantum critical behaviors have been discussed on various degrees of freedom related to phase transitions. In this sense, heavy fermion behavior is recognized as a problem related to residual entropy at low temperature rather than to magnetism.

Microscopic investigations are crucial to discuss which degrees of freedom connect with a quantum critical behavior. One of the probes is hyperfine spectroscopies such as NMR, μSR and Mössbauer spectroscopy. In particular, dynamic contributions through hyperfine interactions are important to discuss the mechanism of quantum critical behaviors.

Sm compounds have been attractive to the researches on quantum critical behavior since discovery of an unconventional heavy fermion behavior in $SmOs_4Sb_{12}$ insensitive to applied magnetic field [2]. One of the possible origin of the heavy fermion behavior is Sm valence degrees of freedom, because Sm is one of a few elements which allows valence degrees of freedom as well as magnetic and/or multipolar degrees of freedom in rare-earth elements. This means that these degrees of freedom allow various quantum critical behaviors in Sm compounds other than the quantum critical behavior discussed in Doniach's phase diagram [1].

$Sm_3T_4Ge_{13}$ compounds (T = Rh, Ru) are attractive as a heavy fermion system among Sm-based intermetallics [3]. These compounds exhibit a heavy fermion behavior at low temperature as well as an antiferromagnetic ordering below about 5 K [3]. Our recent work by means of Sm $L_{\rm III}$-edge X-ray absorption spectroscopy (XAS) and ^{149}Sm synchrotron-radiation-based (SR-based) Mössbauer spectroscopy at 300 K successfully clarified that the Sm valence states in these compounds are fluctuating in MHz region [4-6]. We also performed ^{149}Sm SR-based Mössbauer spectroscopy of these compounds at various temperature. Temperature dependence of the Mössbauer spectra implies observation of dynamical hyperfine interaction, suggesting that electronic states other than the Sm valence state at the Sm sites are also fluctuating in GHz region [7]. However, it is difficult to determine which degrees of freedom, quadrupolar or magnetic degrees of freedom, contribute to the fluctuation from the observed Mössbauer spectra because of the uncertainty relation in the ^{149}Sm Mössbauer transition. This is one of the motivations in the present work.

μ^+SR is a useful tool to conclude which degrees of freedom are fluctuating in $Sm_3T_4Ge_{13}$ compounds, because μ^+SR is sensitive only to magnetic degrees of freedom. In this work, we successfully determine temperature dependence of the relaxation rates related to magnetic degrees of freedom in $Sm_3T_4Ge_{13}$ compounds by means of μ^+SR. Magnetic field dependence of the relaxation rates supports observation of magnetic fluctuation as dynamical hyperfine interactions at ^{149}Sm nuclei.

Experimental Procedure

Pulsed μ^+SR measurements of $Sm_3T_4Ge_{13}$ (T = Rh, Ru) were performed in the S1 line using a single pulse muon beam in the fly-past mode. The longitudinal relaxation rate λ was measured in ZF, LF 0.01 T and LF 0.4 T as a function of temperature between 3 and 300 K. Measured samples were prepared with the polycrystalline ingots of $Sm_3T_4Ge_{12}$ crushed into powder.

Experimental Results and Discussion

The time-differential μ^+SR spectra at ZF are fitted with a single-exponential relaxation function $A\exp(-\lambda t)$. Temperature dependence of the longitudinal relaxation rate λ in $Sm_3Ru_4Ge_{13}$ is shown in Fig. 1. Enhancement of the relaxation rate λ was observed at temperature higher than the Néel temperature of about 5 K in $Sm_3Ru_4Ge_{13}$. Similar behavior was also observed in $Sm_3Rh_4Ge_{13}$. The temperature dependence of the relaxation λ in these compounds is anomalous in magnetically ordered compounds.

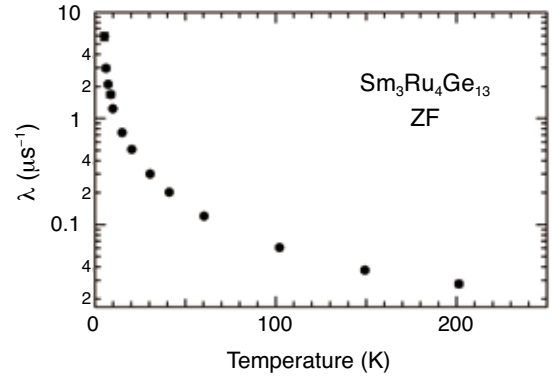

Fig. 1: Temperature dependence of the longitudinal relaxation rate λ in $Sm_3Ru_4Ge_{13}$.

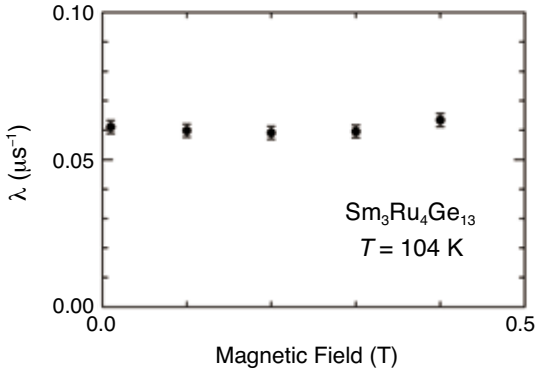

Fig. 2: Applied field dependence of the longitudinal relaxation rate λ in $Sm_3Ru_4Ge_{13}$ at 104 K.

The time-differential μ^+SR spectra at 104 K in various magnetic fields are also fitted with a single-exponential relaxation function. Magnetic field dependence of the relaxation rate λ is shown in Fig. 2. Absence of the magnetic field dependence of λ was observed at 104 K. Assuming that the magnetic field due to Sm magnetic moments of 0.5 μ_B is $\sim$0.1 T at muon sites, the hyperfine coupling constant is estimated to be $\sim$85 μs^{-1}. The absence of the magnetic field dependence of λ demonstrates that spin fluctuation is fast in hundreds GHz order.

Now, we discuss the origin of the dynamical hyperfine interactions at ^{149}Sm nuclei in $Sm_3T_4Ge_{13}$. Since the typical frequency in ^{149}Sm Mössbauer spectroscopy due to Sm valence fluctuation is MHz order, Sm valence fluctuation is ruled out as a candidate of the dynamical hyperfine interactions observed at ^{149}Sm nuclei. This means that possible origins of the dynamical hyperfine interactions come from fluctuating nuclear magnetic interaction or nuclear quadrupole interaction. Judging from the present μ^+SR results, plausible understanding of the dynamical hyperfine interactions observed at ^{149}Sm nuclei is based on magnetic degrees of freedom. Assuming that the magnitude of the magnetic moment at the Sm site is $\sim$0.5 μ_B, the magnitude of the fluctuation frequency estimated from the ^{149}Sm Mössbauer spectra is GHz order in rough estimation. This agrees with the magnitude of the hyperfine interaction at the muon sites.

Summary

μ^+SR measurements of $Sm_3T_4Ge_{13}$ successfully determine temperature and magnetic field dependence of the relaxation rate λ. These also revealed that ^{149}Sm Mössbauer spectroscopy detected Sm magnetic fluctuation as well as Sm valence fluctuation in $Sm_3T_4Ge_{13}$. On the other hand, fast spin fluctuation observed by both ^{149}Sm Mössbauer spectroscopy and μ^+SR seems to be independent of the magnetic ordering at $\sim$ 5 K. Further analyses are required to discuss the correlations between the electronic fluctuations in hyperfine interactions at ^{149}Sm nuclei and muon sites and electronic ground states in both $Sm_3T_4Ge_{13}$ (T = Ru, Rh).

Acknowledgements

The principle investigator ST is grateful to Michael Kenya Kubo for his promotion of this project. He also appreciates Yoshio Kobayashi, Jin Nakamura, Kosuke Fujiwara, Raito Nakamura and Yoshitaka Yoda for their support of ^{149}Sm SR-based Mössbauer spectroscopy experiments and Kiyofumi Nitta and Kazuo Kato for Sm L_{III}-edge XAS experiments.

References

[1] S. Doniach, Physica B **91** (1977) 231–234.

[2] S. Sanada *et al.*, J. Phys. Soc. Jpn. **74** (2005) 246–249.

[3] H. S. Nair *et al.*, J. Alloy Compd. **669** (2016) 254–261.

[4] S. Tsutsui *et al.*, J. Phys. Soc. Jpn. **85** (2016) 083704(1-5).

[5] S. Tsutsui *et al.*, Hyperfine Interact. **240** (2019) 84(1-16).

[6] S. Tsutsui *et al.*, in preparation.

[7] S. Tsutsui *et al.*, Experimental Report of SPring-8 (Proposal Nos. 2019A1226, 2020A1346).

Non-Destructive Detection of Li Deposition in a Li-ion Battery with Muonic X-rays [J-PARC: 2020A0184]

I. Umegaki, Y Kondo, Y. Higuchi, H. Kondo, K. Ninomiya[1], S. Takeshita[2], M. Tampo[2], M. K. Kubo[3], and Y. Miyake[2]

Toyota Central Research & Development Laboratories, Inc.
[1]*Graduate School of Science, Osaka University*
[2]*Muon Science Laboratory, Institute of Materials Structure Science, KEK*
[3]*College of Liberal Arts, International Christian University*

1. Intro

It is known that Li is reduced to metallic Li and to be deposited on a graphite anode in a Li-ion battery (LIB) under an extreme working condition such as at low temperature and at high rate. In order to improve safety of LIBs, it is desire to detect metallic Li deposition in a LIB in a non-destructive way. We have successfully demonstrated that metallic Li deposited on a graphite anode using muonic x-rays in our previous experiments [1]. In the experiment, we used a graphite anode, which was coated by an Al laminated sheet. This time, we applied to this technique to an Al laminated pouch cell (Fig.1) as the next step after measurements of an anode.

Fig. 1: A picure of a laminated LIB. The laminated sheet contains aluminum with 7 μm of thickness. The size of electrodes is 42 × 27 mm^2.

2. Experimental

Three samples with different conditions were prepared in Toyota CRDL; (a) an initial state, (b) after 15 cycles and (c) 30 cycles at a high rate (Fig.2). The deterioration in the capacity of these cells was estimated as 0, 13.6, and 28.0% in electrochemical method (Table 1). Some of the deterioration is caused by deposition of metallic Li. In fact, amount of metallic Li deposition was estimated as 0, 0.015, and 0.046 mg/cm^2 by a combination of destructive measurements of ICP-OES and ^{7}Li-NMR after the experiment.

The experiment was performed at D2 area in MLF, J-PARC. A sample was set in a bag filled with He gas and muonic x-rays emitted by irradiation of negative muons were detected by 3 Ge semiconductor detectors and an SDD (Silicon drift detector) from the upstream of the sample position. The momentum of negative muon beam was adjusted in the range between 14 and 19 MeV/c so as negative muons stop in the anode in a LIB.

In order to investigate the intensity of muonic x-rays from Li, we defined a parameter as $I_{\mathrm{CLi}} = (I_{\mathrm{C4-2}}+I_{\mathrm{Li2-1}})/I_{\mathrm{C2-1}}$, where $I_{\mathrm{C4-2}}$, $I_{\mathrm{Li2-1}}$,$I_{\mathrm{C2-1}}$ represent intensity of muonic x-rays of C(4-2), Li(2-1), and C(2-1), respectively. This is because the peaks of $\mathrm{I_{C4-2}}$ and $I_{\mathrm{Li2-1}}$ were not distinguished by the Ge detectors with its energy resolution, because the difference in energy of these two peaks is 130 eV. Since the ratio of $I_{\mathrm{C4-2}}$ and $I_{\mathrm{C2-1}}$ is constant, increase of I_{CLi} shows the increase in the intensity of muonic X-rays of Li. Since muonic x-rays of C(2-1) at 75 keV cannot be detected by a SDD detector due to out of its energy range, we defined a parameter as $I_{\mathrm{CLi}}' = (I_{\mathrm{C4-2}}+I_{\mathrm{Li2-1}})/I_{\mathrm{C3-2}}$, where $I_{\mathrm{C3-2}}$ represents intensity of muonic X-rays of C(3-2) at 14 keV, instead of I_{CLi}.

Attenuation of muonic x-ray from Li in a LIB by a Cu current collector, which is located at upstream of the sample, should be considered. Based on the location of three Ge detectors, we estimated transmittance rate as 65.2%, 65.2% and 63.6%, respectively. It is noted that attenuation by any other component such as a laminated sheet and Al is negligible. We also estimated transmittance rate as 63.6% for a SDD detector.

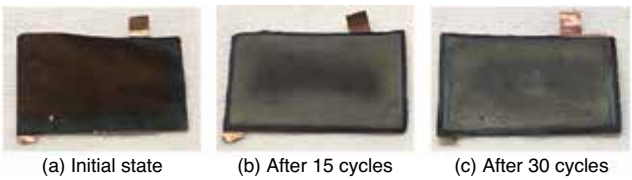

Fig. 2: Photos of the anode sheets in the three samples with (a) initial state, after (b) 15 cycles and (c) 30 cycles. They were took after the experiment in J-PARC.

Table 1: Conditions and amount of metallic Li obtained in samples.

	Condition	Li (mg/cm^2)	Deterioration
A	Initial state	0.0	0
B	15 cycles	0.015	13.6%
C	30 cycles	0.046	28.0%

3. Results

Figure 3 shows the momentum dependence of I_{CLi} for the LIB samples with an initial state and after 30 cycles. We have observed a significant difference in I_{CLi} around the momentum of 18.0 MeV/c, which corresponds to the location of metallic Li deposition in the samples. Below 17.5 and above 18.5 MeV/c, I_{CLi} for the two samples are almost the same level. However, in the range between 17.5 and 18.5 MeV/c, muonic x-ray from Li can be observed as the significant increase of I_{CLi} for the sample after 30 cycles. Then, we plotted the value of I_{CLi} at the momentum of 18.5 MeV/c as a function of Li amount to obtain a standard curve (Fig.4).

Figure 5 shows the momentum dependence of I_{CLi}' obtained by a SDD. I_{Li}' also represents Li in the LIB samples, showing significant difference between LIB samples with an initial state and after 30 cycles around 18.0 MeV/c. This is versy consistent with the results obtained by the Ge detectors.

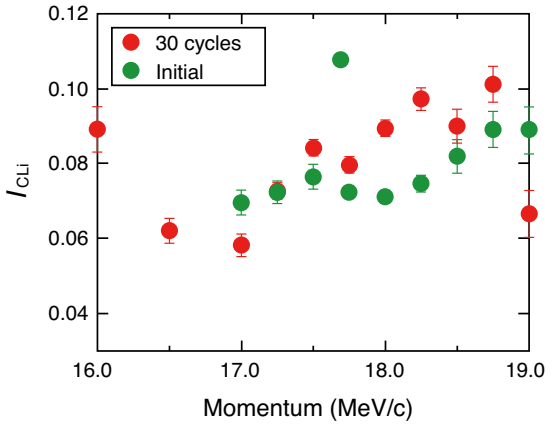

Fig. 3: Momentum dependence of I_{CLi} for LIB samples with the initial state and after 30 cycles at a high rate.

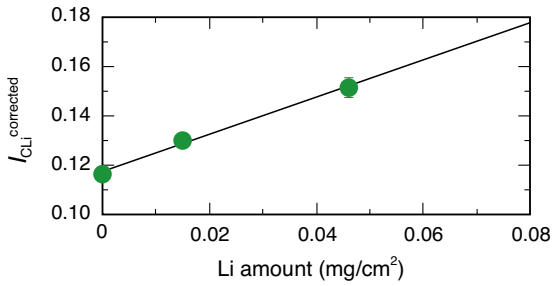

Fig. 4: Standard curve; relationship between I_{CLi} (corrected) and Li amount. The value of vertical axis is estimated from I_{CLi} and transmittance rate.

4. Conclusion

We have successfully detected metallic Li deposited on the anode in the Al laminated LIBs by detecting muonic x-rays by Ge detectors and an SDD. The obtained standard curve indicates that 0.01 mg/cm^2 of metallic Li deposition, which is corresponding to 2% of capacity of the LIB, can be quantitatively measured by this technique. Thus, we believe that this technique can be applied for non-destructive analysis on a laminated LIB. In order to judge the existence of metallic Li in a LIB regardless of the position of its deposition, commercially available LIBs also might be possibly investigated by this technique.

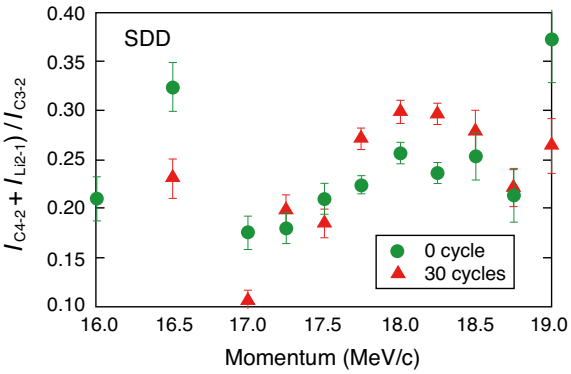

Fig. 5: Momentum dependence of I_{CLi} for LIB samples with the initial state and after 30 cycles at a high rate.

Acknowledgement

This work was supported by MEXT KAKENHI 19H05199.

References

[1] I. Umegaki *et al.*, Anal. Chem. **92** (2020) 8194–8200.

μSR Analysis of Muon/muonium Dynamics of Protein Components, Peptide, Histidine Related Compounds and Microperoxidase-11

[J-PARC: 2020A0191 / 2020A0207 / 2020B0268]

Y. Sugawara, S. Yamamura[1], A. D. Pant[2], M. Kusunoki[3], H. Yamaguchi[3], J. Sugiyama[4], H. Miwa[5], A. Koda[2], W. Higemoto[6], K. Shimomura[2], E. Torikai[7], and K. Nagamine[2]

Toyota Physical and Chemical Research Institute
[1]*Graduate School of Science, Kitasato University*
[2]*Muon Science Laboratory, Institute of Materials Structure Science, KEK*
[3]*School of Science and Technology, Kwansei Gakuin University*
[4]*Neutron Science and Technology Center, CROSS*
[5]*Institute of Catalysis, Hokkaido University*
[6]*Advanced Science Research Center, JAEA*
[7]*Graduate Faculty of Interdisciplinary Research, University of Yamanashi*

Positive muon spin rotation/relaxation/resonance (μ^+SR) spectroscopy is one of the powerful tools in solid-state physics and radical chemistry. Life science is also an attractive field for μ^+SR, although such application is still not widely developed mainly due to the complexity of biomacromolecules. For understanding the μ^+SR data in biomacromolecules, it is inevitable to determine the muon sites and muon states in them.

Proteins, which are a typical biomacromolecule, consist of main chains and side chains. The main chain is made of peptide bonds (-CONH-) linking the Cα carbon atoms of adjacent amino acids. In the periods of 2020A and 2020B, μSR experiments focusing on the following phenomena were carried out.

1. Temperature dependence of the muon spin relaxation property for peptide bonds
2. Hydrogen bond, ion bridge and protonation effects on muon spin relaxation property for glycylglycine and histidine related compounds
3. μSR of micropeptidase-11 (MP-11) which is obtained by proteolytic digestion of cytochrome c and made of a heme moiety and 11 amino acids

The results are described from the first point.

N-methylacetamide (NMAA:CH_3-CONH-CH_3) is the simplest molecule which contains peptide bond. One dimensional hydrogen bonding chain is formed in the crystal. A phase transition occurs around 274 K and disordered structure exists between 273 K and the melting point (301 K) [1]. Temperature dependence of ZF μSR spectra of NMAA from 95 to 293 K is shown in Fig. 1. Above around 200 K μSR changed and the oscillation component was observed around 250 K. The oscillation suggested the formation of μ^+HX (X = N or O), and μ^+-H distances were estimated to be 1.2-1.5 Å, although the effect of nuclear spin of N was not included in fitting procedure at the present stage. The similar phenomenon was observed in the case of triglycine (NH_3^+-CH_2-(CONH-CH_2)$_2$-COO^-) which also contains peptide bonds. The μ^+-H distances of 1.2-1.5 Å suggested the formation of >NHμ^+. Last year, the DFT calculations with the B3LYP/6-31G(d,p) basis set were carried out on an isolated NMAA molecule and the most stable protonation site, which is considered to be the μ^+ stopping site, is an oxygen atom of a peptide bond. The optimized energy of the product protonated at a nitrogen atom (>NH_2^+) was higher than that of C=OH^+ by 70∼80 kJ/mol. This year, ONIOM calculations (wB97XD/6-31G(d,p):PM7) of a crystal model of NMAA was carried out. It was indicated that the protonation at an oxygen atom would cause reorientation of the molecule to form C=OH^+ ... O=C hydrogen bond. In addition, when protonation occurred on >NH and >NH_2^+ is formed, >NH_2^+ hydrogen bonded to two O=C of the neighboring molecules and optimized energy markedly lowered, which is consistent with the experimental results.

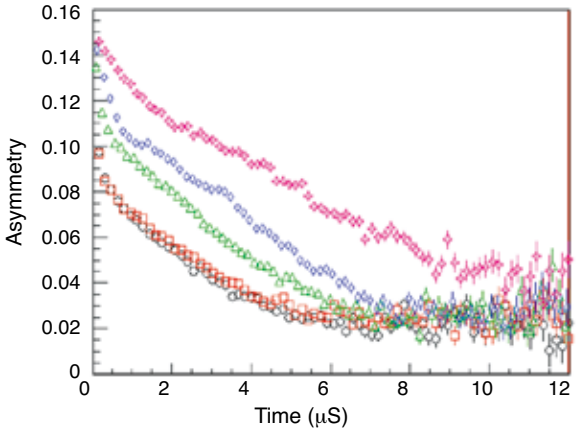

Fig. 1: Temperature dependence of ZF μ^+SR spectrum of N-methylacetamide. 95, 145, 195, 251 and 293 K from bottom to up.

The next point is hydrogen bond, ion bridge and protonation effects on muon spin relaxation property. μSR spectra of (glycylglycine)$_2$· $3H_2O$ and N-acetyl-L-histidine and N-acetylhistamine were examined. In the glycylglycine crystals, carboxyl (-COO^-) and ammonium (-NH_3^+) groups form salt bridges. On the other hand, a water molecule bridges carboxyl (-COO^-) and ammonium (-NH_3^+) groups in the hydrate. The μSR spectra of glycylglycine and its hydrate are shown in Fig. 2. There is extinct difference between them. So were the μSR spectra of histidine related compounds. The analysis of relaxation parameters will be carried out.

The last theme is μSR spectra of MP-11. MP-11 is a heme-peptide made of a heme moiety and 11 amino acids (VAL-GLN-LYS-CYS-ALA-GLN-CYS-HIS-THR-VAL-GLU) obtained by proteolytic digestion of cytochrome *c* and displays the peroxidase activity as cytochrome *c* (Fig. 3). The μSR spectra of MP-11 is shown in Fig. 4 compared with that of cytochrome *c*. The most part of the signals would be originated from the diamagnetic muons and μ^+ would mainly stop at carboxyl and cysteine groups judging from our μSR data of the related amino acids [2]. Although the heme moiety and peptide bonds contain unsaturated bonds, a muoniated radical seemed to be scarcely formed. In the case of cytochrome *c*, the muoniated radical component was approximately one third of the observed signals [Fig. 4(b)]. In cytochrome *c*, muoniated radicals would be formed at the aromatic side chains of phenylalanine, tyrosine, tryptophan and/or histidine.

Among the above reported results, temperature dependence of the muon spin relaxation property for peptide bonds cause attention from the view point of the proton transfer mechanism via peptide bonds which was proposed based on the crystallographic structure of cytochrome *c* oxidase [3]. The dynamic property of protonated peptide bonds should be discussed based on the μSR data and the theoretical calculations.

References

[1] J. Eckert *et al.*, J. Phys. Chem. B **105** (2001) 19–24.

[2] Y. Sugawara, J. Comput. Chem., Jpn. **19** (2020) 71–79.

[3] K. Kamiya *et al.*, J. Am. Chem. Soc. **129** (2007) 9663–9673.

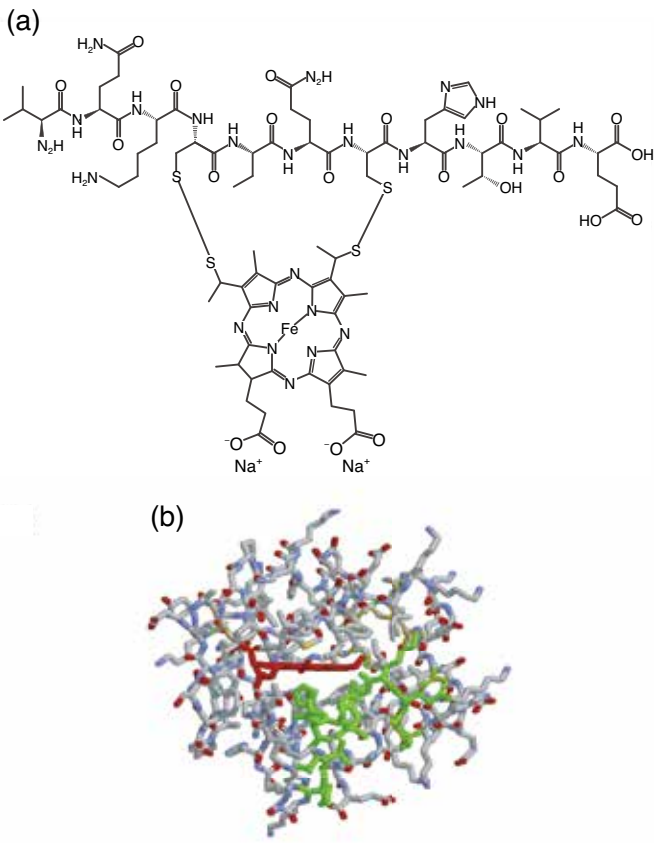

Fig. 3: MP-11 (a) and cytochrome *c* (b). Red: heme, green: the residues which correspond to MP-11.

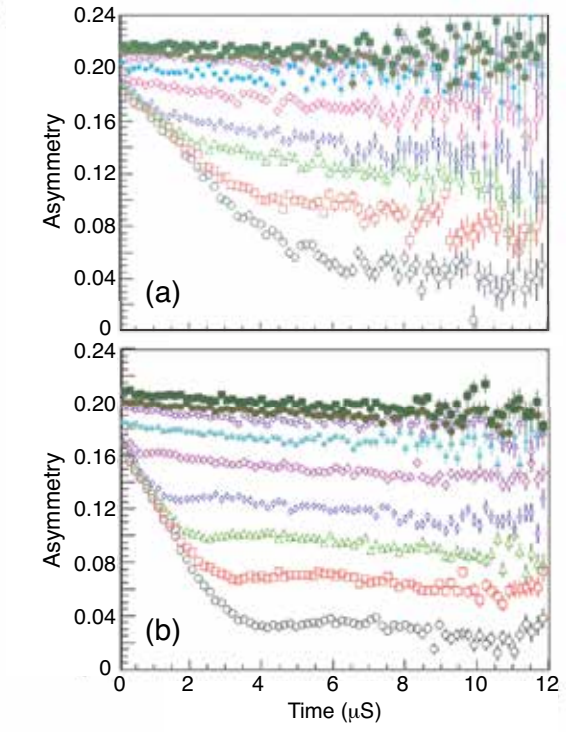

Fig. 2: LF dependence of μSR spectra of glycylglycine (a) and glycylglycine hydrate (b) at 55 K. LF: 0, 7, 12, 20, 50, 139, 373, 610, 1000 G from bottom to top for each figure.

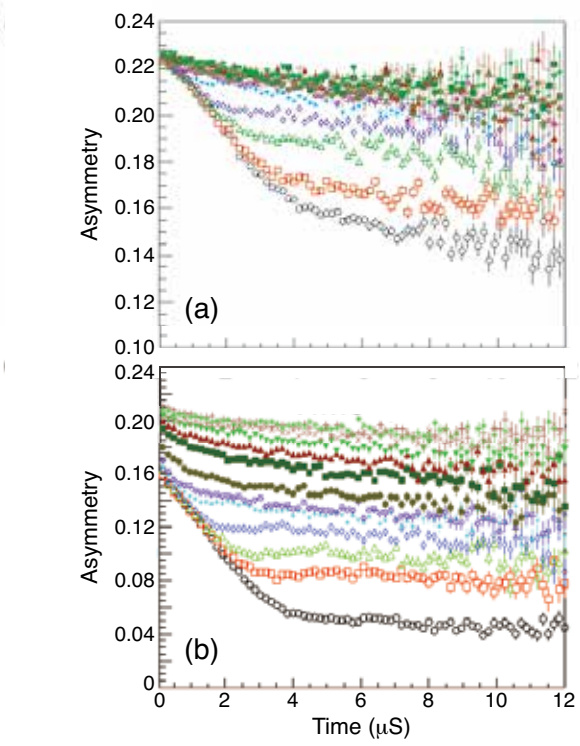

Fig. 4: Longitudinal magnetic field dependence of μSR spectra of MP-11 at 54 K and cytochrome *c* at 48 K. (LF: 0, 5, 10, 15, 20, 30, 50, 85, 139, 228, 373, 610, 1000, 2000 for MP-11 and 0, 7, 10, 15, 20, 30, 50, 139, 373, 610, 1000, 2000, 3000, 3950 for cytochrome *c* from bottom to up.)

Non-destructive Analysis of Light Elements by Negative Muon Lifetime Measurement [J-PARC: 2020A0193]

M. K. Kubo, K. Ninomiya[1], G. Yoshida[2], M. Inagaki[3], S. Doiuchi[4], M. Tampo[4], S. Takeshita[4], P. Strasser[4], N. Kawamura[4], K. Shimomura[4], Y. Miyake[4], W. Higemoto[5], A. Shinohara[1], and T. Saito[6]

College of Liberal Arts, International Christian University
[1]*Graduate School of Science, Osaka University*
[2]*Radiation Science Center, KEK*
[3]*Institute for Integrated Radiation and Nuclear Science, Kyoto University*
[4]*Muon Science Laboratory, Institute of Materials Structure Science, KEK*
[5]*Advanced Science Research Center, JAEA*
[6]*National Museum of Japanese History*

The non-destructive elemental analysis by muonic X-ray measurements at J-PARC MUSE has expanded its use for various samples, including ancient artificial remnants to meteorites. The technique has great merit in analyzing low-Z elements such as lithium, boron, carbon, nitrogen and oxygen by taking advantage of the high energy of the emitted muonic X-rays from low-Z atoms in the range of 10 to 130 keV. However, the self-absorption of muonic X-rays within samples comprising heavy elements makes it difficult to observe the X-ray photons outside the sample. Muonic X-ray measurements are very time-consuming and sometimes practically impossible for such samples.

An alternative approach to quantify the elemental compositions of materials is the negative muon lifetime method. The negative muon decays and emits a decay electron (DE) and two neutrinos with an average lifetime of 2.2 μs. A negative muon captured by an atom forms a muonic atom and the muon orbits around the nucleus. The energy spectrum of the muon DE has a continuous distribution independent of the atom captured the muon. The nucleus has some probability of absorbing the orbiting negative muon like the electron capture decay. The absorption competes with the intrinsic decay of the negative muon. The rate of the absorption process depends on the nuclear property, mainly determined by the number of the protons or the atomic number of the nucleus; the higher the atomic number, the faster the absorption. The lifetimes of the muon in elements determined by measuring the DE time spectrum are compiled by Suzuki [1]. For example, the lifetime of the negative muon in C is 2.0 μs, 1.8 μs for O, 200 ns for Fe. There is no chemical effect on the lifetime. As a result, the DE time spectrum of the muon in material reflects the elemental composition of the substance;

$$N(t) = \sum_i n_i \ \mathrm{e}^{-\lambda_i t} + \mathrm{BG}$$

$N(t)$ is the number of the DE at time t, n_i is the number of the muon captured by the element i with the negative muon lifetime λ_i, and the time-independent background BG. The elemental composition of the material is obtained as the ratio of n_i's. Since the lifetimes are known, the fitting procedure to obtain n_i's is the linear regression analysis, and n_i's are precisely determined within the statistical limit. A comparison with standard materials leads to the quantitative determination of elemental composition. Since the DE has an average energy of 50 MeV, the DE easily comes out of the substance and is measured by plastic scintillation detectors. This technique is called the lifetime method for determining the elemental composition of materials by the negative muon irradiation. The longer lifetime for low-Z elements means the number of DE is larger from the negative muons captured by low-Z elements than heavy ones. Thanks to the high energy of the DE, this method is applicable to depth profiling of low Z elements existing in materials comprising high Z elements or deep in the sample. Another advantage of the lifetime method is that lifetimes for lighter elements are long and easy to measure. Decay electrons from light elements are measurable after the complete decay of the shorter-lived muons captured by high Z atoms. The pulsed mode muon at MUSE is best suitable for this method because the bunch of negative muons is delivered at 25 Hz leaving 40 ms quiet time for the DE measurement with almost no BG between muon pulses. The KALLIOPE scintillator detection system for μSR covering 20% of the solid angle at the D1-port of MUSE is an advantage of the DE counting over the muonic X-ray measurement by Ge detectors with less solid angle coverage.

We conducted the first attempt to analyze the carbon content in iron in 2019. A calibration curve was successfully obtained for standard steel samples containing less than 4.6% carbon[2].

At the first trial last year, a component appeared with a lifetime very close but longer than carbon. The component interferes with the DE curve from carbon and brings a significant error in carbon content. It was suggested that the component arose from muons stopped in oxygen in air or the plastic parts in the detector. This time we replaced the air around the measuring sample with helium by covering the detection space with a thin plastic bag to remove oxygen. This helium bag method leads to a slight decrease in the oxygen component. The limited effect was probably because the muons scattered by the sample arrived at the detector parts. Next, thin tin plates will be used to capture the scattered muons by a material with a short muon lifetime.

Depth selectivity is one of the merits of the negative muon elemental analysis method. We used two stacked samples; a 1.5 mm thick pure iron plate with a thick iron standard block of 4.46% carbon, and a 1.5 mm thick pure iron plate with a thick iron standard block of 0.47% carbon. The result for the 4.7% sample is shown in Fig. 1. A 40 MeV/c muon beam stopped in the pure ion plate and showed a DE time histogram of the negative muon in iron with a lifetime of 200 ns. The 55 MeV/c muon beam penetrated the pure ion plate and stopped in the 4.7% standard. A clear DE curve arising from muons in carbon appears in the histogram. Changing the momentum of the incident negative muon enables us to analyze the part of different depths of the sample.

An old Japanese sword of about 4 cm wide, 60 cm long and 5 mm tick was analyzed at the middle of the sword. The sword is supposed to have a three-layered structure, the inner part and the outer part, made of two iron materials with different carbon contents. Changing the incident muon momentum shows a slightly higher carbon content at the core part of the sword.

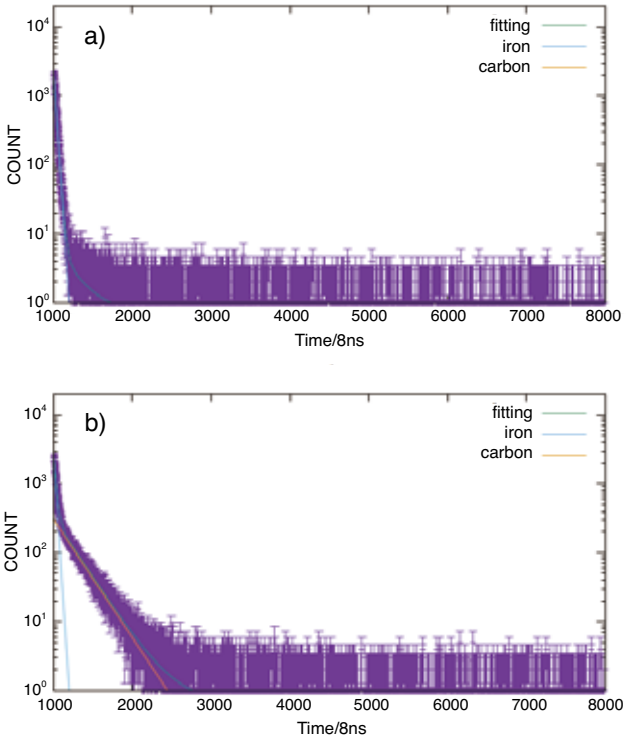

Fig. 1: Decay electron histograms for a) 40 MeV/c and b) 55 MeV/c negative muon irradiation.

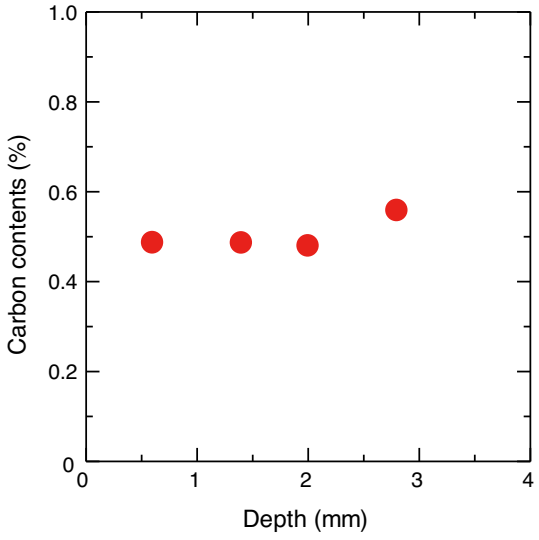

Fig. 2: Carbon content of a Japanese sword at different depths form the surface.

References

[1] T. Suzuki *et al.*, Phys. Rev. C **35** (1987) 2212–2224.

[2] T. Kudo *et al.*, KEK Prog. Rep. **2020-4** (2020) 73–74.

μSR Study of Two Typical Elasticoluminescence Materials Series of $SrAl_2O_4$:Eu and $LiNbO_3$:Pr [J-PARC: 2020A0197]

X. G. Zheng, I. Yamauchi, A. Urata, A. Koda[1], S. Nishimura[1], J. G. Nakamura[1], R. Kadono[1], and C. N. Xu[2]

Department of Physics, Saga University
[1]*Muon Science Laboratory, Institute of Materials Structure Science, KEK*
[2]*National Institute of Advanced Industrial Science and Technology (AIST)*

Mechanoluminescence (ML) is luminescence induced by mechanical stimuli. Photo-emitting phenomenon from crystals during breaking had been reported in 1605. However, it was obtained only during breaking down, thus cannot be used in application. The most important form of ML is elastic-luminescence from elastic deformation which can be repeatedly used in application. First practical materials of elastic-luminescence were discovered to be SAO ($SrAl_2O_4$:Eu) and Mn:ZnS, as reported in 1999 [1,2]. Visible light emission can be easily obtained by touching a volleyball coated with elastic-luminescence materials. Further, a multi-piezo material was recently found with simultaneous piezoelectricity and sensitive piezo luminescence in Li_xNbO_3:Pr(LNO) [3]. It is evaluated as a new type of actually thresholdless elastic ML material, which could predict and quantify the risk level for micro strains below 300 μst. This kind of elastic-luminescence can be used effectively in bio-imaging such as in artificial bones in human bodies, visualization of distribution of stress, prediction of fracture, diagnosis of micro and potential cracks in infra-constructures of bridges, tanks and pipes etc. In special, the multi-piezo material with simultaneous piezoelectricity and sensitive piezoluminescence shows potential to enable multi-conversion of electric-mechanical-photonic energies.

However, previous studies have been concentrated on materials development, performance optimization and application. Meanwhile, the mechanism for the elastic-luminescence in the physics level remains largely unknown. The uncovering of the underlying mechanism should bring a big breakthrough to this technology. In a ML material, rare-earth elements are generally doped to serve as the luminescent center. In related previous re-search, it was found that reversible movement of dislocations in ML material SAO upon applying and releasing a mechanical stress by electron microscopy observation [4]. Therefore, we believe that the key for the ML mechanism in SAO lies in the dynamic interplay between the rare-earth luminescent centers and the crystal defects during mechanical excitation. Meanwhile, the movement of the dislocations may influence the trapping of mu-ons implanted. We thus conceived the idea of studying the dynamic interplay of luminescent centers and crystal defects at an atomic scale using μSR. Although the rare-earth luminescent centers are less than 0.2 at.% in these compounds, the intensely distributed defects may directly interact with the implanted muons. We thus performed μSR measurements at S1 beam line of J-PARC on two representative ML material series of $SrAl_2O_4$:Eu and $LiNbO_3$:Pr. As a preliminary experiment to check the basic behaviors of these materials, pressed pellets of powders were used and an much easier UV-radiation was used instead of the mechanical stimulation. Interesting results were obtained from the SAO samples. We tested four SAO samples with contrastingly different ML intensities (ML photo-emitting counts for JPN-4, 5, 11 and 12 are 130, 134780, 234, and 116830, respectively) at room temperature. The test measurement showed apparent strong and direct correlation of the muonium behaviors to the ML property [Fig. 1]. Detailed LF-μSR measurements suggested the formation of muonium in SAO. UV-radiation effect was not ob-served, probably due to the short penetration depth of light into the pressed pellets.

The preliminary results showed the usefulness of MuSR to ML materials. The formation of muonium, which has a gyromagnetic ratio 103 times of muon, demonstrates the sensibility of MuSR for ML photonics. Therefore, further experiments are in progress.

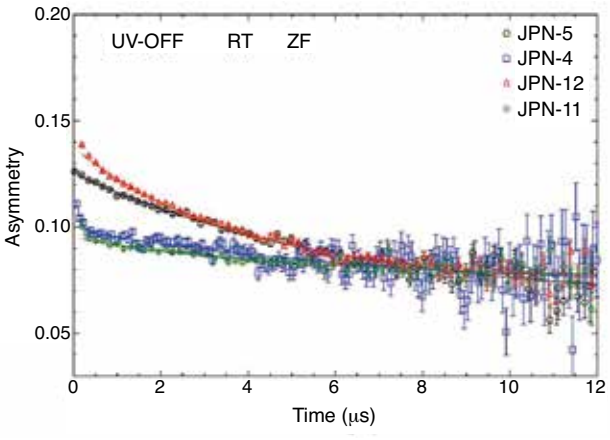

Fig. 1: ZF-μSR spectra showing correlation of the muonium behaviors to the ML property in SAO samples.

References

[1] C. N. Xu *et al.*, Appl. Phys. Lett. **74** (1999) 2414–2416.

[2] C. N. Xu *et al.*, Appl. Phys. Lett. **74** (1999) 1236–1238.

[3] D. Tu *et al.*, Adv. Mater. **29** (2017) 1606914(1-4).

[4] H. Matsuo *et al.*, J. Alloys Compd. **577** (2013) S507–S516.

Measurement of Muon Spin Relaxation Time in Scintillating Materials
[J-PARC: 2020A0204]

S. Shimizu, K. Horie, K. Kamada[1], A. Kobayashi[2], and M. Mihara

Department of Physics, Osaka University
[1] *New Industry Creation Hatchery Center, Tohoku University*
[2] *Department of Physics, Chiba University*

1. Introduction

Time (T) reversal symmetry has long been a subject of interest from pre-modern physics time, since it implies the reversibility of motion. In the $K^+ \to \pi^0\mu^+\nu$ ($K_{\mu 3}$) decay, the transverse muon polarization (P_T) is defined as the polarization component perpendicular to the decay plane. A non-vanishing value of P_T provides clear evidence for T-violation (violation of T reversal symmetry) because spurious effects from final state interactions are negligibly small [1].

Recently, a new T-violation experiment using a sequential CeF_3 calorimeter was proposed. Cross sectional sideview of the new experiment is shown in Fig. 1 [2]. In this experiment which adopts a stopped K^+ method, the μ^+ momentum, the π^0 momentum, and μ^+ polarization will be measured by the same CeF_3 calorimeter, and a magnetic spectrometer for the charged particle measurement will not be used. The μ^+ polarization can be determined by the delayed e^+ signals from the μ^+ decay detected by the calorimeter modules around the muon stop.

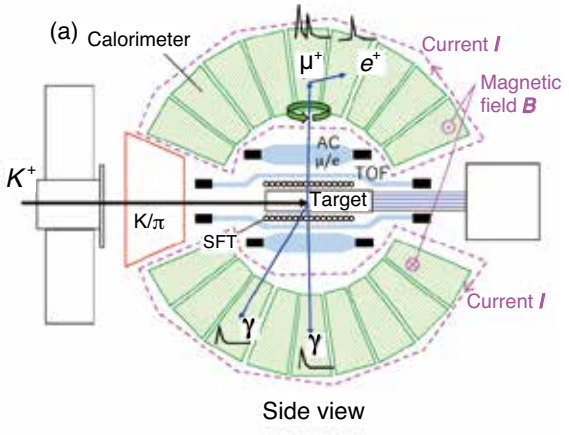

Fig. 1: Cross sectional side view of the setup for the new experiment to search for T-violation. The experiment adopts a stopped K^+ method. The μ^+ momentum vector, the π^0 momentum vector, and the μ^+ polarization are measured by the same electro-magnetic calorimeter surrounding the K^+ stopping target.

2. Beam test of scintillating materials

One of key issues in the new experiment is the choice of a scintillating material that can preserve the μ^+ spin polarization for a long time at room temperature. Fluorine compounds have been known to preserve the μ^+ polarization by forming the diamagnetic F-μ-F state [3]. In May 2019 and Feb. 2021, the measurements of the μ^+ spin rotation/relaxation spectra in scintillating materials was performed at J-PARC MLF using a pulsed μ^+ beam. A 100% polarized surface μ^+ beam was transported through the S1 beam line and stopped in the scintillating materials. The degree of μ^+ polarization and the spin relaxation time were directly observed by the e^+ telescope system. The properties of CeF_3, BaF_2, MgF_2, $CeLiCaAlF_6$, $EuLiCaAlF_6$, LYSO, GAGG, and La-GPS materials were carefully checked in this experiment. The 20-Gauss transverse field muon spin rotation (TF-μSR) spectra, the zero and the 100-Gausss longitudinal muon spin relaxation fields (ZF- and LF-μSR) spectra were obtained at room temperature. The e^+ asymmetry defined as the e^+ yield (N) difference between the forward (F) and backward (B) counters

$$A(t) = \frac{N_F(t) - N_B(t)}{N_F(t) + N_B(t)} \qquad (1)$$

was determined as a function of the $\mu^+ \to e^+\nu\bar{\nu}$ decay time (t).

3. Muon polarization in fluorine compounds

The time-integrated residual polarization in CeF_3 at room temperature was obtained to be higher than 80%, which is high enough to perform the new T-violation experiment at J-PARC (see [2] for details). In the zero-field measurement, the μSR pattern due to a stable F-μ-F diamagnetic state without forming muonium was successfully observed, as shown in Fig. 2 indicated by the red circles. The observed frequency is in good agreement of the reported CaF_2 and BaF_2 results at low temperature [3], strongly indicating the formation of the F-μ-F state in CeF_3.

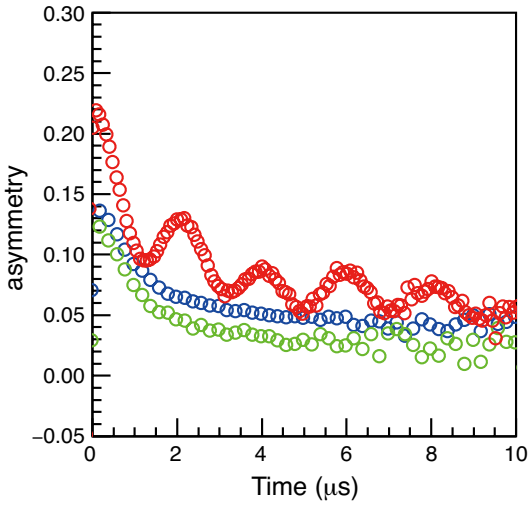

Fig. 2: The μSR spectra obtained in the ZF measurement. The μSR pattern due to a stable F-μ-F diamagnetic state without forming muonium was successfully observed in CeF_3 (red), but not observe in $CeLiCaAlF_6$ (green) and $EuLiCaAlF_6$ (blue).

Fig. 3(a) shows the e^+ asymmetry distribution for $CeLiCaAlF_6$ (green) and $EuLiCaAlF_6$ (blue/circle), which was found to be relatively high. Fluorine atoms must be playing important role for the spin preservation phenomena, although the μSR pattern due to the F-μ-F formation was not observed in the ZF measurement, as shown in Fig. 2. The black dots in Fig 3 are the results of the polarization calibration using a Ag material corresponding 100% level. The initial μ^+ polarizations are 58% and 64% with the relaxation constant of 15 μs and 20 μs for $EuLiCaAlF_6$ and $CeLiCaAlF_6$, respectively. Fig. 3(a) shows the residual polarization in MgF_2 (red) and BaF_2 (blue/triangle), which is only ~10% and much smaller than that in CeF_3, $CeLiCaAlF_6$, and $EuLiCaAlF_6$. It can be concluded that the diamagnetic fraction strongly depends on material spices at room temperature and that in CeF_3, $CeLiCaAlF_6$, and $EuLiCaAlF_6$ is significantly high, but it is not the case for muons in MgF_2 and BaF_2. The reason of this mechanism has not been correctly understood, and it is highly preferable to be settled by further studies.

4. Muon polarization in oxygen compounds

As well as fluorine compounds, oxygen compounds have been expected to generate the diamagnetic O-μ-O state, although it is not experimentally confirmed yet. Therefore, oxygen compounds would preserve the muon polarization due to the same mechanism as fluorine compounds for a long time. Fig.3(b) shows the μSR spectra with the longitudinal field of 100 Gauss in LYSO (red), GAGG (blue), and La-GPS (green) materials. The residual polarization in LYSO is obtained to be ~22% and that in GAGG and La-GPS is only ~10%. Although the residual μ^+ polarization in LYSO is not very high, it can be applied for something in the μ^+ polarization measurement.

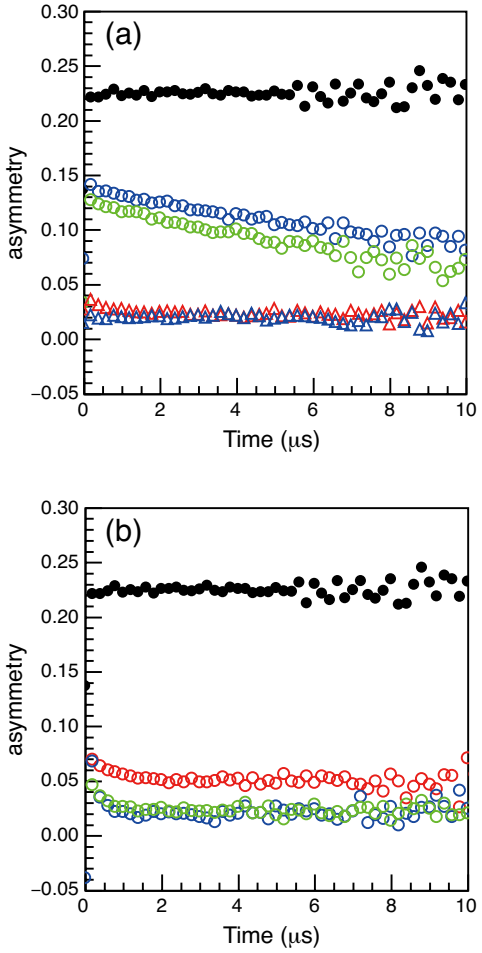

Fig. 3: The μSR spectra in the longitudinal field of 100 Gauss for (a) $EuLiCaAlF_6$ (green), $CeLiCaAlF_6$ (blue/circle), BaF_2 (red), MgF_2 (blue/triangle) and (b) LYSO (red), GAGG(blue), and La-GPS (green). Black dots are the e^+ asymmetry using a Ag material, which corresponds to the 100% level. The diamagnetic fraction in CeF_3, $CeLiCaAlF_6$, and $EuLiCaAlF_6$ at room temperature is significantly high, but it is not the case for muons in MgF_2 and BaF_2.

References

[1] J. J. Sakurai, Phys. Rev. **109** (1958) 980–983.

[2] S. Shimizu *et al.*, Nucl. Instrum. Methods. Phys. Res. A. **945** (2019) 162587(1-4).

[3] J. H. Brewer *et al.*, Phys. Rev. B **33** (1986) 7813–7816.

Investigation on Magnetic Ground state and Spin Dynamic of $Nd_2Ru_2O_7$ [J-PARC: 2020A0210]

U. Widyaiswari[1,2], H. Sakai[3], N. Hanasaki[3], D. P. Sari[4], B. Kurniawan[2], and I. Watanabe[1,2]

[1]*Meson Science Laboratory, RIKEN Nishina Center for Accelerator-Based Science*
[2]*Department of Physics, Universitas Indonesia*
[3]*Department of Physics, Graduate School of Science, Osaka University*
[4]*Innovative Global Program, Shibaura Institute of Technology*

Pyrochlore oxides, $A_2B_2O_7$, with A is a trivalent rare-earth ion and B is a tetravalent transition metal ion. Either magnetic or non-magnetic ions occupy the A and B sites. A pyrochlore lattice constructed from the interpenetrating corner-sharing tetrahedral lattices of A and B sites [1]. Spins at vertices of the tetrahedral lattice are magnetically frustrated and can lead to various novel physical properties, such as the spin-glass, spin-ice, and spin liquid states [1]. The magnetic frustration, competition between the exchange and dipolar interactions, and the crystal electric field effect control the nature of the ground state of the pyrochlore oxide [2]. The pyrochlore oxides with an Ising anisotropy have spins that point in to or out from the center of the tetrahedral lattice. They have a spin-ice ground state with a 2-in-2-out spin configuration when the ferromagnetic (FM) dipolar interaction dominates, while an all-in-all-out (AIAO) ordered state occurs when the antiferromagnetic (AFM) exchange interaction dominates [2,3].

Pyrochlore ruthenate, $A_2Ru_2O_7$, has $4d^4$ electrons of Ru in the low-spin state with $S = 1$. One of the pyrochlore ruthenate systems, $Nd_2Ru_2O_7$, has potential as a candidate of the electrocatalyst material for hydrogen production [4]. In $Nd_2Ru_2O_7$, both Nd and Ru are magnetic ions. $Nd_2Ru_2O_7$ showed magnetic anomalies around 1.8 K, 21 K, and 146 K [5-7]. The anomalies at 1.8 K and 146 K are argued to be due to the magnetic ordering of Nd and Ru moments, respectively [5]. On the other hand, the anomaly at 21 K is suggested to be coming from the impurity component of Nd_3RuO_7 and is still debatable [7]. Accordingly, we investigated the magnetic properties of $Nd_2Ru_2O_7$ by using various measurement techniques, including muon spin relaxation (μSR) measurement. In this report, we show the result of the μSR measurement to confirm the magnetic ground state of $Nd_2Ru_2O_7$.

$Nd_2Ru_2O_7$ polycrystalline sample was prepared by using a solid-state reaction method. The μSR experiments were carried out in the HiFi spectrometer at ISIS, UK and ARTEMIS spectrometer at Material and Life Science Experiment Facility (MLF), J-PARC. We measured the μSR time spectra in the zero-field (ZF) condition at a temperature range of 2 – 150 K at HiFi. To confirm the magnetic transition of Nd spin that was expected to occur below 2 K, we measured the time spectra below 5 K down to 0.3 K by using Heliox cryostat at ARTEMIS.

The time spectra showed no oscillation, as shown in Fig. 1. However, there is a decreasing of initial asymmetry at $t = 0$ in the time spectra with decreasing temperature. It indicates the appearance of a magnetic ordered state. The time spectra were analyzed by using two exponential functions.

$$A(t) = A_1 e^{-\lambda_1 t} + A_2 e^{-\lambda_2 t} \quad (1)$$

The first and second component of Eq. (1) corresponds to the slow and fast components of muon spin relaxation, respectively. λ_1 and λ_2 are the slow and fast muon-spin relaxation rates. The temperature dependence of the best fit parameter is shown in Fig. 2.

The temperature dependence of λ_2 showed a sharp peak around $T_{N1} = 145$ K corresponds to the magnetic ordering of Ru spins. The λ_1 seems to be temperature independent below 140 K down to 50 K. It decreases below 50 K and gradually increases again below 30 K, make a dip around 30 K. This anomaly is not related to the anomaly at 21 K observed from DC susceptibility measurement which is expected to be due to the magnetic property of Nd_3RuO_7 [8]. We confirmed that our sample

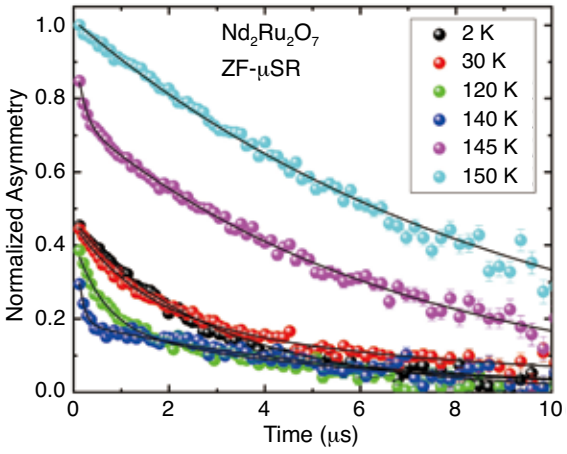

Fig. 1: The ZF-μSR time spectra of $Nd_2Ru_2O_7$.

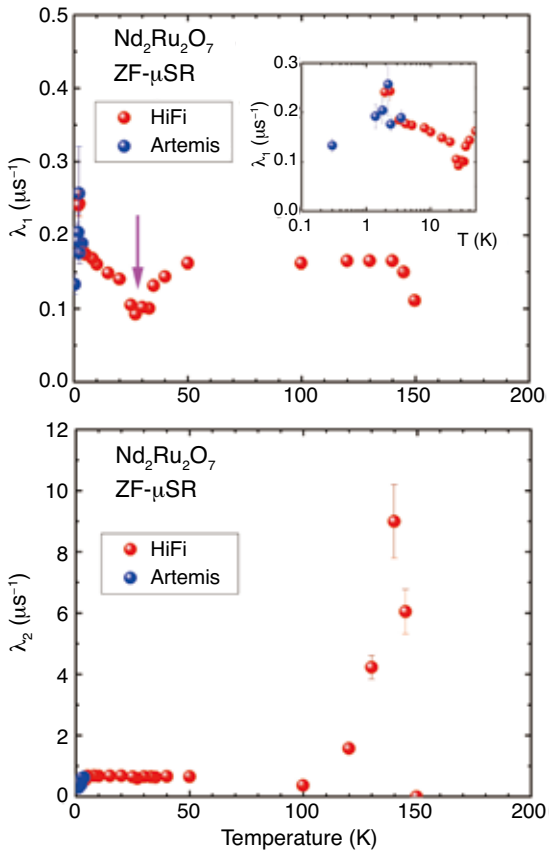

Fig. 2: Temperature dependence of slow and fast muon-spin relaxation rate.

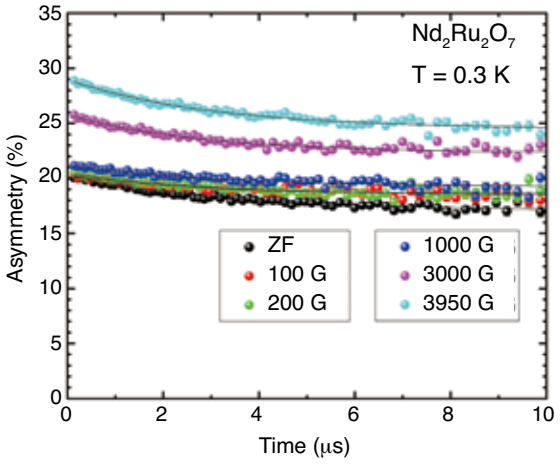

Fig. 3: A figure file is included in a manuscript.

has high purity based on a Rietveld refinement analysis on the XRD pattern. Furthermore, there is no clear anomaly around 21 K from DC susceptibility and heat capacity data of our $Nd_2Ru_2O_7$. In that case, the anomaly around 30 K in the temperature dependence of λ_1 could be related to the short-range magnetic interaction of Nd spins. The long-range ordering of Nd spins was observed around $T_{N2} = 2$ K indicated by a peak in the temperature dependence of λ_1.

The λ_1 did not vanish below T_{N2} and remains down to 0.3 K. It indicates the appearance of remaining spin fluctuation in the ordered state. Such kind of behavior occurs in other Nd-based pyrochlores [9,10]. In order to investigate the spin dynamics of Nd spins below T_{N2}, μSR time spectra were measured in the longitudinal field (LF) condition. The relaxation of muon spins is observed in the time spectrum measured under 3950 G external field at 0.3 K as can be seen in Fig. 3. We expected that it is to be due to the persistent fluctuating spins. Accordingly, we suggest that the Nd spin was divided into two parts, the static ordered state and the fluctuating spin, that coexist below the transition temperature down to 0.3 K.

References

[1] J. S. Gardner *et al.*, Rev. Mod. Phys. **82** (2010) 53–107.

[2] B. C. den Hertog and M. J. P. Gingras, Phys. Rev. Lett. **84** (2000) 3430–3433.

[3] J. Xu *et al.*, Phys. Rev. B **92** (2015) 224430(1-12).

[4] M. Kim *et al.*, ACS Cent. Sci. **6** (2020) 880–891.

[5] S. T. Ku *et al.*, J. Phys.: Condens. Matter **30** (2018) 155601(1-11).

[6] S. W. Chen *et al.*, Phys. Chem. Chem. Phys. **17** (2015) 23667–23673.

[7] M. W. Gaultois *et al.*, J. Phys.: Condens. Matter **25** (2013) 186004(1-10).

[8] U. Widyaiswari *et al.*, Mater. Sci. Forum **1028** (2021) 3–8.

[9] J. Xu *et al.*, Phys. Rev. B **94** (2016) 064425(1-8).

[10] V. K. Anand *et al.*, Phys. Rev. B **95** (2017) 224420(1-9).

Generation of Ultra Cold Muonium into Vacuum [J-PARC: 2020A0253 / 2020B0363]

A. D. Pant, K. Ishida[1], S. Matoba, N. Kawamura, A. Koda, S. Nishimura, and K. Shimomura

Muon Science Laboratory, Institute of Materials Structure Science, KEK
[1]*Meson Science Laboratory, RIKEN Nishina Center for Accelerator-Based Science*

Muonium is the bound state of a positive muon and an electron (Mu = μ^+e^-), and it acts as a light isotope of hydrogen. A material with low thermal energy that facilitates the production of ultracold muonium (UCMu) would be advantageous as a source of Mu used in the generation of ultraslow muon beams [1] with many applications in nanotechnology and understanding hydrogen dynamics. A new Mu source material that can be operated near 20 K would reduce the energy spread of an ultraslow muon beam by 100 times compared to that of existing hot tungsten source [1,2], which operates near 2000 K. The UCMu will aid in the achievement of a coherent and low-energy spread ultraslow muon beam for the studies in nanoscience, surface science, three-dimensional material imaging, the muon g-2 experiment, and in innovative instrumentation technology being developed in the Japan Proton Accelerator Research Complex (J-PARC), Japan, such as the transmission muon microscope and ultraslow muon microscope [3,4]. For the purpose of Mu production source material, a solid sample is preferred.

For the Mu production target, there are several studies found in literatures, and so far two candidates – tungsten at 2000 K [1,2] and laser ablated silica aerogel at room temperature [5] – show the highest yield among solid materials. In our study, we focus on the generation of UCMu at low temperatures (below room temperature). We plan to perform this study in two steps – first of all identify the materials which can emit the Mu and second step is to measure the space-time distribution of emitted UCMu from the materials [6]. In current experiments, we performed the first step.

As the first material, we chose n-Si in which large fraction of mobile tetrahedral Mu (61%) was reported previously [7] but no information was available about its emission from surface at low temperature. The difference in relaxation rate of Mu formed at deep inside of the sample and that formed near surface when the Ag sheet set down-stream (d = 0 mm) pointed out the possibility of emission of UCMu [8]. In these beamtime experiments, we performed distance dependent study at low temperatures in n-Si and a test experiment in SiC.

Muon behaves as a light proton ($m_\mu \sim 1/9\ m_\mathrm{p}$) and acts as a sensitive probe of the materials. Depending on the properties of the material, the incident muon can capture an electron and form Mu. Similar to the H-acceptor in n-type and donor in p-type materials [9], muons can form different charge states based on samples. As Mu is around one hundred times more sensitive to the magnetic field than the muon, the Mu signal can be easily distinguished from that of the muons regardless of the charge states. The muon spin rotation and relaxation (μSR) measurements were performed on n-type Si wafer (diameter 50 mm, thickness 400 μm, orientation (100), resistivity > 1000 Ω-cm) commercially available from Suzuki Shokan, Japan, using surface muon beam ($\sim$ 27 MeV/c) at S1-line, MLF, J-PARC, in temperature range 5 K to 300 K in vacuum. A silver sheet (300 μm) was set downstream to the Si. The distance between Si and silver sheet (d) was varied (d = 0, 1, 3.1, 20 mm). The sample was connected to Helium gas flow cryostat head via a silver holder [Fig. 1] in vacuum ($\sim 10^{-5}$ Pa). First of all, scan of muon beam momentum was performed to achieve two conditions – to stop all muons deep inside from the rear surface of the Si (hereafter full-stop case), and to stop half of the muons in the Si and remaining half in silver sheet set downstream (hereafter half-stop case). Then the temperature dependent (5 K–300 K) study was performed under 1.2 G transverse magnetic field at both momentum cases. By designing new sample holder of silver [Fig. 1], we have solved the temperature stability problem that we reported in last year [Fig. 2b of ref. 10].

The relaxation rate of Mu with temperature at different distances is presented in Fig. 2 (a, b, c). In d = 1 mm, 3.1 mm and 20 mm, the similar difference pattern is observed. If the Mu is emitted from rear surface, the relaxation rate at 20 mm is expected to be different from that with d = 0 mm or d = 1 mm. At d = 20 mm case, even if Mu can emit from Si, they cannot reach Ag sheet due to low

Fig. 1: Images of new sample holder to remove the problem of thermal contact. With this holder, we can cool the sample to 5 K. Left image shows Si sample facing towards muon beam and right image shows the silver sheet in rear side and thermal sensor nearby by the silver and sample.

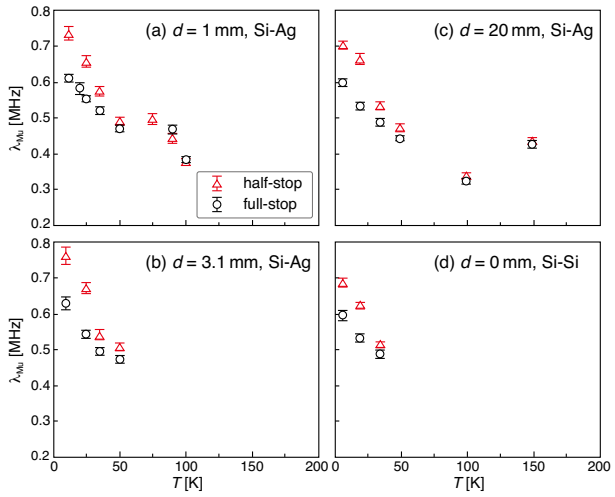

Fig. 2: Relaxation rate of Mu in full-stop and half-stop cases at $d = 1$ mm (a), 3.1 mm (b), and 20 mm (c). The relaxation rate of Mu with two wafers stuck together ($d = 0$ mm).

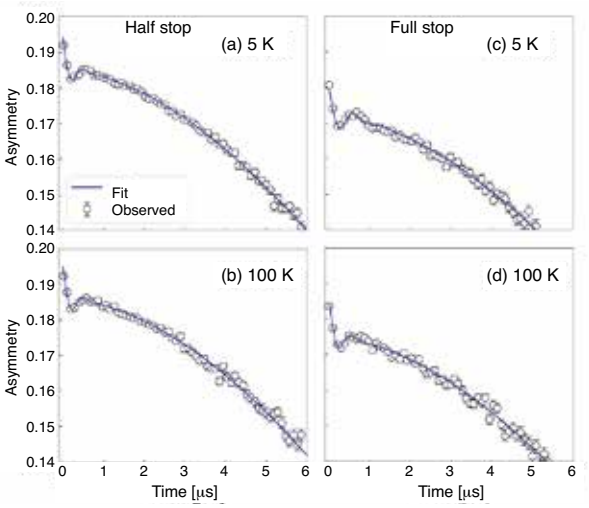

Fig. 3: Muon and Mu spin precession time spectra in SiC at TF 1.2G. (a) half-stop at 5 K, (b) half-stop at 100 K, (c) full-stop at 5 K and (d) full-stop at 100 K. The lines represent the fitted function Eq. (1).

thermal energy and average velocity (1.3 meV, 1.5 mm/μs at 10 K). To understand this point, we have performed the measurement with two n-Si wafers sticked together ($d = 0$ mm). The relaxation of Mu in the case of two wafers is shown in Fig. 2(d).

In this case, the asymmetry of Mu increases in half-stop case however the difference in relaxation rate shows similar pattern to n-Si and Ag sheet $d = 0$ mm case. So the enhanced relaxation rate commonly occur in this n-Si sample whenever Mu is stopped near surface and is difficult to be interpreted as evidence of Mu emission in vacuum.

We have also performed the test measurement in SiC (four 10×10×0.3 mm pieces are tiled up, muon beam ϕ15 mm) using similar experimental set up as used for n-Si. The measurement was performed at $d = 0$ mm case only. The temperature dependent muon and Mu spectra were fitted by a function including both muon and Mu components as,

$$f(t) = A_\mu \exp(-\lambda_\mu t)\cos(\omega_\mu t + \phi_\mu) + A_{\rm Mu}\exp(-\lambda_{\rm Mu} t)\cos(\omega_{\rm Mu} t + \phi_{\rm Mu}) + B \quad (1)$$

where, B is the time-independent baseline. The terms Aμ and AMu are the amplitudes of the spin precession corresponding to the polarization of the μ^+ in diamagnetic states and Mu, respectively. The parameters λ_μ and $\lambda_{\rm Mu}$ are the muon and Mu relaxation rates, ω_μ and $\omega_{\rm Mu}$ are the muon and Mu precession frequencies, ϕ_μ and $\phi_{\rm Mu}$ are the initial phases of precessions of muon and Mu, respectively. The fitted time spectra are presented in Fig. 3.

The relaxation rates of Mu in full-stop and half-stop cases in SiC are presented in Fig. 4. The relaxation rates of Mu in full-stop case lie within error bar of that of half-stop case. It indicates that there is less possibility of emission of Mu from the SiC.

In conclusion, we have tested the emission of Mu from n-Si and SiC at low temperatures (5 K–300 K). The origin of difference in relaxation rate of Mu

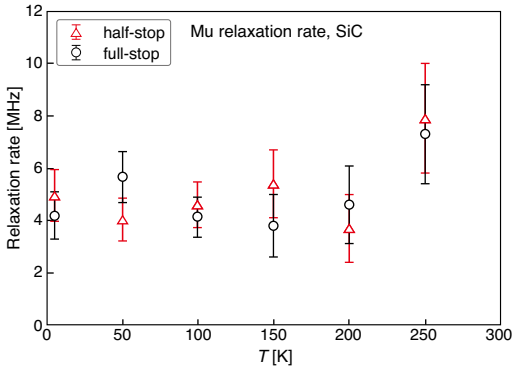

Fig. 4: Relaxation rate of Mu in full-stop and half-stop cases in SiC with $d = 0$ mm.

in full-stop and half-stop cases in n-Si may be due to enhanced relaxation of Mu stopping near rear surface. Further study will be performed in porous silica, KCl, chevron shaped microporous materials etc.

References

[1] K. Nagamine *et al.*, Phys. Rev. Lett. **74** (1995) 4811–4814.

[2] A. Mills *et al.*, Phys. Rev. Lett. **56** (1986) 1463–1466.

[3] Y. Miyake *et al.*, J. Phys.: Conf. Ser. **302** (2011) 012038(1-6).

[4] W. Higemoto *et al.*, Quantum Beam Sci. **1** (2017) 11(1-24).

[5] P. Bakule *et al.*, Prog. Theor. Exp. Phys. **2013** (2013) 103C01(1-10).

[6] G. A. Beer *et al.*, Phys. Rev. Lett. **57** (1986) 671–674.

[7] S. F. J. Cox, Rep. Progr. Phys. **72** (11) (2009) 116501(1-130).

[8] A. D. Pant *et al.*, Physica B **613** (2021) 412997(1-5).

[9] Chris G. Van de Walle and J. Neugebauer, Nature **423** (2003) 626–628.

[10] A. D. Pant *et al.*, KEK Prog. Rep. **2020-4** (2020) 52–53.

μSR Approach to the Understanding of Hydrogen Behavior in Pd-Cu Alloy with B2-type Crystal Structure [J-PARC: 2020A0286]

H. Yukawa, Y. Matsumoto[1], and W. Higemoto[2,3]

Department of Materials Design Innovation Engineering, Nagoya University
[1]*Department of Mechanical Engineering, National Institute of Technology, Oita College*
[2]*Advanced Science Research Center, JAEA*
[3]*Department of Physics, Tokyo Institute of Technology*

Pd-53 mol%Cu (PdCu40) alloy membrane with B2 type crystal structure is widely used practically for hydrogen separation and purification purposes [1]. This high hydrogen permeability, $\phi = D \cdot K$, is mainly attributable to the high hydrogen diffusivity in it. Recently, we have investigated the hydrogen permeability of PdCu40 (Pd-53 mol%Cu) alloy membrane over a wide temperature range below 623 K and found that the hydrogen permeability decreases significantly at lower temperatures, especially at room temperature (298 K).

The motivation for this research is to elucidate the mechanism of the significant decrease in hydrogen permeability at low temperatures and to obtain clues to achieve high permeability at low temperatures. If a PdCu alloy membrane is developed with high hydrogen permeability at low temperatures, we can expect new applications such as hydrogen releasing films [2] that can extract only hydrogen from sealed containers such as aluminum capacitors for power conditioners. However, the low hydrogen solubility of PdCu40 alloy makes it difficult to investigate the hydrogen behavior in the material.

The μSR experiment is a powerful technique for detecting hydrogen behavior in metals with such low hydrogen solubility. In the Pd-Cu system, the stoichiometric PdCu with Pd:Cu=1:1 does not exist in the equilibrium phase diagram, and nonstoichiometry expands toward Cu excess side. According to the positron annihilation experiments, it is suggested the excess Cu atoms occupy Pd sublattice of B2 structure so that unique local BCC-Cu units form around the Cu atoms at Pd site, that will provide different magnetic fields in PdCu alloy with B2 structure.

In this study, PdCu alloy with different degrees of excess Cu atoms, *i.e*, PdCu39 (Pd-51.5 mol%Cu) and PdCu47 (Pd-60 mol%Cu) alloys were examined. Cold-rolled sample foils were annealed at 573 K or 673 K to get B2 crystal structure, while the foils were heat-treated at 1073 K and quenched to get FCC crystal structure. Positron annihilation analysis indicates that the defect densities in these alloys are considered to be low. Schematic models of the local structure that the excess Cu atom occupying Pd sublattice for these two alloys are shown in Fig. 1. For PdCu39 alloy, 3% of Pd sites are substituted for Cu atoms, while excess Cu atoms occupy 20% of Pd sites in PdCu47 alloy.

The μSR experiments were performed in zero magnetic field (ZF) as well as in the external magnetic field of longitudinal fields (LF, 5∼30G) and transverse field (TF, 20 G). The temperature dependence of the spin relaxation was examined from about 5 K up to about 300 K.

Figure 2 shows the muon spin relaxation spectra observed in ZF at various temperatures for PdCu47 alloy with B2 structure. As shown in Fig. 2, the muon spin relaxation gradually became faster below about 100 K, suggesting that the muon diffusion gradually became slower with decreasing temperature.

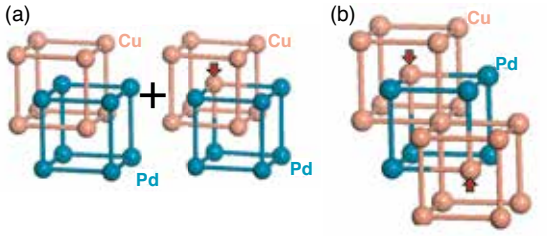

Fig. 1: Schematic models of local structure of Pd-Cu alloy, (a) PdCu39 and (b) PdCu47 alloys.

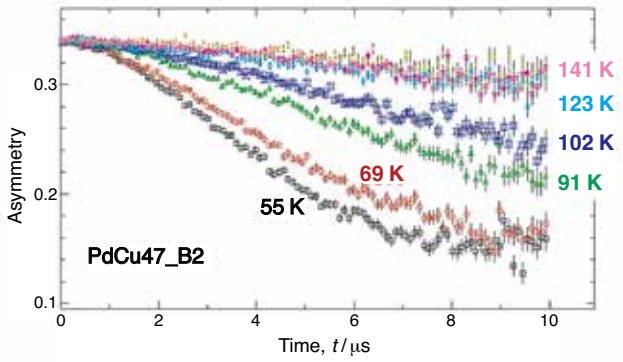

Fig. 2: Zero-Field muon spin relaxation spectra at various temperatures in PdCu47 alloy with B2 type crystal structure.

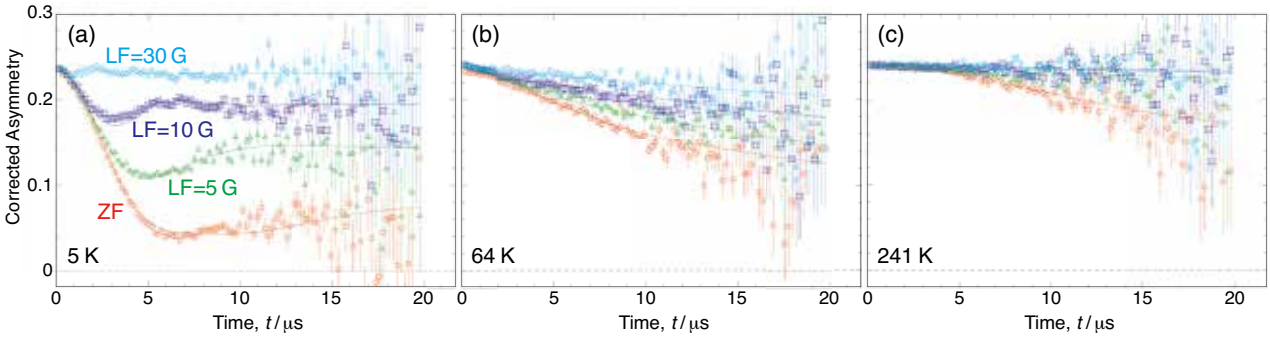

Fig. 3: μSR spectra for PdCu39 with B2 structure measured at (a) 5 K, (b) 64 K and (c) 241 K.

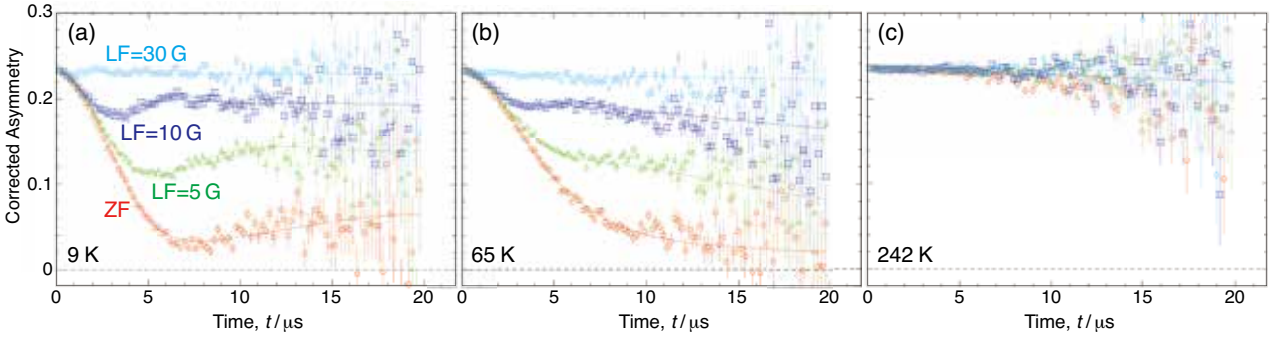

Fig. 4: μSR spectra for PdCu47 with B2 structure measured at (a) 9 K, (b) 65 K and (c) 242 K.

Figure 3 and 4 are the muon spin relaxation spectra observed in LFs at various temperatures for PdCu39 and PdCu47 alloys with B2 structure, respectively. These signals were analyzed by applying dynamic Kubo-Toyabe function, $A{\cdot}G_{KT}\ (\nu, \Delta, t)$, with a slow-relaxing component. It is found from the preliminal analysis that there is complex temperature dependence for the samples with B2 structure, suggesting that there exist multiple hydrogen sites in PdCu alloy with B2 structure, each showing some different temperature dependence.

It is noted that the muon spin relaxation spectra obtained from the samples with FCC crystal structure are different from the results for the samples with B2 crystal structure. For example, the temperature dependence of the fitting parameters is simpler for FCC structure than B2 structure, in agreement with our previous work [3], indicating that the dynamic behavior of the muon in B2 crystal is quite different from that in FCC crystal.

Further investigations of the spectrum are in progress. First-principle calculations on the diffusion barrier and potential energy of hydrogen at various interstitial sites are underway. The distribution of the magnetic field from Cu nuclear is also being examined. Comparing these results with μSR experiments, it is expected to improve our understanding of the hydrogen behavior in PdCu alloys.

References

[1] A. G. Knapton, Platin. Met. Rev. **21** (1977) 44–50.

[2] T. Fukuoka *et al.*, US Patent No. 10,374,202.

[3] H.Yukawa *et al.*, KEK Progress Report **2020-4** (2020) 79–80.

Hyperfine and Thermal Properties of a Muonium Defect in Ferroelectric PZT
[J-PARC: 2020A0288]

T. U. Ito[1,2], W. Higemoto[1,2,3], A. Koda[2,4], and K. Shimomura[2,4]

[1]*Advanced Science Research Center, JAEA*
[2]*Muon Science Section, MLF division, J-PARC Cente*
[3]*Department of Physics, Tokyo Institute of Technology*
[4]*Muon Science Laboratory, Institute of Materials Structure Science, KEK*

PZT, or lead zirconate titanate ($PbZr_xTi_{1-x}O_3$), is a ferroelectric perovskite material that shows excellent piezoelectric, insulating, and dielectric properties. Since its first synthesis around 1952 [1], PZT has been used in a variety of practical applications such as piezoelectric devices, ultrasonic transducers, and capacitors. Compared to another ferroelectric perovskite of barium titanate ($BaTiO_3$), PZT exhibits greater electromechanical properties and has a higher operating temperature. Optimum piezoelectric properties can be obtained at $x \sim 0.52$, the composition of a morphotropic phase boundary of two ferroelectric phases.

Hydrogen is a ubiquitous impurity and can incorporate into the crystalline lattice of functional materials when they are synthesized and/or integrated into devices. The impact of hydrogen on the physical properties of host materials is often not negligible despite its low concentration. Indeed, a hydrogen-induced increase in leakage current was reported in PZT [2], suggesting that hydrogen donates electron carriers. Hydrogen can also cause unignorable degradations in dielectric, ferroelectric, optical, and mechanical properties of PZT. Therefore, a detailed understanding of "unintentionally doped" hydrogen is important for many applications of PZT.

We proposed μ^+SR measurements of $PbTiO_3$ and $PbZrO_3$, the end compounds in the PZT phase diagram, to elucidate the hyperfine and thermal properties of isolated hydrogen defects in PZT by studying muonium analogs formed upon implantation of μ^+. In addition to the practical importance, the electronic structure of muonium defects in PZT is also interesting from an academic point of view. We recently found a Mu^+ donor-bound Ti^{3+} small polaron, a new type of muonium-related paramagnetic center, in the $SrTiO_3$ perovskite [3]. We were interested in whether or not a similar polaronic center is formed in the end compounds of PZT, which commonly have the (distorted) perovskite structure, but have a clear difference in the multivalency of the transition metal ions. This study therefore would provide a clue for understanding the formation mechanism of the Mu^+-bound small polaron in perovskite transition metal oxides.

Pulsed μ^+SR measurements on $PbTiO_3$ and $PbZrO_3$ were performed in the S1 area, MLF, J-PARC using a spin-polarized surface muon beam. Powder samples of $PbTiO_3$ and $PbZrO_3$ were formed into pellets and wrapped with aluminum foil. The sample pellets were mounted on a silver cold finger of a conventional ^{4}He flow cryostat. Time-differential μ^+SR data were taken with the ARTEMIS μSR spectrometer in the temperature range 5-300 K under a zero applied field (ZF), transverse fields (TFs), and longitudinal fields (LFs).

Figure 1 shows comparisons of TF-μ^+SR spectra under 20 G at low temperature blow 10 K and room temperature for (a) $PbTiO_3$ and (b) $PbZrO_3$.

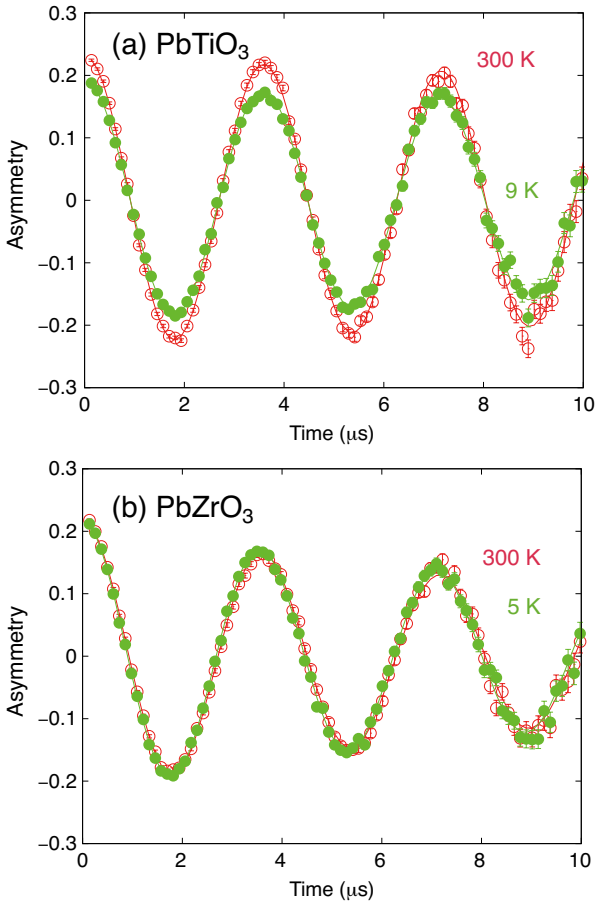

Fig. 1: Comparisons of TF-μ^+SR spectra under 20 G at low temperature blow 10 K and room temperature for (a) $PbTiO_3$ and (b) $PbZrO_3$.

A drop in initial asymmetry is clearly identified in the low temperature spectrum of $PbTiO_3$, indicating the formation of a muon-related paramagnetic defect, most probably, the Mu^+-bound Ti^{3+} small polaron. On the other hand, no asymmetry drop was observed in $PbZrO_3$, which excludes the possibility of the small polaron-like electron localization at the nearest neighbor Zr site as well as the formation of atomic muonium. This is consistent with the fact that the Zr ion does not readily form valence states other than Zr^{4+}.

We performed LF decoupling measurements at 15 K for $PbTiO_3$ to identify the polaronic defect. The LF decoupling curve shows a kink-like anomaly at around 0.15 T, which indicates that a dipolar coupling term dominates in the hyperfine spin Hamiltonian for the paramagnetic defect [4]. Such a situation is consistent with the Mu^+-bound Ti^{3+} polaron picture where the center of gravity of the spin density distribution is displaced from the muon position. The muon-electron distance is estimated to be about 2 Å from the dipolar coupling constant obtained from the LF decoupling curve. The activation energy for the thermal dissociation of the Mu^+-Ti^{3+} complex was roughly estimated to be 0.1 eV from the temperature dependence of the initial asymmetry drop.

In our experiments, the Mu^+-bound small polaron was observed only in the $PbTiO_3$ phase, which reflects that the multivalency of the transition metal ion is an important factor in forming the polaronic defect. This suggests that a similar Mu^+-Ti^{3+} polaronic complex may form in PZT with optimal piezoelectric properties ($x \sim 0.52$) as well.

References

[1] G. Shirane and K. Suzuki, J. Phys. Soc. Jpn. **7** (1952) 333.

[2] H. Y. Huang *et al.*, J. Am. Ceram. Soc. **90** (2007) 2062–2066.

[3] T. U. Ito *et al.*, Appl. Phys. Lett. **115** (2019) 192103(1-4).

[4] S. F. J. Cox *et al.*, Physics Procedia **30** (2012) 82–85.

Temperature Dependent μSR Study in Water [J-PARC: 2020A0298]

A. D. Pant, A. Koda, and K. Shimomura

Muon Science Laboratory, Institute of Materials Structure Science, KEK

We have been applying muon spin rotation and relaxation (μSR) method to understand the life phenomena. In order to understand the electron transfer mechanism in a single active center copper protein – Pseudoazurin (PAz) using the μSR method, we have performed μSR measurements in reduced and oxidized form of PAz [1]. In the preliminary study, we found the zero field (ZF) oscillation signal in reduced PAz and water however no such oscillation was observed in oxidized one. To understand the origin of ZF oscillation, we focus on the temperature dependent μSR study in the water before continuing the biosamples.

Since more than four decades, μSR measurements in water have been reported by several groups [2,3,4]. After first detection of muonium ($Mu = \mu^+e^-$) in water [2], μSR studies to understand the formation, depolarization, missing fraction and hyperfine interaction of Mu in water and ice were reported. In water, Mu relaxation is caused by interaction of Mu with paramagnetic species and the spin conversion. With regard to missing fraction, the 60% of incident muon formed as diamagnetic form, 20% as Mu and remaining as missing fraction is reported [5]. On the other hand, in ice, nearly 50% of incident muon is formed in diamagnetic form and remaining as Mu with almost negligible missing fraction. The interaction of Mu with transient paramagnetic species like hydrated electron, hydroxyl radical and hydrogen atom (even small extent) formed by radiolysis of water are responsible factors for the missing fraction in water [5]. The hyperfine interactions/frequencies of Mu in water were observed due to anisotropy of axial symmetry in the muonium hyperfine interaction. The amplitude of splitting frequency of Mu depends on the angle between applied field and crystal *c*-axis of ice. And the splits of frequencies of Mu at low transverse field (TF) is observed due to small anisotropy of axial symmetry in the Mu hyperfine interaction. From level crossing resonance measurements in ice, Cox *et al.* reported the increase of fraction of muon with temperature and pointed out two diamagnetic states of muon in ice [4]. Similarly, quantum diffusion of Mu in Ih even until 8 K is reported by Markland *et al.* [6]. Most of previous studies were focused on muonium chemistry or muonium behavior in water and ice. The temperature dependent behavior of muon in water is not clearly understood yet. Since the muon and Mu behave differently with materials, it is necessary to understand the behavior of muon in water and ice.

The μSR experiments were performed in S1-line, MLF using surface muon ($\sim$ 4 MeV). Water (8.5 mL) collected from Milli-Q (Advantage A10 system) water purification system was sealed in aluminum (Al) cell (volume 10 mL) which is connected to Helium cryohead during measurement. The muon beam (20 mm collimeter) incident on water through the Al windows (thickness 0.1 mm, diameter of cross-sectional area of water 43 mm) placed in high vacuum chamber ($\sim 10^{-5}$ Pa). The ZF, TF 2.3 G and TF 20 G measurements were performed at different temperatures.

The TF 2.3 G data were fitted by using a fitting function which includes muon and muonium components. The spin rotation spectra of Mu superposed with that of muon. Figure 1 shows the temperature dependent relaxation of Mu in water (ice) which shows qualitative agreement with that in single crystal of ice [7]. To estimate the fraction of diamagnetic muon in water and ice, TF 20 G measurements were performed at different temperatures. Considering the full asymmetry of muon as 23% in S-line, the fraction of muon (initial asymmetry from fitted data of TF 20 G) is presented in Fig. 2, which agrees well with Cox *et al.* [4] and Percival *et al.* [5].

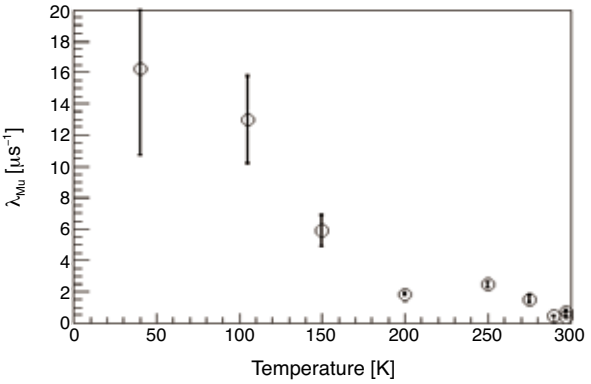

Fig. 1: Temperature dependent relaxation rate of Mu in water and ice which shows agreement with previously reported data of Percival *et al.* [7].

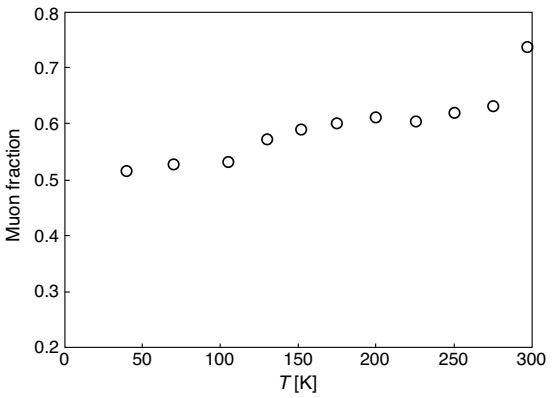

Fig. 2: Fraction of diamagnetic with temperature in water and ice which agrees well with Cox *et al.* [4] and Percival *et al.* [5].

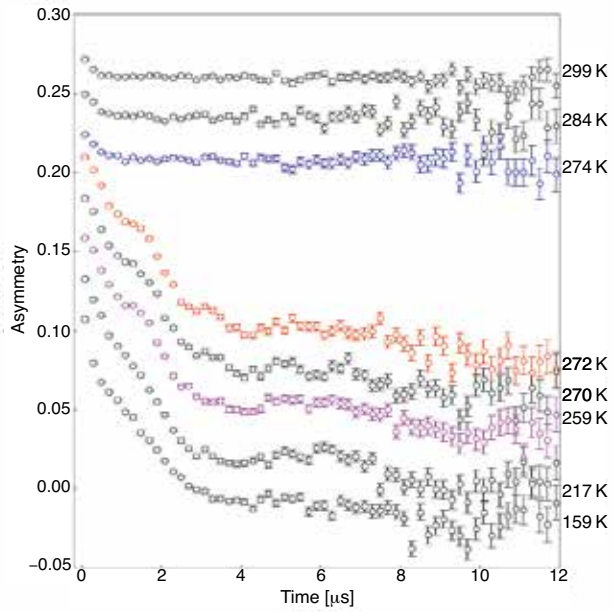

Fig. 3: ZF spectra in water and ice. Clear oscillation is observed in ice which disappeared around/below 150 K.

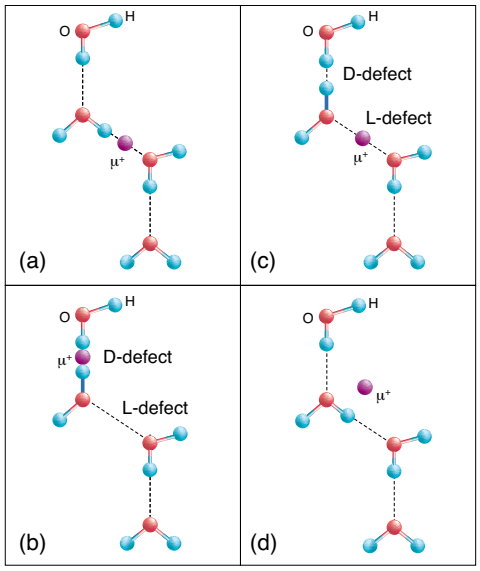

Fig. 4: Schematic diagram for stopping site of muon in defective and without defect hexagonal ice. Red ball, blue ball and purple ball are used for oxygen, hydrogen and muon, respectively.

The ZF spectra at different temperatures are presented in Fig. 3. In water phase there is no oscillation however in ice phase, clear oscillation is observed. The oscillation signal depolarized with decreasing temperature and almost disappeared around 150 K. Generally, the oscillation is appeared in magnetic ordered materials [8] but the water is not such sample. Following the interpretation of Brewer *et al.* [9] the oscillation in ZF is also found due to spin dipole interaction between muon and nearby spin-half particles/nuclei. In the ice at pressure (around 10^{-5} Pa) and different temperatures, the phase should be hexagonal ice (Ih) and IX [10]. The oscillation in ZF is observed only in Ih phase. To derive the polarization function, we have been performing DFT calculations in Ih ice and solving spin dipole interaction between muon and protons around stopping site of the muon.

To understand the muon behavior in Ih, we have been estimating the stopping site of muon in different sites following the ice rules and defects [Fig. 4]. There are two ice rules [11] - (1) two H atoms are joined with O through covalent bond, (2) one H atom remains between two O vertices in Ih ice. The violation of one of the ice rules creates defects in ice. Ionic defects can be created by violation of first rule and Bjerrum defects (D-defect and L-defect) can be created by violation of second rule. When there is no H atom between two O, it is called as L-defect and if there are two H between two O, it is called as D-defect [12]. Especially D- and L-defects are created by orientation of water molecules. As shown in schematic diagram Fig. 4, some possibilities of stopping sites of muon are mentioned. Fig. 4(a) shows possibility of formation of D-type defect after stopping of muon between O and H in without defect Ih. Fig. 4(b) and (c) are corresponding to stopping of muon in D-defect and L-defect, respectively. There is another possibility which may not follow neither L nor D-defect but muon stops in the position at equal distance from three protons.

In summary, we have observed the oscillation in ZF spectra in freezed water (ice). The origin of oscillation may be due to coupling of muon spin with nearby protons spin. The detail analysis is in progress. Furthermore, molecular oxygen contained in the water sample may affect the oscillation spectra which is our future work.

References

[1] A. D. Pant *et al.*, KEK Prog. Rep. **2020-4** (2020) 112–113.

[2] P. W. Percival *et al.*, Chem. Phys. Lett. **39** (1976) 333–335.

[3] K. Nagamine *et al.*, Chem. Phys. Lett. **87** (1982) 186–191.

[4] S. F. J. Cox *et al.*, Hyperfine Interact. **86** (1994) 747–752; S. F. J. Cox *et al.*, Hyperfine Interact. **65** (1991) 993–1003.

[5] P. W. Percival *et al.*, Chem. Phys. **32** (1978) 353–367.

[6] T. E. Markland *et al.*, J. Chem. Phys. **128** (2008) 194506(1-11).

[7] P. W. Percival *et al.*, Hyperfine Interact. **18** (1984) 543–550.

[8] L. P. Le *et al.*, EPL **15** (1991) 547–552.

[9] J. H. Brewer *et al.*, Phys. Rev. B **33** (1986) 7813–7816.

[10] T. Bartels-Rausch *et al.*, Rev. Mod. Phys. **84** (2012) 885–944.

[11] J. D. Bernal and R. H. Fowler, J. Chem. Phys. **1** (1933) 515–548.

[12] N. Bjerrum, Science **115** (1952) 385–390.

Dynamics of Polymers at Solid Interface Revealed by Muon Spin Relaxation Technique [J-PARC: 2020B0096]

H. Aoki[1,2], S. Takeshita[1], and T. Kayana[3]

[1]*Neutron Science Division, Institute of Materials Structure Science, KEK*
[2]*Materials and Life Science Division, J-PARC Center, JAEA*
[3]*Kyoto University*

Recent works on polymer materials showed that there exists "bound layer" at the substrate interface in a polymer film, where the polymer chain is tightly bound to the substrate. Because such the bound chain directly affects the adhesion phenomenon between the adhesive polymer and adherend material, the properties of the bound chain attracts much attention. However, because the bound layer with a thickness less than 10 nm has been difficult to be observed, much remains unknown about the fundamental properties such as the conformation and dynamics of the polymer chain in the bound layer. The objective of the current work is to clarify the chain dynamics in the μs - ms range by a muon spin relaxation (μSR) technique. The sample volume of the bound layer at the interface is very small; therefore, our approach is to use a nano-particle dispersed polymer system as a sample. The polymer chain within several nm from the surface of the particle is in "the interface region". The increase of the amount of the particle and decrease of the particle size results in the increase of the total amount of the interface region in the sample. The fraction of the interface region is estimated to be 20 – 30% when the particle with a size of 50 nm is dispersed at the weight fraction of 50%, resulting in the comparable signals from bulk and interface regions. The final objective of this study is to discuss the polymer dynamics of the interface by separating the signals from the bulk and interface regions. This proposal was approved as a P-type experiment to explore the feasibility of this project; therefore, we conducted the μSR measurement to examine the dynamics of the bulk region as a preliminary information.

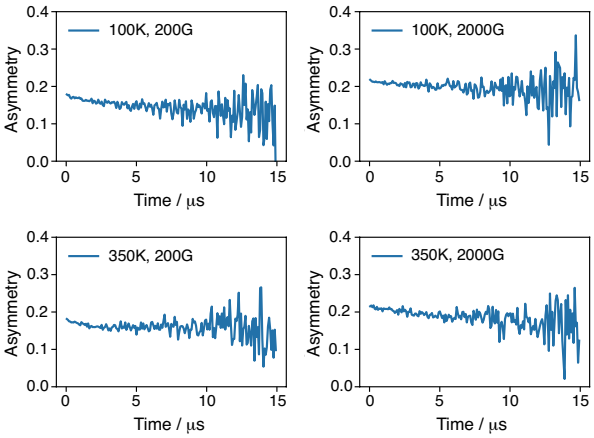

Fig. 1: Asymmetry decay curves at 100 and 350 K in LF of 200 and 2000 G

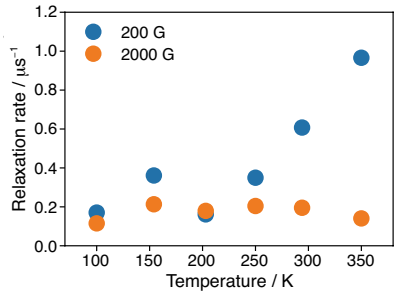

Fig. 2: Temperature dependence of the relaxation rate in LF of 200 and 2000 G

Poly(butyl acrylate) (PBA) was used as a sample, which is widely used as a base component of pressure-sensitive adhesives. A sample piece of PBA with a size of 30 × 30 × 2 mm^3 was measured at the S1 beam line using the surface positive muon beam in the longitudinal magnetic field (LF) from 10 to 3950 G. The temperature range of the measurement was 100 – 350 K.

Figure 1 shows the asymmetry decay in the LF of 200 and 2000 G at the temperatures of 100 and 350 K, indicating that the decay profile is dependent on the temperature and magnetic field. The asymmetry decay curves were fitted to a stretched exponential function,

$$A(t) = A_0 \exp(-(t/\tau)^{-\beta}) + A_\infty,$$

to evaluate the correlation time, $\langle\tau_c\rangle$, defined as $\langle\tau_c\rangle = (\tau/\beta)\Gamma(1/\beta)$. Figure 2 shows the temperature dependence of the relaxation rate, $\langle\tau_c\rangle^{-1}$, in LF of 200 and 2000 G. The relaxation rate in LF of 200 G was constant below 200 K and increased with the increase of the temperature above 250 K. The glass transition temperature of PBA is 220 K; therefore, the increase of the relaxation rate at the temperature higher than 250 K is attributed to the segmental motion of the PBA chain. On the other hand, the temperature dependence of the relaxation rate is not observed in LF of 2000 G. This is probably due to the difference between the frequency of the muon and dynamics of PBA. The further analysis of the LF dependence of the relaxation rate will be necessary to discuss the frequency dispersion of the dynamics of PBA.

Investigation of Superconducting Pairing in $(La_{0.5-x}Na_{0.5+x})Fe_2As_2$ [J-PARC: 2020B0111]

K. Iida, A. Iyo[1], H. Okabe[2], A. Koda[2], and R. Kadono[2]

Neutron Science and Technology Center, Comprehensive Research Organization for Science and Society, CROSS
[1]*National Institute of Advanced Industrial Science and Technology, AIST*
[2]*Muon Science Laboratory, Institute of Materials Structure Science, KEK*

1. Introduction

Recently, Iyo *et al.* reported that $(La_{0.5-x}Na_{0.5+x})Fe_2As_2$ can be a potential platform for both hole- and electron-doping by simply changing the composition value x [1, 2]. Contrary to conventional doped systems such as hole-doped $(Ba_{1-x}K_x)Fe_2As_2$ and electron-doped $Ba(Fe_{1-x}Co_x)_2As_2$, substitution at the A site in $(La_{0.5-x}Na_{0.5+x})Fe_2As_2$ can induce both electron and hole doping. $(La_{0.5}Na_{0.5})Fe_2As_2$ ($x = 0$) is a non-superconducting compound with structural and antiferromagnetic transition at $T_N = 130$ K. Since the valences of La and Na are 3+ and 1+, $(La_{0.5}Na_{0.5})Fe_2As_2$ shows properties similar to those of the 122 systems such as AFe_2As_2 [1]. By increasing x ($0.15 < x < 0.35$), the antiferromagnetic order is suppressed and $(La_{0.5-x}Na_{0.5+x})Fe_2As_2$ exhibits superconductivity due to hole-doping. The maximum $T_c = 27$ K was found with $x = 0.3$ [1]. On the other hand, only $LaFe_2As_2$ ($x = -0.5$) is synthesized and exhibits $T_c = 12$ K in the electron doping side [2]. As such, it is of particular interest to investigate the doping dependence of the superconducting paring symmetry in $(La_{0.5-x}Na_{0.5+x})Fe_2As_2$.

As is well established, muon spin rotation (μSR) is a powerful technique to determine the superconducting pairing symmetry and size of superconducting gap(s) by comparing the temperature dependence of penetration depth [$\lambda(T)$] with superconducting paring models since $\lambda^{-2}(T)$ is proportional to the effective superfluid density. Therefore, to fully understand the doping dependence of superconducting paring symmetry in $(La_{0.5-x}Na_{0.5+x})Fe_2As_2$, we performed μSR measurements on $(La_{0.5-x}Na_{0.5+x})Fe_2As_2$ for both the hole- and electron-doping sides.

2. Experimental details

Using the S1 beamline, we performed μSR measurements on polycrystalline $(La_{0.2}Na_{0.8})Fe_2As_2$ (x=0.3) and $LaFe_2As_2$ ($x = -0.5$) under transverse magnetic field (TF). For this experiment, we used the ^{3}He cyostat (Fig. 1) and measured dwon to 0.3 K.

Fig. 1: Photo of the ^{3}He cyostat installed at S1.

3. Results

Muon spin relaxation was observed above T_c due to muon spin flip by TF [Figs. 2(a) and 2(c)]. Upon cooling below T_c, vortex lattice is formed by eternal magnetic field, which makes further muon spin relaxation [Figs. 2(b) and 2(d)].

We first fit the TF-μSR time spectra as in Fig. 2. Temperature dependence of the muon spin relaxation rate σ was obtained for each sample (Fig. 3).

To evaluate the superconducting gaps, muon spin relaxation rate σ is converted to penetration depth via λ^{-2} (μm^{-2}) $= 11.656\sigma$ (μs^{-1}) after subtracting σ of the normal state as background. Temperature dependences of penetration depth after subtracting the penetration depth above T_c as background are plotted in Figs. 4(a) and 4(b). We then fit the temperature dependences of penetration depth using the following equations based on the multi-gap model [3]:

$$\lambda^{-2}(T) = \lambda^{-2}(0)\left[\omega\lambda^{-2}(T,\Delta_1) + (1-\omega)\,\lambda^{-2}(T,\Delta_2)\right]$$

$$\lambda^{-2}(T,\Delta_i) = 1 - \frac{2}{k_BT}\int_{\Delta_i(T)}^{\infty}\left(\frac{\partial f}{\partial E}\right)\frac{EdE}{\sqrt{E^2-\Delta_i^2(T)}}$$

where $f = [1+\exp(E/k_BT)]^{-1}$ and $\Delta_i(T) = \Delta_i \tanh\{1.82\,[1.018\,(T/T_c-1)]^{0.51}\}$. In the current moment, the fitting does not work well, and we are now trying to fix it.

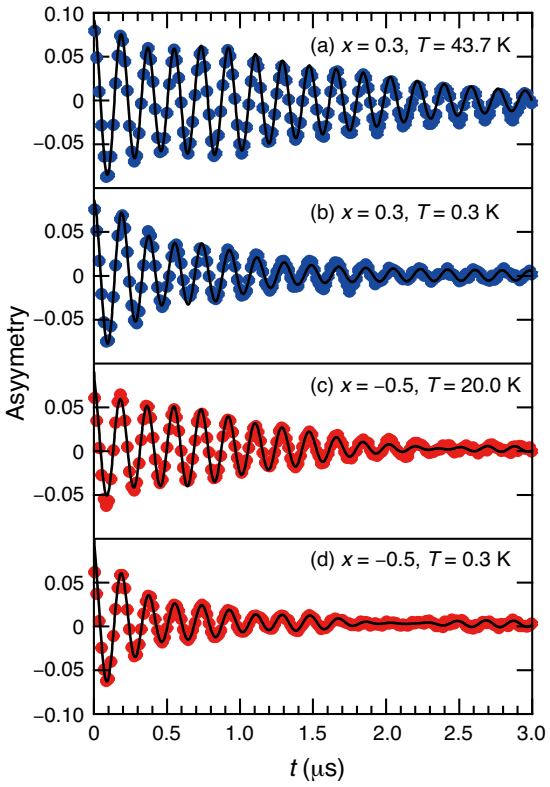

Fig. 2: μSR results on $(La_{0.5-x}Na_{0.5+x})Fe_2As_2$ measured at the S1 beamline. (a,b) μSR time spectra in $(La_{0.2}Na_{0.8})Fe_2As_2$ at (a) 43.7 K and (b) 0.3 K under $H = 400$ G. (c,d) μSR time spectra in $LaFe_2As_2$ at (c) 20.0 K and (d) 0.3 K under $H = 400$ G.

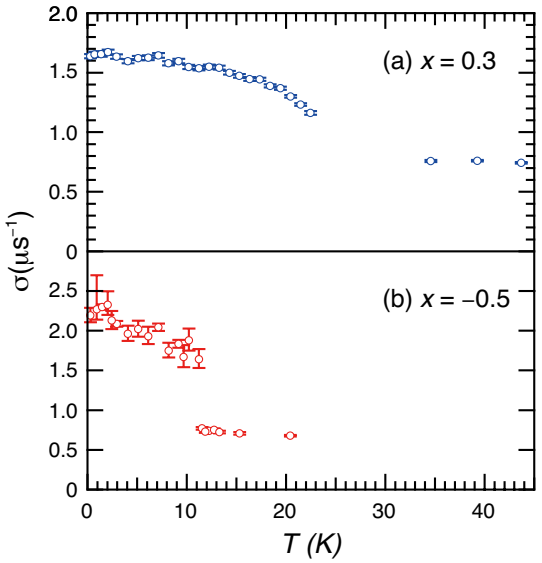

Fig. 3: Temperature dependences of the muon spin relaxation rate σ in (a) $(La_{0.2}Na_{0.8})Fe_2As_2$ and (b) $LaFe_2As_2$.

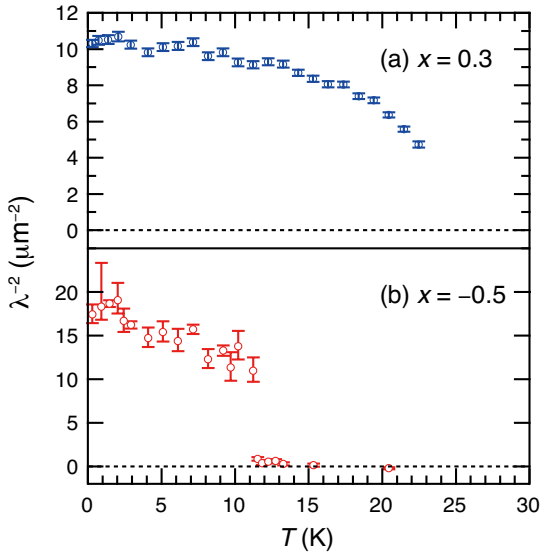

Fig. 4: Temperature dependences of penetration depth in (a) $(La_{0.2}Na_{0.8})Fe_2As_2$ and (b) $LaFe_2As_2$. Solid lines are fitting results described in the main text.

4. Summary

We performed TF-μSR measurements on polycrystalline $(La_{0.2}Na_{0.8})Fe_2As_2$ and $LaFe_2As_2$ using the S1 beamline, and will obtain the superconducting gaps for each compound.

References

[1] A. Iyo *et al.*, J. Am. Chem. Soc. **140**, (2018) 369–374.

[2] A. Iyo *et al.*, J. Phys. Chem. Lett. **10**, (2019) 1018–1023.

[3] P. K. Biswas *et al.*, Phys. Rev. B **95**, (2017) 140505(R)(1-5).

Interrelationship Between Na Dynamics and Microstructure in Hard Carbon as an Anode Material for Na-ion Battery [J-PARC: 2020B0252]

J. Sugiyama, K. Ohishi, D. Igarashi[1], R. Tatara[1,2], S. Komaba[1,2], S. Nishimura[3], and A. Koda[3]

Neutron Science and Technology Center, CROSS
[1]*Department of Applied Chemistry, Tokyo University of Science*
[2]*Elements Strategy Initiative for Catalysts and Batteries (ESICB), Kyoto University*
[3]*Muon Science Laboratory, Institute of Materials Structure Science, KEK*

1. Introduction

For the future Na-ion battery, the most common anode material for the current Li-ion battery, i.e., graphite and soft carbon are unavailable, because they are electrochemically inactive in Na insertion and extraction reactions. Instead, non-graphitizable carbon (hard carbon) is heavily investigated as an anode material for the Na-ion battery [1], because they are electrochemically active as a Na insertion host. However, the relationship between the structure of hard carbon and dynamics of Na insertion are still not fully clarified. We have therefore attempted to study the Na dynamics in C_xNa with μ^+SR.

2. Experimental

A C_xNa sample was synthesized by an electrochemical reaction between Na metal and a hard carbon anode sheet in a test cell. The anode sheet was prepared by casting the slurry, which consists of 85 wt% hard carbon, 10 wt% acetylene black, 2.5 wt% styrene-butadiene rubber, and 2.5 wt% sodium carboxymethyl cellulose, on 20 μm thick Al foil. The charged anode sheet was removed from a test cell and then three sheets were packed into a titanium cell in a He-filled globe box. The μ^+SR time spectra were measured on the surface muon beam line S1 at MUSE MLF in J-PARC. In order to extract the signal from the Al foil, the μ^+SR spectrum for the Al foil was also measured using a same setup to the sample. The recorded μ^+SR spectra were analyzed with musrfit.

3. Results

Figure 1 shows the temperature variation of the μ^+SR spectrum recorded in a zero field (ZF). Since the relaxation is suppressed with temperature, μ^+SR is most likely to observe Na diffusion in the sample, as in the case for C_6Li and C_{12}Li [2]. The ZF- and longitudinal field (LF-) μ^+SR spectra were fitted by a combination of three dynamic Kubo-Toyabe (KT) signals: that is, two from the C_xNa phase and one from the Al foil.

Figure 2 shows the temperature dependencies of the field distribution width (Δ) and the field fluctuation rate (ν) of the major KT component from C_xNa. This clearly shows the diffusive behavior of Na particularly above 150 K. In order to study the relationship between such diffusive behavior and the Na content in C_xNa, i.e., a state of charge (SOC), we plan to measure several C_xNa samples with different SOCs.

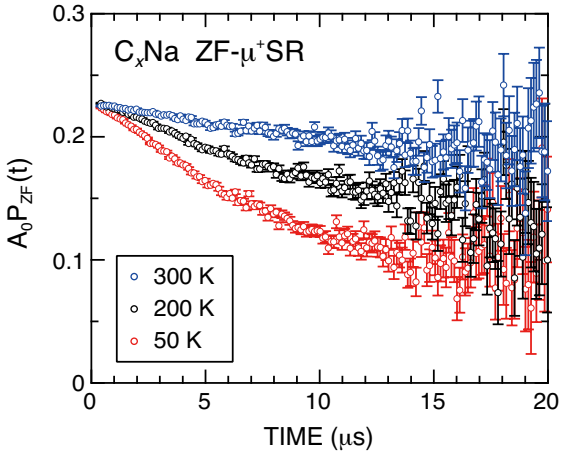

Fig. 1: The ZF-μ^+SR spectra for C_xNa recorded at 50, 200, and 300 K.

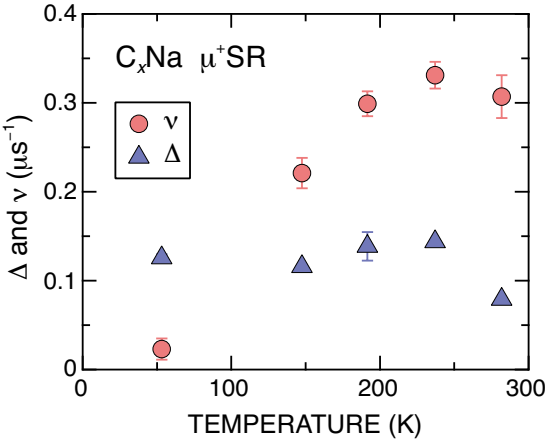

Fig. 2: The temperature dependencies of Δ and ν for C_xNa.

References

[1] K. Kubota *et al.*, Chem Mater. **32** (2020) 2961-2977.

[2] I. Umegaki *et al.*, Phys. Chem. Chem. Phys. **19** (2017) 19058-19066.

Detection of Functional Processes of Photoreceptive Proteins by Muon [J-PARC: 2020B0262]

T. Kiyotani, K. Inoue[1], I. Tanaka[2], F. Koyanagi[2], N. Niimura[2], J. G. Nakamura[3], M. Hiraishi[3], A. Koda[3], and H. Kandori[4]

Department of Pharmacy, Showa Pharmaceutical University
[1]*The Institute for Solid State Physics, The University of Tokyo*
[2]*Graduate School of Science and engineering, Ibaraki University*
[3]*Muon Science Laboratory, Institute of Materials Structure Science, KEK*
[4]*Department of Frontier Materials, Nagoya Institute of Technology*

μSR experiment is considered to be one of the most effective experimental techniques that can observe the details of proton and electron transfer by enzyme reaction in proteins at the atomic level. However, protein is too complicated, and there are many positions where the muons are captured in protein. It is difficult to judge whether μSR observation results are truly attributed by the intrinsic function of the protein. The functional correlation of the μ SR observation has been always question. To overcome this problem, functional process of protein should be extracted by some stimuli, such as light for photoreceptive proteins.

As a biophysicist, Drs. Kandori, Inoue *et al.* have been long time studying on photoreceptive proteins such as the light-driven proton pump bacteriorhodopsin (BR); the BR study includes the first observation of protein-bound water molecules [1][2], the first functional conversion [3], light-switch function [4][5], the real-time/real-space observation by high-speed AFM [6]. Recently they extended the BR study into other microbial rhodopsins [7] [8] [9].

BR contains a single light absorbing prosthetic group called retinal, and retinal is covalently linked to a lysine side chain of the protein. When it is activated by a single photon of light, the excited chromophore causes conformational changes in the protein that results in the H^+ transport from the inside to the outside of the cell (Fig. 1). The primary H^+ transfer takes place from the retinal Schiff base (SB) to D85 in 50 μsec, which triggers subsequent H^+ transfer reactions that complete within 100 msec. BR is the best known membrane protein, but the mechanism of vectorial H^+ transport is not fully understood and new methods to describe vectorial proton transfer in atomic details are desired. In this sense, muon, the entirely new method, is potential for the research of BR and related proteins.

While muon is a potential tool for the BR research, BR is also a powerful system for the muon research, as atomic structure and functional details are well known (Fig. 1). In particular, functional correlation can be identified by comparing with/without light illumination. In the present experiments, we synchronize light illumination onto BR with the incident of muon, by which various

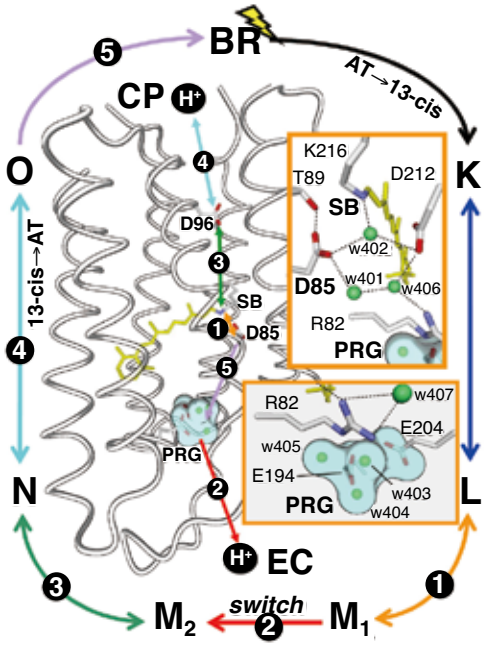

Fig. 1: Light-driven H^+ pump of BR is the result of 5 concerted H^+ transfer reactions [5].

dynamical processes happening inside protein will be analyzed.

We have conducted three experiments (2017A, 2019A, 2019B), and observed a slight difference between light illumination on and off in each experiment.

At this beam time, in order to make the μSR time spectra clear whether the difference is due to the optical response of the BR, we tried to match the selection of the sample cell, the thickness of the degrader (polyimide film) and BR to match the permeability condition of μ. Unfortunately, since the difference between light illumination on and off became more unclear, the experimental results are being analyzed by SRIM Program [10].

Light illumination experiments on membrane proteins are unprecedented, and there are numerous difficulties in obtaining good data. However, we are convinced that this study is worth overcoming many difficulties.

References

[1] H. Kandori *et al.*, J. Am. Chem. Soc. **117** (1995) 2118–2119.

[2] H. Kandori and Y. Shichida, J. Am. Chem. Soc. **122** (2000) 11745–11746.

[3] J. Sasaki *et al.*, Science **269** (1995) 73–75.

[4] H. Kandori *et al.*, PNAS **98** (2001) 1571–1576.

[5] V. A. Lórenz-Fonfria and H. Kandori, J. Am. Chem. Soc. **131** (2009) 5891–5901.

[6] M. Shibata *et al.*, Nat. Nanotechnol. **5** (2010) 208–212.

[7] K. Inoue *et al.*, Nat. Commun. **4** (2013) 1678–1687.

[8] H. E. Kato *et al.*, Nature **521** (2015) 48–53.

[9] K. Inoue *et al.*, Nat. Commun. **7** (2016) 13415(1-10).

[10] James F. Ziegler, Jochen P. Biersack, Matthias D. Ziegler, `http://www.srim.org/`

μSR Study on Paramagnetic State of Chromium Ion at $AgCrSe_2$
[J-PARC: 2020B0278]

J. G. Nakamura[1,2], Y. Kawakita[3], B. Li[4], K. Shimomura[2], and T. Suemasu[1]

[1]*Institute of Applied Physics, University of Tsukuba*
[2]*Muon Science Laboratory, Institute of Materials Structure Science, KEK*
[3]*Neutron Science Section, Materials and Life Science Division, J-PARC center, Japan Atomic Energy Agency*
[4]*Shenyang National Laboratory (SYNL) for Materials Science, Institute of Metal Research*

1. Introduction

$AgCrSe_2$ is a layered material (see Fig.1), and shows an antiferromagnetic property at low temperatures [3], whereas Ag ion shows superionic conduction at high temperatures [4]. Previous studies on magnetism have shown that the Néel and Curie temperatures are about 50 K and 70 K, respectively [3,5,6], and neutron diffraction experiments have shown that the spin 3/2 chromium ion (Cr^{3+}) has a magnetic moment of 2.55 (3) μ_B [1]. Recent study of quasi-elastic neutron scattering (QENS) has also shown that short-range spin correlations (short-range order) of Cr ions exist up to 200 K, much higher than the Néel temperature [7].

$AgCrSe_2$ has recently been paid attention about a possibility of high thermoelectric performance [8], rather than the superionic conduction. This high thermoelectric performance is partly caused by low thermal conductivity, which was also investigated by QENS [9]. The principle shown in the study is that the liquid-like behavior of Ag ions prevents the transverse mode phonon from propagating across the Ag ion layer, which causes of low thermal conductivity. In contrast of the QENS analysis on diffusion of Ag ion and TA phonons, a magnetic property of $AgCrSe_2$ is necessary to be verified experimentally to some extent. Our interest is the contribution of Cr spins. However, experimental methods to observe microscopic magnetic properties are limited. In this study, we focus on μSR experiments with using muons as local magnetic field probes.

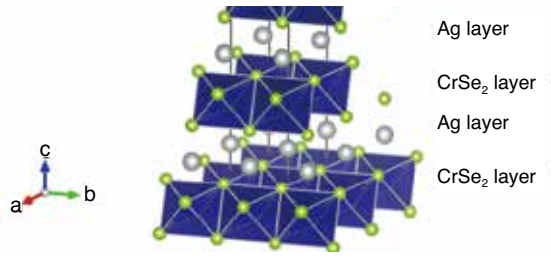

Fig. 1: Crystalline structure of $AgCrSe_2$[1,2].

2. Experimental

A powder sample of $AgCrSe_2$ (99.9%, Kojundo Chemical Laboratory Co., Ltd.) was molded into a shape of 32×32 mm^2 sheet with a thickness of 250 mg cm^{-2}. Conventional μSR experiment was carried out using the ARTEMIS spectrometer installed in the S1 area of MLF, J-PARC. Sample was loaded to a He-flow cryostat furnished with fly-past chamber, and temperature was varied from 9.5 to 450 K. The time spectra were analyzed using the muSRfit software.

3. Results and Discussion

Figure 2 shows some examples of zero-field (ZF) time spectra over a time range of 0∼20 μs. These spectra were reproduced by the simple function showing magnetic transition as follows,

$$Asy(t) = A_1 \times \exp(-\lambda_1 t)\exp\left(-\frac{\lambda_2^2 t^2}{2}\right) + A_2 \quad (1)$$

The first term is used to reproduce the evolution of temperature from exponential to Gaussian spectrum.

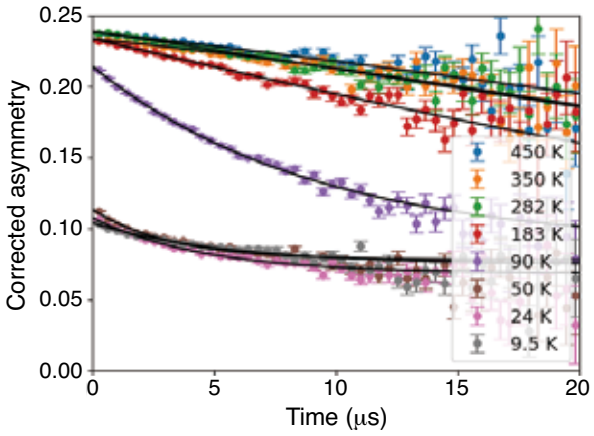

Fig. 2: ZF-μSR time spectra of $AgCrSe_2$.

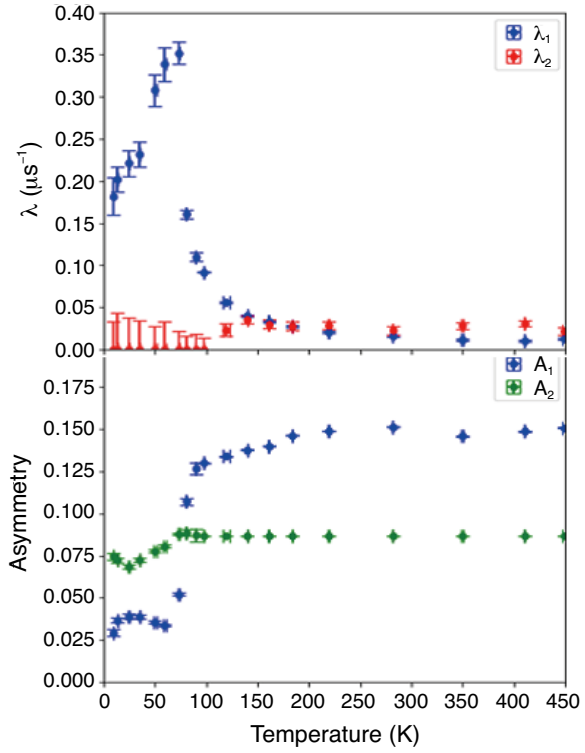

Fig. 3: Temperature dependence of relaxation rate λ_1 and λ_2(upper), partial asymmetries A_1 and A_2 (lower), by curve fit (see text).

Figure 3 shows the obtained parameters using the Eq. (1). It clearly shows antiferromagnetic phase below 58 K, and paramagnetic phase above 183 K. From 58 K to 183 K, the results show exponential spectra. At this temperature region, $AgCrSe_2$ is in a paramagnetic phase, and the exponential spectra show short-range spin correlations. In addition, the temperature dependence of partial asymmetry A_1 has a qualitative change at 89 K, which means clearly that some modification of the short-range order occurs. The interaction of the spins needs to be further scrutinized using some kind of model.

4. Summary and Conclusion

The temperature evolution of the short-range order of Cr spins in the paramagnetic phase of $AgCrSe_2$ was clarified with μSR experiments.

Below 183 K, the exponential μSR time spectra indicate relaxation by electron spins showing a short-range order of Cr spins. And, the temperature dependence of the spectra also show a qualitative change of the short-range order at 89 K

References

[1] F. M. R. Engelsman *et al.,* J. Solid State Chem. **6** (1973) 574–582.

[2] COD 9012117: Crystallography Open Database; A. Vaitkus *et al.,* J. Appl. Cryst. **54** (2021) 661–672.

[3] P. F. Bongbrs *et al.,* J. Phys. Chem. Solids. **29** (1968) 977–984.

[4] D. W. Murphy *et al.,* J. Electrochem. Soc. **124** (1977) 1268–1271.

[5] U. K. Gautam *et al.,* Solid State Commun. **122** (2002) 607–612.

[6] M. Baenitz *et al.,* arXiv:2109.02582.

[7] F. Damay *et al.,* Sci. Rep. **6** (2016) 23415(1-7).

[8] D. Wu *et al.,* Phys. Chem. Chem. Phys. **18** (2016) 23872–23878.

[9] B. Li *et. al.,* Nat. Mater. **17** (2018) 226–230.

Nucleation, Evolution and Expulsion of Spontaneous Vortices in Superconductor/ferromagnet Nanocomposites Probed by μSR [J-PARC: 2020B0279]

T. Uchino, K. Ohishi[1], Y. Sakaguchi[1], and A. Koda[2]

Department of Chemistry, Graduate School of Science, Kobe University
[1]*Neutron Science and Technology Center, CROSS*
[2]*Muon Science Laboratory, Institute of Materials Structure Science, KEK*

The interaction between different cooperative phenomena in a solid has long been an important topic in condensed matter physics. Among the phenomena, the interplay between superconductor (S) and ferromagnet (F) and the resulting spontaneous generation of vortices in zero applied field has attracted a lot of attention. Another intriguing example of the interaction is the proximity effect in superconductor/normal-metal (S/N) heterostructures and the subsequent formation of magnetic-field-induced vortices, called proximity Josephson vortices. However, the simultaneous occurrence of the above two phenomena, i.e., the spontaneous formation of proximity Josephson vortices, has not been observed before. Here, we present zero-field muon-spin relaxation (ZF-μSR) and bulk magnetization measurements on the S/N/F hybrid nanocomposite, in which the remote electromagnetic interaction between the S and F regions as well as a robust Josephson coupling over the whole volume of the sample is realized. Our observations provide evidence for the spontaneous modification/development of the internal magnetization at the onset of proximity-induced superconductivity.

The S/N/F nanocomposites were synthesized by the solid phase reaction of Mg, B_2O_3, B and $MnCO_3$ powders under Ar atmosphere at 700°C on the basis of the method reported recently by us [1]. The thus formed sample powders were compacted into a dense bulk sample by a subsequent spark plasma sintering (SPS) procedure. The powder X-ray diffraction (XRD) Rietveld analysis revealed the three major phases, i.e., MgO (73 wt%), Mg (7 wt%), and MgB_2 (20 wt%), yielding the corresponding ideal volume fraction of ∼63 ∼13 and ∼24 vol% for MgO, Mg and MgB_2, respectively. In addition to these major phases, a minor ferromagnetic component due to α'-MnB with a Curie temperature T_{FM} = ∼545 K was also recognized in the XRD pattern. We also confirmed from bulk magnetic measurements that the present S/N/F nanocomposite exhibits the proximity-induced superconducting temperature T_{cJ} at ∼30 K along with an almost full Meissner shielding signal at temperatures below T_{cJ}. Zero-field (ZF) muon spin rotation (μSR) experiments were performed at the Japan Proton Accelerator Research Complex (J-PARC) in the Materials and Life Science Experimental Facility (MLF) using the Advanced Research Targeted Experimental Muon Instrument at the S1 line spectrometer with a conventional ^{4}He flow cryostat, allowing a temperature range between 8 and 300 K.

Figure 1 shows representative ZF-μSR asymmetry spectra obtained at different temperatures. All the temperature-dependent ZF-μSR spectra do not show any oscillatory signal, indicating the absence of uniform internal magnetic fields associated with the embedded ferromagnetic particles. In the normal state, the ZF-μSR data are almost temperature independent. As the temperature of the system decreases below T_{cJ}, a substantial muon-spin relaxation especially in the time window below ∼5 μs was observed. If a pre-existing magnetic phase simply competes with an emerging superconducting phase, the ZF muon relaxation rate has been shown to decrease [2]. Hence, the observed enhancement of the muon spin relaxation gives evidence for the spontaneous and anomalous modification of the magnetic distribution at the onset of proximity-induced superconductivity. It is most likely that a drastic change in the magnetic field distribution has taken place in the sample even under zero applied field at temperatures below T_{cJ}. We also confirmed from the bulk magnetic measurements that the local internal field generated by the magnetic inclusions (H_{in} ∼ 6150 Oe) is far larger than H_{c1J} ∼ 220 Oe but is smaller than H_{c2J} ∼ 80 kOe. Thus, the most reasonable origin of the observed temperature dependence of the ZF-μSR is the spontaneous formation of Josephson vortices.

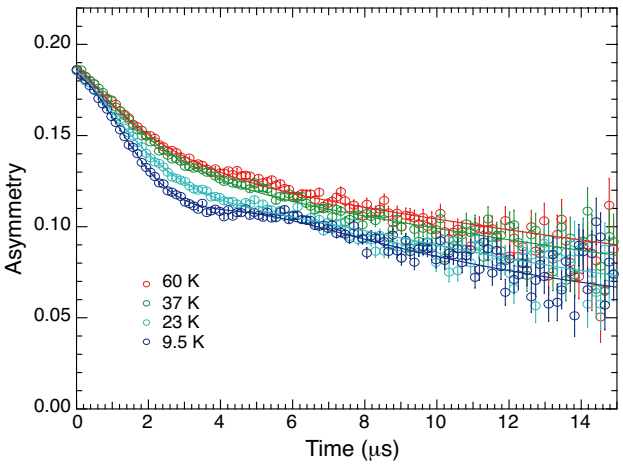

Fig. 1: Temperature dependence of the ZF-μSR spectra.

References

[1] T. Uchino *et al.*, Phys. Rev. B **101** (2020) 035146(1-12).
[2] F. K. K. Kirschner *et al.*, Phys. Rev. B **94** (2016) 134509(1-5).

μSR Study on the Randomness-induced Quantum Disordered Ground State of Spin-1/2 Random Bond FCC Lattice Antiferromagnets [J-PARC: 2020B0326]

M. Watanabe[1], Y. Miyata[1], N. Kurita[1], T. U. Ito[2,3], W. Higemoto[1,2,3], and H. Tanaka[1]

[1]*Department of Physics, Tokyo Institute of Technology*
[2]*Advanced Science Research Center, JAEA*
[3]*Muon Science Section, Materials and Life Science Division, J-PARC Center*

1. Introduction

The exploration of quantum spin liquid (QSL) ground states is currently an active research endeavor in condensed matter physics [1]. The QSL is characterized by the absence of magnetic ordering without a break in translational symmetry due to strong quantum fluctuations and many-body effects. Not only two-dimensional (2D) frustrated magnets, in which quantum effects are prominent, but also three-dimensional (3D) frustrated magnets such as a spin-1/2 pylochlore antiferromagnet $Ce_2Zr_2O_7$ [2] have been reported as a promising candidate of QSL.

It was theoretically demonstrated that randomness in the magnitude of exchange interactions suppresses magnetic ordering and induces the QSL-like state both in 2D and 3D frustrated quantum magnets [3,4]. The QSL-like state is thought to be a random singlet state (RSS) composed of randomly frozen singlets with various coupling energy. Our recent μSR experiments revealed the absence of long-range order in spin-1/2 random $J_1 - J_2$ square lattice Heisenberg antiferromagnet $SrLaCuSb_{0.8}Nb_{0.2}O_6$ and spin-1/2 random-bond triangular lattice antiferromagnet $Ba_2La_2CoTeWO_{12}$. However, whether the suppression of magnetic ordering by exchange randomness occurs only in 2D frustrated quantum magnets is yet to be confirmed experimentally.

Recently, we successfully synthesized polycrystalline samples of $Sr_2CoTe_{1-x}W_xO_6$ with $0.1 \leq x \leq 0.5$. The Co^{2+} ions with an effective spin-1/2 form a pseudo face-centered cubic (FCC) lattice, as shown in Figs. 1(a) and (b). Quantum effects due to geometric frustration are expected even in the 3D FCC lattice. The random substitution of W^{6+} for Te^{6+} gives rise to randomness in the magnitude of nearest-neighbor interaction J since the super-exchange paths via Te^{6+} and W^{6+} make antiferromagnetic and ferromagnetic exchange interactions, respectively. Thus, $Sr_2CoTe_{1-x}W_xO_6$ is a promising candidate of a spin-1/2 random-bond FCC lattice antiferromagnet. To clarify the effect of exchange randomness on the ground state of the spin-1/2 FCC lattice antiferromagnet, we carried out muon spin rotation and relaxation (μSR) measurements on a sample with $x = 0$ and 0.5 at S1 and D1 area of J-PARC MUSE, respectively.

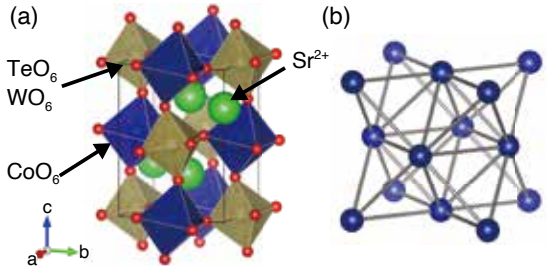

Fig. 1: (a) Crystal structure of $Sr_2CoTe_{1-x}W_xO_6$. (b) Schematic picture of FCC lattice.

2. Experiment

Powder samples of $Sr_2CoTe_{1-x}W_xO_6$ with $x = 0$ and 0.5 were prepared via a conventional solid-state method. The μSR measurements on the parent compound ($x = 0$) were performed at temperatures down to 3.5 K using a ^{4}He-flow cryostat at S1 area. The μSR measurements on the mixed system ($x = 0.5$) were performed at temperatures down to 35 mK using a dilution refrigerator installed at D1 area. At each temperature, we carried out measurements in the zero field (ZF) and transverse field (TF) of 20 G. Longitudinal fields (LF) μSR experiments were also conducted in magnetic fields up to 3900 G at several temperatures.

3. Results and Discussion

Figures 2 (a) and (b) show the ZF- and TF- μSR time spectra, respectively, for the sample with $x = 0$ measured at temperatures between 3.5 and 123 K. In all the temperatures, ZF-μSR spectra for the case with $x = 0$ were reasonably fitted by a stretched exponential decay, which is described by

$$A(t) = A_1 \exp((-\lambda t)^{\beta}) + A_2 + A_{\mathrm{BG}}, \qquad (1)$$

where λ is the depolarization rate of muon spin, A_1 and A_2 are asymmetries of the relaxed and constant components, respectively, and β is the stretch parameter. The background constant A_{BG} was fixed to the value estimated from the TF measurement. Below 17 K, A_1 steeply decreases with decreasing temperature and reaches the smallest value around 12 K. A_2 also increases below 17 K with decreasing

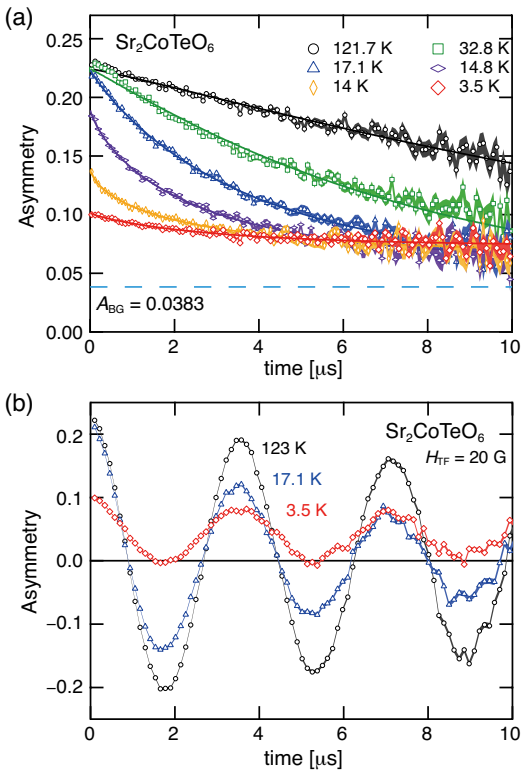

Fig. 2: (a) ZF- and (b) TF-μSR spectra for $x = 0$ measured at various temperatures. Solid lines are the best fits to the model functions described in the text.

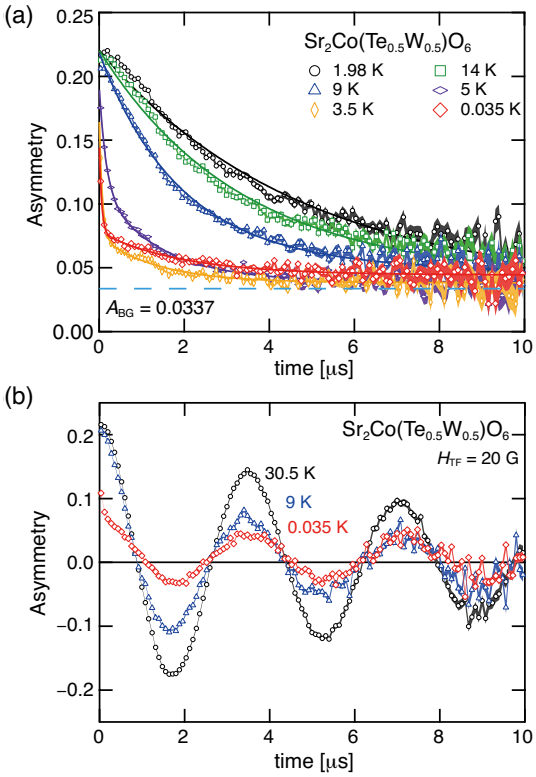

Fig. 3: (a) ZF- and (b) TF-μSR spectra for $x = 0.5$ measured at various temperatures. Solid lines are the best fits to the model functions described in the text.

temperature and saturates at 12 K. These behaviors is ascribed to the development of a static internal field. The magnetic ordering in Sr_2CoTeO_6 is characterized by the loss of the asymmetry and the emergence of the constant term (so-called "1/3-tail"). In the TF-μSR spectra shown in Fig. 2 (b), loss of the asymmetry and the 1/3-tail were also observed, which is consistent with the scenario deduced from the ZF spectrum.

Figures 3 (a) and (b) show the ZF- and TF- μSR time spectra, respectively, for the sample with $x = 0$ measured at temperatures between 0.035 and 30.5 K. ZF-μSR spectra for the samples with $x = 0.5$ can be reproduced by the two-component relaxation and the constant term in all the temperature range, which is described as

$$A(t) = A_1 \exp(-\lambda_1 t) + A_2 \exp(-\lambda_2 t) + A_3 + A_{\mathrm{BG}}. \quad (2)$$

Loss of the asymmetry and a partial development of the constant term were also found in the ZF-μSR spectra of the $x = 0.5$ sample below 10 K. This indicates that a static internal magnetic field develop even in $x = 0.5$ at low temperatures, while the temperature dependence of the asymmetries A_1, A_2, and A_3 are more gradual in comparison to that for $x = 0$. This is also confirmed by TF-μSR as shown in Fig. 3(b). These results suggest some kind of ordered ground state involving spin-freezing.

4. Summary

We found a loss of initial asymmetry and a recovery of the 1/3-tail in ZF-μSR spectra for the $x = 0$ sample below $T = 17$ K indicating the presence of a static internal field. These behaviors were partially confirmed in ZF-μSR spectra below 10 K for the $x = 0.5$ sample with exchange randomness. The ground state of the $x = 0.5$ sample is considered to be some kind of magnetic order involving spin-freezing.

References

[1] L. Balents, Nature (London) **464** (2010) 199–208.

[2] B. Gao *et al.*, Nat. Phys. **15** (2019) 1052–1057.

[3] H. Kawamura and K. Uematsu, J. Phys.: Condens. Matter **31** (2019) 504003(1-18).

[4] K. Uematsu and H. Kawamura, Phys. Rev. Lett. **123** (2019) 087201(1-6).

Non-destructive Measurements of Carbon Contents of Japanese Swords
[J-PARC: 2020B0330]

Y. Kiyanagi[1,†], K. Watanabe[1,‡], S. Nishiura[1], M. K. Kubo[2], K. Ninomiya[3], K. Oikawa[4], M. Tampo[5], Y. Miyake[5] and M. Ito[6]

[1]*Graduate School of Engineering, Nagoya Universit*
[2]*Graduate School of Science, Osaka University*
[3]*College of Liberal Arts, International Christian University*
[4]*J-PARC Center, JAEA*
[5]*Muon Science Laboratory, Institute of Materials Structure Science, KEK*
[6]*Former Visiting Professor of Shimane University*

1. Introduction

The Japanese swords have gotten the attention of people as a beautiful art object and its toughness as a sword. There still exist some unknown things about a making process and material properties since the process was not transferred by written documents despite of their long history. Metallurgical characteristics are important information to speculate the sword characteristics. As neutrons have a higher penetration power than X-rays, neutron diffraction and radiography methods have been widely used as a non-destructive method to study crystallographic structure. On the other hand, carbon content in iron is one of the most important information to assess the characteristics of iron, since it relates to hardness of iron, original iron material and forging procedure. There are several structure types in the Japanese sword; some are monolith and others are layered structure. In the layered structure, the iron in core area has lower carbon content to keep ductility and outside higher carbon content to keep hardness. Therefore, the absolute value of the carbon content is important to understand iron characteristics and the distribution of carbon is useful to identify the layered structure. Recently, it was indicated that the carbon content could be measured by using a μ^- decay, a muon life measurement. Since the life time of captured muon by an atom varies depending on the element, it is possible to identify the element by measuring the muon life. This method is a very attractive method since it can give the carbon content at different depths of the sword by ad-justing muon momentum. It is necessary to assess feasibility to measure the carbon content and to identify the sword structure.

In this experiment, we examined background suppression methods and various experimental conditions to obtain meaningful results. After then, we measured carbon contents in two swords, one of which has a layered structure with known carbon contents and the other unknown

† Present affiliation: Japan Neutron Optics Inc.
‡ Present affiliation:
Graduate School of Engineering, Kyushu University

2. Experimental

Experiments were performed at Muon D1 beam line us-ing large-solid angle decay electron counting system developed for μSR study. In order to analyze a small amount of carbon contained in the sword, it is necessary to suppress the background signals caused by the capture in surrounding light elements such as carbon and air (nitrogen and oxygen). Two kinds of background suppression methods were examined. One was that scattered muons were incident on the plastic detectors. The other was muon absorption in the air after passing through the sword sample. To check the former case a Sn plate was placed in front of each detector. Muon decay in Sn is very fast, about 90 ns and it is easily distinguished from the decay in C, 2026 ns. In the latter case a Sn sheet was placed just behind the iron stacked sample as shown in Fig. 1 to reduce effect of air, where a large Sn plate was seen after a two layered Fe sample. Finally, we measured carbon contents in two sword, 'Okimitsu' and 'Bizen Osafune Norimitsu'. 'Okimitsu' is known as a layered structure sword by destructive analysis and was measured to check feasibility of muon method to check reliability of quantity of carbon and to identify the layered structure. Its carbon contents are 0.02% at a core region and 0.69% at a sur-face region [1]. 'Norimitsu' was measured to identify its carbon contents and to know whether it had layered structure or not. Figure 2 shows a setup of 'Norimitsu' in a sample setting flame. We measured 'Okimitsu' at three points along thickness direction, namely, three momentums of muon, and 'Norimitsu' at two points.

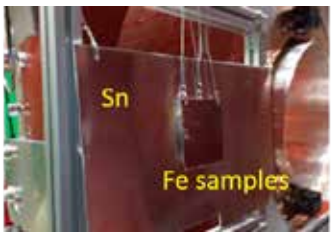

Fig. 1: Setup of a Sn plate behind the Iron samples.

The beam collimator of 10 mm diameter was used and the full width at half maximum of the actual elliptical beam, observed using an imaging plate, was 16 mm width and 12 mm height.

Fig. 2: Phot of Norimitsu set in a sample flame. A Sn plate was placed behind the sword.

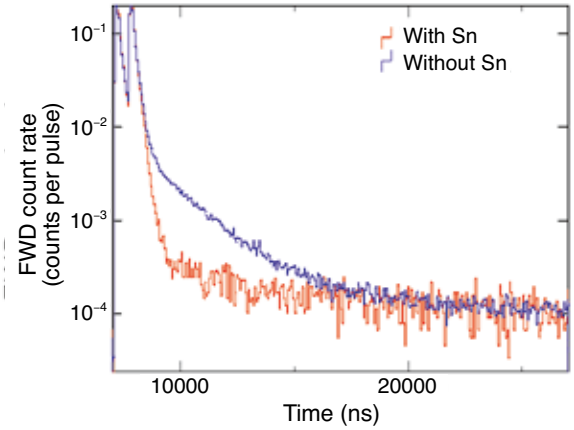

Fig. 3: Comparison of decay data with and without a Sn plate.

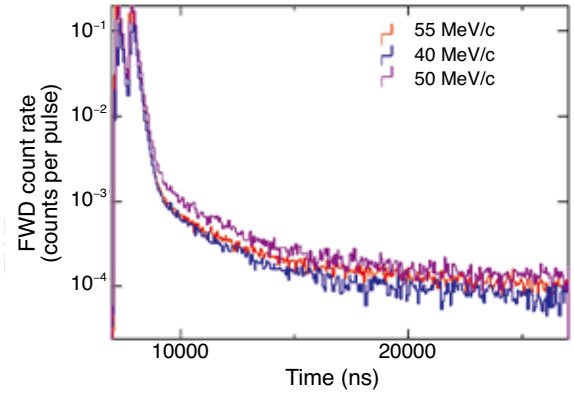

Fig. 4: Decay data observed for Okimitsu at three momentums of 40, 50 and 55 MeV/c.

3. Results

Firstly, it was shown that the sample scattering did not affect the background. Next, effect of air after sample was examined. Figure 3 shows the effect of the Sn plate set behind the iron sample. It is clearly indicated that the muons transmitting through the sample was major origin of the background. Therefore, we put a Sn plate behind the sample at all experiments.

We measured a part near nakago of Okimitsu at muon momentums of 40, 50 and 55 MeV/c, which momentums roughly corresponded to muon stopping depth of 0.7, 1.5 and 2.1 mm, respectively. The nakago is a part corresponding to the handle area, Tsuka in Japanese. Measured spectra are shown in Fig. 4. The carbon contents were 0.67, 0.61 and 0.48% at 40, 50 and 55 MeV/c, respectively. The contents decreased with increasing the momentum, namely, with moving on to the center. The values of the first two are almost the same as the value obtained by a destructive method. This suggests reliability of the muon method as a quantitative evaluation method of the carbon contents. However, the value 0.48% at 55 MeV/c is much higher than the value 0.02% at a core region. The value would change depending on the position and in the present measurement muons may stop at different areas of the Japanese sword and then gave a mixed value of center and peripheral areas. However, the result suggested the sword had a layered structure.

We performed similar measurements on 'Norimitsu' at 40 and 50 MeV/c. Obtained carbon contents were 0.101% and 0.057%. The content near surface (40 MeV/c) is larger than thicker place (50 MeV/c) by about 2 times. However, the values are very small and will correspond to center area, suggesting a monolith structure.

4. Conclusion

We applied the method of muon life measurement to obtain quantitative information of the carbon contents in Japanese sword. Before the measurements on Japanese swords, we examined various conditions and found a Sn plate behind the sample was effective to reduce the background. Carbon contents were observed for two swords. One has a layered structure and the other is unknown. The carbon contents around the shallow areas of the first sword were almost the same as the value obtained by a destructive method and the content decreased at deeper position, which may be an evidence of the layered structure. The second sword also showed much lower content compared with the first one and the value was about 0.1 or less. These values are similar to a content in a core part of the layered structure. From these results, it is indicated the muon method is very powerful tool to measure the carbon content in the Japanese swords along thickness direction. A smaller beam size of the muons is desired to obtain more precise thickness dependence.

References

[1] M. Yaso *et al.*, Materials Science Forum, **738-739** (2013) 222–227.

Negative Muon Spin Rotation Study for Antiferromagnetism of Na Nanoclusters Arrayed in Sodalite [J-PARC: 2020B0332]

T. Nakano, H. Baba, S. Takeshita[1], and J. Sugiyama[2]

Institute of Quantum Beam Science, Graduate School of Science and Engineering, Ibaraki University
[1]*Muon Science Laboratory, Institute of Materials Structure Science, KEK*
[2]*Neutron Science and Technology Center, CROSS*

1. Introduction

The muon spin rotation/relaxation method has been used as a sensitive local magnetic probe in a wide range of fields including magnetism. Positive muons (μ^+), which are usually used, stop at interstitial sites, and their positions are often difficult to determine precisely. On the other hand, negative muons (μ^-) are captured by nuclei and have different lifetimes for each nuclide, so their stopping sites are clear, but they have the disadvantage that their spin polarization decreases to 1/6 during the capture process. However, at the J-PARC MLF D1 beamline, μ^-SR experiments have become feasible due to the increased beam intensity and detection efficiency, and are now being used to study ion dynamics in solids from fixed observation sites [1]. The present study is an attempt to apply this technique to the study of magnetic materials.

In sodalite, β cages with an inner diameter of about 7 Å are arranged in a bcc structure, and when Na_4^{3+} clusters (Fig. 1) are formed in all the cages, the interaction between the arranged clusters leads to an antiferromagnetic order with a Néel temperature of 50 K. In the zero-field μ^+SR, a homogeneous local magnetic field of 92 Oe is observed at low temperature [2]. It has recently been found that this is due to the Fermi-contact interaction between the s-electron and μ^+ located at the cage center [3].

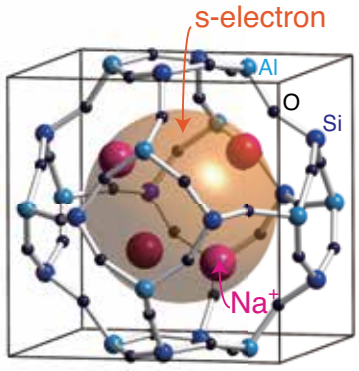

Fig. 1: Schematic of Na_4^{3+} cluster formed in β cage of sodalite crystal.

2. Experimental

A 7-gram powder sample of Na clusters in sodalite was prepared and sealed with helium gas in a copper container with an inner diameter of 36 mm and a depth of 12 mm in the sample space. The μ^-SR time spectra were measured at the D1 beamline at MUSE MLF in J-PARC. We used decay negative muons with the momentum of 40 MeV/c.

3. Results

The analysis of the lifetime of the histogram shows that the signal at the oxygen position of the cage is dominant. The initial asymmetry of the zero-field μ^-SR time spectrum drops sharply below the Néel temperature as shown in Fig. 2, but there is no signal of muon spin precession due to the homogeneous local field. From the analysis of the decoupling by the longitudinal field, the local field at the oxygen position was found to be about 0.4 kOe. This value is about two times larger than the value calculated assuming that the electron spin is a point dipole. We are considering the spatial extension of the s-electron wave function to explain the observed local field quantitatively.

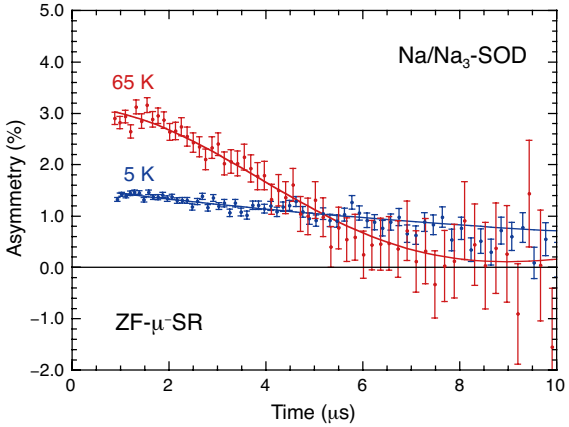

Fig. 2: ZF-μ^-SR spectra of Na clusters in sodalite.

References

[1] J. Sugiyama *et al.*, Phys. Rev. Lett. **121** (2018) 087202(1-5); Phys. Rev. Research **2** (2020) 033161(1-6); Phys. Rev. B **102** (2020) 144431(1-7).

[2] T. Nakano *et al.*, J. Phys. Soc. Jpn. **79** (2010) 073707(1-4).

[3] T. Nakano *et al.*, The Physical Society of Japan, 2021 Annual (76th) Meeting, 14aG1-4.

Measurement of Muonic Helium Atom HFS at Zero Field [J-PARC: 2020B0333]

P. Strasser[1], S. Fukumura[2], H. Tada[2], H. Yamauchi[3], K. Shimizu[3], S. Nishimura[1], S. Kanda[1], S. Seo[3,4], T. Tanaka[3,4], H. Yasuda[5], H. A. Torii[5], and K. Shimomura[1], on behalf of the MuSEUM collaboration

[1]*Muon Science Laboratory, Institute of Materials Structure Science, KEK*
[2]*Department of Physics, Nagoya University*
[3]*Graduate School of Arts and Sciences, The University of Tokyo*
[4]*Advanced Meson Science Laboratory, RIKEN Nishina Center for Accelerator-Based Science*
[5]*Graduate School of Science, The University of Tokyo*

Measurements of the muonic helium atom hyperfine structure (HFS) is a sensitive tool to test three-body atomic system, bound-state quantum electrodynamics (QED) theory, and determine fundamental constants of the negative muon magnetic moment and mass. The world most intense pulsed negative muon beam at J-PARC MUSE gives an opportunity to improve previous measurements and to test further CPT invariance through the comparison of the magnetic moments and masses of positive and negative muons (second generation leptons).

In a muonic helium atom one of the two electrons is replaced by a negative muon (μ^-). The Bohr radius of the bound μ^- in helium is roughly 400 times smaller than that of a hydrogen atom, thus the bound system $(^4\mathrm{He}\mu^-)^+$ in the ground state can be regarded as a "pseudo-nucleus" with a positive effective charge and a magnetic moment nearly equal to that of a negative muon μ_{μ^-}. The ground state HFS results from the interaction of the remaining electron and the negative muon magnetic moment. Indeed, muonic helium and muonium (a bound state of a positive muon and an electron) are very similar, and their ground state HFS are almost equal but inverted because of the different signs of their respective muon magnetic moments. High-precision measurements of the muonium ground state HFS are regarded as the most sensitive tool for testing QED theory, and determining fundamental constants of the positive muon magnetic moment μ_{μ^+} and its mass m_{μ^+}. New precise measurements are now in progress at J-PARC by the MuSEUM collaboration [1].

In muonic helium too, the HFS interval is sensitive to variations of basic physical constants, and the same technique as with muonium can be used to measure the muonic helium ground state HFS transition frequency $\Delta\nu$ and the negative muon magnetic moment μ_{μ^-} and mass m_{μ^-}. Previous measurements were performed in 1980s at PSI and LAMPF with experimental uncertainties dominated by statistical errors. In ^{4}He, $\Delta\nu$ was measured to a level of 13 ppm (weak field) [2], 6.5 ppm (high field) [3], and 47 ppm for μ_{μ^-}/μ_p (high field) [3], respectively. The high-intensity pulsed negative muon beam at MUSE brings an unique opportunity to significantly improve those measurements [4].

We have recently started measurements of the muonic helium atom HFS by using the apparatus that was developed by the MuSEUM collaboration to determine with high precision muonium HFS at zero field. A first experiment was performed in February 2020 at area D2 with a 2-atm helium gas target. Only six resonance frequencies were measured but no clear resonance signal could be observed due to possibly a DAQ problem with the microwave ON/OFF measurements [5].

A second attempt to measure muonic helium atom HFS at zero field was performed in March 2021 also at area D2 with the same apparatus. The schematic view of the experimental setup is shown in Fig. 1. Pulsed polarized μ^- are stopped into a microwave (RF) cavity located inside a gas chamber containing pressurized helium gas to form muonic helium atoms. An admixture of 2% CH_4 is added as an electron donor to efficiently form neutral muonic helium atoms. CH_4 is preferred to Xe used in previous experiments [2,3] because of its reduced total charge (Z=10) and similar ionization potential of 12.5 eV, and gives a residual μ^- polarization of ∼5% [6]. The muon spin is flipped by applying a microwave magnetic field in the cavity. Electrons (e^-) from μ^- decay are emitted prefer-

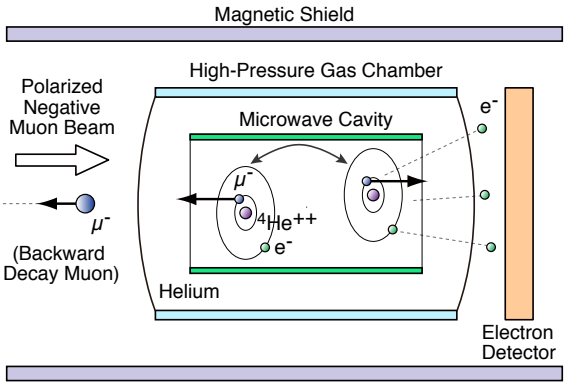

Fig. 1: Schematic view of the experimental setup to measure ground state muonic helium atom HFS at zero field. The experimental apparatus is enclosed in magnetic shield box made of permalloy.

entially in the direction antiparallel to the μ^- spin. At the resonance, the microwave field induces the μ^- spin flip changing the angular distribution of decay e^-, which are detected with segmented scintillation counters placed downstream. Muonic helium atom HFS measurements are performed by scanning the microwave frequency and measuring the electron asymmetry (RF_{ON}/RF_{OFF}) to determine the resonance frequency $\Delta\nu$ at zero field.

In this experiment, a helium gas target pressure of 4 atm was used. The entrance beam window of the gas chamber was made of a 0.1-mm thick beryllium-copper foil. A backward decay muon beam of 27 MeV/c was optimum to stop μ^- in the microwave cavity. Since the cavity as well as the downstream beam stopper placed before the electron detector are all made of copper, muonic helium (μHe) signals were clearly separated from muonic copper (μCu) background events due to different muon lifetimes. By selecting delayed events, more than 70% of μHe signals remains while reducing μCu events to a few percent only (double-pulse muon beam condition).

We successfully measured the muonic helium HFS resonance at zero-field and 4 atm He gas pressure with 2% CH_4 admixture. Figure 2 shows the resonance curve obtained using delayed events from 2 μs after the second muon pulse (online analysis). When using backward decay μ^- (spin antiparallel to the muon momentum), the direction of the decay e^- emission will change from preferentially downstream to upstream when the microwave field is applied, thus resulting into a negative resonance curve. A preliminary result gives $\Delta\nu$ (4 atm) = 4464.07(2) (analysis in progress). The obtained precision is significantly better than the previous measurement at zero field and a gas pressure of 20 atm [2], and comparable to previous high-field measurements [3] (see Fig. 3). It should be noted that this muonic helium HFS measurement is the first one ever performed using CH_4 as an electron donor and also at the lowest He gas pressure.

In order to obtain the muonic helium hyperfine frequency $\Delta\nu$ at zero pressure, a pressure shift correction, which is due to competing short- and long-range interactions between μHe atom and the buffer gas at a given pressure, has to be applied to the measured frequency. Previous measurements done with He + Xe(1.5%) [2,3] cannot be used because it is most likely different for He + CH_4(2%). Indeed, 1.5% Xe reduces the linear pressure shift coefficient in He by nearly 8% in the case of hydrogen; no isotopic effect being observed for H, D and T in noble gases [7,8]. Unfortunately, no pressure shift data were ever been reported for hydrogen like atoms in CH_4. So, our next goal will be to measure muonic helium HFS at different gas pressures to obtain the pressure shift in He + CH_4(2%), and then determine $\Delta\nu$ at zero pressure.

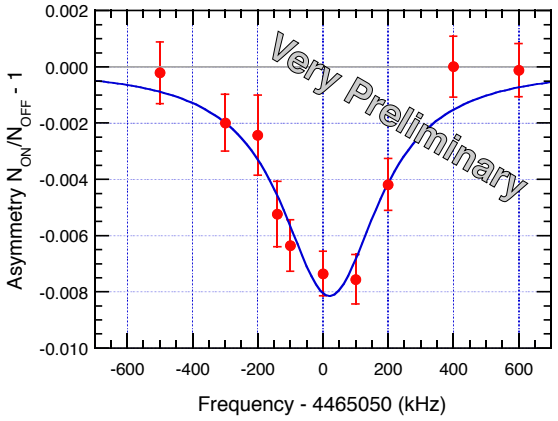

Fig. 2: Muonic helium HFS resonance curve measured with He + CH_4(2%) at 4 atm and zero field.

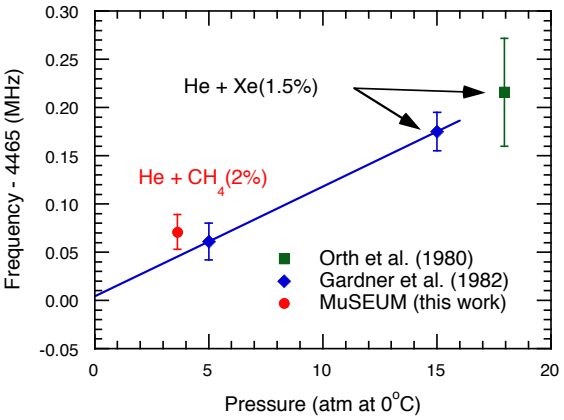

Fig. 3: $\Delta\nu$ as a function of He gas pressure. Results from Ref. [2] and [3] are shown.

References

[1] S. Seo *et al.*, KEK Progress Report **2020-4** (2020) 47–48.

[2] H. Orth *et al.*, Phys. Rev. Lett. **45** (1980) 1483–1486.

[3] C. J. Gardner *et al.*, Phys. Rev. Lett. **48** (1982) 1168–1171.

[4] P. Strasser *et al.*, JPS Conf. Proc. **21** (2018) 011045(1-6).

[5] P. Strasser *et al.*, KEK Progress Report **2020-4** (2020) 75–78.

[6] D. J. Arseneau, D. G. Fleming, *et al.*, J. Phys. Chem. B **120** (2016) 1641–1648.

[7] F. M. Pipkin and R. H. Lambert, Phys. Rev. **127** (1962) 787–792.

[8] E. S. Ensberg and C. L. Morgan, Phys. Lett. **28A** (1968) 106–107.

Emergence of Optical Activity in Achiral Amino Acids and Their Precursor Molecules by Spin-polarized Muon Beam [J-PARC: 2020B0334]

J. Takahashi, T. Sakamoto, H. Shibata[1], M. K. Kubo[2], T. Shima[3], Y. Miyake[4], N. Globus[5], Y. Kebukawa, and K. Kobayashi

Faculty of Engineering, Yokohama National University
[1]*SANKEN (The Institute of Scientific and Industrial Research), Osaka University*
[2]*Colledge of Liberal Arts, International Christian University*
[3]*Research Center for Nuclear Physics, Osaka University*
[4]*Muon Science Laboratory, Institute of Materials Structure Science, KEK*
[5]*New York University and Flatiron Institute (USA)*

1. Introduction

The origin of terrestrial bioorganic homochirality (the enantiomeric domination of L-form amino acids in proteins and D-form sugars in DNA/RNA) is among the most important problems in astrobiology. One of the most attractive hypotheses is that chiral chemical reactions in the primitive interstellar media were induced by polarized quantum radiation in space, such as circularly polarized photons or spin-polarized leptons (electrons and muons) [1,2]. Supporting this scenario, L-form enantiomeric excesses of α-methyl amino acids exist in Murchison meteorite [3] and circularly polarized infrared photon radiation areas are widely spreading in star forming regions [4,5]. This knowledge has been gained by analytical and astronomical observations, respectively. Meanwhile, optical activity in amino acids or their precursor molecules has emerged in ground simulation experiments using circularly polarized photons from synchrotron radiation or free electron lasers [6,7].

In natural lepton radiation, leptons are intrinsically spin-polarized to one helicity by parity symmetry breaking in weak interactions. Spin-polarized electrons and positrons can be radiated from natural beta-decay nuclei in astronomical objects, such as the parent bodies of meteorites in interstellar environments. Ground simulation experiments using spin-polarized electrons from intense beta-decay sources (^{90}Sr - ^{90}Y) have shown that optical activity emerges through asymmetric reactions [8].

Conversely, in the Earth's atmosphere, high energy protons in cosmic rays generate pions through collisions with atmospheric atomic nuclei. Positive and negative muons are then generated as secondary cosmic rays. In recent theoretical studies, it was proposed that homochirality is a deterministic consequence of the weak interaction, expressed by muons and other spin-polarized cosmic radiation [9].

The muon mass is much higher than the electron mass (m_μ/m_e ~207) and is similar to the proton mass (m_μ/m_p ~1/9). Meanwhile, the magnetic moment of muon is 1/207 that of electrons and more than 3 times that of protons. The magnetic moment of spin-polarized muons is expected to interact strongly and asymmetrically with both the electric and magnetic dipole moments of molecules and induce asymmetric reactions in molecules. These effects should depend on the charge and spin states of muons. The emergence of optical activity in molecules might depend on the muon beam helicity (projection of the spin angular momentum vector onto the kinetic momentum vector) or lodacity (projection of the magnetic moment vector onto the velocity vector) [9].

2. Experiment

Previous feasibility studies of spin-polarized muon irradiation on materials have reported asymmetric reactions of organic compounds [10] and asymmetric muonium formation in chiral quartz crystals [11], but no significant effects of muon spin polarization have been observed to date.

Given that spin-polarized muon irradiation can potentially induce novel types of optical activities, we conducted a feasibility study of spin-polarized muon beams combined in four ways (positive and negative charges with positive and negative helicities) to obtain optical activity in DL-alanine (a racemic mixture of chiral amino acids) with the approved proposals (2018B0339(P), 2019B0179, 2020B0334).

The sample DL-alanine crystal powders were densely packed into potassium bromide cylindrical pellets (bottom face diameter = 5 mm, thickness = 1 mm). The density of the sample DL-alanine crystal powders was 50 wt% for the total pellet weight.

In the experiments of our first proposal (2018B0339(P)), we irradiated positive muons with negative helicity and negative muons with positive helicity perpendicularly on the bottom face of the sample. Experiments were conducted on surface muon beamline S1 (29.4 MeV/c). In the experi-

ments of the second proposal (2019B0179), we irradiated positive muons with positive helicity using the decay muon beamline D1 in backscattering mode (55 MeV/c). In the experiments of the third proposal (2020B0334), we irradiated negative muons with negative helicity using the decay muon beamline D1 in backscattering mode (45 MeV/c). Because the estimated penetration depth of the muon beams through the samples was less than 1 mm, almost all the muons should be captured by the target materials packed into the samples. The number of activated target molecules in the sample, estimated from the muon capture rate, was deemed sufficient to detect optical activity emergence.

The enantiomeric excesses $\big((\mathrm{L}-\mathrm{D})/(\mathrm{L}+\mathrm{D})$ in $\%\big)$ in the irradiated DL-alanine samples were analyzed by gas chromatography-mass spectroscopy (GC-MS; Yokohama National University) with a chiral column after derivatization process.

3. Results and Discussion

The enantiomeric excesses in the irradiated samples measured by GS-MS are shown in Table 1. Listed are the results of positive muon irradiation with positive and negative helicities, and the negative muon irradiation with positive and negative helicities. The enantiomeric excesses in all non-irradiated samples before were zero within the statistical error range, and all enantiomeric excesses measured in the irradiated samples were D-form enantiomeric excesses, including the preliminary values in the most recent experiment (under detailed analysis). At present no clear correlation between the direction of enantiomeric excess type (L- or D-form dominant) and spin polarization (helicity or lodacity) has emerged.

Because the interactions of muon beams with organic molecules differ between positive and negative muons, we must study the chiral chemical reaction peculiar to positive and negative muons separately.

Positive muons in organic molecules trap bound electron and generate muonium, Mu (bound state of a positive muon and an electron pair). Mu formation induces dissociation of a double bond into a single bond, with subsequent radical formation and isomerized molecules. Hot Mu generated by high-energy muon beams extract hydrogens from organic molecules (Mu* + RH $\rightarrow$ MuH + R*). These types of chiral inversion reactions are expected to realize enantiomer-type conversion of chiral molecules. The Mu formation site on an organic molecule strongly depends on the electronic structure of the molecule [12]. Mu formation, especially with the non-bonding electrons of carboxyl bases of amino acids, is expected to asymmetrically excite both electric and magnetic dipoles, depending on the spin state of the muon beam (helicity or lodacity).

Negative muons in molecules trapped by atomic nuclei can generate a muonic atom (bound state of an atomic nucleus and a negative muon pair). Muonic atom formation can induce a charge-shielding effect because a heavy negative muon is captured within a small-radius orbit, forming an apparent Z - 1 nucleus and a negative ion. Furthermore, nuclei with large atomic number can be converted to smaller nuclei (Z $\rightarrow$ Z - 1) via the muon capture by proton ($\mathrm{p} + \mu^- \rightarrow \mathrm{n} + \nu_\mu$). Although the trapping efficiency and lifetime of negative muons depend on the species of atomic nuclei in organic molecules, a chemically active muonic atom should asymmetrically distort the molecular structures depending on the muon spin state (helicity or lodacity). Furthermore, the Auger electrons and X-rays emitted in the muonic atom formation can generate secondary ions or radical molecules, followed by isomerization or asymmetric dissociation.

4. Conclusion

These experimental results strongly suggest that spin-polarized muon irradiation can induce novel types of optical activity, which differ from those of circularly polarized photon and spin-polarized electron irradiation. We are planning further experiments that will clarify the dependence of optical activity emergence on the spin polarization (helicity or lodacity) and on the charge states of muon beams. Further analytical experiments are expected to reveal the active atomic sites (C, N, O) of Mu (for positive muons) and muonic atom generation sites (for negative muons). To identify the active atomic sites in molecules, we will use isotopic-substituted samples.

Table 1: Enantiomeric excesses $\big((\mathrm{L}\text{-}\mathrm{D})/(\mathrm{L}+\mathrm{D})$ in $\%\big)$ of DL-alanine before and after muon irradiation.

Charge / Helicity / Lodacity Beamline (Proposal No.)	Enantiomeric excess [%]
$\mu^+/-/-$ S1 29.4 MeV/c (2018B0339(P))	-0.68 ± 0.49
$\mu^+/+/+$ D1 55 MeV/c (2019B0179)	-1.23 ± 0.17
$\mu^-/+/-$ S1 29.4 MeV/c (2018B0339(P))	-0.75 ± 0.20
$\mu^-/-/+$ D1 45 MeV/c (2020B0334)	~ -0.12 (preliminary)

References

[1] W. A. Bonner, Orig. Life Evol. Biosphere **21** (1991) 59–111.

[2] J. Takahashi and K. Kobayashi, Symmetry **11** (2019) 919(1-11).

[3] J. R. Cronin *et al.*, Science **275** (1997) 951–955.

[4] J. Bailey *et al.*, Science **281** (1998) 672–674.

[5] T. Fukue *et al.*, Astrophys. J. Lett. **692** (2009) L88–L91.

[6] Y. Takano *et al.*, Earth Planet. Sci. Lett. **254** (2007) 106–114.

[7] J. Takahashi *et al.*, Int. J. Mol. Sci. **10** (2009) 3044–3064.

[8] V. I. Burkov *et al.*, Orig. Life Evol. Biosph. **39** (2009) 295–296.

[9] N. Globus and R. D. Blandford, Astrophys. J. Lett. **895** (2020) L11(1-14).

[10] R. M. Lemmon *et al.*, Nature **252** (1974) 692–694.

[11] D. P. Spencer *et al.*, in *Origins of Optical Activity in Nature*, ed. D. C. Walker (Elsevier Science Ltd., Amsterdam, 1979) p.87–99.

[12] A. D. Pant *et al.*, JPS Conf. Proc. **21** (2018) 011038(1-4).

In-situ Measurements of Metallic Li in a Lithium-ion Battery Using Negative Muons [J-PARC: 2020B0338]

I. Umegaki, Y. Kondo, H. Kondo, H. Kawaura, S. Takeshita[1], M. Tampo[1], S. Nishimura[1], and Y. Miyake[1]

Toyota Central Research & Development Laboratories, Inc.
[1]*Muon Science Laboratory, Institute of Materials Structure Science, KEK*

1. Intro

One of the most important issues of a Li-ion battery (LIB) to solve is deposition of metallic Li on an anode, which is caused in an improper way of use. Since such deposition of metallic Li on an anode may cause finally short-circuit or heating in a LIB, it is crucially demanded to detect metallic Li in a LIB to ensure that the battery is safe before reuse. In addition, Li is easily oxidized in air to change conditions of an electrode. However, there is only destructive ways to investigate amount of Li deposition, such as Inductivity coupled plasma optical emission spectrometer (ICP-OES) or ^{7}Li-NMR.

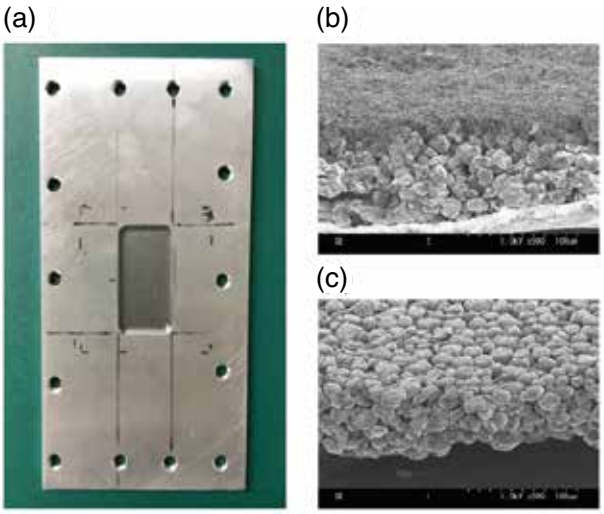

Fig. 1: Photo of (a) aluminum mask with a Be window, and SEM poctires of (b) an anode after 20 cycles and (c) an initial condition of an anode.

An elemental analysis with muonic x-ray can be a candidate to achieve this. In our previous experiment in June 2018 (2018A0246), we found that the sensitivity of muonic X-rays of Li (Li-Kα) in Li metal is about 50 times higher than one in Li intercalated compound C_6Li). This is because almost fiftyfold negative muons are trapped by C in C_6Li, comparing with the case for Li. Using this high intensity in metallic Li, it was supposed to be possible to distinguish metallic Li and Li ion in C_6Li, a fully charged state of an anode. Then, we have tried to apply this technique to detect non-destructively Li deposition, where Li ion is reduced to metallic Li at the surface of an anode in a LIB. Retrieving a fully charged anode with Li deposition from a LIB, we succeeded to detect Li deposition by this technique by demonstrating that this technique is not sensitive to Li in an anode but to metallic Li on the anode [1]. In the latest experiment (2020A0184), we succeeded to apply this non-destructive technique to a laminated LIB to obtain relation between capacity retention and amount of Li deposition. As a result, we found the detection limitation has become to 0.02 mg/cm^2. This is most likely due to an improvement of S/N using an Al mask or/and finely tuned negative muon beam in the D line. Finally, this detection limit is small enough to detect metallic Li corresponding to the deterioration, for which a used LIB should be collected in terms of safety.

2. Experimental

This experiment was carried out by exposing negative muons to a sample and detecting muonic x-ray emitted from the sample with four Ge semiconductor detectors for low energy gamma rays. We have prepared a Li-ion battery, which is composed by electrodes, a separator, and electrolyte solution. Metallic Li deposition is produced by applying charging cycles. The LIB was sandwiched by an Al holder and a 100 μm Be window [Fig.1(a)] in order to work properly in charge discharge process to get metallic Li on the anode [Fig.1(b) and (c)]. The momentum of negative muon beam was 19-25 MeV/c. This was predicted by simulation by PHITS code2 [2] and experimentally confirmed in our experiment. In order to avoid attenuation of incident negative muon and muonic x-ray, a sample chamber filled with He gas is used. The amount of Li was confirmed after the measurements by ICP-OES and ^{7}Li-NMR. When the charging cycles started, we started exposing negative muons to a LIB with and then, we continued measuring muonic x-rays until 17 cycles finished. Although energy spectrum was obtained as an integration during the cycles, data can be extracted with any duration of time in the cycles since each count is recorded with time when muonic x-ray is detected. The intensity of peak count around 18 keV, which corresponds to Li, was obtained as an average in each cycle, respectively.

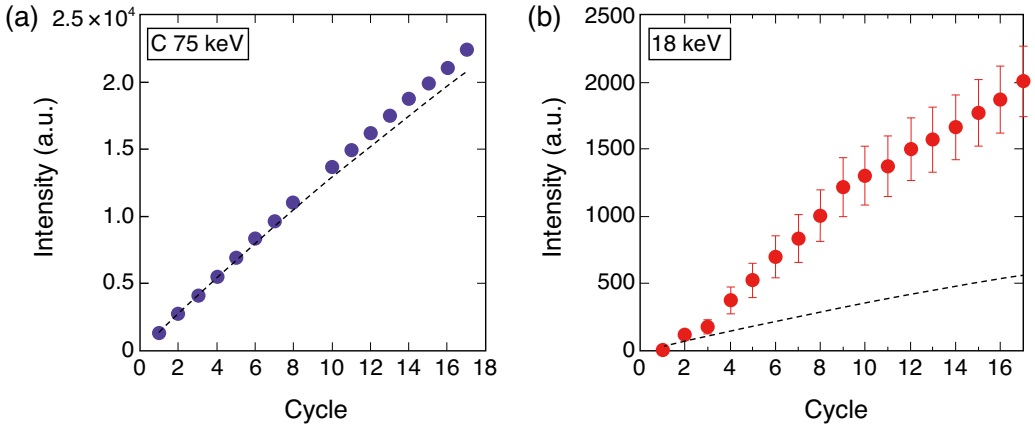

Fig. 2: Intensity of peaks at (a) 75 keV for Carbon and (b) 18 keV corresponds to Li and C.

3. Results

Figures 2 show intensity of signals at 75 keV corresponds to Carbon and that at 18 keV, respectively. Each plot represents peak count between 0 and each cycle, and dotted line shows a prediction from the initial condition. For C (75 keV), all plot follows the dotted line [Fig.2(a)]. On the other hand, for 18 keV, deviation from the predicted dotted line became larger after 4 cycles, which means that a peak of Li grows due to metallic Li deposition.

Figure 3 shows a cycle dependence of peak count intensity, which is estimated by difference between each intensity in Fig.2 (b). The count increases with increasing cycles, it become almost constant after 5 cycles, and then increases after 15 cycles again. It is noted that there is no explain for a gap between 9 and 10 cycles. Such behavior seems to be similar to results of electrochemical method, where electrical capacity decreases rapidly until 5 cycles and its slope becomes gentle after that. We consider that metallic Li deposition during charging cycles were observed by muonic x-rays. In the end, amount of metallic Li deposition was estimated as 0.088 mg/cm^2 in total.

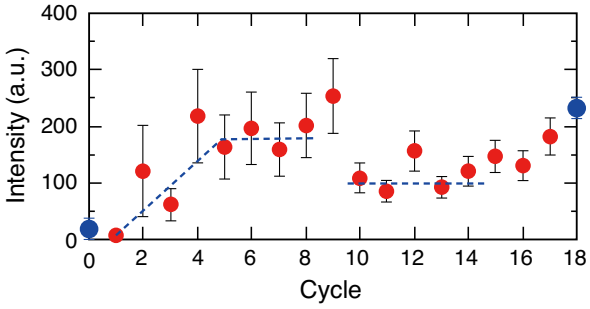

Fig. 3: Peak count intensity at each cycle normalized by 180,000 pulses. The intensity at 0 and 18 represent initial and final conditions, respectively.

4. Conclusion

Therefore, we consider that elemental analysis with muonic x-rays can be applied to observation of metallic Li deposition in a LIB during charging cycles. We estimated that the detection limit of metallic Li was 0.01 mg/cm^2, which corresponds to the deterioration rate of 2%. Then, such a non-destructive detection of metallic Li deposition in a LIB will not only provide a useful tool for development of a LIB, but also help to ensure the safety of a battery before its reuse.

References

[1] I. Umegaki *et al.*, Anal. Chem. **92** (2020) 8194–8200.

[2] T. Sato *et al.*, J. Nucl. Sci. Technol. **55** (2018) 684–690.

Local Dynamics of Polar Nanoregions in Magnetic Relaxor Ferroelectrics
[J-PARC: 2020B0354]

H. Okabe, M. Hiraishi, S. Nishimura, J. G. Nakamura, A. Koda, and R. Kadono

Muon Science Laboratory, Institute of Materials Structure Science, KEK

Our study focused on the local dynamics of polar nanoregions via spin fluctuation in the magnetic relaxor ferroelectrics $(1-x)BiFeO_3-xBaTiO_3$ (BF-xBT). Strongly disordered ferroelectric materials have attracted much interest as relaxor ferroelectrics due to its huge responses to weak outer field [1]. Relaxor ferroelectrics are characterized by the presence of polar nanoregions where the growth and fluctuation of small domains play an important role in the relaxor properties (see Fig.1) [2]. The structural studies of the polar nanoregions have progressed smoothly, however the dynamics have been poorly understood so far, because of only few ways to know local dynamics in the disordered system. The dynamics for polar nanoregions are presumed to be within a range of 10^5 Hz to 10^9 Hz (see Fig. 2) [3]. In this project, we clarify the local dynamics of polar nanoregions via spin fluctuation in BF-xBT by μSR.

Polar nanoregions are considered as a sort of intrinsic inhomogeneity and may be related to internal friction. Intrinsic inhomogeneity is also linked to high-temperature superconductivity and frustrated system, which are major topics of solid-state physics. Our project significantly contributes to further understanding of these physics. High-performance relaxor ferroelectrics, such as morphotropic phase boundary of lead-based perovskites $Pb(Mg_{1/3}Nb_{2/3})O_3-PbTiO_3$ [4], show excellent piezoelectric characteristics and are highly suitable for actuator applications. Our study will elicit the further performance of these materials. In addition, our target materials BF-xBT are superior in terms of lead-free requirements from environmental and social aspects.

The goal of the experiment is clarifying the local dynamics of the polar nanoregion in the magnetic relaxor ferroelectrics BF-xBT through the longitudinal relaxation rates of muon spin. BF-xBT has the wide range of solid solution [5], so it can be easily obtained different relaxor compositions. Comparing a polar and a non-polar nanoregion in different compositions, we extract a nature of the local dynamics linked to relaxor behaviors. Another key factor is a strength of the coupling between electric and magnetic dipoles via lattice strain. We have previously studied a relation between magnetization and electric polarization in multiferroic $MnWO_4$ [6]. $MnWO_4$ exhibits a sufficiently strong coupling on the magneto-dielectric transition temperature. As $BiFeO_3$ is one of the most promising multiferroic materials with high transition temperatures [7], muon probably detects the fluctuation of the local field related to the nanoregion dynamics in BF-xBT system. To make the project successful, it is imperative to probe a longitudinal relaxation as precisely as possible. The conventional μSR experiment with higher flux and longer time window of observation is more advantageous to accomplish this. We believe that the world highest intensity pulsed muon source in J-PARC MLF MUSE is ideal for our purpose.

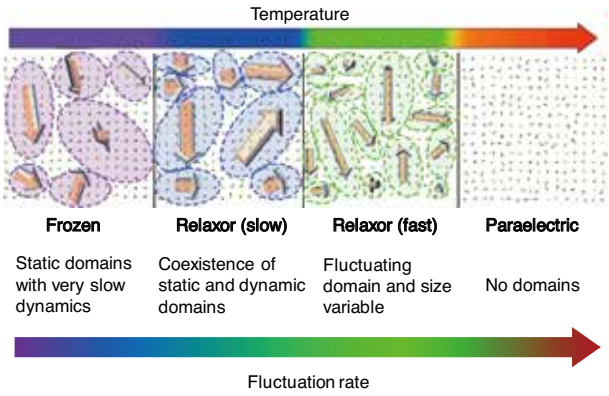

Fig. 1: Schematics of polar nanoregions [2].

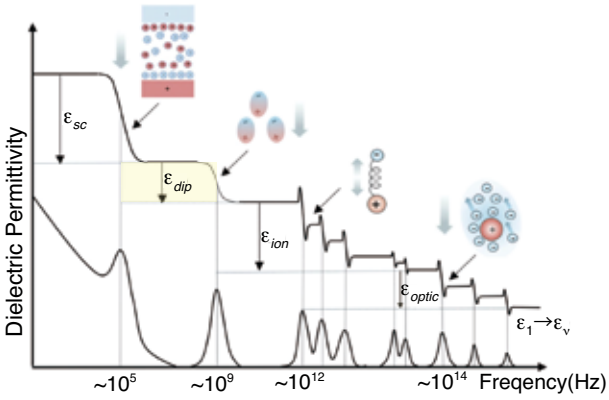

Fig. 2: Illustration of the frequency dependent dielectric spectrum in typical dielectrics [3]. The yellow part represents the contribution from orientational polarizations arising from polar nanoregions.

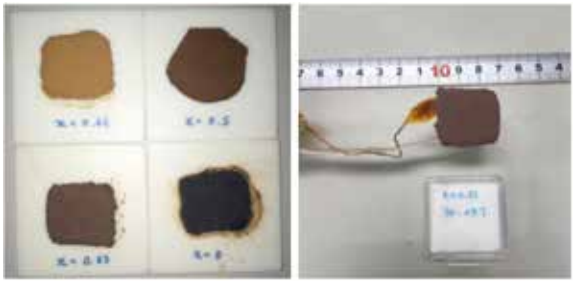

Fig. 3: Polycrystalline plates of $(1-x)BiFeO_3-xBaTiO_3$ in four compositions (x = 0, 0.33, 0.50 and 0.66) synthesized by a conventional solid-state reaction.

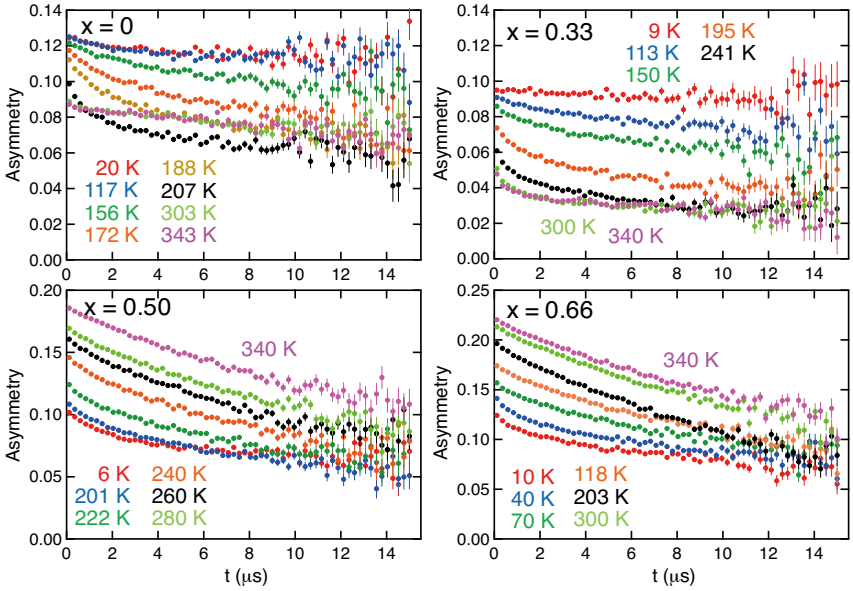

Fig. 4: Zero-field μSR time spectra of $(1-x)\mathrm{BiFeO_3}-x\mathrm{BaTiO_3}$ in four compositions ($x = 0$, 0.33, 0.50 and 0.66). Only $x = 0$ sample is not a magnetic relaxor.

We carried out the μSR experiments on polycrystalline plates of BF-xBT using Microstat with Flypast chamber installed at S1 area. We synthesized four samples with different compositions and mounted them on the silver holder as shown in Fig. 3. In order to investigate the local dynamics of BF-xBT, high statistics of muon decay events (more than 80,000,000 events for each spectrum) are required to obtain reliable data. Fluctuations related to polar nanoregions are extracted from the longitudinal relaxation rates through a comparison with different compositions.

Figures 4 show the typical zero-field μSR time spectra at several temperatures for each composition. One can see the increase of asymmetry in $x = 0$ and 0.33 as temperature decreases, which is due to a recovery of static 1/3 component of the long-range antiferromagnetic state formed at T_N far above room temperature. On the other hand, the asymmetry of $x = 0.50$ and 0.66 decrease monotonically as temperature decreases, accompanying a missing initial asymmetry probably due to a formation of muonium in $BaTiO_3$-rich phases.

Figures 5 summarize the temperature dependence of longitudinal relaxation rates λ obtained by fitting with the exponential decay function [$A(t) = A\exp(-\lambda t) +$ const.] in the late time window between 2 and 15 μs. λ of $x = 0$ shows a peak around 250 K, which may be a characteristic feature of a magnetic transition of trace impurities (e.g., Morin transition of α-Fe_2O_3). As increasing x, the peak of λ tends to become broader and each temperature change becomes smaller. Comparing λ below 150 K, it turns out that samples closer to the center of the relaxor composition ($x \sim 0.5$) exhibit a larger λ ($x = 0.50$, 0.66, 0.33 and 0 in that order). This implies that the relaxor state becomes more stable, λ becomes larger. These features may indicate that there is relationship between the local dynamics of polar nanoregions and the longitudinal relaxation rate. The next step is to find a way to remove the

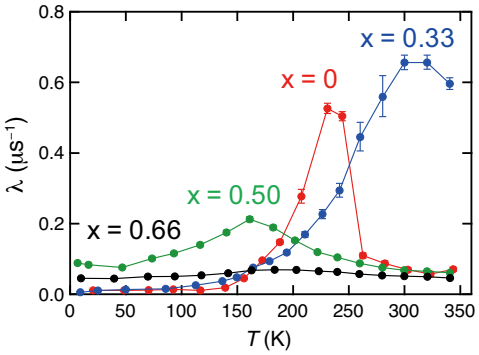

Fig. 5: Temperature dependence of longitudinal relaxation rates λ of $(1-x)\mathrm{BiFeO_3}-x\mathrm{BaTiO_3}$ in four compositions ($x = 0$, 0.33, 0.50 and 0.66).

contribution of magnetic fluctuations from these λ.

Given this situation, we are now planning detailed measurements near the antiferromagnetic transition in high temperature region (T_N = 500∼700 K) to separate the components of magnetic and charge fluctuation in BF-xBT by considering the universality of critical phenomena.

Acknowledgments

This work was supported by the MEXT under Grant No. JPMXP0112101001 and 20K05312.

References

[1] A. A. Bokov and Z. -G. Ye, J. Mater. Sci. **41** (2006) 31–52.

[2] H. Takenaka *et al.*, Nature **546** (2017) 391–395.

[3] J. N. Wilson *et al.*, APL Mater. **7** (2019) 010901(1-14).

[4] T. R. Shrout *et al.*, Ferroelectr. Lett. Sect. **12** (1990) 63–69.

[5] R. Kiyanagi *et al.*, J. Phys. Soc. Jpn. **81** (2012) 024603(1-6).

[6] H. Sagayama *et al.*, KEK Prog. Rep. **2019-3** (2019) 111–114.

[7] P. Fischer *et al.*, J. Phys. C: Solid State Phys. **13** (1980) 1931–1940.

Investigations of Unusual Heavy Fermion State in Partially Ordered State of $SmAu_3Al_7$ [J-PARC: 2020B0357]

R. Higashinaka, T. Iwami, K. Saitou, T. U. Ito[1], J. G. Nakamura[2], W. Higemoto[1], A. Koda[2], S. Kambe[1], T. D. Matsuda, and Y. Aoki

Physics Department, Tokyo Metropolitan University
[1]*Advanced Science Research Center, JAEA*
[2]*Muon Science Laboratory, Institute of Material Structure Science, KEK*

1. Introduction

Unique strongly correlated electronic properties specific to Sm systems have been discovered in recent studies, such as unusual magnetic-field-insensitive heavy-fermion behavior in $SmOs_4Sb_{12}$[1], magnetic-field-insensitive phase transitions and largely enhanced Sommerfeld coefficients γ in $Sm\,Tr_2Al_{20}$ (Tr = Ti, V, Cr, and Ta) [2-4] and partial Kondo screening state in $SmPt_2Si_2$[5].

Recently, we discovered that $SmAu_3Al_7$ is a new candidate for partial Kondo screening state. This compound crystallizes in the rhombohedral $ScRh_3Si_7$-type structure with the space group $R\bar{3}c$ (#167) [6], in which the symmetry at Sm site is trigonal. Magnetic susceptibility M/H exhibits a small cusp, evidencing the existence of a phase transition at $T_{\rm N1}$ = 2.8 K. Interestingly, the pronounced Curie-type behavior, as seen in the paramagnetic state, reappears below $T_{\rm N1}$. This behavior can be interpreted as "partially disordered phase", in which ~60% of the Sm magnetic moments remains paramagnetic below $T_{\rm N1}$. This compound shows another transition at $T_{\rm N2}$ = 0.9 K, whose origin is not clarified yet, and below $T_{\rm N2}$, a largely enhanced Sommerfeld coefficient γ ~1.5 J/K^2 mol is observed. These behaviors are similar to those of $SmPt_2Si_2$ and could be attributed to the formation of a Kondo sublattice with heavy quasi-particles in partially disordered Sm ions but this possibility has not been also clarified yet. In order to reveal the unusual magnetic ground state of $SmAu_3Al_7$ by means of a microscopic probe we performed μSR measurements.

2. Experiment

The single crystals of $SmAu_3Al_7$ were grown by Al-self flux method. μSR experiments for the single crystalline $SmAu_3Al_7$ were carried out at the S1 area of J-PARC MUSE. Fourteen pieces of single-crystalline samples were mounted on a silver sample holder with the (0001) plane perpendicular to the muon incident direction. Only the contribution from the fluctuation in local magnetic field perpendicular to the [0001] direction is observable in this experimental setup. μSR experiments were performed under zero field (ZF), weak transverse field (wTF) of 2 mT applied perpendicular to the [0001] direction and longitudinal fields (LF) up to 395 mT applied parallel to the [0001] direction over the temperature range of 0.3 - 5.1 K with a ^{3}He refrigerator. All the data were analyzed using the software suite musrfit [5].

3. Results and Discussion

Figure 1 shows asymmetry data of the ZF-μSR spectrum of $SmAu_3Al_7$ at 5.1, 2.0 and 0.31 K. Clear spin precession pattern and the decrease of $A(t=0)$ below T_{N1} indicate the development of spontaneous local field at muon stopping site in the ordered phase. In addition, the magnetic relaxation with slow relaxation rates remains even at the temperature range in which the precession appears. To estimate the magnitude of the local magnetic field $B_{\rm loc}$ at the muon site and its temperature evolution, we fitted the data below 5.1 K to the following function,

$$\begin{aligned} A(t) &= A_1 \exp(-\lambda t) + \\ & A_2 \cos(2\pi f t + \phi) \exp\left[-\frac{1}{2}(\sigma_2 t)^2\right] + \\ & A_3 \exp\left[-\frac{1}{2}(\sigma_3 t)^2\right] + A_{\rm BG}, \end{aligned} \quad (1)$$

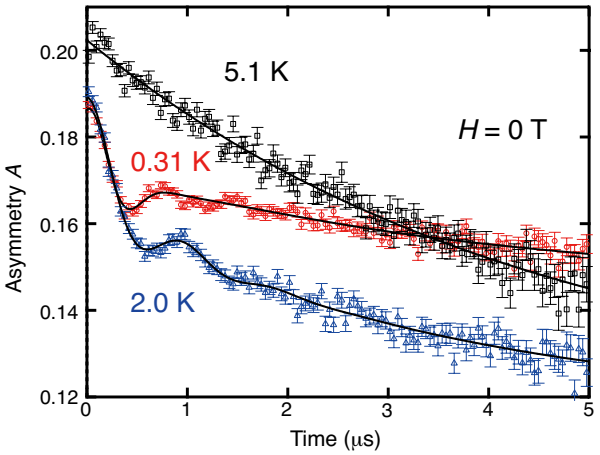

Fig. 1: ZF-μSR spectra of $SmAu_3Al_7$ at 5.1, 2.0 and 0.31 K. The solid curve represents the best fit to Eq. (1).

where A_1 (λ) and A_2 (σ_2) are the partial asymmetry (relaxation rate) for the longitudinal component and transverse component of the oscillating term, respectively. The third term(A_3 and σ_3) is for expressing the relaxation related to the development of local magnetic field. f ($= \gamma_\mu B_{\rm loc}/2\pi$) is the muon spin precession frequency, γ_μ is the muon gyromagnetic ratio ($= 2\pi \times 135.53$ MHz/T), and ϕ is the initial phase. $A_{\rm BG}$ is the background constant.

From the fitting we obtained the temperature dependence of $B_{\rm loc}$ as preliminary result (not shown). With decreasing temperature, $B_{\rm loc}$ starts to increase at around 2.8 K and saturates at around 10 mT. This temperature is consistent with $T_{\rm N1}$ determined from the temperature dependence of the magnetic susceptibility and specific heat. From this result we clarify that the transition at $T_{\rm N1}$ is a magnetic phase transition. In contrast, there is no clear anomaly at $T_{\rm N2}$. This indicates that changes of the ordered magnetic moment and/or the magnetic structure at $T_{\rm N2}$ is small and is difficult to be detected within the experimental accuracy. We also performed LF-μSR measurements at various LF at 0.31, 1.6 and 5.1 K to estimate another $B'_{\rm loc}$ attributed to the decrease of $A(t = 0)$ and revealed that $B'_{\rm loc}$ of about 0.1 T also appears below $T_{\rm N1}$. From these analyses, we found that there are at least two local magnetic fields at muon trapping sites.

To estimate the volume fraction of regions having magnetic order according to the method in Ref. [8], we performed μSR measurements under a wTF of 2 mT. The results suggest that the magnetic order develops homogeneously in the full volume fraction and that the phase separation of magnetic ordered phase and paramagnetic phase is unlikely.

In order to investigate the longitudinal component remaining below $T_{\rm N1}$, we performed the LF-μSR at 395 mT(Fig. 2) and fitted the data to the following function,

$$A(t) = A_1 \exp(-\lambda t) + A_{\rm BG}. \qquad (2)$$

From the fitting we obtained the temperature dependence of λ as preliminary result (not shown). λ shows a peak at $T_{\rm N1}$ and decreases down to lowest temperature. There are no anomaly at $T_{\rm N2}$ similar to $B_{\rm loc}(T)$. This behavior indicates that the magnetic fluctuation is gradually suppressed with decreasing temperature although the Curie-type behavior reappears below $T_{\rm N1}$. In order to clarify the inconsistency between them, further investigations by μSR for the fluctuation in $B_{\rm loc}||$ [0001] with different experimental setup, NMR and neutron experiments are required.

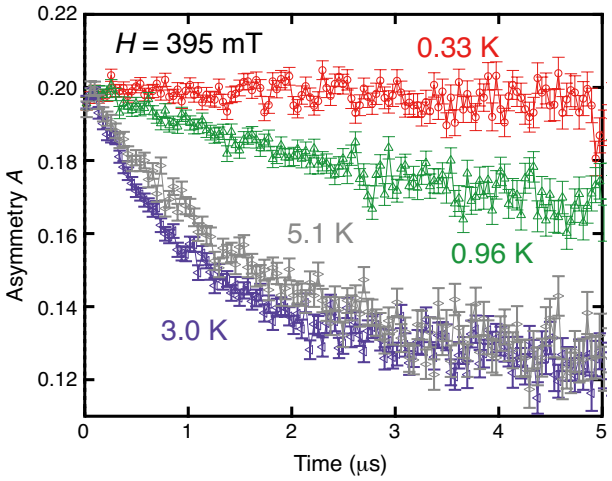

Fig. 2: LF-μSR spectra of $SmAu_3Al_7$ at 395 mT and at several temperatures.

References

[1] S. Sanada *et al.*, J. Phys. Soc. Jpn. **74** (2005) 246–249.

[2] R. Higashinaka *et al.*, J. Phys. Soc. Jpn. **80** (2011) 093703(1-4).

[3] A. Sakai and S. Nakatsuji, Phys. Rev. B **84** (2011) 201106(R)(1-5).

[4] A. Yamada *et al.*, J. Phys. Soc. Jpn. **82** (2013) 123710(1-5).

[5] K. Fushiya *et al.* J. Phys. Soc. Jpn. **83** (2014) 113708(1-4), K. Fushiya *et al.* J. Phys.: Conf. Ser. **683** (2016) 012033(1-5).

[6] S. E. Latturner *et al.*, J. Solid State Chem. **170** (2003) 48–57.

[7] A. Suter and B. M. Wojek, Physics Procedia **30** (2012) 69–73.

[8] S. R. Dunsiger *et al.*, Nat. Mater. **9** (2010) 299–303.

Effect of Bond-randomness on Mo Spin Dynamics in Geometrically Frustrated Pyrochlore Compound $Lu_2Mo_2O_5N_2$ Probed by μSR [J-PARC: 2020B0388]

S. K. Dey[1], H. Okabe[1], M. Hiraishi[1], A. Koda[1], S. Kanda[1], Y. Nagatani[1], K. Shimomura[1], K. Ishida[2], H. Kageyama[2], and R. Kadono[1]

[1]*Muon Science Laboratory, Institute of Materials Structure Science, KEK, Japan*
[2]*Department of Energy and Hydrocarbon Chemistry, Graduate School of Engineering, Kyoto University, Japan*

Geometrically frustrated magnets have been quite extensively studied in the quest of exotic magnetic ground states like quantum spin liquid (QSL), spin glass (SG) [1, 2, 3]. The local spins in these magnetic lattices are arranged on the vertices of the corner shared triangular or tetrahedral units so that the pairwise satisfaction of minimizing energy is not achieved under isotropic antiferromagnetic interaction with the nearest neighbor leading to the macroscopic degeneracy of ground states. In the geometrically frustrated lattices with small spin quantum numbers (such as $S = 1/2$), quantum fluctuation can give rise to novel QSL states without any long-range magnetic order (LRO) or spontaneous symmetry breaking down to absolute zero temperature. Low energy fractionalized magnetic excitations, called spinons, are the hallmark of the QSL states in these systems [2, 4]. While there have been several 2D-materials which show QSL-like characteristics, the candidates in 3D-materials are still scarce [1]. In this regard, geometrically frustrated quantum spin $S = 1/2$ pyrochlore antiferromagnet can be a promising candidate in realizing the 3D QSL state [1, 2].

Gapless QSL state have been suggested in a molybdate pyrochlore antiferromagnet $Lu_2Mo_2O_5N_2$ from the linear temperature dependence of magnetic specific heat down to 0.5 K and broad dynamical magnetic structure factor in the inelastic neutron scattering at 1.5 K [2]. However, the parent compound $Lu_2Mo_2O_7$ undergoes spin-glass freezing at $T_g \sim 16$ K although the system is nominally disorder free [3]. This suggests that the quantum fluctuation in $Lu_2Mo_2O_5N_2$ originates from the random substitution of O^{2-} with N^{3-} anions at both $48f$ and $8b$ Wyckoff positions [1, 4]. It is presumed that the inclusion of nitrogen also leads to the change in the Mo valence from Mo^{4+} ($4d^2$, $S = 1$) to Mo^{5+} ($4d^1$, $S = 1/2$) [1].

The randomness- or inhomogeneity-induced gapless QSL state is also called "random singlet state" [1]. It has been theoretically predicted that, when the randomness in the system is present beyond a certain critical value, this frustrated Heisenberg antiferromagnet can host a robust random spin-singlet ground state [1]. This state can be visualized as the random arrangement of nearest neighbor singlet dimer to further-neighbor singlet states. The unpaired spins which fail to form singlet dimer or are generated when a singlet dimer breaks due to spinon excitation, migrate in the sea of singlet dimer [1]. The μSR study has been proven to be a potential technique to study the local excitations of spin-singlet ground states [5, 6]. It allows to detect the spin dynamics over the frequency range of 10^5-10^9 Hz in between that of NMR and neutron experiments. While the specific heat is sensitive to all kinds of excitations, muons ($S = 1/2$) are selectively sensitive to magnetic excitations. The longitudinal muon spin relaxation rate (λ) is related to the spin-spin correlation function as

$$\lambda \sim 1/T_1 \sim \int_0^\infty \langle \vec{S}(0) \cdot \vec{S}(t) \rangle \cos(\gamma_\mu H_L t) dt \quad (1)$$

where, H_L is the applied longitudinal field along the direction of initial muon polarization and γ_μ is the muon gyromagnetic ratio = $2\pi \times 135.54$ MHz/T.

We have performed μSR measurements to study the spin dynamics in the magnetic ground state in $Lu_2Mo_2O_5N_2$. The observed zero field (ZF) μSR time spectra are shown in Fig. 1. For the temperature $\geq$ 15 K, the relaxation rate is almost in-

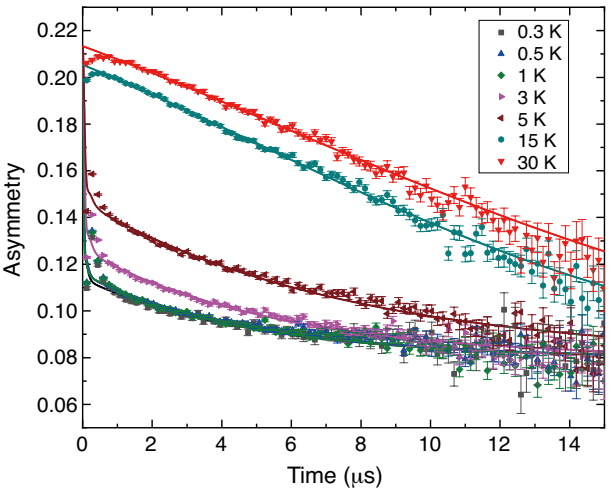

Fig. 1: ZF-μSR time spectra at various temperatures in $Lu_2Mo_2O_5N_2$.

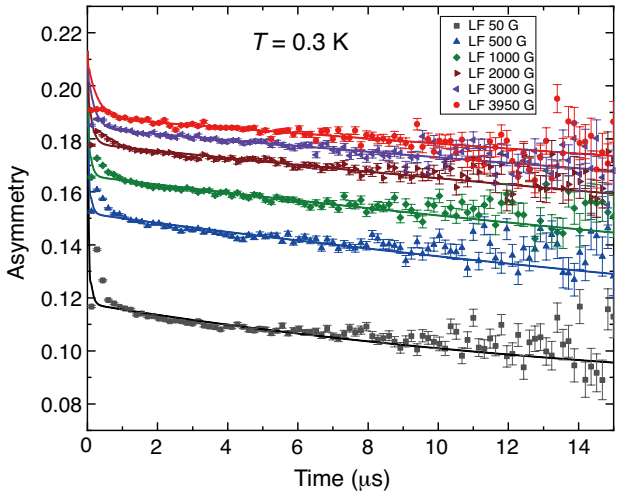

Fig. 2: Longitudinal field dependent μSR time spectra obtained at 0.3 K in $Lu_2Mo_2O_5N_2$.

dependent of temperature and mainly due to the static random distribution of nuclear magnetic moments, where the time evolution is well described by the static Gaussian Kubo-Toyabe (GKT) function. The slowing down of paramagnetic spin fluctuation leads to exponential relaxation for the dense systems. The multiplication of these two functions describes the depolarization spectra well for $T \geq$15 K. Below 15 K, the correlation of electrons starts to develop. The absence of spontaneous oscillating signal in these time spectra indicates the absence of long-ranged magnetic order. The spectra below 15 K show a fast depolarization in the early time region (t < 2 μs) followed by a slow relaxation tail. At the temperature $\leq$ 1 K, we see the upward shift of the tail which suggests the partial recovery of the 1/3 tail and emergence of quasistatic magnetic behavior due to spin-glass freezing.

We have performed longitudinal field (LF) μSR measurements in order to extract the effect of dynamical fluctuation from that of static local field distributions (which are superposed in ZF spectra). The LF-μSR time spectra at 0.3 K are shown Fig. 2. The conventional (GKT) function fails to reproduce the entire ZF- and LF-μSR time spectra. We found that all these spectra can satisfactorily be fitted with realistic physical parameters if we consider two channels of depolarization originating from two different spin dynamics. One is attributed to the "sporadic field fluctuation" [5, 6, 7] and another is to the conventional Markovian modulation [6, 7].

We have adopted "undecouplable Gaussian" function for analyzing the μSR spectra which was also used to describe the muon depolarization due to "sporadic field fluctuation" in frustrated Kagomé bilayer systems like SCGO and BSZCGO [5, 6], spinel compound $CuAl_2O_4$ [7] and quantum antiferromagnet $PbCuTe_2O_6$ [8]. The muon decay asymmetry function can be written as

$$\begin{aligned} A(t) =& A_0[x \cdot G_z^{\mathrm{GKT}}(f \cdot t, H_{\mathrm{L}}, \Delta, \nu) \\ &+(1-x) \cdot \exp(-\lambda' t)] + A_{\mathrm{bg}} \end{aligned} \tag{2}$$

Here, "x" is the volume fraction of the "sporadic field fluctuation" component and (1-x) represents the conventional Markovian dynamics in the system. Here the conventional dynamical GKT function G_z^{GKT} is scaled by a factor "f". The μ^+ spin couples to the local electronic spin for a short fraction of time "ft" of the total time "t" after its implantation in the sample [5, 6, 7] when unpaired spin originated from unconfined spinon excitation pass close to the muon site. The local field at the muon site is present not persistently but sporadically. The width of the Gaussian distribution of local field at the muon site is described by Δ and the ν is the fluctuation frequency of the local field at the muon site for the conventional dynamical GKT function. H_{L} is the longitudinal applied magnetic field in the direction of the initial muon polarization (equal to zero for the fitting of ZF spectra). The λ' represents the muon relaxation rate due to the Markovian dynamics in the system. It can be shown [5] from the scaling factor calculation that

$$\begin{aligned} &G_z^{\mathrm{GKT}}(f \cdot t, H_{\mathrm{L}}, \Delta, \nu) = \\ &G_z^{\mathrm{GKT}}(t, f \cdot H_{\mathrm{L}}, f \cdot \Delta, f \cdot \nu) \end{aligned} \tag{3}$$

Thus, the muon polarization function can be rewritten as,

$$\begin{aligned} A(t) =& A_0[x \cdot G_z^{\mathrm{GKT}}(t, f \cdot H_{\mathrm{L}}, f \cdot \Delta, f \cdot \nu) \\ &+(1-x) \cdot \exp(-\lambda' t)] + A_{\mathrm{bg}} \end{aligned} \tag{4}$$

Thus, the distribution width of the effective random field of this "undecouplable GKT" function is reduced to $f \cdot \Delta$. This function with H_{L}=0 reproduces the ZF spectra, as shown in Fig. 1 by the solid curves obtained by least-squares fits. From the analysis of the ZF spectra with Eq. (4), we found the volume fraction "x" of the sporadic field fluctuation decreases with the increase of temperature (Fig. 3) which suggests that the sporadic fluctuation transforms to the more conventional Markovian dynamics with increasing temperature. The relaxation rate λ' obtained from the Markovian dynamical part increases towards $T \to 0$ which symbolizes the slowing down of spin fluctuation (Fig. 3). Here, we do not see a λ-like peak which would signify the spin glass freezing in the system. Unlike spin-glass systems where the value of relaxation rate increases by several orders of magnitude towards the T_{g} [9], we see relatively smaller increase towards the absolute zero temperature. The relaxation rate λ'

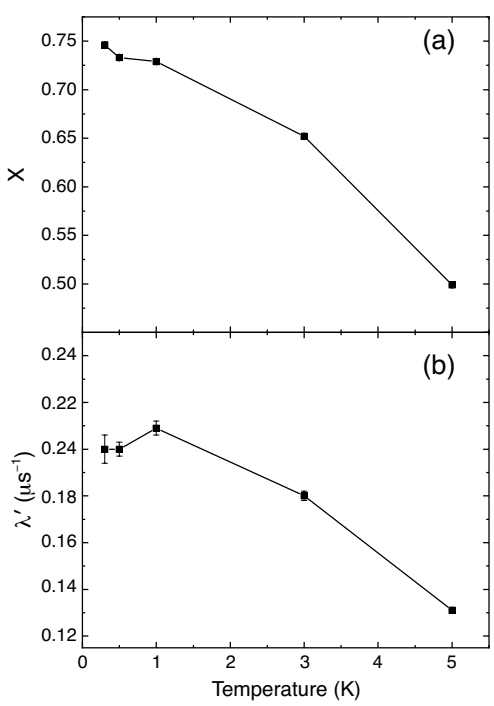

Fig. 3: Temperature dependence of the (a) volume fraction of the sporadic field fluctuation component "x", and (b) the exponential relaxation rate λ' obtained by fitting ZF-μSR time spectra in $Lu_2Mo_2O_5N_2$.

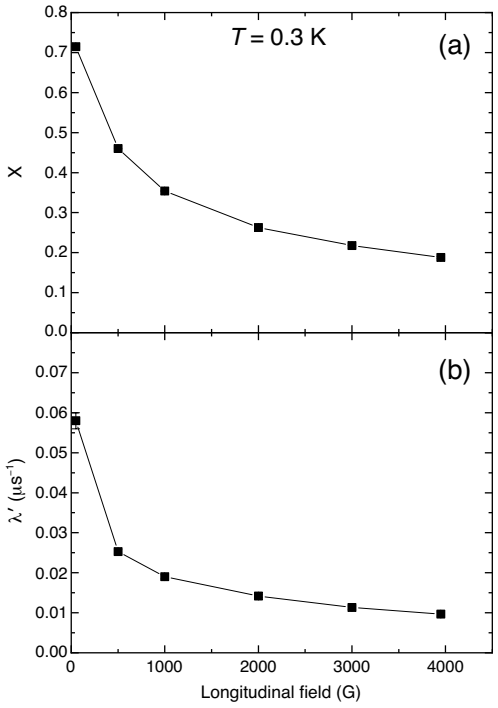

Fig. 4: Longitudinal field dependence of the (a) volume fraction of the sporadic field fluctuation component "x", and (b) the exponential relaxation rate λ' at 0.3 K in $Lu_2Mo_2O_5N_2$.

almost shows a plateau behavior towards the low temperature region below 1 K, which indicates persistent Markovian fluctuation although the dynamics have relatively slowed down.

The LF spectra obtained at 50 G and above at 0.3 K are shown in Fig. 2 in order to extract the electronic contribution by decoupling the contribution of nuclear magnetic moments. With increasing LF, we see the upward shift of the horizontal tail due to the decoupling of quasistatic local fields. This suggests that the significant amount of implanted muons probes quasistatic fields from Mo electronic magnetic moments. The initial Gaussian decay of the depolarization with the strong dependence of depolarization on LF and the upward shift of the ZF spectra at temperature ≤ 1 K point out the presence of sporadic field fluctuation in the system where relatively slow spin dynamics prevails ($\nu \sim \Delta$). The values of Δ and ν were found to be ~ 100 μs^{-1} and 80 MHz, respectively, from the analysis of the ZF and LF spectra. The value of "f" was found to be ~ 0.3 at the base temperature 0.3 K. The f, Δ and ν values are shared for all $H_{\rm L}$ values. The value of "x" decreases with increasing LF (Fig. 4), which may indicate that the sporadic dynamics is suppressed by LF to invoke the conventional Markovian dynamics. The $H_{\rm loc} \sim \Delta/\gamma_\mu \sim$ 1180 G is the local field created by unpaired spin released from the dimer due to unconfined spinon excitation or the orphan spins at the muon site with the fluctuation frequency ν and time correlation function $\sim \exp(-\nu t)$. The field exists for the time "ft", whereas $H_{\rm loc} = 0$ for the rest of the time $(1-f)\cdot t$ from the sporadic field fluctuation. Relaxation is observed during "ft" where the fluctuation of $H_{\rm loc}$ is governed by Markovian dynamics. This model seems to reproduce the LF- and ZF-μSR spectra coherently without introducing additional assumptions. The Gaussian-like lineshape is expected for $\Delta \geq \nu$. When the Mo^{5+} $4d^1$ $S = 1/2$ spin moments nearby muons form singlet pair, we only expect very small fields from distant unpaired spins. But, if the adjacent spin is unpaired, it can produce significant local field. The unpaired time fraction "f" can be understood as the ratio of the orphan spins or the unpaired spins due to spinon excitation migrating in the sea of spin-singlet dimer to the number of spin-singlet pairs at any instant of time [5].

The sporadic dynamics are persistent at the lowest temperature and the values of Δ and ν, which determine the relaxation rate, do not decrease with decreasing temperature. Thus, the classical thermal fluctuation does not apply here as it is expected that the relaxation rate would decrease with decreasing temperature without showing any plateau [5]. Here

saturation of the relaxation rate from the sporadic field fluctuation component suggests that the spin dynamics in this quantum spin $S = 1/2$ system are purely due to the quantum fluctuation at the lowest temperature. The exponentially relaxing component shows a slowing down of the spin dynamics towards the absolute zero temperature and probably, static order emerges in these magnetic domains in the system.

References

[1] K. Uematsu and H. Kawamura, Phys. Rev. Lett. **123** (2019) 087201(1-6).

[2] L. Clark *et al.*, Phys. Rev. Lett. **113** (2014) 117201(1-5).

[3] L. Clark *et al.*, J. Solid State Chem. **203** (2013) 199–203.

[4] Y. Iqbal *et al.*, Phys. Rev. Mater. **1** (2017) 071201(R)(1-6).

[5] Y. J. Uemura *et al.*, Phys. Rev. Lett. **73** (1994) 3306–3309.

[6] D. Bono *et al.*, Phys. Rev. Lett. **93** (2004) 187201(1-4).

[7] H. Cho *et al.*, Phys. Rev. B **102** (2020) 014439(1-11).

[8] P. Khuntia *et al.*, Phys. Rev. Lett. **116** (2016) 107203(1-5).

[9] M. Hiroi *et al.*, Phys. Rev. B **88** (2013) 024409(1-11).

Noncentrosymmetric Hyperkagome Germanide Magnets [J-PARC: 2020B0399]

S. Shamoto[1,2,3,4], D. P. Sari[4,5], I. Watanabe[4], T. U. Ito[3], W. Higemoto[3], Y. Chen[2], M. K. Lee[2], H. Yamauchi[3], A. Koda[6], and L.-J. Chang[2]

[1]*Comprehensive Research Organization for Science and Society, CROSS*
[2]*National Cheng Kung University*
[3]*Advanced Science Research Center, JAEA*
[4]*Meson Science Laboratory, RIKEN Nishina Center for Accelerator-Based Science*
[5]*Shibaura Institute of Technology*
[6]*Muon Science Laboratory, Institute of Materials Structure Science, KEK*

Unconventional phase transitions have been discovered in various materials[1]. One of them is a phase separation at the tri-critical point of quantum phase transition[2]. Partial magnetic order has been observed in a noncentrosymmetric compound of MnSi near the quantum phase transition under pressure[3, 4]. The partial magnetic order is accompanied with heavy Fermion behavior in the pressure region. The large electronic specific heat is attributed to the existence of the slowly fluctuating partial magnetic order. On the search of new unconventional magnetic transition, we occasionally discovered the highest-temperature magnetic short-range order (SRO) in a new noncentrosymmetric magnet Mn_3RhSi by the complementary use of muon spin relaxation, neutron, X-ray scattering, electron diffraction, and magnetization measurements[5]. The magnetic Mn ions form a hyperkagome network as observed in β-Mn. β-Mn (a=6.315 Å) is also known to exhibit the heavy Fermion behavior at the quantum critical point, in addition to the spin liquid behavior[6]. Mn_3RhSi is an ordered β-Mn-type alloy, where non-magnetic Mn atoms (screened by conduction electrons) in β-Mn are replaced by Rh and Si. We think that the unconventional magnetic SRO emerges due to the spatially inhomogeneous order parameter, where the Lifshitz condition is violated by the Dzyalonshinskii-Moriya interaction in a noncentrosymmetric magnet. The intriguing point is not limited in the highest-temperature record of magnetic SRO at 720 K, but also in the observed **Q**-position different from the long- range antiferromagnetic (AF) order **Q**-position. Similar magnetic SRO is also observed in a skyrmion phase [7]. To reveal the mechanism, it is necessary to complete the phase diagram by measuring the related family compounds such as Mn_3IrGe (a=6.6279 Å) and Mn_3CoGe (a=6.3977 Å) with larger lattice constant (or narrower bandwidth) than those of Mn_3RhSi (a=6.4665 Å). Mn_3IrGe exhibits peculiar temperature dependence of resistivity ($10^{-1}\mu\Omega$cm). Our preliminary measurements of resistivity of Mn_3CoGe and Mn_3CoSi show nonmetallic behavior with higher resistivity than that of Mn_3IrGe, which increases as decreasing temperature.

The μSR results are summarized in Fig. 1. The Néel temperatures of Mn_3CoGe and Mn_3IrGe were estimated as 175 and 234 K, respectively. In this germanide system, however, we did not observe any magnetic short-range order above the Néel temperature, in contrast to Mn_3RhSi case[5]. Instead, we observed μSR anomaly at a temperature well below T_N as a further drop in initial asymmetry. We also study them by neutron total scattering at NOVA@J-PARC/MLF (2020B0415) as a complementary use of neutron and muon. The detailed analysis is underway.

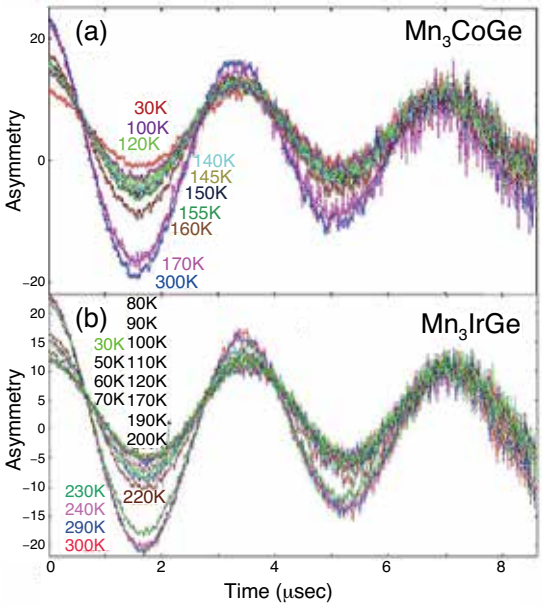

Fig. 1: μSR time spectra of Mn_3CoGe and Mn_3IrGe under a transverse field of 20 G at various temperatuers.

References

[1] S. Shamoto, J. Phys. Soc. Jpn. **88** (2019) 081008(1-11).
[2] D. Belitz, *et al.*, Rev. Mod. Phys. **77** (2005) 579–632.
[3] C. Pfleiderer *et al.*, Nature **427** (2004) 227–231.
[4] Y. J. Uemura *et al.*, Nat. Phys. **3** (2007) 29–35.
[5] H. Yamauchi *et al.*, Commun. Mat. **1** (2020) 43(1-6).
[6] H. Nakamura *et al.*, J. Phys.: Condens. Matter **9** (1997) 4701–4728.
[7] V. Ukleev *et al.*, npj Quant. Mat. **6** (2021) 40(1-8).

The μSR observation of the magnetic double transition in $YbCu_4Au$
[J-PARC: 2020B0402]

T. Taniguchi[1], K. Osato[1,2], T. Kitazawa[1,2] D. P. Sari[3,4], I. Watanabe[3], A. Koda[5] and M. Fujita[1]

[1]*Institute for Materials Research, Tohoku University*
[2]*Department of Physics, Tohoku University*
[3]*Meson Science Laboratory, RIKEN Nishina Center for Accelerator-Based Science*
[4]*College of Engineering, Shibaura Institute of Technology*
[5]*Muon Science Laboratory, Institute of Materials Structure Science, KEK*

f electron systems show a variety of quantum critical phenomena by applying pressure or magnetic field, due to the small energy scale. This system is an ideal situation to research the whole quantum critical phenomena. The previous works done with high-quality crystals and state-of-the-art experimental methods brought a lot of knowledge of the quantum critical phenomena originating from the spin degree of freedom[1]. In these days, the quantum critical phenomena attributed to the novel degree of freedoms is much attracted. The valence is the most promising candidate, and actual candidate materials are being extensively explored.

$YbCu_4Au$ is a candidate material, which shows the unconventional quantum critical phenomena derived from valence fluctuation [2,3]. This compound has been extensively studied with polycrystalline samples. It was reported that the field-tuned QCP emerges at $H = 13$ kOe and antiferromagnetic ordered phase exists in low magnetic fields below the the critical magnetic field. Furthermore, in a high magnetic field region, evidence of valence crossover was observed. The crossover temperature becomes 0 K at 13 kOe with decreasing the magnetic field. In order to study the quantum criticality in $YbCu_4Au$ more precisely, a single crystal is indispensable.

Recently, we succeeded in growing crystals of $YbCu_4Au$ for the first time and performed XRD, EDS, Laue-diffraction measurements to characterize the sample. We confirmed that the sample is of single crystal of $YbCu_4Au$ and no impurity phase is included. We have measured the magnetization, specific heat, and electrical resistance on the crystal. Due to the improvement of the crystal quality, we revealed that the temperature dependence of the specific heat exhibits anomalies at two certain temperatures below 1 K in zero and low magnetic fields. The two transitions were also observed in different single crystal samples synthesized differently, suggesting that the anomalies are intrinsic nature of $YbCu_4Au$.

The purpose of this research is to determine the order parameters of $YbCu_4Au$ under zero- and low-fields. Muon spin relaxation (μSR) measurement is a powerful tool to obtain information on static and dynamic magnetism. We, therefore, performed μSR measurements using pulsed positive muon beam in Material and Life Science Experimental Facility (MLF) in J-PARC, Japan, and in RIKEN-RAL Muon Facility (RAL) in Rutherford Appleton Laboratory, UK.

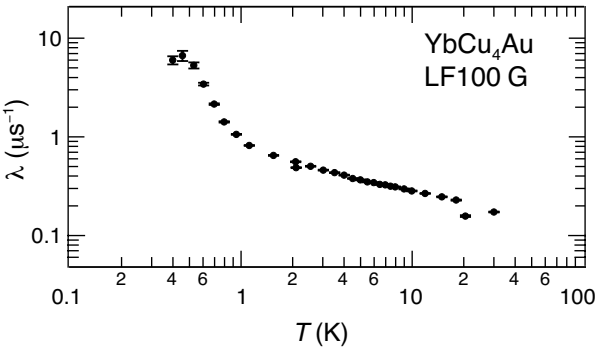

Fig. 1: Temperature dependence of the muon spin relaxation rate λ of $YbCu_4Au$ in a longitudinal field of 100 G.

Figure 1 shows the temperature dependence of the muon spin relaxation rate λ down to 0.4 K. To derive the magnetic fluctuation of the f electron, we applied a longitudinal magnetic field of 100 G. Since λ is rapidly enhancement below 1 K, the order parameters are magnetic. However, the muon time spectra don ' t show rotation behavior even at the lowest temperature (0.4 K), and thus we could not determine the order parameters in this measurement. Further measurement, particularly ultra-low temperature μSR measuements would give a clue to determine the electronic states of $YbCu_4Au$.

References

[1] G. R. Stewart, Rev. Mod. Phys. **56** (1984) 755–787.

[2] E. Bauer *et al.*, Phys. Rev. B **50** (1994) 9300–9307.

[3] S. Wada *et al.*, J. Phys.: Condens. Matter **20** (2008) 175201(1-8).

REPORT
OF THE
INTERNATIONAL ADVISORY
COMMITTEE
ON THE J-PARC PROJECT

IAC REPORT

The International Advisory Committee (IAC) on J-PARC met virtually on March 4th and 5th, 2021 to review the progress and prospects since the last in person meeting of March 2019. (The 2020 meeting was cancelled due to first wave of the COVID-19 pandemic.)

All the presentations were made available ahead of time, questions from IAC members were solicited and addressed in the 2 video calls. Overall, the committee was able to fulfill its mandate as set by the director.

SUMMARY OF THE RECOMMENDATIONS BY SECTIONS IN THE REPORT

Recommendations:
The IAC recommends making available additional staff with part of their duties assigned to the 'instrument scientist' role. Developing a strong and stable muon users community relies on such support from the facility:

- IAC recommends strengthening the group of MUSE people being responsible for the M1/M2 proton beam line/muon production target. On a medium-term, the IAC recommends that J-PARC manages the safe delivery of proton beam to the muon production target by a J-PARC group.
- IAC strongly recommends that MUSE management establishes new links of MUSE with other organizations to widely support the muon activities and community by increasing the number of staff to keep and enhance the current and future activities.

The IAC considers it urgent that a spare muon target should be constructed as soon as possible. MUSE should work on a spare target with highest priority, and the management should guarantee the required funding.

The IAC recommends a re-evaluation of the laser systems for USM generation within the next two years and reiterates its recommendation to set up a "laser development team" under the responsibility of J-PARC to ensure long-term stable laser operation for all experiments requesting USM.

MUSE management should clearly articulate the priorities of the various projects. It is also essential to develop a plan for the resources required to run MUSE as a user facility with all beam lines completed.

SCIENTIFIC PROGRAMS:

- **MUSE Facility**

The IAC is pleased to see the continuing outstanding work of the MUSE team in all fields of its responsibilities, and the increase of permanent staff by two people. The MUSE team overcame the challenges of the COVID-19 pandemic by quickly reorganizing the beam schedule and enabling a mail-in-service and remote control of experiments. This allowed minimizing the loss of beam days, while putting additional load on MUSE staff. IAC acknowledges the very safe and stable operation of the facility at 600 kW proton beam power at an outstanding availability of 95.3%. Another test at 1 MW during a period of 36 h demonstrated that the facility and instruments are well prepared for higher beam power operation.

The IAC highly appreciates the continuing interest from broad scientific communities in muon science at J-PARC, which we attribute to the well-balanced program of MUSE between fundamental physics, materials science, and developing new research directions. These include the muon microscope, new mSR techniques to measure changes of sample properties on a minutes time scale ("transient mSR"), and the negative muon program. The negative muon program is making significant progress, including industrial applications and joint projects of humanities and sciences in non-destructive elemental analysis, and the combination of latest x-ray detector technologies for observations in space with negative muons to develop high-resolution spectroscopy of muonic atoms and "m- 3D non-destructive imaging".

In the ongoing transition from the construction phase to operational mode, the IAC appreciates the impressive progress in instrumentation for user operation in the D1/D2 and S1 areas, and the first successful test of the new high field (5 Tesla) mSR spectrometer "CYCLOPS" in S1. The IAC is pleased to see the efforts and progress in constructing the S2- and H-lines. These are important steps to start the long-awaited particle physics program in S2 (Mu 1s-2s two-photon spectroscopy) and the MuSEUM and DeeMe experiments in H1 in 2021, and to prepare for the extension of the H-line to start the gm-2 experiment in 2025. Commissioning of the U-line for the generation of ultra-sow muons (USM) is continuing, with detailed studies to improve the transmission of USM. The USM-mSR spectrometer has been commissioned, and the users program at the U-line is expected to start within the next three years.

The Lyman-a laser for generation of USM by laser ionization is making progress, and the energy per pulse has been increased by a factor of two in 2020. The improved laser will be used for USM generation in 2021. Since the generation of USM is of pivotal importance for the muon program at MUSE (USM-mSR, muon microscope, gm-2), IAC is looking forward with great interest to the results of the improved system.

Instead of the Lyman-a laser, the Mu 1s-2s two photon transition could be a promising backup scheme for the generation of USM. The laser for the Mu 1s-2s experiment in the S2 area is currently being developed and will be tested at the end of 2021 in the S2 area.

At the moment, no backup muon target is available after replacing the first rotation target in 2019, which was five years in operation. Unanticipated problems at 1 MW operation may cause a reduction of target lifetime. Failure of the present target risks the entire muon program.

Insufficient manpower for user operation and the laser for USM generation are the most important concerns about the operation and further development of the facility. These pose a risk for the full exploitation of the extraordinarily rich scientific opportunities of muon applications from fundamental to applied/materials science.

Appendix

List of Publication, 2020

1. S. Abe and T. Sato, J. Kuroda, S. Manabe, Y. Watanabe, W. Liao, K. Ito, M. Hashimoto, M. Harada, K. Oikawa, and Y. Miyake, "Impact of Hydrided and Non-Hydrided Materials Near Transistors on Neutron-Induced Single Event Upsets", IEEE International Reliability Physics Symposium Proceedings (IRPS), (2020) 9128951(1-7).
2. T. Aoyagi, Y. Honda, H. Ikeda, M. Ikeno, K. Kawagoe, T. Kohriki, T. Kume, T. Mibe, K. Namba, S. Nishimura, N. Saito, O. Sasaki, N. Sato, Y. Sato, H. Sendai, K. Shimomura, S. Shirabe, M. Shoji, T. Suda, T. Suehara, T. Takatomi, M. Tanaka, J. Tojo, K. Tsukada, T. Uchida, T. Ushizawa, H. Wauke, T. Yamanaka, and T. Yoshioka, "Performance evaluation of a silicon strip detector for positrons/electrons from a pulsed a muon beam", J. Instrum. **15** (2020) P04027(1-16).
3. J. Beare, G. Beer, J. H. Brewer, T. Iijima, K. Ishida, M. Iwasaki, S. Kamal, K. Kanamori, N. Kawamura, R. Kitamura, S. Li, G. M. Luke, G. M. Marshall, T. Mibe, Y. Miyake, Y. Oishi, K. Olchanski, A. Olin, M. Otani, M. A. Rehman, N. Saito, Y. Sato, K. Shimomura, K. Suzuki, M. Tabata, and H. Yasuda, "Study of muonium emission from laser-ablated silica aerogel", Prog. Theor. Exp. Phys. **2020** (2020) 123C01(1-26).
4. M. Fujihala, K. Morita, R. Mole, S. Mitsuda, T. Tohyama, S. Yano, D. Yu, S. Sota, T. Kuwai, A. Koda, H. Okabe, H. Lee, S. Itoh, T. Hawai, T. Masuda, H. Sagayama, A. Matsuo, K. Kindo, S. Ohira-Kawamura, and K. Nakajima, "Gapless spin liquid in a square-kagome lattice antiferromagnet", Nat. Commun. **11** (2020) 3429(1-7).
5. H. Fujii, K. Hara, K. Hayashi, H. Kakuno, H. Kodama, K. Nagamine, K. Sato, S. Kim, A. Suzuki, T. Sumiyoshi, K. Takahashi, F. Takasaki, S. Tanaka, and S. Yamashita, "Investigation of the Unit-1 nuclear reactor of Fukushima Daiichi by cosmic muon radiography", Prog. Theor. Exp. Phys. **2020** (2020) 043C02(1-14).
6. M. Fujita, K. M. Suzuki, S. Asano, H. Okabe, A. Koda, R. Kadono, and I. Watanabe, "Magnetic behavior of *T'*-type Eu_2CuO_4 revealed by muon spin rotation and relaxation measurements", Phys. Rev. B **102** (2020) 045116(1-7).
7. D. Hirai, A. Koda, A. Matsuo, K. Kindo, T. Yajima, and Z. Hiroi, "Muon Spin Rotation, High-Field Magnetization, and Structural Study on a Spin–Orbit-Entangled Mott Insulator Ba_2MgReO_6", JPS Conf. Proc. **30** (2020) 011143(1-6).
8. M. Hiraishi, K. M. Kojima, H. Okabe, S. Takeshita, A. Koda, R. Kadono, R. Khasanov, S. Iimura, S. Matsuishi, and H. Hosono, "Magnetism driven by strong electronic correlations in the heavily carrier-doped iron oxypnictide $LaFeAsO_{0.49}H_{0.51}$", Phys. Rev. B **101** (2020) 174414(1-7).

9. T. Ishida, E. Wakai, S. Makimura, A. M. Casella, D. J. Edwards, R. Prabhakaran, D. J. Senor, K. Ammigan, S. Bidhar, P. G. Hurh, F. Pellemoinee, C. J. Denshamf, M. D. Fitton, J. M. Bennett, D. Kim, N. Simos, M. Hagiwara, N. Kawamura, S. Meigo, K. Yonehara, On behalf of the RaDIATE COLLABORATION, "Tensile behavior of dual-phase titanium alloys under high-intensity proton beam exposure: Radiation-induced omega phase transformation in Ti-6Al-4V", J. Nucl. Mater. **541** (2020) 152413(1-12).
10. Y. Ishii, S. Horio, Y. Noda, M. Hiraishi, H. Okabe, M. Miyazaki, S. Takeshita, A. Koda, K. M. Kojima, R. Kadono, H. Sagayama, H. Nakao, Y. Murakami, and H. Kimura, "Electronic charge transfer driven by spin cycloidal structure", Phys. Rev. B **101** (2020) 224436(1-7).
11. T. U. Ito, W. Higemoto, and K. Shimomura, "Negatively Charged Muonium and Related Centers in Solids", J. Phys. Soc. Jpn. Phys. **89** (2020) 051007(1-8).
12. K. Kuramochi, T. Shimano, T. Nishio, H. Okabe, A. Koda, K. Horigane, J. Akimitsu, and H. Ogino, "Synthesis and physical properties of the new iridium oxyfluoride $Sr_2Ir(O,F)_{6-\delta}$ using a topochemical reaction method", Phys. Rev. Materials **4** (2020) 013403(1-6).
13. J. Kuroda, S. Manabe, Y. Watanabe, K. Ito, W. Liao, M. Hashimoto, S. Abe, M. Harada, K. Oikawa, and Y. Miyake, "Measurement of Single-Event Upsets in 65-nm SRAMs Under Irradiation of Spallation Neutrons at J-PARC MLF", IEEE Trans. Nucl. Sci. **67** (2020) 1599-1605.
14. W. Liao, M. Hashimoto, S. Manabe, Y. Watanabe, S. Abe, M. Tampo, S. Takeshita, and Y. Miyake, "Impact of the Angle of Incidence on Negative Muon-induced SEU Cross Sections of 65-nm Bulk and FDSOI SRAMs", IEEE Trans. Nucl. Sci. **67** (2020) 1566-1572.
15. S. Makimura, J. Park, A. Sato, S. Matoba, N. Kawamura, T. Yamazaki, K. Ninomiya, D. Tomono, N. Nakazato, M. Calviani, and I. L. Garcia, "Feasibility Study for NITE SiC/SiC as the Target Material for Pions/Muons Production at High-Power Proton Accelerator Facilities", JPS Conf. Proc. **28** (2020) 031005(1-6).
16. S. Makimura, S. Matoba, and N. Kawamura, "Status and Future Prospect of Muon Target at J-PARC MLF", PoS (NuFACT2019) **369** (2020) 124(1-5).
17. S. Meigo, M. Ooi, and H. Fujimori, "Two-parameter model for optimizing target beam distribution with an octupole magnet", Phys. Rev. Accel. Beams **23** (2020) 062802(1-24).
18. H. Natori, "Development of very slow negative muon beam", PoS (NuFACT2019) **369** (2020) 090(1-4).
19. T. Ogitsu, M. Iio, N. Kawamura, and M. Yoshida, "Development of Radiation-Tolerant HTS Magnet for Muon Production Solenoid", Instruments **4** (2020) 30(1-13).

20. S. Okada, T. Azuma, D. A. Bennett, P. Caradonna, W. B. Doriese, M. S. Durkin, J. W. Fowler, J. D. Gard, T. Hashimoto, R. Hayakawa, G. C. Hilton, Y. Ichinohe, P. Indelicato, T. Isobe, S. Kanda, M. Katsuragawa, N. Kawamura, Y. Kino, Y. Miyake, K. M. Morgan, K. Ninomiya, H. Noda, G. C. O'Neil, T. Okumura, C. D. Reintsema, D. R. Schmidt, K. Shimomura, P. Strasser, D. S. Swetz, T. Takahashi, S. Takeda, S. Takeshita, H. Tatsuno, Y. Ueno, J. N. Ullom, S. Watanabe, and S. Yamada, "X-ray Spectroscopy of Muonic Atoms Isolated in Vacuum with Transition Edge Sensors", J. Low Temp. Phys. **200** (2020) 445-451.
21. Y. Sue, M. Yotsuzuka, K. Futatsukawa, K. Hasegawa, T. Iijima, H. Iinuma, K. Inami, K. Ishida, N. Kawamura, R. Kitamura, Y. Kondo, T. Mibe, Y. Miyake, T. Morishita, Y. Nakazawa, M. Otani, N. Saito, K. Shimomura, Y. Takeuchi, T. Ushizawa, T. Yamazaki, and H. Yasuda, "Development of a bunch-width monitor for low-intensity muon beam below a few MeV", Phys. Rev. Accel. Beams **23** (2020) 022804(1-7).
22. J. Sugiyama, I. Umegaki, S. Takeshita, H. Sakurai, S. Nishimura, O. K. Forslund, E. Nocerino, N. Matsubara, M. Månsson, T. Nakano, I. Yamauchi, K. Ninomiya, M. K. Kubo, and K. Shimomura, "Nuclear magnetic field in $Na_{0.7}CoO_2$ detected with μ^-SR", Phys. Rev. B **102** (2020) 144431(1-7).
23. C. Tan, Z. F. Ding, J. Zhang, Z. H. Zhu, O. O. Bernal, P. C. Ho, A. D. Hillier, A. Koda, H. Luetkens, G. D. Morris, D. E. MacLaughlin, and L. Shu, "Slow magnetic fluctuations and critical slowing down in $Sr_2Ir_{1-x}Rh_xO_4$", Phys. Rev. B **101** (2020) 195108(1-9).
24. S. Tsunoda, K. Horigane, H. Okabe, K. Machida, M. Akimitsu, K. Kawashima, R. Horie, K. Kobayashi, A. Koda, R. Kadono, and J. Akimitsu, "μSR study of the magnetic state in hole and electron doped Sr_2IrO_4", JPS Conf. Proc. **30** (2020) 011145(1-6).
25. T. Uchino, N. Teramachi, R. Matsuzaki, E. Tsushima, S. Fujii, Y. Seto, K. Takahashi, T. Mori, Y. Adachi, Y. Nagashima, Y. Sakaguchi, K. Ohishi, A. Koda, T. Sakurai, and H. Ohta, "Proximity coupling of superconducting nanograins with fractal distributions", Phys. Rev. B **101** (2020) 035146(1-12).
26. I. Umegaki, Y. Higuchi, Y. Kondo, K. Ninomiya, S. Takeshita, M. Tampo, H. Nakano, H. Oka, J. Sugiyama, M. K. Kubo, and Y. Miyake, "Nondestructive High-Sensitivity Detections of Metallic Lithium Deposited on a Battery Anode Using Muonic X-rays", Anal. Chem. **92** (2020) 8194-8200.
27. Z. Xu, T. Sato, J. Nakamura, A. Koda, K. Shimomura, A. Filonov, D. Migas and T. Suemasu, "Hydrogen states in hydrogen-passivated semiconducting barium disilicide measured via muon spin rotation", Jpn. J. Appl. Phys. **59** (2020) 071004(1-7).
28. S. Yamamoto, K. Ninomiya, N. Kawamura, and Y. Hirano, "Optical imaging of muons", Sci. Rep. **10** (2020) 20790(1-11).

29. 三宅 康博 , “J-PARC ミュオン施設「J-PARC MUSE」” (J-PARC Muon Facility, MUSE), J. Comput. Chem., Jpn. **19** (2017) A12-A18 [in Japanese].
30. 下村 浩一郎 , “ ミュオニウム ー基礎から応用までー ” (Muonium -from fundamental to application-), J. Comput. Chem., Jpn. **19** (2017) 80-86 [in Japanese].
31. 平石 雅俊, 小嶋 健児, 岡部 博孝, 幸田 章宏, 門野 良典, 井手 啓介, 松石 聡, 雲見 日出也, 神谷 利夫, 細野 秀雄 , “ 擬似水素としてのミュオンと第一原理計算の組み合わせによる水素の電子状態研究 ” (Study of the Electronic State of Hydrogen by a Combination of the Muon as Pseudo Hydrogen and First-Principles Calculation), J. Comput. Chem., Jpn. **19** (2020) 106-114 [in Japanese].

List of Proposals in FY2020 (2020-A) MLF

Exp-No.	Spokesperson	Title
2020A0002	K. Nishimura	Hydrogen trapped sites in aluminum alloys studied by zero-field muon spin relaxation method
2020A0019 (P-type)	S. Ito	Detailed μSR study of thiocarbonyl-muonium adducts
2020A0051	L. Shu	Muon Spin relaxation/rotation studies of non-centrosymmetric superconductor $NbGe_2$
2020A0066	M. Fujihara	muSR study of the spin-1/2 one-dimensional Heisenberg antiferromagnet $Cd_2Cu_2SO_4(PO_4)_2$ $5H_2O$
2020A0078	J. sugiyama	Negative muon spin rotation and relaxation on battery materials
2020A0079	K. Terada	Development of non-destructive elemental analysis of Lunar sample using negative Muon beam
2020A0130	W. Higemoto	Negative Muon capture process and electronic state in correlated electron systems
2020A0131	T. Taniguchi	the novel quantum criticality in $YbCu_4Ni$
2020A0132	S. Tsutsui	Magnetic dynamics in quasi-skutterudite compounds $Sm_3T_4Ge1_3$ (T: transition metal) probed by mu^+SR
2020A0184	I. Umegaki	Non-Destructive Detection of Li Deposition in a Li-ion Battery With Muonic X-rays
2020A0186	I. Yamauchi	muSR study on the exotic ground state of the diamond lattice magnet
2020A0191	Y. Sugawara	μSR analysis of muon/muonium dynamics of protein components
2020A0193	K. Kubo	Non-destructive analysis of light elements by negative muon lifetime measurement
2020A0197	X. Zheng	muSR study of two typical elasticoluminescence materials series of Eu:$SrAl_2O_4$ and $LiNbO_3$:Pr
2020A0202 (P-type)	K. Takahisa	Measurement of the muon capture on ^{3}He to study the nuclear three body force
2020A0204	S. Shimizu	Measurement of muon spin relaxation time in scintillating materials
2020A0205	W. Hong	Searching for the antiferromagnetic quantum critical point in $Sr_2CuTe_{1-x}W_xO_6$
2020A0207	Y. Sugawara	Approach to site selective μSR measurements of histidine
2020A0208 (P-type)	S. K. Dey	Quantum magnetism in spinel oxide $CuAl_2O_4$

Exp-No.	Spokesperson	Title
2020A0210	U. Widyaiswari	Investigating the Magnetic Ground State and Spin Dynamics of $(Nd_{1-x}Ca_x)_2Ru_2O_7$ by ZF and LF-muSR
2020A0253	A. D. Pant	Generation of Ultra Cold Muonium into Vacuum
2020A0284	S. Takeshita	Negative muon spin relaxation measurement to probe molecular dynamics in polymer
2020A0286	H. Yukawa	μSR approach to the understanding of hydrogen behavior in Pd-Cu alloy with B2-type crystal structure
2020A0288	T. U. Ito	Hyperfine and thermal properties of a muonium defect in ferroelectric PZT
2020A0298	A. D. Pant	muSR Study on the Electron Transfer Mechanism of a Blue Copper Protein, Pseudoazurin
2020A0009*	S. Hayashida	Evolution of magnetic state in the chemically doped quantum magnet $Cs_{1-x}Rb_xFeCl_3$
2020A0026*	P. Wu	Investigation of exotic magetic structures in kagome magnet Fe_3Sn_2 by muSR
2020A0050*	K. Iwasa	Magnetic penetration depths of superconductivity in chiral lattice materials $La_3Tr_4Sn_{13}$ (Tr = Co and Rh)
2020A0196*	K. Kubo	Synthesis of boratabenzene by negative muon capture
2020A0198*	J. Zhao	Detecting magnetic ground state in a layered frustrated quantum magnet
2020A0199*	M. Mihara	Negative muon spin relaxation measurements in water and ice
2020A0200*	T. Nakano	Negative muon spin rotation study for antiferromagnetism of Na nanoclusters arrayed in sodalite
2020A0201*	J. Takahashi	Emergence of optical activity in achiral amino acids and their precursor molecules by spin-polarized muon beam
2020A0212*	T. Kiyotani	Visualization of the electron and proton transfer associated with biochemical reaction process
2020A0257*	J. Nakamura	Electronic structure of impurity muonium in tin telluride and lead telluride
2020A0290*	M. Kusunoki	Muon spin rotation experiment of higher plant photosystem II protein in order to elucidate phtosynthetic electron transport mechanisms
2020A0297*	N. Nishida	μSR Approach to the understanding of Hydrogen Embrittlement in Steels
2020A0302*	T. Hirata	Impact Assessment of the Integrated Functional Mineral Crystal (IFMC.) Containing Magnetic Elements on Biological and Non-biological Substances

* Reserved

List of Proposals in FY2020 (2020-B) MLF

Exp-No.	Spokesperson	Title
2020B0043	C. Cao	The muon spin relaxation to confirm the intrinsic ferromagnetism of $Ba_{1-x}K_x(Zn_{1-y}Mn_y)_2Sb_2$
2020B0044	K. Shimomura	Kr/He mixture ratio determination for the systematic uncertainty reduction of muonium hyperfine measurement
2020B0092 (P-type)	S. Kanda	Feasibility study of a search for atomic parity violation in muonic atoms
2020B0096 (P-type)	H. Aoki	Dynamics of polymers at solid interface revealed by muon spin relaxation technique
2020B0111	K. Iida	Investigation of superconducting pairing in $(La_{0.5-x}Na_{0.5+x})Fe_2As_2$
2020B0116	H. Guo	MuSR studies on the magnetic ground state of the double perovskite iridate
2020B0244	T. U. Ito	Determination of the electron g-factor for a muonium-related paramagnetic center in rutile TiO_2 using the ESR technique
2020B0245	C. Ohmori	Temperature shift measurements of nano-crystalline formation for $Fe_{81}Cu_1B_{15}Nb_3$ and Febal.$Cu_1Nb_3Si_{15.5}B_7$ by high-temperature muSR
2020B0252	J. Sugiyama	Interrelationship between Na dynamics and microstructure in hard carbon as an anode material for Na-ion battery
2020B0259	T. Kiyotani	muSR study of the internal magnetic fields of human protein related amino acids
2020B0262	T. Kiyotani	Detection of functional processes of photoreceptive proteins by muon
2020B0264	M. Månsson	Ion Dynamics in Novel Potassium Fluorosulphate Battery Materials
2020B0268	Y. Sugawara	muSR approach to monitor peroxidase function of microperoxidase-11
2020B0277	M. Takahama	μSR study of magnetic properties in undoped and lightly-doped T*-type $La_{1-x/2}Eu_{1-x/2}Sr_xCu_1O_{4-y}F_y$
2020B0278	J. Nakamura	μSR study on paramagnetic state of chromium ion at $AgCrSe_2$
2020B0279	T. Uchino	Nucleation evolution and expulsion of spontaneous vortices in superconductor/ferromagnet nanocomposites probed by μSR
2020B0322	J. Sugiyama	Negative muon spin rotation and relaxation on battery materials
2020B0323 (P-type)	Y. Kobayashi	Study on ion conductivity of fluoride ion-battery
2020B0324	M. Mihara	Negative muon spin relaxation measurements in water and ice
2020B0326	M. Watanabe	muSR study on the randomness-induced quantum disordered ground state of spin-1/2 random bond FCC lattice antiferromagnets

Exp-No.	Spokesperson	Title
2020B0327	J. Sugiyama	Negative muon spin rotation and relaxation on Li metal
2020B0330	Y. Kiyanagi	Non-destructive measurements of carbon contents of Japanese swords
2020B0332	T. Nakano	Negative muon spin rotation study for antiferromagnetism of Na nanoclusters arrayed in sodalite
2020B0333	P. Strasser	Measurement of muonic helium atom HFS at zero field
2020B0334	J. Takahashi	Emergence of optical activity in achiral amino acids and their precursor molecules by spin-polarized muon beam
2020B0338	I. Umegaki	In-situ measurements of metallic Li in a Lithium-ion battery using negative muons
2020B0341	X. Zheng	Investigation of muonium formation and defect trapping in multipiezo materials of $LiNbO_3$ and $Sr_3Sn_2O_7$
2020B0350	W. Higemoto	Quantum Spin Fluctuations and Unconventional Superconductivity in $CeCoIn_5$
2020B0354	H. Okabe	Local dynamics of polar nanoregions in magnetic relaxor ferroelectrics
2020B0357	R. Higashinaka	Investigations of Unusual Heavy Fermion State in Partially Ordered State of $SmAu_3Al_7$
2020B0363	A. D. Pant	Generation of ultra cold muonium into vacuum from *n*-Si
2020B0366	W. Higemoto	Negative Muon capture process and electronic state in correlated electron systems
2020B0388	S. K. Dey	Investigation of magnetic spin dynamics in quantum spin liquid (QSL)-like state- “random spin-singlet state” in $Lu_2Mo_2O_5N_2$ by μSR spectroscopy
2020B0392	W. Higemoto	Anomalous Hall effect and spin frustration in chiral antiferromagnet Mn_3Ge and Mn3Sn
2020B0397	T. Adachi	Relationship between the developed Cu-spin correlation and superconductivity in the electron-doped high-T_c cuprates $Pr_{1.3-x}La_{0.7}Ce_xCuO_4$
2020B0398	S. Shamoto	Uniaxial strain induced metal-insulator transition
2020B0399	S. Shamoto	Highest tmperature magnetic short-range order in noncentrosymmetric magnets
2020B0401	S. Takeshita	Negative muon spin relaxation measurement as a method for probing molecular dynamics in polymers
2020B0402	T. Taniguchi	Competition between valence and spin fluctuations in novel single crystal $YbCu_4Au$
2020B0454	Y. Nagatani	Spectroscopy of muon emitted from muon-catalyzed dd fusion

Exp-No.	Spokesperson	Title
2020B0016*	P. Miao	Magnetism in a new spin chain system $Sr_6Co_5O_{15}$
2020B0045*	K. Mukherjee	Probing the unconventional superconductivity in the $ZrPd_2In$ Heusler alloy
2020B0064*	W. Hong	Searching for the antiferromagnetic quantum critical point in $Sr_2CuTe_{1-x}W_xO_6$
2020B0081*	J. Ma	Muon spin relaxation study on the spin dynamics of $NaTmSe_2$
2020B0085*	A. Bhattacharyya	Bhattacharyya Investigation of spin dynamics in spin chain compound Li_4NiOsO_6 and $Li_3Ni_2OsO_6$
2020B0115*	L. Shu	Muon Spin relaxation/rotation studies of non-centrosymmetric superconductor $NbGe_2$
2020B0249*	J. sugiyama	Fluoride ion diffusion in a novel oxyfluoride $Bi_{0.7}Fe_{1.3}O_{1.5}F_{1.7}$
2020B0254*	S. Tsutsui	Magnetic ordered states in quasi-skutterudite compounds $Sm_3T_4Ge1_3$ (T: transition metal) probed by mu^+SR
2020B0256*	H. Aoki	Mode analysis of polymer chain motion at solid interface revealed by muon spin relaxation method
2020B0266*	R. Palm	Muon investigation of H-storage materials confined in porous scaffolding compounds
2020B0267*	X. Zheng	muSR study of the correlation of muonium formation defects and elasticoluminescence in Eu:$SrAl_2O_4$ to reveal the mechanism of elasticoluminescence
2020B0268*	Y. Sugawara	muSR approach to monitor peroxidase function of microperoxidase-11
2020B0275*	I. Yamauchi	muSR study on the exotic ground state of the diamond lattice magnet
2020B0298*	T. U. Ito	Search for effective-mass shallow donor muonium in perovskite stannates with s-like conduction bands
2020B0299*	F. Koyanagi	Visualization of the electron and proton transfer associated with biochemical reaction process
2020B0303*	A. D. Pant	Generation of Ultra cold muonium into vacuum from KCl
2020B0312*	Y. Nagashima	Studies of muon and muonium emission from cooled metal surfaces
2020B0314*	D. T. Adroja	$K_3Ir_2O_6$: Potential candidate for Quantum Spin Liquid State to be Investigated Using Muon Spin Rotation and Relaxation Measurements
2020B0329* (P-type)	T. Kiyotani	Negative muSR study of the internal magnetic fields of human protein related amino acids
2020B0335*	I. Umegaki	Analysis of salinity of electrolyte solution in a Lithium-ion battery using negative muons

Exp-No.	Spokesperson	Title
2020B0336*	S. Yamamoto	Measurements of bremsstrahlung X rays during irradiation of muons for quality assessment of the beams
2020B0359*	N. Nishida	μSR Approach to the understanding of hydrogen embrittlement in Stees
2020B0375*	J. Song	MuSR study on a new triangular antiferromagnetic compound
2020B0387*	Z. Fu	Complex magnetic order in Fe(II)-azido layered magnetic honeycombs
2020B0396*	H. Yukawa	μSR approach to the understanding of hydrogen behavior in B2-type intermetallic compounds
2020B0400*	M. Miyazaki	Determination of muon site on La_2CuO_4 by mu-LCR via nuclear quadrupolar level-crossing resonance
2020B0404*	T. Adachi	muSR study of disorder effects on the chiral superconductivity in $BaPtAs_{1-x}Sb_x$

* Reserved

List of Proposals in FY2020 S-Type

Exp-No	Spokesperson	Title	Status
2011MS01	K. Shimomura	Precise Measurement of Muonium Hyperfine Structure and muon magnetic moment	2nd stage
2011MS02	A. Koda	μSR study of the metal-insulator transition of supercritical metal fluid	1st stage
2011MS03	M. Aoki	Experimental Search for mu-e Conversion in Nuclear Field at Sensitivity of 10^{-14} with Pulsed Proton Beam from RCS	2nd stage
2011MS05	N. Kawamura	Fundamental study towards the generation of negative slow muon beam	1st stage
2011MS06	T. Mibe	New Measurement of the Muon Anomalous Magnetic Moment $g-2$ and Electric Dipole Moment at J-PARC	1st stage
2013MS02	A. Koda	Study of superconductivity on the strongly correlated electron system probed by μSR experiments under high magnetic fields	1st stage
2014MS01*	Y. Miyake	Application of Muon Radiography for the "Photon and Quantum Basic Research Coordinated Development Program (MEXT scientific grants)"	2nd stage
2014MS02*	W. Higemoto	Development of D1 spectrometer instruments and μSR experiment in strongly correlated electron systems	2nd stage
2014MS04	K. Ishida	Measurement of the proton radius from the hyperfine splitting energy in the ground-state muonic hydrogen	1st stage
2015MS01*	Y. Miyake/ Y. Nagatani	Transmission Muon Microscopy	2nd stage
2019MS01	T. Takahashi	Development of new negative muon experiments using advanced space technology for X-ray and Gamma-ray observation: from atomic physics to high-precision 3D non-destructive element analysis	2nd stage
2019MS02* (S2-type)	R.Kadono	Microscopic mechanism of hydrogen-sensitive properties in inorganic materials	APPD
2020MS01	S. Uetake	ミュオニウムの 1S -2S レーザ分光によるミュオ ン質量精密測定	1st/2nd stage

* Start : the second half of year

Program Advisory Committee of
Muon Science Laboratory (April 2019 – March 2021)

T. Adachi	Condensed Matter Physics, Experiment	Associate professor, Sophia University
K. Amemiya	Condensed Matter Physics, Experiment	Professor & Head, KEK-IMSS
T. Azuma	Atomic Physics, Experiment	Chief Scientist, RIKEN
K. Fukutani	Condensed Matter Physics, Experiment	Professor, The University of Tokyo
W. Higemoto	Condensed Matter Physics, Experiment	Principal Scientist, JAEA-ASRC
K. Inoue	Condensed Matter Physics, Experiment	Professor, Hiroshima University
R. Kadono	Condensed Matter Physics, Experiment	Professor, KEK-IMSS
N. Kawamura	Subatomic Physics, Experiment	Associate professor, KEK-IMSS
Y. Kino	Subatomic Physics, Theory	Associate professor, Tohoku University
A. Koda	Condensed Matter Physics, Experiment	Associate Professor, KEK-IMSS
T. Kohzuma	Life sciences, Experiment	Professor, Ibaraki University
M. K. Kubo	Radiation Chemistry, Experiment	Professor, International Christian University
T. Mibe	Particle Physics, Experiment	Associate professor, KEK-IPNS
Y. Miyake	Radiation Chemistry, Experiment	Professor & Head, KEK-IMSS
C. Ohmori	Accelerator Physics, Experiment	Professor & Head, KEK-AL
T. Otomo	Condensed Matter Physics, Experiment	Professor & Head, KEK-IMSS
H. Seto	Condensed Matter Physics, Experiment	Professor & Deputy Director, KEK-IMSS
T. Shima	Nuclear Astrophysics	Associate Professor, Osaka University
K. Shimomura	Condensed Matter Physics, Experiment	Associate Professor, KEK-IMSS
Y. Sugawara	Biophysics, Experiment	Professor Emeritus, Kitasato University
J. Sugiyama	Materials Science, Experiment	Science Coordinator, CROSS-Tokai
M. Sugiyama	Materials Science, Experiment	Professor, Kyoto University
T. Takayanagi	Chemical Kinetics,, Theory	Professor, Saitama University

Muon Instrument Committee

(April 2019 – March 2021)

K. Aizawa	Materials Science	Section Leader, JAEA
M. Futakawa	Nuclear Engineering, Experiment	Division Deputy Director, JAEA
W. Higemoto	Condensed Matter Physics, Experiment	Principal Scientist, JAEA-ASRC
R. Kadono	Condensed Matter Physics, Experiment	Professor, KEK-IMSS
N. Kawamura	Subatomic Physics, Experiment	Associate Professor, KEK-IMSS
A. Koda	Condensed Matter Physics, Experiment	Associate Professor, KEK-IMSS
M. K. Kubo	Radiation Chemistry, Experiment	Professor, International Christian University
Y. Kuno	Subatomic Physics, Experiment	Professor, Osaka University
Y. Miyake	Radiation Chemistry, Experiment	Professor & Head, KEK-IMSS
J. Murata	Subatomic Physics, Experiment	Professor, Rikkyo University
S. Nakamura	Condensed Matter Physics, Experiment	Professor, Tohoku University
H. Nojiri	Condensed Matter Physics, Experiment	Professor, Tohoku University
T. Ogitsu	Cryogenics, Experiment	Professor, KEK-Applied Research
T. Otomo	Condensed Matter Physics, Experiment	Professor & Head, KEK-IMSS
K. Saitoh	Condensed Matter Physics, Experiment	Professor, Nagoya University
T. Shima	Nuclear Astrophysics	Associate Professor, Osaka University
K. Shimomura	Condensed Matter Physics, Experiment	Associate Professor, KEK-IMSS
K. Soyama	Quantum Beam Science	Deputy Division Head, JAEA
K. Yoshimura	Condensed Matter Physics, Experiment	Professor, Okayama University

KEK-MSL Personnel

Staff

K. Shimomura (Head, Professor)
R. Kadono (Professor)
A. Koda (Associate Professor)
P. Strasser (Associate Professor)
T. Yamazaki (Assistant Professor)
S. Kanda (Assistant Professor)
Y. Ikedo (Senior Engineer)
Y. Kobayashi (Engineer)
J. G. Nakamura (Engineer)
T. Yuasa (Technical Associate)
Y. Miyake (Professor)
N. Kawamura (Associate Professor)
Y. Oishi (Associate Professor)
Y. Nagatani (Associate Professor)
S. Matoba (Assistant Professor)
S. Takeshita (Assistant Professor)
H. Natori (Assistant Professor)
M. Hiraishi (Assistant Professor, August, 2020 ~)
H. Fujimori (Senior Fellow)
Y. Irie (Research Fellow)

S. Nishimura (Postdoctoral Fellow)
D. S. Kumar (Postdoctoral Fellow)
H. Okabe (Researcher)
T. Adachi (Researcher)
M. Tampo (Researcher)
A. D. Pant (Researcher)

H. Li (Technician)
S. Doiuchi (Technician)
A. Hashimotto (Technician)
Y. Ito (Technician)
T. Tachibana (Technical Staff)

I. Umegaki (Joint Research Visiting Scientist)

N. Nishida (Associate Researcher)
Y. Sugawara (Associate Researcher)
E. Torikai (Associate Researcher)
J. Sugiyama (Associate Researcher)

K. M. Kojima (Visiting Professor, TRIUMF)
S. Kurashima (Visiting Professor, QST)
S. Wada (Visiting Professor, RIKEN)
T. Nakano (Visiting Associate Professor, Ibaraki University)

Secretary

N. Nagata (Administrative Official)
N. Ichimura
Y. Gunchi
M. Koshida
N. Chinone
H. Shiosaka